Role of Carboxylate ligands in the Synthesis of AuNPs: Size Control, Molecular Interaction and Catalytic Activity

Dissertation by

Hind.AL-johani

In Partial Fulfillment of the Requirements

For the Degree of

Doctor of Philosophy

King Abdullah University of Science and Technology

Thuwal, Kingdom of Saudi Arabia

The dissertation of Hind Al-johani is approved by the examination committee.

Committee Chairperson: Prof. Jean-Marie Basset

Committee Member: Prof. Didier Astruc

Committee Member: Prof. Luigi.Cavallo

Committee Member: Prof. Kuo-Wei Huang

Committee Member: Prof. Pascal Saikaly

ABSTRACT

Role of Carboxylate ligands in the Synthesis of AuNPs: Size Control, Molecular Interaction and Catalytic Activity

Hind Al-johani

Nanoparticles (NPs) are the basis of nanotechnology and finding numerous applications in various fields such as health, electronics, environment, personal care products, transportation, and catalysis. To fulfill these functions, the nanoparticles must be synthesized, passivated to control their chemical reactivity, stabilized against aggregation and functionalized to achieve specific performances. The chemistry of metal nanoparticles especially that of noble metals (Gold, Platinum…) is a growing field. The nanoparticles have indeed different properties from those of the corresponding bulk material. These properties are largely influenced by several parameters; the most important are the size, shape, and the local environment of the nanoparticles.

One of the most common synthetic methods for the preparation of gold nanoparticles (AuNPs) is based on stabilization by citrate. Since it was reported first by Turkevich et al. in 1951, this synthetic scheme has been widely used, studied and a substantial amount of important information regarding this system has been reported in the literature. The most popular method developed by Frens for controlling the size of the noble gold nanoparticles based on citrate was achieved by varying the concentration of sodium citrate. Despite a large number of investigations focused on utilizing Cit-AuNPs, the structural details of citrate anions adsorbed on the AuNP surface are still unknown. It is known only that citrate anions “coordinate” to the metal surface by inner sphere

complexation of the carboxylate groups and there are trace amounts of $AuCl_4^-$, Cl^-, and OH^- on the metal surface.

Moreover, it is generally accepted that the ligand shell morphology of Au nanoparticles can be partly responsible for important properties such as oxidation of carbon monoxide. The use of Au-NPs in heterogeneous catalysis started mostly with Haruta who discovered the effect of particle size on the activity for carbon monoxide oxidation at low temperature.

The structure of the citrate layer on the AuNP surface may be a key factor in gaining a more detailed understanding of nanoparticle formation and stabilization. This can be affecting the catalytic activity.

These thoughts invited us to systematically examine the role of sodium citrate as a stabilizer of gold nanoparticles, which is the main theme of this thesis. This research is focused on three main objectives, controlling the size of the gold nanoparticles based on citrate (and other carboxylate ligands Trisodium citrate dihydrate, Isocitric Acid, Citric acid, Trimesic acid, Succinic Acid, Phthalic acid, Disodium glutarate, Tartaric Acid, Sodium acetate, Acetic Acid and Formic Acid by varying the concentration of Gold/sodium citrate, investigating the interaction of the citrate layer on the AuNP surface, and testing the activity of the Au/TiO_2 catalysts for the oxidation of carbon monoxide.

This thesis will be divided into five chapters.

In Chapter 1, a general literature study on the various applications and methods of synthesis of Au nanoparticles is described. Then we present the main synthetic pathways of Au nanoparticles we selected. A part of the bibliographic study was given to the use of Au nanoparticles in catalysis.

In Chapter 2, we give a brief description of the different experimental procedures and characterization techniques utilized over the course of the present work. The study of the size control and the interaction between gold nanoparticles and the stabilizer (carboxylate groups) was achieved by using various characterization techniques such as UV-visible spectroscopy, Transmission Electron Microscopy (TEM), X-ray diffraction (XRD), X-ray photoelectron spectroscopy (XPS), Nuclear Magnetic resonance spectroscopy (NMR) and Fourier transform infrared spectroscopy (FTIR).

In Chapter 3, we discuss the synthesis and size control of Au nanoparticles by following the growth of these nanoparticles by UV-Visible spectroscopy and TEM. We then describe the effect of the concentrations and of various type of the stabilizer, and the post-synthesis treatment on gold nanoparticles size.

In Chapter 4, we focus on determining the nature of the interactions at molecular level between citrate (and other carboxylate-containing ligands) and AuNP in terms of the mode of coordination at the surface, and the formal oxidation state of Au when interacting with these negatively charged carboxylate ligands (i.e., LX^- in the Green formalism). We achieve this by combining very advanced ^{13}C CP/MAS, ^{23}Na MAS and low-temperature SSNMR, high-resolution transmission electron microscopy (HRTEM)

and density functional theory (DFT) calculations. A particular emphasis will be based on SS-NMR.

In Chapter 5, we study the influence of pretreatment of 1% Au/TiO_2 catalysts on the resulting activity in the oxidation of carbon monoxide, the effect of the concentration and the type of the ligands on the catalytic activity. The catalysts were characterized by TPO, XRD, and TEM spectroscopy.

ACKNOWLEDGEMENTS

It is my great pleasure to take this as an opportunity to thank all the people because of whom this PhD thesis was possible.

I express my heartfelt gratitude and sincere thanks to Prof. Jean-Marie Basset for introducing me to the field of Nano science and providing me with an opportunity and resources to work under his valuable guidance. His ceaseless enthusiasm, resourcefulness, ingenuity in research and his constant motivation, support and constructive criticism have made a profound influence on me. It has been my great pleasure for being a part of his group and to work under such a close association with him. I owe him a lot for giving me a stable ground in all his capabilities and for the care he has shown towards me. My special thanks to Dr. Mohamad El Eter, especially for helping me out of the way by spending his valuable time in correcting and giving me important suggestions for compiling this thesis. I once again thank him along with Dr. Dr. Youssef Saih, Dr. S. Shiv Shankar for their constant encouragement, support and their elderly advise thinking about my betterment. My special thanks to Dr. Edy Abou Hamad for helping me out with the Solid NMR characterization at any odd time, I thank him for his moral support and for facilitating all requirements as an eminent collaborator and scientist. My sincere thanks to Dr. Dalaver.Anjum for helping me out with the transmission electron microscopy characterization at any odd time, giving me valuable training on using the instrument .

My gratitude's also goes to the Professors prof. Lyndon Emsley and Prof. Luigi Cavallo who have worked together since the beginning of my study

My special regards to many teachers because of whose teaching at different stages of education has made it possible for me to see this day and I thank all fellow labmates I could not mention one by one for their great support and valuable discussions.

One of the best things in my life. I was blessed with a loving and caring my Kids. Since then they become one of my biggest support and motivation to pursue and achieve my goal in this study. I am so much grateful for them understanding about my busy life with full schedule of research and study. Not only them supported my PhD, they are become the motivation and energy for me towards bigger dream and contribution afterward. Thanks for always be there in every steps I take. I would like thank my husband Ahmed and at this point I am lost for words to express how grateful I am for his unparalleled support while I have been working on my PhD.

Finally, my family; my mom, and brothers and sisters are the source of my joy happiness. Nothing I want in this life other than to make them happy and proud of me. Especially for my late father, he may not be here anymore but there is always a place in my heart for him. There is always a believed that he sees me from his place and making the best of his will is always my goal in this life. I can still feel his presence. I thank them for their endless love and support.

Hind AL-johani

TABLE OF CONTENTS

LIST OF FIGURES

Chapter 1

Chapter 2

Chapter 3

Chapter 4

Chapter 5

LIST OF TABLES

Chapter 4

Chapter 5

Chapter 1.

Introduction

The beginning of the colloid chemistry dates from the mid-19th century when Michael Faraday[1] performed the synthesis of gold nanoparticles by reducing tetrachloro-aurate white phosphorus in the presence of carbon disulfide CS_2. In the early 20th century, Wilhelm Ostwald contributed to the development of the science of gold colloids. He was the first to demonstrate that the metal nanoparticles have different properties from the bulk materials and concluded that these properties are mainly determined by the surface atoms. The physical and chemical properties of the particles have been affected by miniaturization of Au particles to the nanoscale. This is explained by the fact small particles have an increasing the number of surface atoms. The surface atoms have low coordination number. Gold nanoparticles have numerous applications in various areas, For example, optics, electronics, catalysis, and pharmaceutical. The first part of this chapter will be devoted to a literature review of the use of these gold nanoparticles in these various fields. In the second part, we will focus more particularly on the different methods of synthesis of gold nanoparticles.

1.1 Overview on gold nanoparticles

Nanotechnology, Nanoscience, nanostructure, and nanoparticles are highly represented presently in the scientific literature. Nanotechnology includes the characterization, manipulation and fabrication of materials and devices at the "nano" scale (1 nanometer is equivalent to one-billionth (10^{-9}) of a meter). The rough estimate for defining nanotechnology is the measurement of a material or device at one or more dimensions in the range of 1-100 nm. To put this into perspective, "a human hair is approximately 80,000 nm wide, and red blood cells roughly 7000 nm wide[2]." Nanotechnology and nanoscale materials are not entirely new. There have always been nanoscale materials in the environment, and it could be argued that many biological substances such as DNA (strands which have a 2 nm diameter) are a form of nanotechnology. Humans inadvertently have even made use of nanotechnology's wonderful properties. The Damascus Sabre from the seventeenth century has been shown to have carbon nanotubes and cementite nanowires which help give the blade "unusual mechanical properties and an unusually sharp cutting edge[3]." The difference is, today, we are gaining the ability to create nanomaterials and nanotechnologies for our own specifications; creating new devices that have new and novel properties. **Figure 1.1** shows the examples of man-made and natural fabrication of materials at small scale routinely.

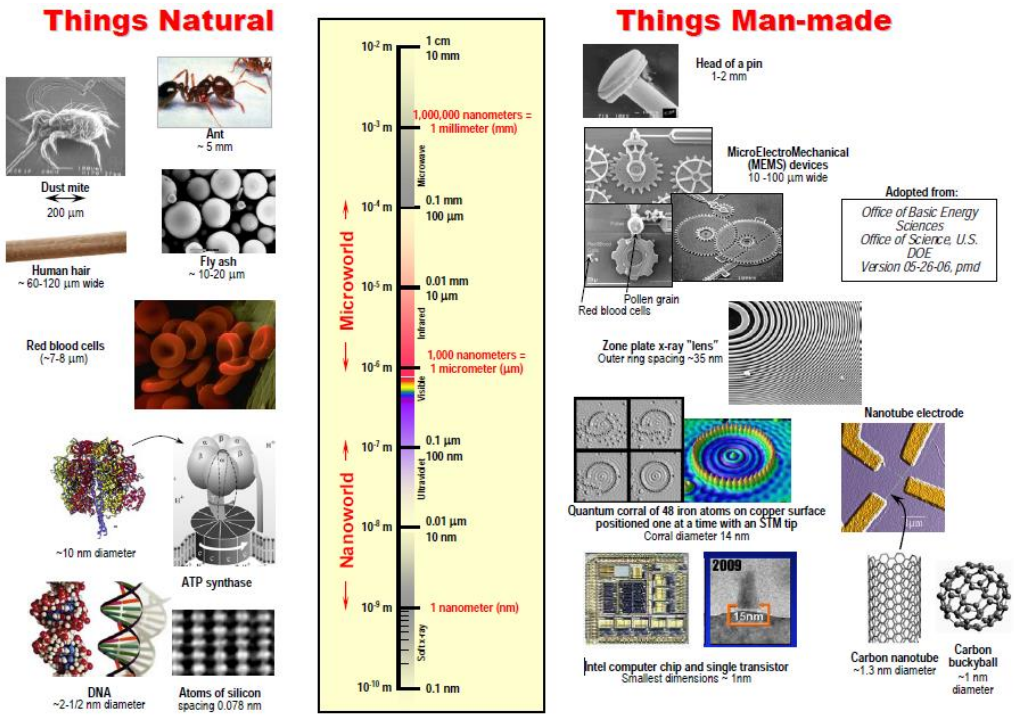

Figure 1.1 Picture demonstrating the comparative sizes of several naturally happening objects/species and man-made materials.

So that let us ask the question: What are the properties of gold, which make it so broadly applicable? The chemistry of gold is considerably different compared to other metals and the main reason for this is its relativistic special effects, As it can be seen from **Figure 1.2** this effect is most pronounced for gold, which explains the unique position of gold among all the elements[4].

This impact which unequivocally impacts its physical and chemical properties[5].

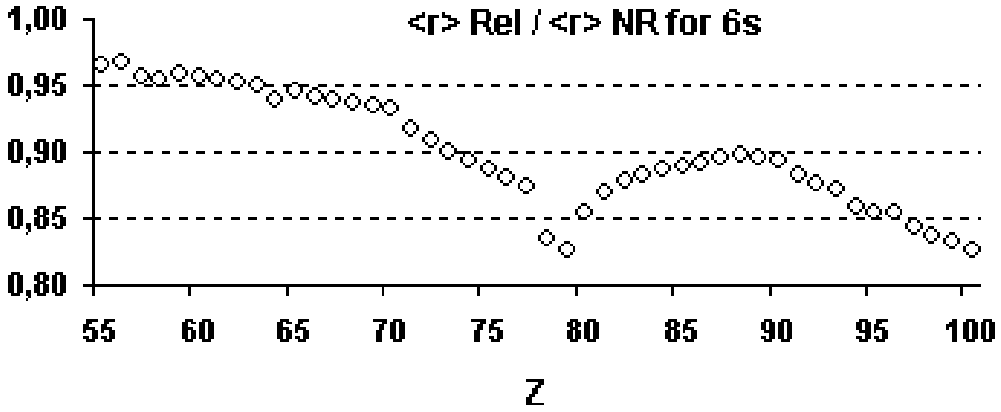

Figure 1.2 Calculated relativistic contraction of the 6s orbital. The relativistic (<r>rel.) and non-relativistic (<r>non-rel.) 6s orbital radii were determined computationally. The relativistic effects on electrons are most pronounced at 79Au[4].

Gold has the highest electrochemical potential and the highest electronegativity of all the metals.

The electronic configuration of Au^0 is $5d^{10}6s^1$, of Au^+ is $5d^{10}6s^0$ and of Au^- is $5d^{10}6s^2$ [6]. Au^+ or Au^- could be expected based on the well-known electron configurations.

The electrons on the 6s orbital being closer to the nucleus also explain why gold has a high electron affinity, which leads for example, to the formation Cs^+Au^- and $NMe_4^+Au^-$ [7]. The captivating yellow color of gold can be also attributed to relativistic effects. The energy of the 5*d* electrons is raised and the energy of the 6s electrons is lowered[8]. Therefore, the light absorption (primarily due to the $5d \rightarrow 6s$ transition) takes place in the blue visual range (2.50–2.75 eV). It absorbs blue light and reflects the rest of the

spectrum which results in a yellowish golden colour[9]. In contrast, another element of the group 11, silver absorbs at around 3.7 eV in the ultraviolet region[6, 10]. Due to this $4d \rightarrow 5s$ transition, silver does not absorb in the visible range and has a metallic shine. The "non-relativistic band structures" of silver and gold are very similar, so if relativistic effects did not exist, gold would look like silver[10].

Indeed, for a long time metal nanoparticles have been used. Emerged in the 5th and 4th century Before Christ, the soluble gold was used in China, Egypt and India to curative and artistic goals. In the middle ages, gold was already used for artistic purposes among which we can mention the color of the windows. e.g. during the past decade, people used metal nanoparticles to create rich colors in stained glass from the Roman times (4th century AD), though likely without realizing it.

This glass reflected and transmitted light showing unusual color changes caused by the precious metal bearing material added by the Roman glassworkers when the glass was molten. It appeared red in transmitted light and green in reflected light because of the presence of gold colloids. The reason behind the color is the presence of nanoparticles in the glass which is formed by the reduction of earlier dissolved gold during heat-treatment of the glass resulting in a fine dispersion of gold nanoparticles.

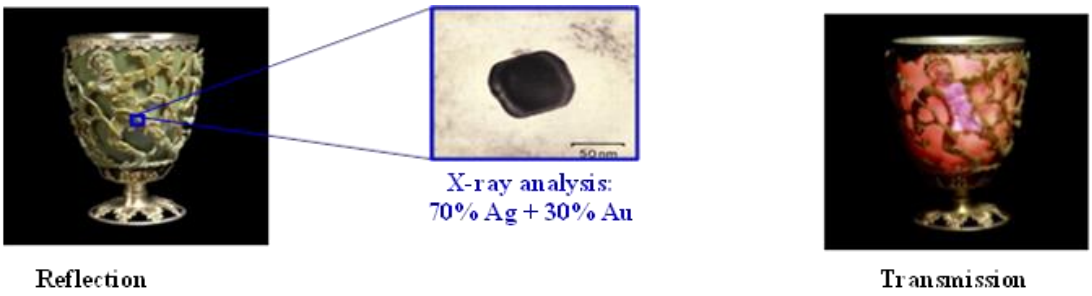

Figure 1.3 Lycurgus Cup.

These nanoparticles(see **Figure 1.3**) [11] By X-beam examination demonstrated that the proportion of silver to gold of around 7:3, containing 10% of copper.

The most important property obviously is size effect, and many applications depend on it. The beginning of the colloid chemistry dated from the mid-nineteenth century when Michael Faraday [12] carried out a systematic study. By reduction of an aqueous solution of chloroauric ($AuCl_4^-$) by white phosphorus (phosphorus diethyl ether solution) in the presence of carbon disulfide CS_2 (a two-phase system). He explored the optical properties of thin films set from dried of deep red colloidal solutions and notification the color of the films upon mechanical compression was changing reversibly (from bluish-purple to green upon pressurizing)[1]. In the early 20th century, Wilhelm Ostwald contributed to the development of the science of gold colloids. It was found that the first metal nanoparticles have different properties in bulk materials and deduced that these properties are mainly determined by the surface atoms. The miniaturization of Au particles at the nanoscale has a significant effect on the physical and chemical properties of the particles. This is due to the fact that increasing the number of surface atoms will be obtained by reducing particle size. The surface atoms have a low coordination number of atoms relative to the central and, therefore, are more mobile. In 1861, Graham coined the term

"colloid". Until the 20th century, gold colloid was used in medicine for the diagnosis of syphilis, a method which remained in use until the 20th century; the test is not totally reliable[13]. The most popular method for the synthesis of AuNPs is by using citrate reduction of gold (III) in water found by J. Turkevich et al in 1951. He described that this method generally produces gold nanoparticles of size around 10-20 nm[14]. This method was refined by G. Frens in the 1970s to obtain AuNPs of prechosen size (in the range 16 to 147 nm) by varying the reducing agent to stabilizing agent ratio(the trisodium citrate to- gold ratio This is a frequently used method by researchers and could control the size by varying the stabilizer to gold ratio[15].

In the following sections of this chapter: the first section will be devoted to a literature review of the use of these gold nanoparticles in various fields and brief introductions to the process of particle formation and we will consider 3 aspects pertaining to gold nanoparticles synthesis, i) will relate to the reduction mechanism of Au (III) ions to the Au(0) state necessary for the formation of the nanoparticles. ii) Will relate to the kinetics of particles formation focusing on the nucleation and growth pathway of gold nanoparticles in the presence of Citrate. iii) Will relate to the surface studies that investigate the mode of interaction between citrate and the metal surface responsible for the stabilization. With reference to the second section of this chapter, we will talk about the catalytic test based on their synthesis and the mechanism we proposed.

The properties developed by the nanoparticles of Au (catalytic, biomedical and optical) are influenced by the shape and size of the nanoparticles. The control of the shape and size of the nanoparticles is mainly based on the method of synthesis used for their preparation. Before talk about the different synthesis methods developed for the preparation of nanoparticles. We will use quite a lot of space on the propriety of gold nanoparticles.

1.2 The propriety of gold nanoparticles

1.2.1 The plasmon resonance

Noble metals such as Au and Ag respective electronic structures [Xe] $4f^{14}5d^{10}6s^{1}$ and [Kr] $4d^{10}5s^{1}$ have filled *d* orbital electron and one electron in the s orbital. It is these electrons that once relocated within the crystal lattice fill the conduction band. At the nanoscale, the metal nanoparticles can absorb and scatter electromagnetic radiation of wavelength greater than the size of the particles. In a particular field frequency, the surface Plasmon resonance phenomenon is a collective oscillation of the conduction electrons when the nanoparticles interact with an incident light for diffusive overall because of that. This effect is particularly noticeable in the visible part of the absorption spectrum of the nanoparticles of Au, Ag, and Cu. The Plasmon resonance of a metallic nanoparticle is characterized by two parameters:

Its energy E

$$\boldsymbol{E = \hbar\omega\rho = \hbar\frac{\sqrt{4\pi ne^2}}{m_0}} \qquad (\mathbf{1})$$

(n is the conduction electron density, m_0 the actual mass electrons, and ωρ is the Plasmon frequency).

And its uniform width Γ which is connected to the damping time (or phase shift) T_2 of the oscillation by the relationship:

$$\boldsymbol{\Gamma = \frac{2\hbar}{T_2}} \qquad \textbf{(2)}$$

These two parameters are largely influenced by nature, size, shape of the metal nanoparticle[16] and also the surrounding environment[17], but also by the dielectric medium in which the nanoparticles are. Only metals with free electrons have a plasmon resonance in the visible spectrum and are, therefore, intense colorations.

The size of the nanoparticles is a significant parameter in the interaction between the light and particles. The color of a colloidal gold solution varies from blue to orange through various purples and reds when the nanoparticle size is reduced to ~ 3 nm. Au nanoparticles exhibit an intense absorption band in the visible region around 520nm.

1.3 Methods of preparation of nanoparticles

In 1959, Richard Feynman was the first researcher to propose that devices and materials could one day be created to atomic particulars without consider the laws of physics[18]. He anticipated concepts that are nowadays commonly used in nanotechnology such as bottom up and top down approaches to the fabrication of miniaturized objects.

In general two basic approaches are accepted for the synthesis as well as the fabrication of nanomaterials. Since that time the researchers are trying to follow both:

“top-down” and “bottom up” approach **Figure 1.4**. Top-down fabrication mainly processes from breaking down of bulk starting materials to make nanomaterials. In the top-down systems, the preferences are composed straightforwardly onto a substrate, for instance, by electron beams, and then by applying suitable engraving and deposition processes, the nanoscopic features are engraved. The biggest disadvantage with a top-down approach is that it is expensive to perform slow and not suitable for large-scale production. But this method is suitable for the bulk production of nanomaterials. In this case, the nanoparticles are mainly produced by reducing the size of fragments of metal oxides or metals. As an example, include The mechanical alloying[19]; this method does not lead to a control of the size and morphology of the particles because the structures are broken down gradually until the nanoscale particles. The particles obtained by this method have a size of between 0.5 and ten microns. [20].

Although by the Bottom up approach can obtain more homogeneous chemical composition they contain fewer amounts of defects. There are some explanations for this; First of all, it assumes a critical part in both manufacture and preparing of nanostructures. At the point when the building blocks fall into nanometer scale, the top-down methodology is unlikely. The tools that we possess are too huge to manage such small objects. Second Fabrication is much less expensive, also fast and suitable for up-scaling.

In general, in the "bottom-up" approach, there are two types of reactions: the reduction reaction and decomposition. Both reactions can occur in gaseous, liquid or solid phase.

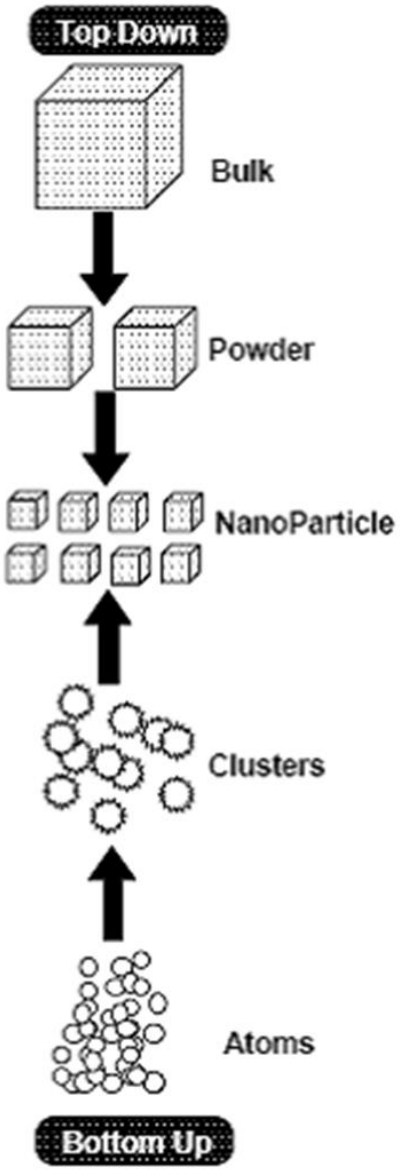

Figure 1.4 Pictorial representation of the two basic approaches used for the production of Nanostructures.

With increasing importance and applications of nanomaterials a number of physical and chemical routes for their synthesis has been reported and can be broadly classified as presented in **Figure 1.5**:

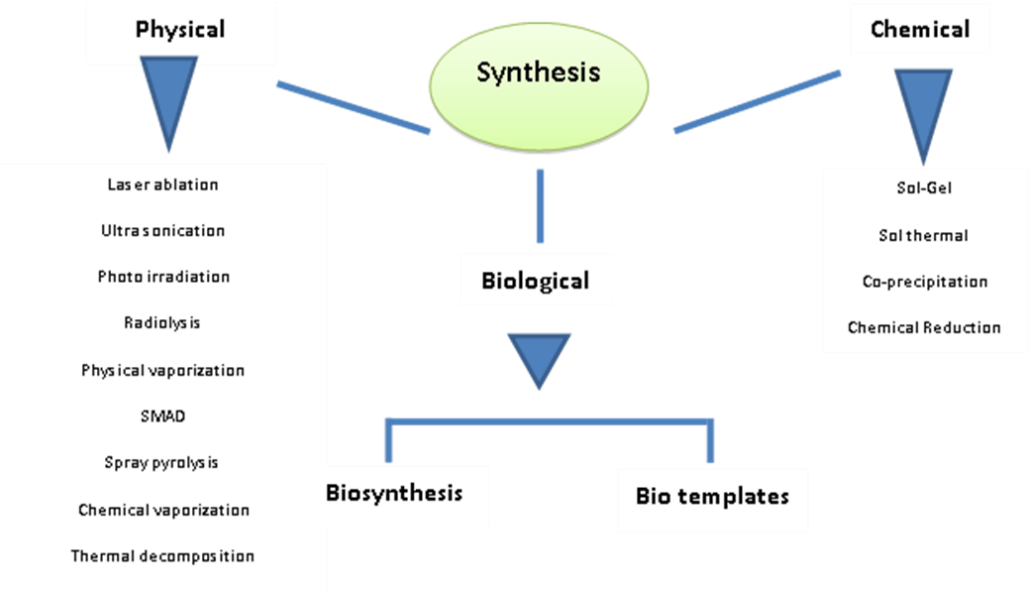

Figure 1.5 Illustration outlining the several methodologies for the synthesis of nanoparticles.

1.3.1 Methods of preparation of nanoparticles chemically: gas phase.

Most union strategies for nanoparticles in the gas stage depend on homogeneous nucleation in the gas stage and consequent buildup and coagulation, the generation of nanoparticles from the vapor stage requires the establishment of super immersion. This is made by physical or chemical techniques. The physical techniques include some type of mixing of the monomers, by extension, with a cooler gas or by warmth exchange to the environment. Supersaturation can be accomplished additionally by concoction responses which deliver the anon unstable condensable item. These responses are normally

decomposition reactions started by an ascent in temperature and utilized widely as a part of laser and fire reactors[21].

1.3.2 Methods of preparation of nanoparticles chemically: liquid-phase (colloidal).

The first use of the colloidal method dates back to Faraday who in 1857 prepared the colloids[1], Wet synthesis methods (liquid-phase) are a smart system as a minimum for two causes: first they are more energy effectual. Second they produce nanoparticles by using the regular device obtainable in a laboratory. Colloidal methods let prepare large amounts of products and are suitable for the manufacture of nanoparticles[22].

1.3.3 Reduction

The reduction of an ion or a complex can be achieved by following:

- Chemical reducing agent ex. alcohols (polyol synthesis), [23] [24] Citrate, [14]hydrazine[25] and borohydrides[26].
- Electrochemical reduction[27] [28].
- Microwave irradiation, radiolysis, photochemistry and sonochemistry[29] [30].
- Chemical reduction in micellar medium (nanoreactors) [31] [32].
    - Biological production of reducing species such as radicals or electrons by radiolysis.

1.3.3.1 Chemical reduction

It is by far the most broadly used method for the synthesis of nanoparticles. Obtaining metal nanoparticles are done here in a liquid medium. It can be passed out in aqueous or organic phase and the main reactants are as follows:

Metal salt + solvent + Gear + Surfactant

In this diagram, the salt is the metal-containing precursor, the solvent may be aqueous or organic for example toluene. The solvent should be polar and have a relatively high dipole moment in order to break the bonds of salt and dissolve. The gear is selected to reduce the dissolved metal species so that they precipitate metal particles. The surfactant plays the role of a protective agent of metal particles by adsorbing to the particle surface and making it possible to prevent them from agglomerating. The morphology and the size distribution of nanoparticles controlled by parameters such as the reduction kinetics and the nature of the stabilizer.

1.3.3.1.1 Reduction by citrate and hydrazine

Reducing a salt of Au by sodium citrate in aqueous solution is the most known method. A century after the synthesis of Faraday, it is developed to the first time in 1951 by Turkevich et al[14]. It can produce spherical nanoparticles by reduction of tetrachloroauric acid ($HAuCl_4$) using citrate. The beauty of this method lies in its simplicity and the fact that it provides easily stable and monodisperse colloids by the in situ reduction of gold salts in solution water at a temperature of 100° C. In this synthesis, citrate plays both the role of reducing and surfactant agent as it prevents aggregation by

introducing a charge to the particle surface. Further work on the synthesis of Au nanoparticles resulting from the reduction of Au salt citrate was performed by Frens [15]. Thus in 1973, he showed the possibility to control the average particle size by varying the "concentration of gold salt" ratio of "concentration of citrate" ($[HAuCl_4]$ / [citrate]). Thus, by reducing the amount of citrate used in the synthesis, is reduced citrate ion quantity necessary for the stabilization of particles causing aggregation smaller grit particles until the surface becomes large enough to be covered by the current citrate ions.

Hydrazine (N_2H_4) is a weak base with reducing properties. In the presence metal ions, it is associated with the latter to form complexes. Hydrazine as an example was used to prepare Au[25], Ag[33], CdSe[34] and Ni[35] nanoparticles. The redox process to use hydrazine as reducing is easy and inexpensive. In addition, hydrazine is oxidized to N_2 during the reduction, and therefore considered as "clean" [36] gear. However, the literature on mechanisms of reduction of metal ions in the attendance of hydrazine is undeveloped.

1.3.3.1.2 Reduction by borohydrides

Borohydrides are very strong reducing agents and are therefore good candidates to reduce the metal ions. However, it very difficult to control the size of particles due to the rapid reaction kinetics. The best-known method of synthesis is that developed by Brust et al[37] for the synthesis of Au nanoparticles stabilized by thiols. Synthesis of nanoparticles using toluene as a solvent has inspired by the two-phase system made by Faraday in 1861[13a] and was developed in 1993 by Giersig et al[38]. It provides monodisperse nanoparticles sizes and well-controlled forms. Generally, the particles obtained by this method have a size less than 10 nm. In 1994, Brust et al develop a method of synthesis of

Au nanoparticles in toluene known today as the synthesis of Brust[37]. It provides protected nanoparticles by a monolayer of thiol, a simple procedure during which the chemical reduction of salt occurs in a biphasic system (H_2O + Toluene) in the presence of a thiol as a surfactant. The aqueous phase contains the gold salt and reducing agent ($NaBH_4$aq) while the organic phase consists of toluene, a transfer agent (usually tretraoctylammonium bromide (TOAB)) and surfactant **Figure 1. 6**. The resulting particles are very stable and have an average size between 1.5 and 5.3 nm. They are also very soluble in most polar solvents. Thiols attached to the surface of the Au nanoparticles provide not only the stability of the nanoparticles but also allows to adjust the properties of the resulting nanohybrid. Brust method can also be used for the synthesis of Au nanoparticles stabilized with amines. For this, it suffices to replace the alkyl thiol with an amine in the synthesis[39]. In this synthesis, the size particles depend here on the ratio of the Au salt and the surfactant (amine or thiol). Being As the primary amines are strong enough reducing agents to yield the nucleation of nanoparticles, the particle formation is observed even in the absence of $NaBH_4$[26].

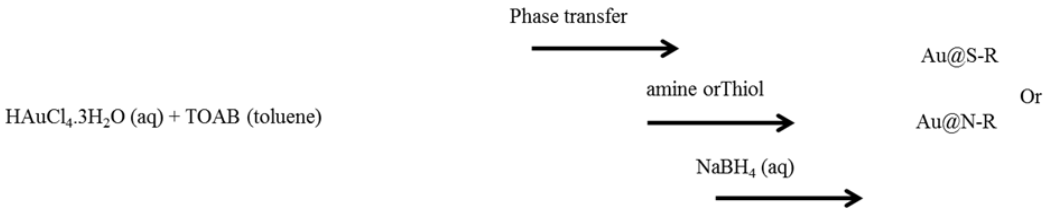

Figure 1. 6 Scheme of Brust method for Synthesis of Au nanoparticles

Other reducing agents may be used in aqueous solution to obtain nanoparticles, for examples; polysorbate [80] [40], cephalexin[41] and mercaptosuccinic acid[42, 43].

.

1.4 Modes of stabilization

Nanoparticles in suspension do not represent a thermodynamically stable system. They tend to agglomerate to form solid metal, less energy object, which precipitates in solution[44]. Therefore, suspension needs to be stabilized. There are generally two types of stabilization: electrostatic and steric ones. Steric stabilization represents a method commonly used in colloidal suspension. It consists to add to the solution an element which presents a large volume, typically a polymer or organic ligand, which adsorbed on the surface of the NPs prevents from agglomeration. These large molecules form a barrier around the NPs and avoid them to coalesce **Figure 1.7**.

Figure 1.7 Steric stabilization of NPs; a) short and b) long surfactant chains.

Electrostatic stabilization is achieved by introducing ionic species in solution such as carboxylates. Indeed, Van der Waals forces lead to an attraction between NPs in suspension. To relieve this phenomenon and stabilize NPs, the addition of ionic compounds that will adsorb on the surface of NPs leads to the formation of an NPs protective layer. This surface electrostatic repulsion will insure repulsive forces between

NPs and drive to the stabilization of the nanoparticles suspension as displayed in **Figure 1. 8**.

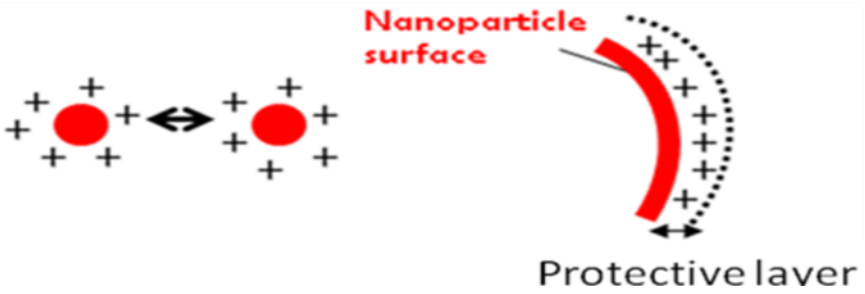

Figure 1. 8 Mechanism of stabilization of NPs by electrostatic repulsion.

The stability of a colloidal solution results from the balance between attractive and repulsive interactions acting on the particles. These interactions also depend on various parameters such as temperature and pH of the solution. In addition, stabilizers combine these two phenomena and are entitled ***electrostatic*** ones. Numerous endeavors were dedicated to synthesizing colloidal gold nanospheres. In reality, three ways were generally utilizing the precipitation procedure for the synthesis

The synthesis of larger Au NPs involves yet a decrease of the shape and size NPs distribution in the suspension. As previously mentioned, the stability of the suspension is insured by the presence of charged surfactant: citrate molecules surrounding the Au NPs **Figure 1.9**.

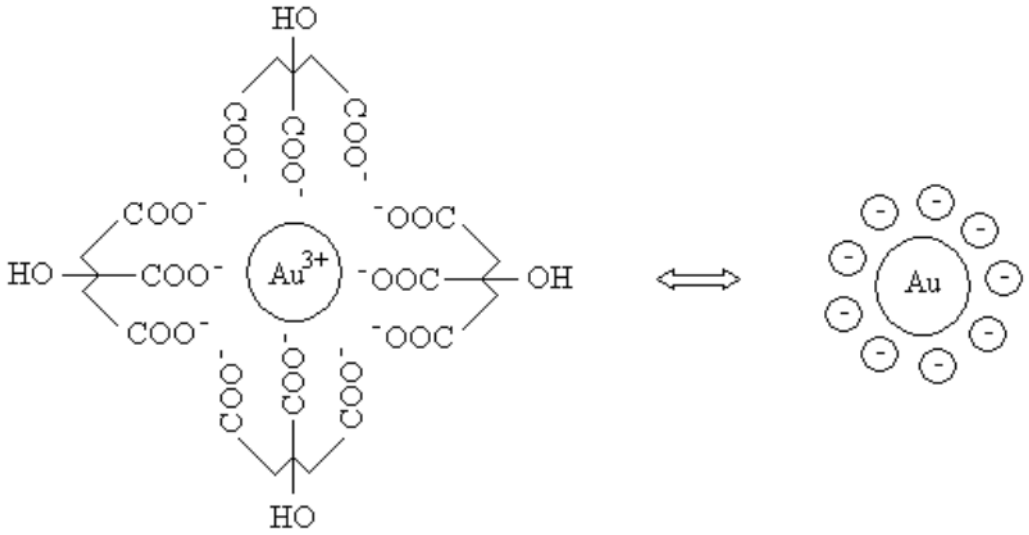

Figure 1.9 Representation of a colloid spherical gold nanoparticle (relative size of molecules and NPs are not at scale).

In our research work, we have prepared gold nanoparticles of spherical forms by Turkevich synthesis methods modified by reduction of $HauCl_4$ by sodium borohydride as reducing agents. The ratio change of common precursor tetra chloroauric acid to stabilize as citrates allows in principle to control the size.

1.4.1 Features of the citrate process

1.4.1.1 Method of Turkevich;

Developed in 195148, it is a fairly simple method for obtaining spherical colloids by in situ reduction of gold salts in aqueous solution with citrate sodium at a temperature of 100°C **Figure 1.10.**

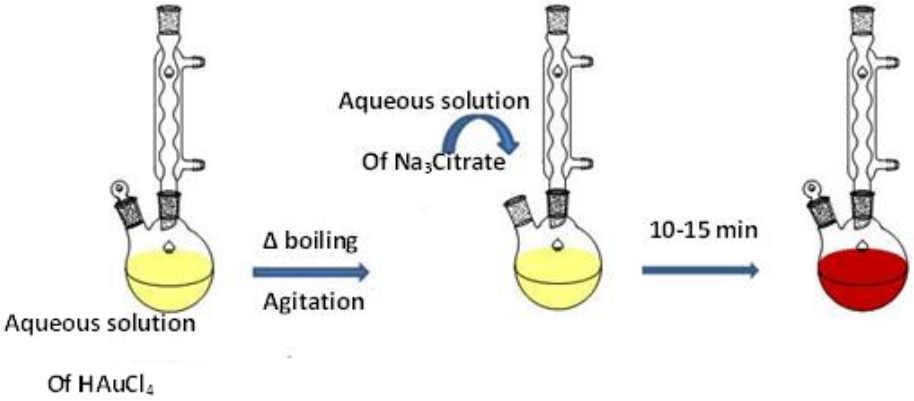

.

Figure 1.10 Experimental scheme for the synthesis of nanoparticles of Au by the method of Turkevich.

Figure 1. 11 show the reaction mechanism of the reduction of salt by the citrate. According to this mechanism, we need 3 moles of citrate to reduce one mole of Au^{3+} ions into Au^0. Thus, the reduction of the salt to metallic gold is only possible in the presence of an excess of reducing agent. This corresponds to a molar ratio of 1/3 between the sodium citrate and Au.

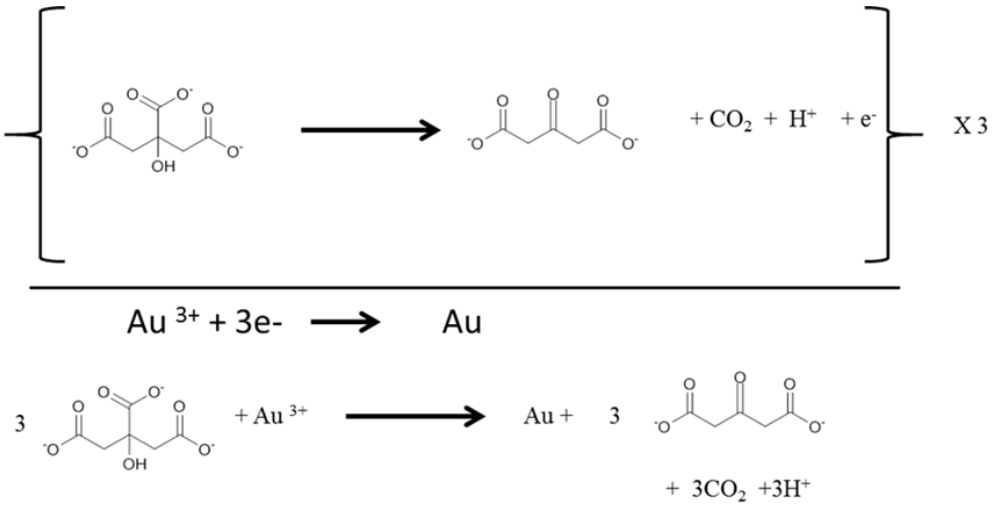

Figure 1. 11 Reaction mechanism for the reduction of the salt citrate.

This method of synthesis remains one of the most used because it permits to obtain spherical particles of different sizes by changing the ratio [$HAuCl_4$] / [Citrate]. Sodium citrate plays a dual role: it allows on one hand to reduce Au^{3+} ions in Au^0 and its stabilizing nanoparticles by adsorbed on their surface. This despite widespread in the literature, this reaction is complex in many parameters.

1.4.1.2 Method of Frens:

From Turkevich[14], we concluded that his method might be promising for the preparation of monodisperse gold suspensions with broadly dissimilar particle diameters by reduction of gold chloride with sodium citrate in aqueous solution.

Unlike the Turkevich method[14], the method of Frens [15] is carried out in two steps following the experimental procedure is shown in Figures 1.10. During the first step is obtained spherical gold particles of sizes between 15 and 20 nm in diameter **Figure 1.12**.

These are used as seeds in the second step to obtain spherical particles of larger sizes **Figure 1.13**.

Step 1: Synthesis of spherical nanoparticles: (Ø ~ 15-20nm).

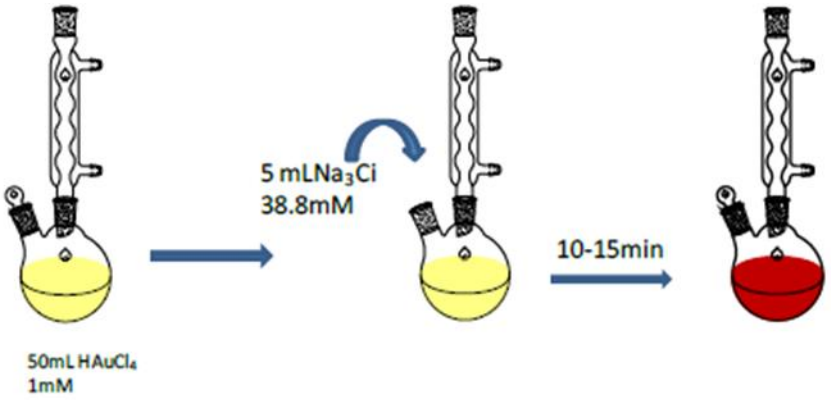

Figure 1.12 Experimental scheme for the synthesis of 15 nm diameter gold nanoparticles.

Step 2: Synthesis of spherical nanoparticles of larger sizes.

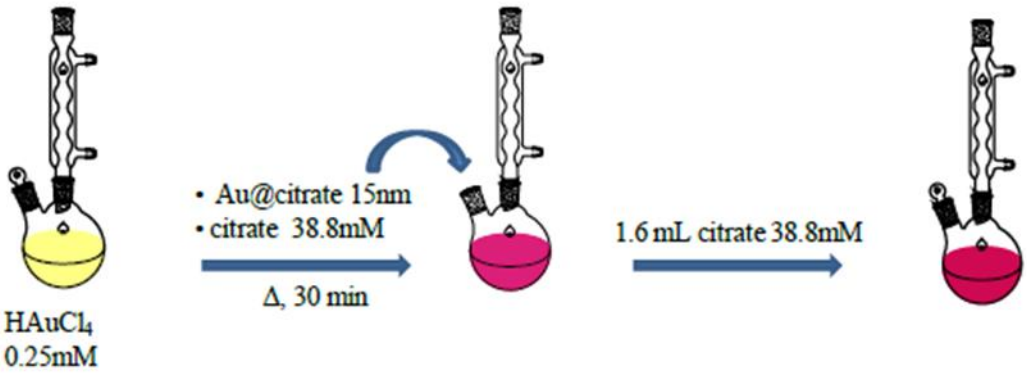

Figure 1.13 Experimental scheme for the synthesis of nanoparticles of at sizes greater than 15 nm.

Frens proposed technique where reducing stabilizing agent, citrate to gold proportion was changed. This outcome in particles is easily obtained with a wide size range (diameters between 10 and 20 nm). Nevertheless, it is critical to note that from 20 nm diameter, deformation of the particles is observed leading to a higher polydispersity in forms and monodispersity was observed to be poor.

1.4.1.3 Freund and Spiro method:

The monodisperse citrate-stabilized gold colloids were prepared from $HAuC1_4$ and trisodium citrate by the method of Frens[15] with some modifications[45].

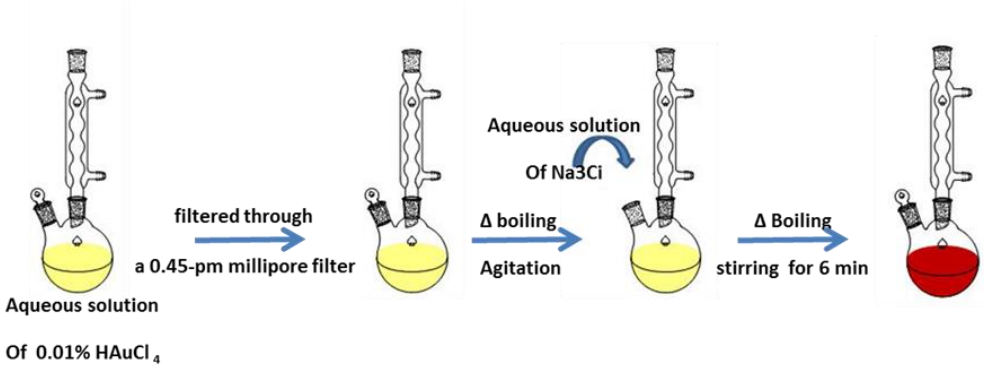

Figure 1.14 Investigational pattern for the synthesis of nanoparticles of Au by the strategy of Freund and Spiro.

The solution was at 25°C and stored in a 25 mL volumetric flask. The colloids were indefinitely stable if stored at 5-10°C.

1.4.1.4 Chow and Zukoski method[46]

For this type reaction conditions used here, in agreement with Frens [15], when boiling the $HAuCl_4$ and citrate solutions were mixed, there was almost instantaneous appearance

of dark red color indicating the formation of 15 to 25 nm diameter gold particles **Figure**

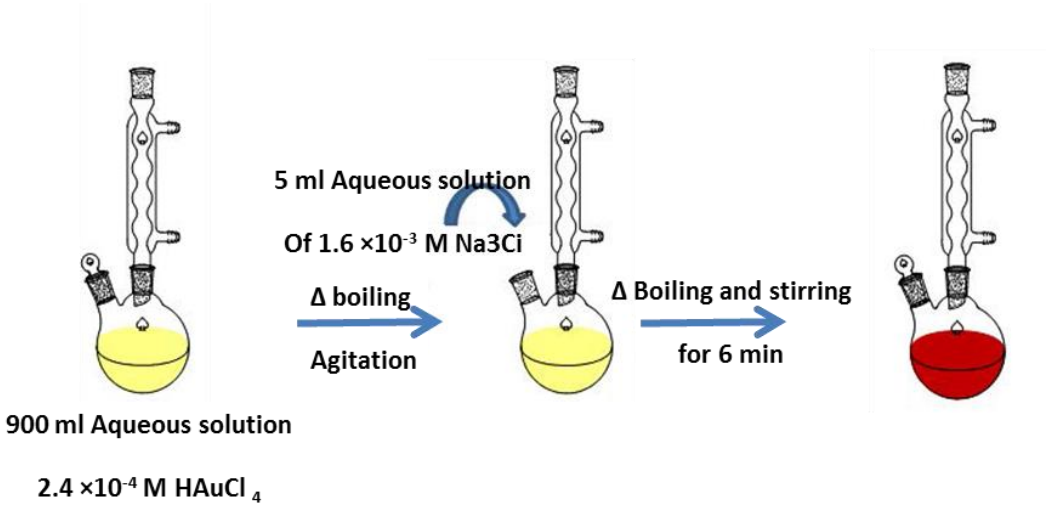

1.15.

Figure 1.15 Experimental scheme for the synthesis of nanoparticles of Au by the Chow and Zukoski method.

1.5 Catalytic test

Catalytic reactions play important roles in our daily life. Catalysis contributes to sustainable development through a decrease of the energy consumption of the endothermic processes and eliminating or at least dramatically decreasing pollution from chemical and refining processes. The development of selective, highly active catalysts working under mild conditions meets the requirements of green chemistry. Application of nanoparticles and nanostructures in catalytic materials may generate improved unique properties.

Gold the most stable among all metals was thought to be inactive in catalysis until Haruta's discovery of the catalytic power of gold in carbon monoxide oxidation when its

size is in the nanometer range. Later high activity of gold nanoparticles was demonstrated in various oxygen– transfer and hydrogenation reactions such as hydrogenation of alkenes. Gold catalysts have many advantages compared to platinum group metals; it is resistant to the oxidative atmosphere, moreover gold has greater price stability, high resistance to corrosion, flexibility[47] and very high electron negativity. In fact, gold has a stable form with an oxidation state of +1.

In my work, I focused on supported gold catalysts in TiO_2 support for CO oxidation reactions to understand better the nature of the active sites and on reaction specific modifications to develop more efficient catalysts for the reaction.

1.5.1 Gold nanoparticles: catalysis and environment

Au nanoparticles dispersed metal oxide supports reducible (MnO_2, α- Fe_2O_3, Co_3O_4, NiO, CuO, and TiO_2) and not reducible (SiO_2, Al_2O_3) are considered very promising catalysts in the field of electrochemistry, environmental protection, and chemical synthesis. Most of these catalysts are active, selective and durable to moderate temperatures and efficiency generally depends on the interaction between the nanoparticles and the substrate. These properties depend on some parameters, among which one can mention:

- **Particle size**; in the sense that the particles of smaller sizes have a larger specific surface area which therefore provides a more activity high Janssens et al. have drawn a curve (
- **Figure 1.16**) of the catalytic activity of gold supported on different oxides for oxidation of CO[48].

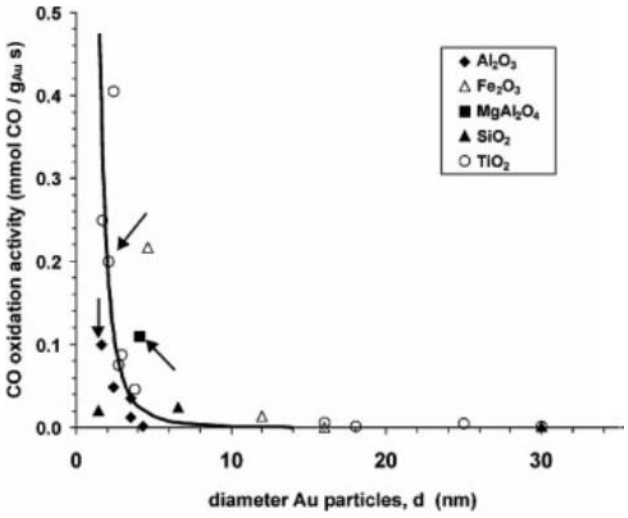

Figure 1.16 Catalytic activity of the gold for the complete oxidation of CO as a function of the size of nanoparticles.

- **Nature of support**; because it is essential that it has a surface specific capable of providing a strong interaction with the particles. The support facilitates the formation of extremely small metal particles having a high proportion of their atoms at the surface; With regard to the oxidation of CO, the catalyst supports were divided by Schubert et al[49] into two categories: the supports "active" and "inert" materials. Gold supported on the irreducible oxides as Al_2O_3, MgO, and SiO_2, are not very active while those employing reducible oxides as Fe_2O_3, NiOx, CoO_X, TiO_2, are active. The activity of gold supported shows a strong dependence on the particle size and thus those that have more surface defects (corners, stops) on which is adsorbed oxygen[50].

- **The method of preparation**; In the first work that studied the effect of the preparation method on the activity of the oxidation of CO, Bamwenda et al [48]

have concluded that the catalysts from the deposition - precipitation are more active than those prepared by impregnation or photo deposition. However, Schüth et al. showed that colloidal gold deposit is capable of generating as active catalysts than those prepared by deposition-precipitation and thermally more stable[51].

- **Heat treatment**; one consequence of, the small size of the nanoparticles is lowered the melting point. The heat treatment can cause melting and sintering of nanoparticles hence the importance of the choice of the calcination temperature. The majority of work in the literature notes a decrease in the catalytic activity accompanying heat treatment. Park and Lee reported a decrease in the activity of the catalysts Au/Fe_2O_3, Au/TiO_2, Au/Al_2O_3 with increasing calcination temperature[52]. Haruta attributed the good thermal stability of the catalysts obtained by deposition-precipitation on TiO_2 epitaxial contact between nanoparticles and support[53]. The calcination atmosphere also has a great influence on the catalytic performance; gold supported on manganese oxide treated air is more active than it was treated in hydrogen or vacuum due to a stronger interaction between the oxidized metal and manganese[54]. Boccuzzi et al[55] Followed the evolution of sintering of gold supported on TiO_2 synthesized by deposition-precipitation "function of the calcination temperature". They observed that the particle size changes from 2.4 to 10.6 nm with increasing the calcination temperature from 200°C to 600°C. This increase in temperature results in a different distribution of corners and edges.

Thanks to this important chemical reactivity catalysis based on nanoparticles of Au has a great potential for many applications including, among others, the control of pollutants, the detection of flammable gasses and transformations of organic substances. In this section, we will list some examples of catalysts based applications of nanoparticles of Au.

1.6 Oxidation reaction of CO

The interest in the oxidation reaction of CO to CO_2 comes from the fact that it is a simple reaction, easy to implement and can be catalyzed by metal oxides. The CO oxidation reaction takes place at a high temperature in general (> 1000 ° C) in the presence of cyclohexane. This reaction causes many environmental damages. These reasons have led many researchers to find a way to turn at low temperatures this toxic gas into a less harmful compound. Haruta et al. showed that the nanoparticles of Au supported on TiO_2 and Al_2O_3 ensured 50% of the CO conversion CO_2 and O_2 at very low temperatures down to -70 °C[56]. They also found that the chemical yield of this reaction became more important when the particle size was ≤ 4 nm.

The oxidation reaction at a low temperature of the CO by the nanoparticles of Au having size, less than 5nm opened the field of research into the chemical reactions can be catalyzed by the Au nanoparticles.

1.6.1 Mechanism for CO oxidation

There are many mechanisms could explain this reaction such as a mechanism including the oxide support and mechanism involving gold particles only that mean

When the support is non-reducible, a CO oxidation mechanism involves gold nanoparticles only. For instance, Schubert et al[49] conclude that when gold is supported on magnesia, silica or alumina, the O_2 adsorption on low coordinated sites of the gold surface and caused to a lower activity than when oxygen can be activated on a reducible support. In this study, I will focus on the first due to support to our idea.

1.6.1.1 Mechanisms including the oxide support

All the mechanisms proposed in the literature are based on the nature of the active phase. Two general mechanisms for catalysts gold supported on reducible oxides: Haruta's mechanism with fully metallic gold particles and including unreduced gold species at the metal – support interface such as Bond and Thompson's mechanism. The differences arise from the nature of the active phase and intermediates of the reaction.

1.6.1.1.1 Metal gold particles: Haruta's mechanism

According to Haruta proposition in CO oxidation, we conclude that reducible supports such as Fe_2O_3 or TiO_2 lead to more active catalysts than non-reducible supports such as Al_2O_3 or SiO_2. O_2 can be absorbed and activated on these supports when gold is fully reduced extremely high activity is obtained. Semicircular gold particles are more active than spherical particles due to the greater boundary of the interface between the gold and the support[49, 57].

Haruta al[55] proposed a four-step mechanism for the catalysts Au/ZnO, Au/TiO_2 assuming that the active sites are metallic gold particles. The mechanism includes the CO

adsorption on gold followed by adsorption of oxygen on the support around the perimeter of the gold particles, the formation of carbonaceous species on the support and their CO_2 decomposition. This mechanism was modified later by Haruta and have considered active sites Au(0) and $Au^{\delta+}$ at the interface Au-TiO_2 [58] **Figure 1.17**.

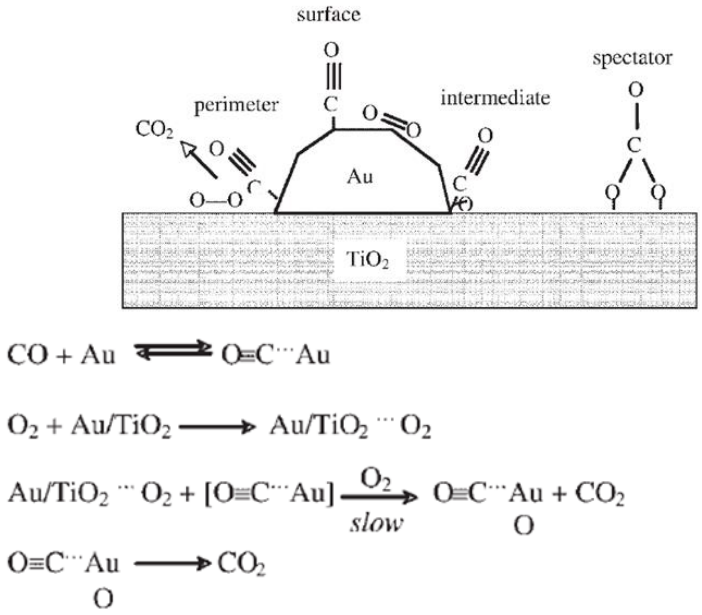

Figure 1.17 as proposed by Haruta et al. Mechanism of CO oxidation on supported fold catalysts[59].

1.6.1.2 Bond and Thompson's mechanism: unreduced gold at the interface

Bond and Thompson proposed a mechanism that involved metallic gold and Au^{3+} as active sites **Figure 1.18**. CO is first adsorbed on a gold weakly coordinating atom and an OH group of the carrier moves to the 3+ to form a carboxylic group and an anionic gap, the latter being filled with oxygen in the form of O_2^-. This ion (O_2^-) will oxidize the

carboxylic group by forming CO_2 and OH_2^- group to the surface. This group (OH_2^-) again reacts with CO and CO_2 giving two OH groups on the surface[60].

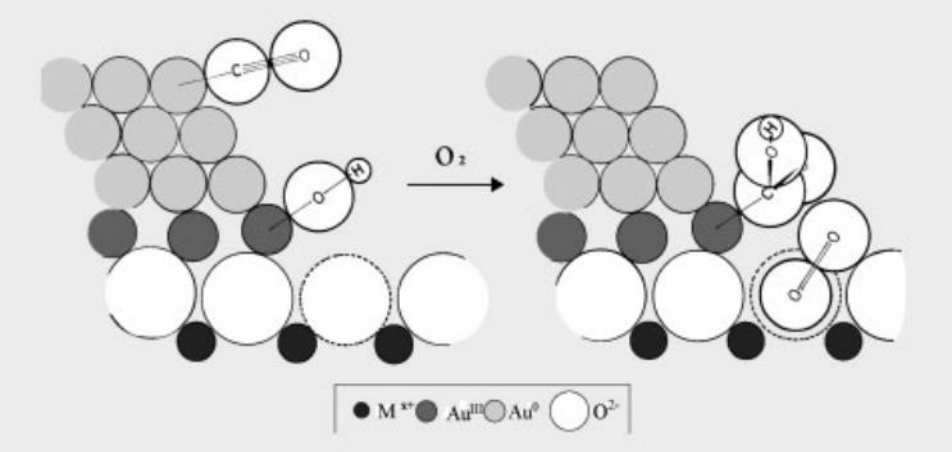

Figure 1.18 Mechanism as proposed by Bond and Thompson of co-oxidation on supported fold catalysts[60].

Chapter 2.

Characterization Techniques

The different experimental procedures utilized over the course of the present work are discussed in this chapter.

2.1 Introduction

The work presented in this chapter lays emphasis on the study of gold nanoparticles by using various techniques such as UV-visible Spectroscopy, X-ray Diffraction (XRD), Scanning Electron Microscope (SEM),Transmission Electron Microscopy (TEM), ICP Mass Spectrometry, X-ray Photoelectron Spectroscopy (XPS), Nuclear Magnetic Resonance Spectroscopy (NMR) and Fourier Transform Infrared Spectroscopy (FTIR).

This chapter is devoted to explaining the basic principles of the different techniques used for the characterization.

2.2 UV-Vis spectroscopy

UV-visible spectroscopy is a powerful tool for the characterization of colloidal particles[61].

Many molecules are transparent in portions of the electromagnetic spectrum called visible and ultraviolet regions (VIS) radiation (UV), in the wavelength range of 200 nm to 800 nm. When continuous radiation passes through a material part of the radiation can be absorbed, if this occurs, the residual radiation passing through the prism leaves gaps spectrum, called absorption spectrum. As a result, of the absorption energy of atoms or molecules move from a low energy state (ground state) to an (excited state) higher energy state.

Differences between electronic energy levels of the molecules varies from 125 to 650 kJ / mol.[62]

When a spherical metal nanoparticle is irradiated by light, the oscillating electric field causes consistent oscillation of the electrons as shown in

Figure 2.1**.**

The oscillation frequency is controlled by four elements:

1. The density of electrons,
2. the effective mass of the electrons
3. The shape
4. The size of the charge distribution [63].

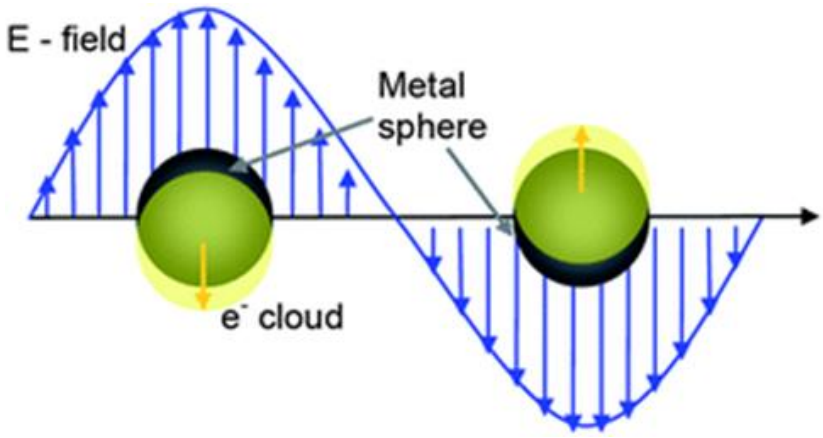

Figure 2.1 Plasmon oscillation of a sphere Scheme, showing the displacement of theelectron cloud on the cores.

In the work described in this thesis, the measurements were done on Hewlett-Packard diode array spectrophotometer (model HP-8452) operated at a resolution of 2 nm.

2.3 X-Ray Diffraction (XRD)

We now know that X-rays are electromagnetic radiation found in a portion of the spectrum between ultraviolet and gamma rays, and occur when a beam of electrons accelerated by a high voltage (a few tens of kilovolts), strikes a metal target.

When a beam of X-rays incident on a crystalline material, the electrons of the atoms constituting the solid oscillate with the same frequency as the incident radiation. Each of these electrons will be considered as a separate oscillator, its amplitude is very low when compared with the incident wave but all these coherent sources interfere with each other to give a resultant wave corresponding to the atom.

X-ray diffraction (XRD) patterns were collected on a Bruker D8 Advanced A25 diffractometer equipped with a Cu X-ray tube (Cu–Kα; λ = 0.15418 nm) operated at 40 kV and 40 mA in the Bragg–Brentano geometry using a linear position-sensitive detector with an opening of 2.9°. The diffractometer was configured with a 0.44° divergence slit, a 2.9° anti-scatter slit, 2.5° Soller slits, and a nickel filter to attenuate contributions from Cu–Kβ fluorescence. Data sets were acquired in continuous scanning mode over the 2θ range of 10–80°. The XRD data were analyzed using the Rietveld method with the fundamental parameters approach, as implemented in the software TOPAS V4.2 (Bruker-AXS) [64].

2.4 The Scanning Electron Microscope (SEM)

The scanning electron microscope instrument (SEM) is an instrument that permits to investigate the surface morphology and topography of both inorganic and organic materials. It is capable of providing morphological data of the investigated material with spatial resolution of about one nanometer[65].

When the sample is bombarded with electrons, electron beam propagation within it is mainly due to the multiple collisions experienced by electrons with atoms of the sample while losing their energy. Some of these are elastic collisions, and in such cases, the electron beam passed through the sample without significant loss of energy. However, most collisions are inelastic, so that the distribution of emitted electrons have a very large peak in the region of energies of 0-50 eV[66].

The collisions of electron beam with atom electrons result in the electron emission from the sample. When an electron from an inner shell of the atom is removed by a high-energy electron beam, the atom can return to ground state, by two different ways: an electron from the upper layers can fill the gap in the inner layer emitting a photon, or other electron emitting an upper layer. Photon emission produces a characteristic X-ray spectrum while the electrons emitted are known as Auger electron. Both effects are very important in the microstructural analysis because their energies are characteristic of the elements that issued them. Therefore, measurement of these energies allow the elemental analysis of the sample and measuring the emission intensity gives a quantitative chemical analysis[66]. The actual content of Au was determined by EDS on a scanning electron microscope (FEI Nova NanoSEM) with microanalysis system model EDAX.

2.5 Transmission Electron Microscopy (TEM)

As mentioned above, the size of the deposited particles is of great importance for a material with a good catalytic performance. To find the average particle size observations Transmission electron microscopy (TEM) of the catalysts were performed. The transmission electron microscope basically consists of an electron gun, condenser lens, objective lens, intermediate lens and projecting lens. The electron gun is the only electrostatic lens having a microscope and theothers are electromagnetic lenses. It means that the magnetic field in the center is of the TEM column is produced by applying an electron current to the copper coils. It is pertinent to note that the magnetic field exist only in the location of coils.

When the electron beam of a typical energy of 300 keV interacts with a thin (< 500 nm) sample several types of signals are produced. Itallows us to make the elemental and structural characterization. Just to briefly mention that the produced signals include elastic, back-scattered, absorbed secondary electrons, Auger, and characteristic X-rays.

The electrons passing through the sample can be classified into two main types:, i.e. those going through the sample without being diverted from their incident direction and are called the direct electrons. There is another type are diverted from their direction of incidence. If the energy of diverted electrons is the same of incident electron, then these are called diffracted electrons. On the other hand, if their energy is not the same, then these are called energy-loss electrons. The diffracted electrons combined with direct electrons give rise to the conventional TEM techniques such as nright-field TEM (BF-TEM), dark-field TEM (DF-TEM), and selected area electron diffraction (SAED). The

energy loss electrons give rise to TEM techniques such as electron energy loss spectroscopy (EELS) and energy-filtered TEM (EF-TEM). The EFTEM technique is important to make the elemental maps of samples by using a TEM. The detection of characteristic x-rays in a TEM leads to energy dispersive spectroscopy (EDS) technique and is very useful in identifying the presence of elements in the samples.

It is important to note that the TEM images suffer from lens aberrations and the spherical aberration is the largest contributor to these aberrations. This is why the latest TEM instruments are equipped with spherical aberration correctors and are called Cs-correctors.

TEM imaging samples were prepared by drop casting the as-prepared gold nanoparticles solution over a 150-mesh Formvar-coated copper grid. TEM imaging was done using an FEI Titan G2 80-300 CT electron microscope, equipped with a charge-coupled device (CCD) camera (model US4000) from Gatan, Inc. The particle size distribution of the gold nanoparticles was determined by calculating the size of at least 200 nanoparticles from the bright field (BF)-TEM electron micrographs using Image J software. The presence of a ligand around the NP was investigated in two steps. The first step included the acquisition of a BF-TEM micrograph from a region of the specimen to allow a view of the ligand as a shell around the AuNP. Second, an energy-dispersive X-ray spectroscopy (EDS) spectrum from the same region was acquired in order to show the presence of sodium through the demonstration of a Na-K peak at 1.04 keV in the spectrum. The high-resolution TEM (HRTEM) analysis of the samples was performed by using an aberration-corrected FEI TEM (model Titan G2 60-300 ST) equipped with an Image-Corrector from CEOS. The image corrector was aligned to reduce the spherical

aberration coefficient (Cs) of the objective lens to about -2 µm prior to the acquisition of aberration-corrected electron micrographs containing the AuNP.

There are a couple of TEM instruments were employed to analyze the samples. These both instruments are from FEI Company (Hillsboro, OR). The model of the instruments are Titan 80-300 CT and Titan 60-300 ST. The latter instrument was also equipped a spherical aberration corrector. The point resolutions of these instruments were 0.24 nm and 0.08 nm, respectively and both of them were equipped with EDS detectors from EDAX. Moreover the both instrument were also capable of allowing having a scanning TEM (STEM) analaysis of samples.

2.6 Inductively Coupled Plasma Mass Spectrometry (ICP-MS) analysis

ICP can be performed on solid and liquid samples to calculate the quantitative and subjective information of various metals and non-metals and trace unknowns. The Procedure for the ICP is the following:

1. Select the mass of the sample for proper digestion depending on the type of matrix, analytic levels
2. Detection method to be used
3. Weigh each sample (analytical samples and controls)
4. Record all mass transfer in the sample vessels
5. Select acid (s) for digestion based on the matrix and vessels
6. Transfer the sample vessels containing the samples
7. Added record numbers of each acid.

In my case i used 1: 3 HCl: HNO_3. Select the microwave digestion program. Quantitatively transfer each cooled digest to appropriately labeled plastic bottle and diluted as appropriate to the detection technique; labels, volume or mass and reagents used for dilution. Data interpretation ICP-MS analysis is straightforward. Its result is reported as a concentration in mg / L, which can be easy, converted into the mass concentration.

Elemental analyzes of Au, B and Na were conducted by inductively coupled plasma-atomic emission spectrometry (ICP-AES) using a Thermo iCap 6500. Before analysis, 15 mg of the sample was decomposed by an acid mixture of nitric acid and hydrochloric acid (under pressure and high temperature).

2.7 X-ray Photoelectron Spectroscopy (XPS)

X-ray Photoelectron Spectroscopy known as XPS has been developed from the fifties by professor K. Siegbahn for which he was awarded the Physics Nobel Prize in 1981.

In XPS, a X-ray beam irradiates the sample and ejects core-level electrons from sample atoms. The kinetic energy of the ejected electrons from the top 1 to 10 nm of the material is analyzed. The binding energy of electrons can be determined as below:

$$E_{binding} = E_{photon} - E_{kinetic} - \Phi_{spectrometer}$$

Where $E_{binding}$ is the binding energy of the electron, E_{photon} is the energy of the X-ray photons, $E_{kinetic}$ is the measured kinetic energy of the emitted electron and $\Phi_{spectrometer}$ is the work function of the spectrometer.

The binding energy provides information on sample elemental composition, as well as on chemical and electronic state of the elements in the sample.

From the XPS spectra, the quantification of the elements can be calculated from the ratio of integrated peak areas normalized by respective sensitivity factors.

XPS studies were carried out in a Kratos Axis Ultra DLD spectrometer equipped with a monochromatic Al Kα X-ray source (hv=1486.6 eV) operating at 75 W, a multichannel plate and delay line detector under a vacuum of ~10^{-9} mbar. The survey and high-resolution spectra were collected at fixed analyzer pass energies of 160 eV and 20 eV, respectively. Binding energies were referenced to the C 1s binding energy of adventitious carbon contamination which was taken to be 284.8 eV. The data were analyzed with commercially available software, CASAXPS. The metallic peaks were fitted with an asymmetric hybrid Doniach-Sunjic function.

convoluted with a Gaussian/Lorentzian product while non-metallic peaks were fitted with mixed Gaussian (70%)–Lorentzian (30%) (GL30) function after a Shirley-type background subtraction. The sample for XPS was filtered three times using a 3-kDa cutoff centrifugation filter to remove any excess free ions or stabilizers.[67]

2.8 Concepts and techniques in solid-state Nuclear Magnetic Resonance (NMR)

Nuclear magnetic resonance spectroscopy (NMR) is the powerful analytical tool that provides greater information in physical, chemical, and biological properties of matter. This technique is non-destructive and has finds applications in several areas of science. Simple one-dimensional techniques NMR can be routinely used by chemists to study chemical structure. Two-dimensional techniques can be also used to determine the structure of more complicated molecules.

The key parts of NMR spectrometers are persistent superconducting magnets to generate the magnetic and a coil of wire through which a current passes generating another magnetic field and a computerized system that governs the entire apparatus which includes an amplification system and registry.

2.8.1 Fundamental of NMR

2.8.1.1 Magnetic properties of the nucleus: nuclear spin

Spin is an intrinsic quantum property of all nucleuses and is determined by the unpaired number of elementary particles (neutrons and protons) that form. The overall spin of the nucleus is determined by the spin quantum number *I*. If the numbers of both the protons and neutrons are even then $I = 0$. For nuclei with an odd number of neutrons and protons generally have a quantum number of nonzero integer spin (I= ½, 2/3, 3/5,). Within this last group of nuclei, nuclei are chemically important as ^{1}H, ^{13}C, ^{15}N, ^{19}F and ^{31}P having an equal number of spin ½,.

2.8.1.2 Spin precession in the magnetic field

The magnetic moment associated with an electron orbit is defined as;

$$\boldsymbol{\mu=\gamma L} \qquad \textbf{(1)}$$

Where L is the angular momentum of the electron and the gyromagnetic ratio is γ. As shown in figure 2 atom in a magnetic field, B, has the energy, E, given by

$$\boldsymbol{E = -\mu \cdot B = \mu B \cos\theta} \qquad \textbf{(2)}$$

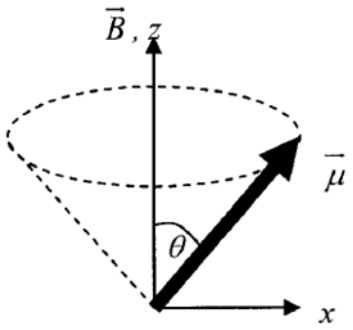

Figure 2. 2 Nuclear spin precession under an external magnetic field, B.

The spin precession around the magnetic field applied to the Larmor frequency, ω_L, given by,

$$\boldsymbol{\omega_L = \gamma B} \qquad (\mathbf{3})$$

2.8.1.3 The Zeeman interaction

In the presence of magnetic field the energy of a nucleus split and has a minimum when its magnetic moment is parallel to the magnetic field where it has maximum when it is anti-parallel to the magnetic field. For a I=1/2 the splitting so-called Zeeman effect and 2I+1 possible orientation is produced as shown in **Figure 2.3**.

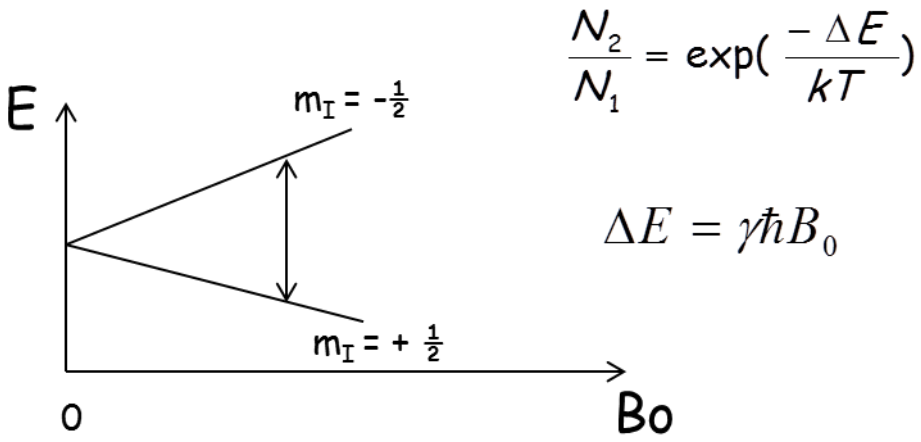

Figure 2.3 Splitting of the energy levels I = 1/2 and I = -1 / 2 the presence of an applied magnetic field B_0.

The energy ($\Delta E = \gamma h B_0$) in the range of radio frequencies can be detected between levels which allows us to measure the NMR parameters.

2.8.1.4 Transitions: applying a second magnetic RF- B1 (pulse) perpendicular to B_0

When the sample is placed under the magnetic field B_0 applied to z axis **Figure 2. 4**, magnetic moment of the sample start to process with Larmor frequency along the z axis. When a radio frequency (RF) pulse B_1 close to Larmor frequency is applied to the x axis through the solenoid coil the magnitude rotate from the z to x axis. Once the RF is turned

off the rotated magnetic moment begin relaxed to the equilibrium state and turn back to z axis. And produce free induction decay (FID) as shown in **Figure 2.5**. An FID is a superposition of several FIDs corresponding to spin in different chemical environment. Finally the Fourier transformation will transform the FID into the frequency scale in the usual NMR spectra.

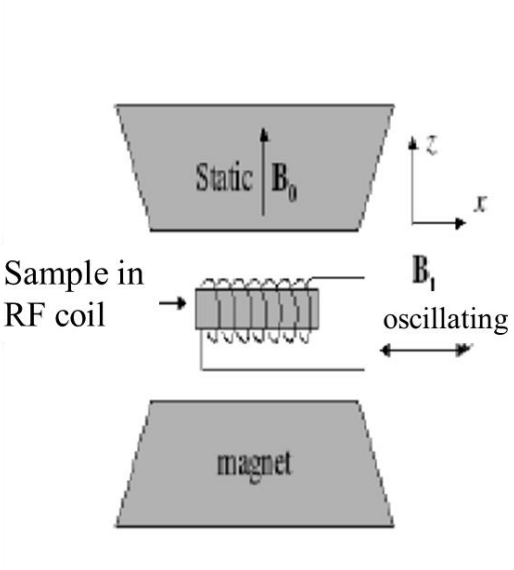

Figure 2. 4 The schematic diagram of NMR spectroscopy.

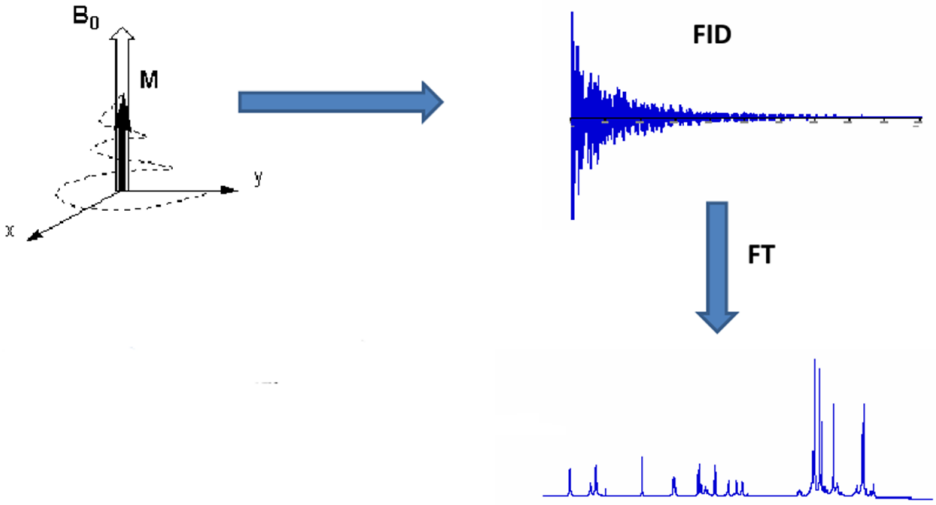

Figure 2.5 Free induction decay (FID) and Fourier transformation of FID of NMR signal.

2.8.1.5 Chemical shift

The chemical shift depends on many factors, but the most important and significant are the electron density of the environment **Figure 2. 6**. It helps distinguish spins that lie within different chemical groups, such as the ^{13}C nuclei of aromatic groups, CH_3, CH_2 COOH.

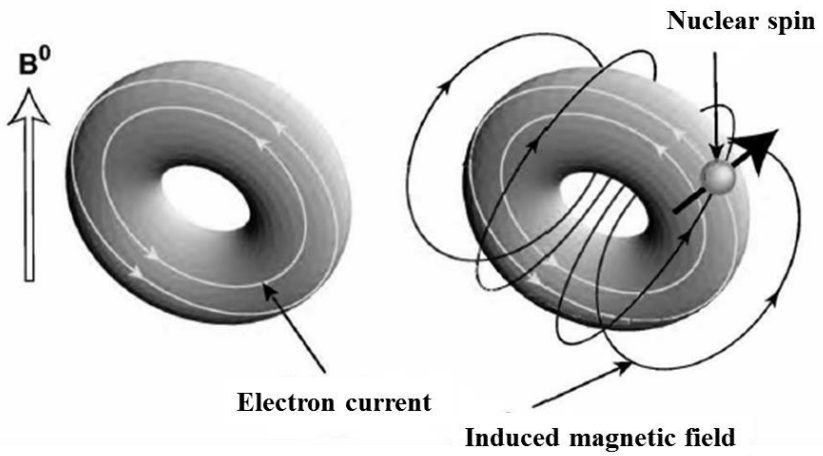

Figure 2. 6 A mechanism that produces the chemical shift. Figure obtained from ref[68].

The chemical shift cannot be compared with results from different teams because it depends on the properties of the magnetic field. For these reasons, the chemical shift is defined in terms of the difference of resonance between the core nucleus of interest and a reference. Therefore, it is convenient to express the chemical shift, δ, by comparing the Larmor frequency of the atom of interest to that of a reference atom, as shown in the equation:

$$\boldsymbol{\delta = \frac{\omega_L - \omega_L^{Ref}}{\omega_L^{Ref}}}$$

Where $\boldsymbol{\omega_L}$ is the Larmor frequency in a sample and $\omega^{\boldsymbol{Ref}}$ in the reference sample under the same magnetic field. Usually tetramethylsilane is used as reference sample for ^{1}H and ^{13}C.

2.8.1.6 Nuclear magnetic resonance Magic Angle Spinning MAS

To obtain a well resolved spectrum for solid samples, technique as magic angle spinning was introduced. As outlined in **Figure 2.7.** The angle between the vector connecting the spins and the applied magnetic field so-called magic angle is equal to 54.74^0. By the mechanical rotation of the sample with the magic angle, the molecule feel like they are isolated without coupling as in liquid state, resulting a very well resolved signals.

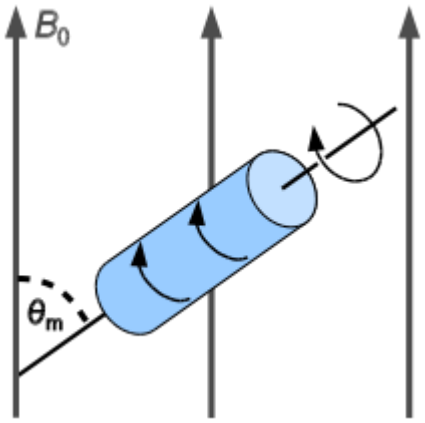

Figure 2.7 Magic Angle Spinning (MAS) NMR technique.

2.8.1.7 Cross Polarization (CP)

The low natural abundance and the long relaxation times of the nucleus make a long time of wait between acquisitions implies that the signal is very poor. Both problems can be solved using the MAS technique combined with the cross-polarization (CPMAS) sequence as shown in **Figure 2. 8 .** The abundant nucleus is excited, and its energy is then transferred to the observed nucleus. So that for instance for the polarization transfer from a ^{1}H to a ^{13}C.

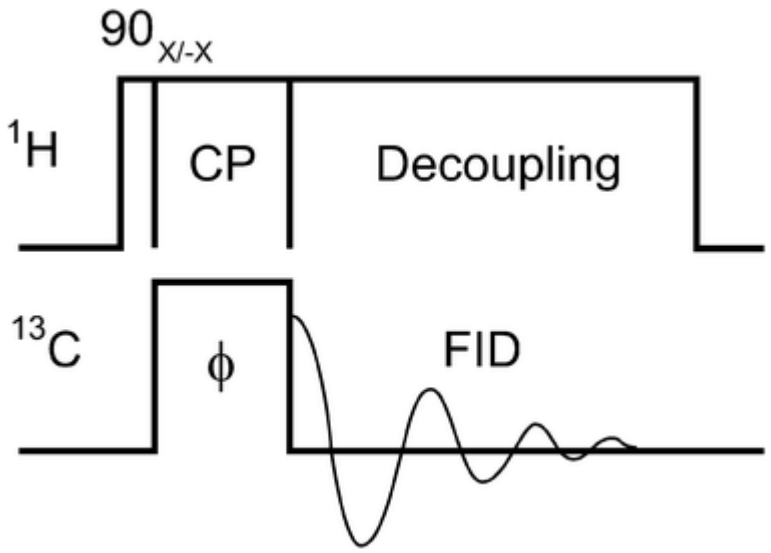

Figure 2. 8 Scheme of the pulse sequence employed for CPMAS experiments.

One-dimensional (1D) **13**C CP/MAS solid-state NMR spectra at room temperature were recorded on a Bruker AVANCE III spectrometer operating at 400MHz resonance frequency for ^{1}H with a conventional double resonance 4 mm MAS probe. For the 100K experiment at 400 MHz, a bruker low temperature 3.2 mm double resonance probe was employed. The spinning frequency was set to 10 kHz. **13**C NMR chemical shifts are reported with respect to TMS as an external reference. The following sequence was used: 90° pulse on the proton (pulse length 2.4 µs), then a cross-polarization step with contact time of 2 ms, and finally acquisition of the ^{13}C signals under high-power proton decoupling. The delay between the scans was set to 5 s, to allow for the complete relaxation of the ^{1}H nuclei, and the number of scans collected varied between 50 000 and 100 000 at room temperature and 1024 scans at 100K. An exponential apodization function corresponding to a line broadening of 80 Hz was applied prior to Fourier transformation.

The 2D 1H-13C heteronuclear correlation (HETCOR) solid state NMR spectroscopy experiments at 100 K were conducted using a low temperature 3.2 mm MAS probe. The experiments were performed according to the following scheme: 90^0 proton pulse, t_1 evolution period, CP to ^{13}C and detection of the ^{13}C magnetization under TPPM decoupling. For the cross-polarization step, a ramped radio frequency (RF) field centered at 75 kHz was applied to the proton while the ^{13}C channel RF field was matched to obtain an optimal signal. A total of 64 t_1 increments with 512 scans each was collected and 8 ms contact time. During t_1, *e*-DUMBO-1 homonuclear ^1H decoupling was applied and proton chemical shift was corrected by applying a scaling factor of 0.57.

1D ^{23}Na MAS solid state NMR spectra at room temperature were recorded on a Bruker AVANCE III spectrometer operating at 900MHz resonance frequency for ^1H with a conventional double resonance 3.2 mm MAS probe with a spinning frequency of 18 kHz and repetition delay of 1s.

2.9 Infrared Spectroscopy Fourier Transforms (FTIR)

Infrared spectroscopy is based on the absorption of infrared radiation by the material being analyzed. The analysis is performed using a Fourier Transform Spectrometer (FTIR) on the sample sending infrared radiation and measuring the wavelengths and intensities at which the material absorbs. An IR spectrometer is comprised of:

- The radiation source that contains two beams. A beam path of a fixed optical path (reference beam) and the other optical path of a variable wavelength (sample beam).

- The detector compares the intensity of the reference and sample segments for each frequency and outputs a transmission spectrum (%) or absorbance (A).

IR spectra of the samples were recorded using an FTIR spectrometer (Perkin Elmer Spectrum 100) with a mid-infrared deuterated triglycine sulfate (MIR- DTGS) detector. The spectra were obtained at a resolution of 4 cm−1 in the range of 4000-650 cm−1 and with the accumulation of 32 scans.

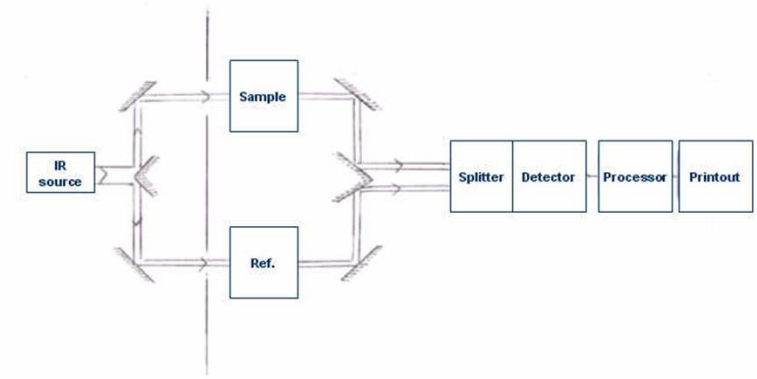

Figure 2.9 Operation infrared spectrometer schema.

Chapter 3.

Control The Size of Gold Nanoparticles By Using Carboxylic Ligands As Stabilizer

The use of citrate as a stabilizer on the gold nanoparticles preparation is known from 60 years ago. However, understanding the role of the stabilizer on the formation of nanoparticles remains an unsolved challenge. In this chapter, in order to understand their role in the stabilization and the size control of Au nanoparticles, we have prepared gold nanoparticles with different carboxylate ligand. These particles were obtained by treatment of $HAuCl_4$ with different carboxylate ligands as stabilizer agents and sodium borohydride as a reducer in order to obtain highly stable metal nanoparticles.

3.1 Introduction

Gold nanoparticles were considered highly interesting in a wide variety of fundamental research and technical applications because of their exceptional optical, electric and catalytic properties[69]. The fundamental work by Haruta[70]. exhibited that diminishing the size of gold nanoparticles expanded their activity in CO oxidation[71]. Since the researchers started with a report on the preparation of gold nanoparticles by reducing tetra chloroauric acid ($HAuCl_4$) in aqueous solution[72] incredible exertion has been dedicated to controlling the size and shape of the gold nanoparticles[15, 73]. Earlier this exertion focus on tuning the size of gold particles reported by Frens[15]. He was varying the ratio of the reductant (sodium citrate) and $HAuCl_4$. In the investigations that followed, a range of reductants has been used to obtain different sized gold nanoparticles by reduction of $HAuCl_4$. For example, such that sodium borohydride[74], hydroxylamine[75], ascorbic [76,27,28] and some biomolecules[77].

However, the Citrate-based reduction is now one of the most common methods for routinely synthesizing monodisperse gold nanoparticles (AuNP) for a wide-range of applications[78]. The use of citrate as a stabilizer is not restricted to gold or other metals[79] but includes a wide range of materials[80.] Despite widespread use of gold nanoparticles, apart from the knowledge of their ability to render the region surrounding the Au particle negatively charged because of the anionic carboxylate groups.

In this work, we investigated the effect of carboxylic ligand ions on the size of the gold nanoparticles. It was found that the size of the gold nanoparticles could be tuned by changing the type of carboxylic ions and their concentration in the reaction system.

We achieve this by combining Ultraviolet–Visible Spectroscopy, Transmission Electron Microscopy (TEM) and High-Resolution Transmission Electron Microscopy (HRTEM).

3.2 Experimental details

3.2.1 Materials

All chemicals were reagent grade, purchased from Sigma-Aldrich, and were used without further purification: Tetrachloroaurate trihydrate ($HAuCl_4 \cdot 3H_2O$); Trisodium citrate dihydrate ($Na_3C_6H_5O_7 \cdot 2H_2O$), Isocitric Acid ($C_6H_8O_7$), Citric Acid ($C_6H_8O_7$), Trimesic acid ($C_9H_6O_6$), disodium succinate ($Na_2C_4H_4O_4$), Phthalic acid ($C_6H_4(COOH)_2$), Disodium glutarate ($Na_2C_5H_6O_4$), Tartaric acid ($C_4H_6O_6$), Sodium acetate ($NaCH_3COO$) , Acetic acid ($C_2H_4O_2$) And Formic acid ($CH_2O_2$) were used as stabilizers and sodium borohydride ($NaBH_4$) was used as a reducing agent. All reactions were done in aqueous media using deionized water (Millipore Milli-Q system, 18.2 MΩ-cm). All glassware was treated with aqua-regia (3:1, HCl/HNO_3) during washing.

3.2.2 Preparation of gold nanoparticles

100 mL of 0.1 M aqueous stock solutions of trisodium citrate, Isocitric acid, Citric acid, Trimesic acid, disodium succinate, Phthalic acid, Disodium glutarate, Tartaric acid, Sodium acetate, Acetic acid, Formic acid (CH_2O_2) and chloroauric acid were prepared separately by dissolving the required amount of $Na_3C_6H_5O_7 \cdot 2H_2O$, $C_6H_8O_7$, $C_6H_8O_7$, $C_9H_6O_6$, $C_4H_4Na_2O_4$, $C_6H_4(COOH)_2$, $Na_2C_5H_6O_4$, $C_4H_6O_6$, $NaCH_3COO$, $C_2H_4O_2$, CH_2O_2 and $HAuCl_4 \cdot 3H_2O$, respectively in water. The 0.25 mL of the chloroauric acid stock

solution was placed in separate 100 mL round bottom flasks equipped with a stir bar to which the required amount of the ligands stock solution was added to reach the desired ligands:Au molar ratio between 0.2:1 to 30:1. Necessary amounts of water were then added so that the reaction mixture volume measured 50 mL. Within approximately 2 min, 3 mL of freshly prepared 0.1 M (10 equivalent) aqueous sodium borohydride solution was added and the resultant solution was maintained under stirring conditions (600 rpm) for 1 hour. The final concentration of gold chloride in all of the reaction mixtures was 5×10^{-4} M. Stable solutions were obtained for all reactions with the exception of ligands: Au ratio of 30:1, where spontaneous precipitation was observed: After the addition of the equivalent amount of ligand (20:1 ratio) slow precipitation was observed over an extended period of time.

The capping and stabilizing by the Carboxylates is achieved through charge stabilization mechanism showed below **Figure 3.1**.

$$HAuCl_4 \xrightarrow{H_2O} H^+ [AuCl_4]^- \quad (1)$$

$$H^+ [AuCl_4]^- + 3\,(Na^+ + RCOO^-) \rightarrow (Au^{3+} - 3\,RCOO^-) + 3\,NaCl + HCl \quad (2)$$

$$NaBH_4 + 4H_2O \rightarrow H_3BO_3 + NaOH + 4H_2 \quad (3)$$

$$(Au^{3+} - 3\,RCOO^-) + 3/2\,H_2 \rightarrow Au^0 + 3\,(H^+ - RCOO^-) \quad (4)$$

$$(H^+ - RCOO^-) + NaOH \rightarrow (Na^+ - RCOO^-) + H_2O \quad (5)$$

Figure 3.1 Proposed stabilization Mechanism of gold nanoparticles

3.2.3 Methods of characterization

The results of each freshly prepared Au NPs suspension treated by analytical techniques such as UV-visible spectroscopy (UV-Vis), Transmission electron microscopy (TEM) measurements and high-resolution transmission electron microscopy (HRTEM) are presented in the results and discussion sections.

3.3 Results and discussion

3.3.1 UV-Vis spectral analysis of gold colloidal suspension

Gold nanoparticles exhibit a distinct optical feature commonly referred to as Localized Surface Plasmon Resonance (LSPR), that is, the collective oscillation of electrons in the conduction band of gold nanoparticles in resonance with a specific wavelength of incident light. LSPR of gold nanoparticles results in a strong absorbance band in the visible region (500 nm-600 nm), which can be measured by UV-Vis spectroscopy.

The LSPR spectrum is dependent both on the size and shape of gold nanoparticles. The peak absorbance wavelength increases with particle diameter. UV-VIS measurements can also be used to evaluate the functionalization of gold nanoparticles. Upon binding of ligands to the gold nanoparticle surface, the LSPR spectrum will red-shift by a few nanometers.

In order to study the effect of the ligands structure and concentration on the gold nanoparticles sizes, UV-Visible spectra of gold colloids prepared with different types of

carboxylate stabilizer (try, di and mono) for [0.2:1], [0.8:1], [1:1], [3:1], [5:1] and [10:1] = [Stabilizer: Au] ratio were collected.

The gold nanoparticle solutions synthesized with different tricarboxylate ligands (trisodium citrate, citric acid, isocitric acid and trimesic acid)Au ratios from 0.2:1 to 10:1, exhibited a localized surface plasmon resonance peak (λ_{max}) at ca. 520 nm, confirming the total reduction of $HAuCl_4$ and the presence of gold nanoparticles. This peak is strong size-dependent and shifts to a longer wavelength with increasing the size of gold nano particles[69b]. However, the size distribution of gold nanoparticles has a significant effect on the width of the peak: wider peak represents wider size distribution of nanoparticles. By comparing the different tricarboxylic ligand **Figure 3.2**, sodium citrate and isocitric acid give the smaller nanoparticles and the best size distribution (sharp peak at 520 nm). However, by increasing the ratio (5:1 and 10:1), all the ligands show a large distribution (wider peak) and big size nanoparticles (shift to the highest value).

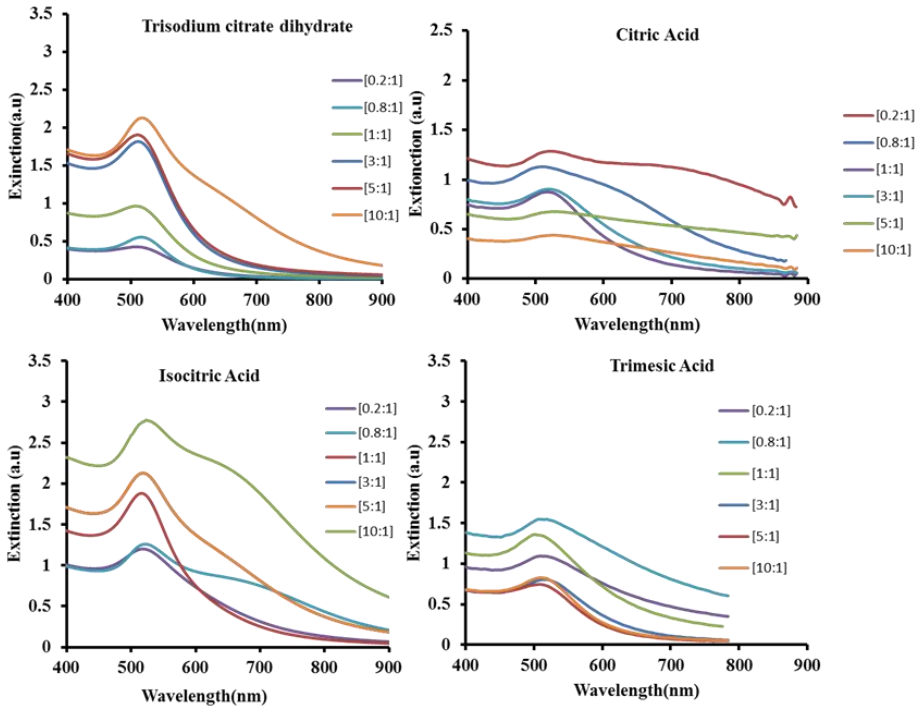

Figure 3.2 UV- Visible spectrum of gold colloid suspensions as a function of [0.2:1], [0.8:1], [1:1], [3:1], [5:1] and [10:1] = [tri-carboxylic acid (trisodium citrate, citric acid, isocitric acid and trimesic acid): Au].

Figure 3.3 shows the UV-vis spectra of Dicarboxylic ligand (disodium succinate, phthalic acid, sodium glutarate and tartaric acid) with different stabilizer:Au ratio. The results show a very similar behavior in all the spectra: relatively small nanoparticles for the size between 0.2 and 1 and a larger one for the higher ratio (shift to the red zone).

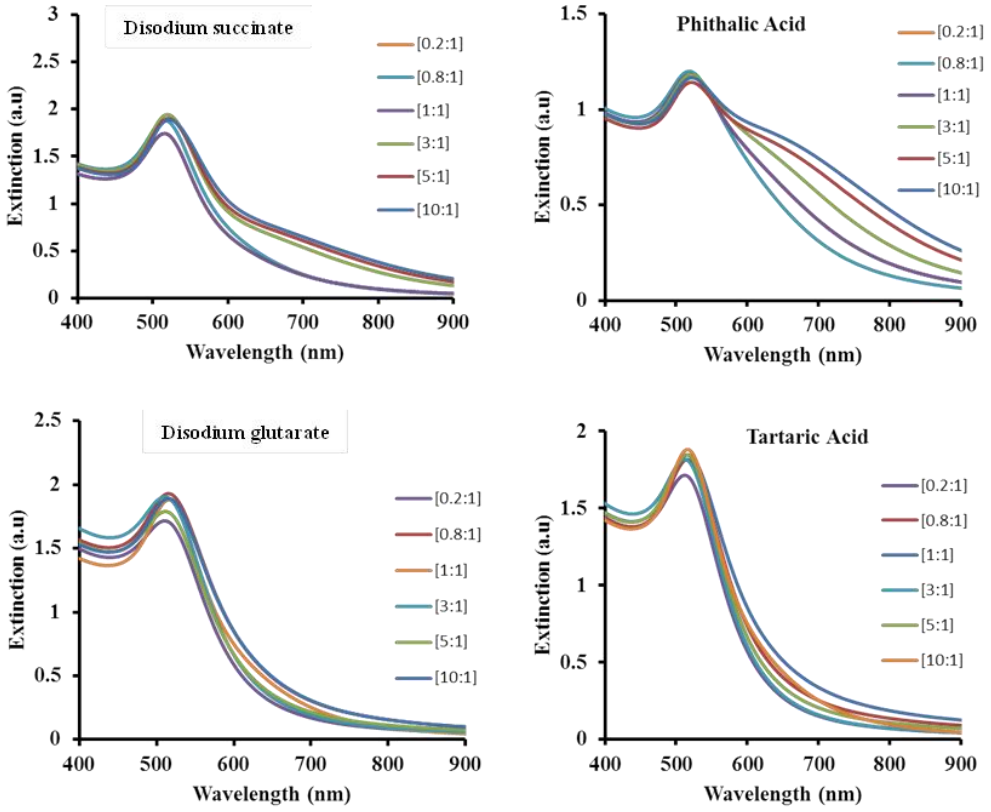

Figure 3.3 Visible spectrum of gold colloid suspensions as a function of [0.2:1], [0.8:1], [1:1], [3:1], [5:1] and [10:1] = [Di carboxylic acid (sodium succinate, phthalic acid, sodium glutarate and tartaric acid): Au].

In **Figure 3.4**, by varying the mono-carboxylic ligand (acetic acid, sodium acetate and formic acid) to Au ratio, we observe that the acetic acid gives the larger distribution with the higher size. As the results below, the more ligand we add, the bigger size of gold particles thus formed and larger is the distribution.

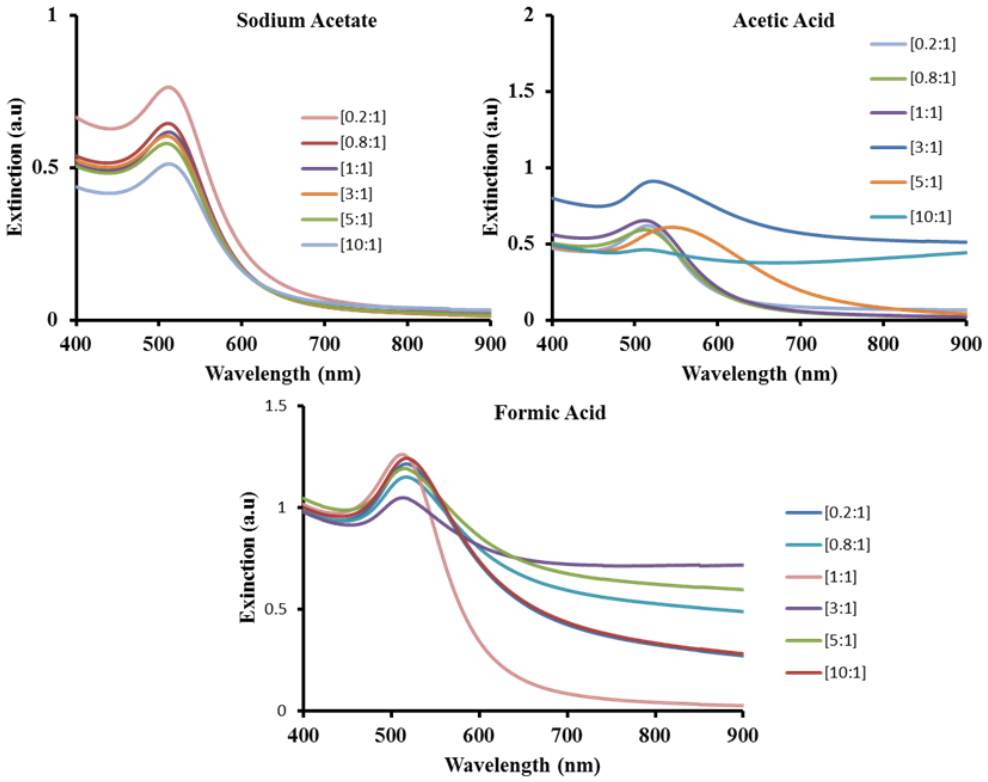

Figure 3.4 Visible spectrum of gold colloid suspensions as a function of [0.2:1], [0.8:1], [1:1], [3:1], [5:1] and [10:1] = [Mono carboxylic acid (acetic acid, sodium acetate and formic acid): Au].

The color of colloidal dispersions of gold particles with all the ligands (Mono-, Di- and Tricarboxylate) in water varies from red, purple to clear color, depending upon the shape and size of particles. The color and optical properties of gold nanoparticles originate from localized surface plasmon and are sensitive to their local dielectric environment. With the increase in particle size, the absorption band shifts to longer wavelengths. When the gold sol is partially coagulated the color becomes purple to clear color.

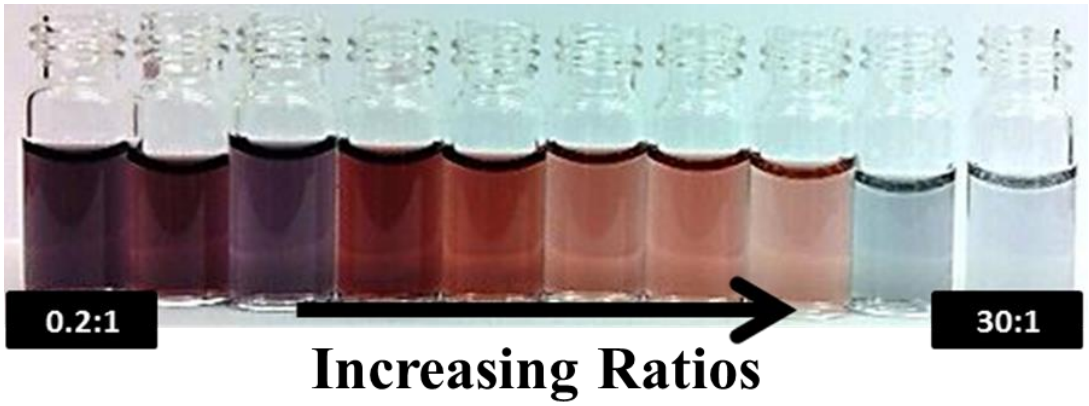

Figure 3.5 The color of the suspension varies from red to no color (light scattering by particles in a colloid or particles in a fine suspension) for the bigger ones (high ratio). These are respectively pink and red for the small particles suspensions.

From the figure above, Unaggregated gold nanoparticles will have a red color in solution as seen in the picture above. If the particles aggregate, the solution will appear blue/purple and can progress to a clear solution with black precipitates.

The surrounding environment is usually the surfactant with great importance as it prevents the particles from aggregating. This paragraph was detailed later in this Chapter.

In accordance with Lorenz-Mie-Debye theory for an arbitrary size of the particle, the surface plasmon resonance of the gold particles is redshifted with increasing of particle size **Figure 3.6,**

Figure 3.7 and Figure 3.8 [61a, 81].

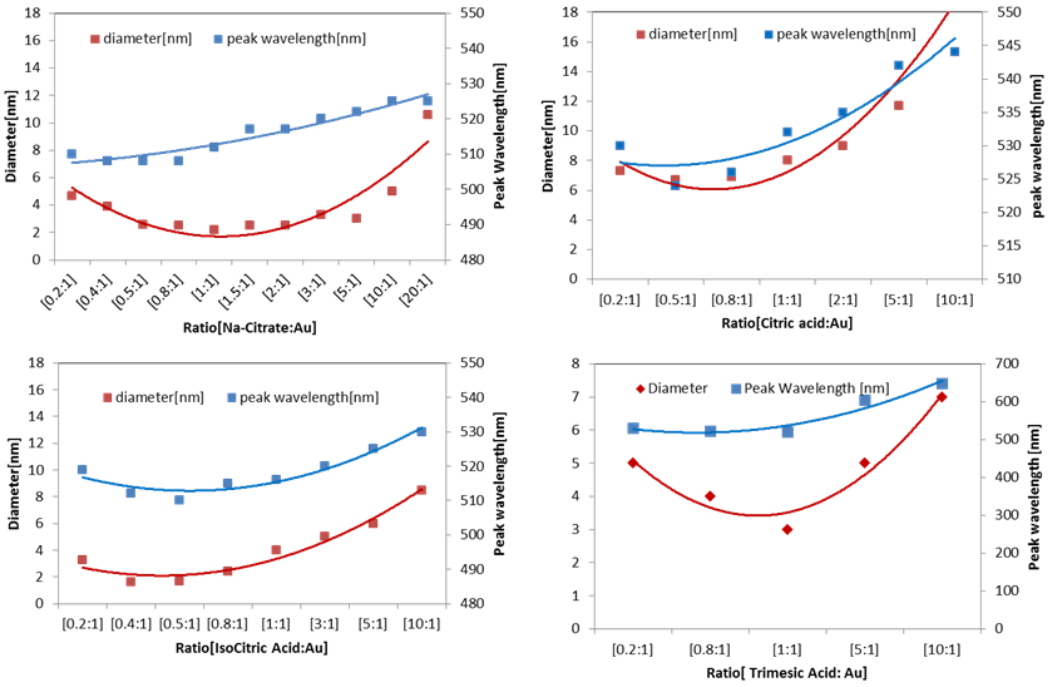

Figure 3.6 The absorption spectra of Gold nanoparticles (UV-Visible) and the diameters (TEM) ranging from 2 - 10 nm of [0.2:1], [0.8:1], [1:1], [3:1], [5:1] and [10:1] = [tri carboxylic acid (trisodium citrate, citric acid, isocitric acid and trimesic acid): Au].

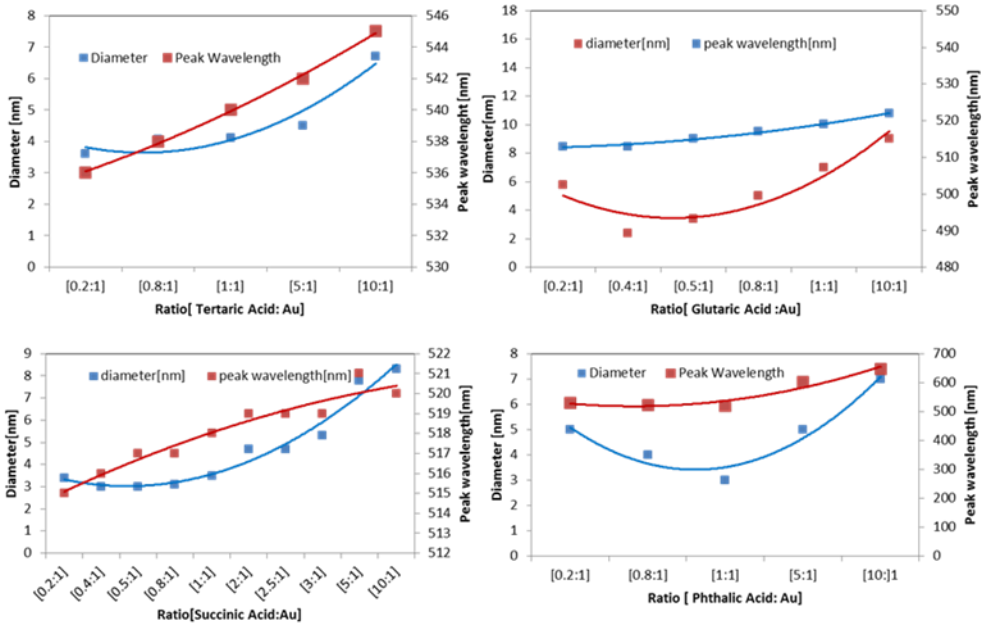

Figure 3.7 The absorption spectra of Gold nanoparticles (UV-Visible) and the diameters (TEM) ranging from 2 - 10 nm of [0.2:1], [0.8:1], [1:1], [3:1], [5:1] and [10:1] = [Di carboxylic acid (succinic acid, phthalic acid, sodium glutarate and tartaric acid): Au].

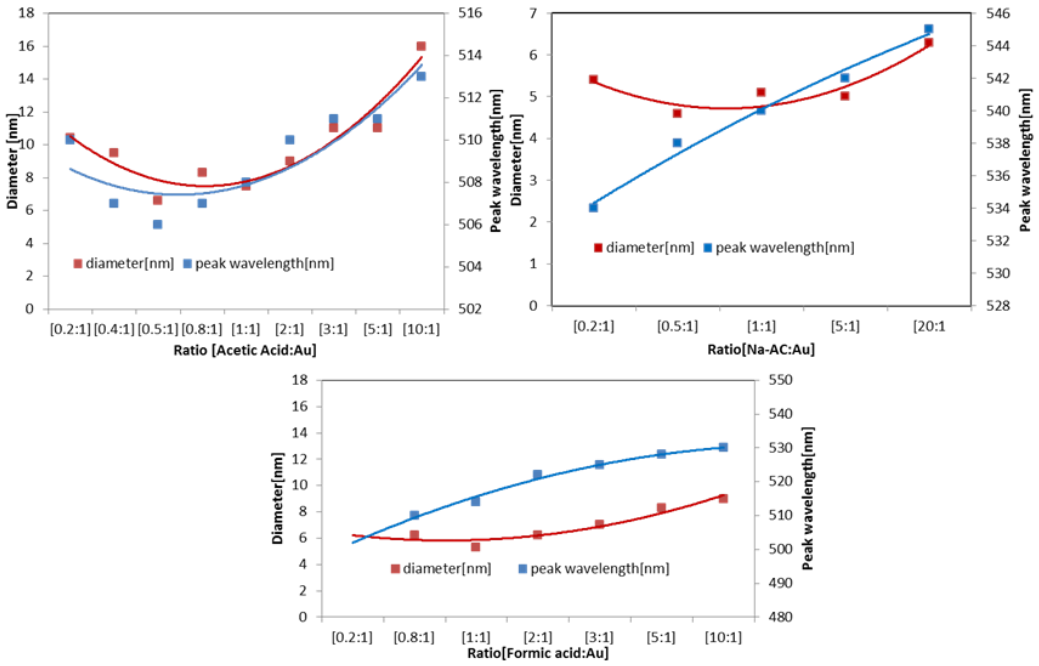

Figure 3.8 The absorption spectra of Gold nanoparticles (UV-Visible) and the diameters (TEM) ranging from 2 - 10 nm of [0.2:1], [0.8:1], [1:1], [3:1], [5:1] and [10:1] = [Mono carboxylic acid (acetic acid, sodium acetate and formic acid): Au].

We have extracted the wavelength at the maximum absorbance peak for NPs diameter ranging from 3 up to 16 nm diameter and displayed results in **Figure 3.6**,

Figure 3.7 **and Figure 3.8**.

Results show that;

- The absorbance increases quite linearly with the size of NPs (below 6nm diameter).
- The peaks shifted to red with simultaneous broadening as the particle size and elongation increased.

In addition, the intensity of the absorbance in the 600–800 nm window gradually increased with the increased stabilizer ratios, possibly due to the increased polydispersity and/or anisotropic shape of the particles.

3.3.2 Transmission electron microscopy (TEM) analysis of gold colloidal suspension

TEM has been one of the most used techniques to estimate the gold nanoparticle size. TEM was used to observe the changes in the particle size of Au with change the ratio of the stabilizer. TEM images and size distribution histograms for the metallic AuNPs@ Sodium Citrate are illustrated in **Figure 3.9**. TEM observations show very well dispersed nanoparticles at a low ratio with some aggregation for the higher one (5:1 and 10:1). The average particle sizes for the AuNPs were 4.7, 2.5, 2.2, 3.3, 3 and 5 nm, with Sodium Citrate/Au ratio of 0.2:1, 0.8:1, 1:1, 3:1, 5:1, and 10:1 respectively. Indicating that smaller Au nanoparticles size was obtained for the 1:1 ratio.

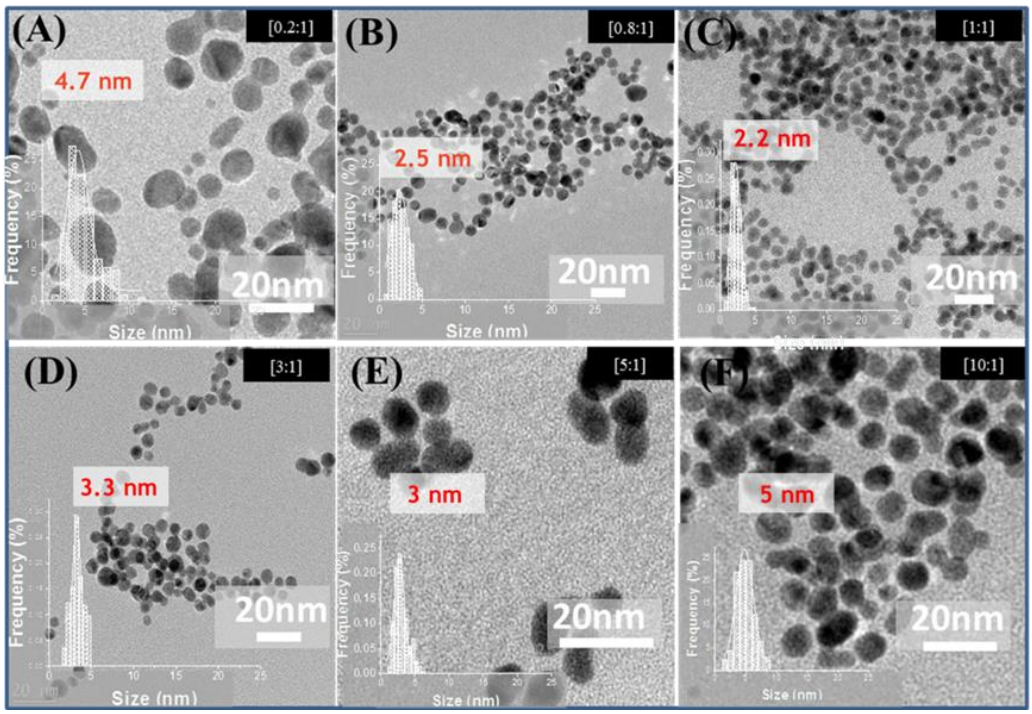

Figure 3.9 TEM images of AuNP synthesized by $NaBH_4$ reduction in the presence of different amounts of Sodium Citrate ($Na_3C_6H_5O_7$. $2H_2O$) Sodium Citrate/Au ratio: from (A) [0.2:1] to (F)[10:1]. The inset in each image shows the particle size distribution for respective samples fitted by a Gaussian curve.

The same study was repeated in the acidic form of citrate which is citric acid **Figure 3.10**. The TEM images of gold nanoparticles synthesized with citric acid show a relatively bigger size comparing to the sodium citrate, 7 nm at 1:1 ratio to 2.2 nm in the case of sodium citrate. It can be seen that at high concentration of stabilizer, and also at low concentration, a broad particle size distribution with agglomerated fine nanoparticles are observed.

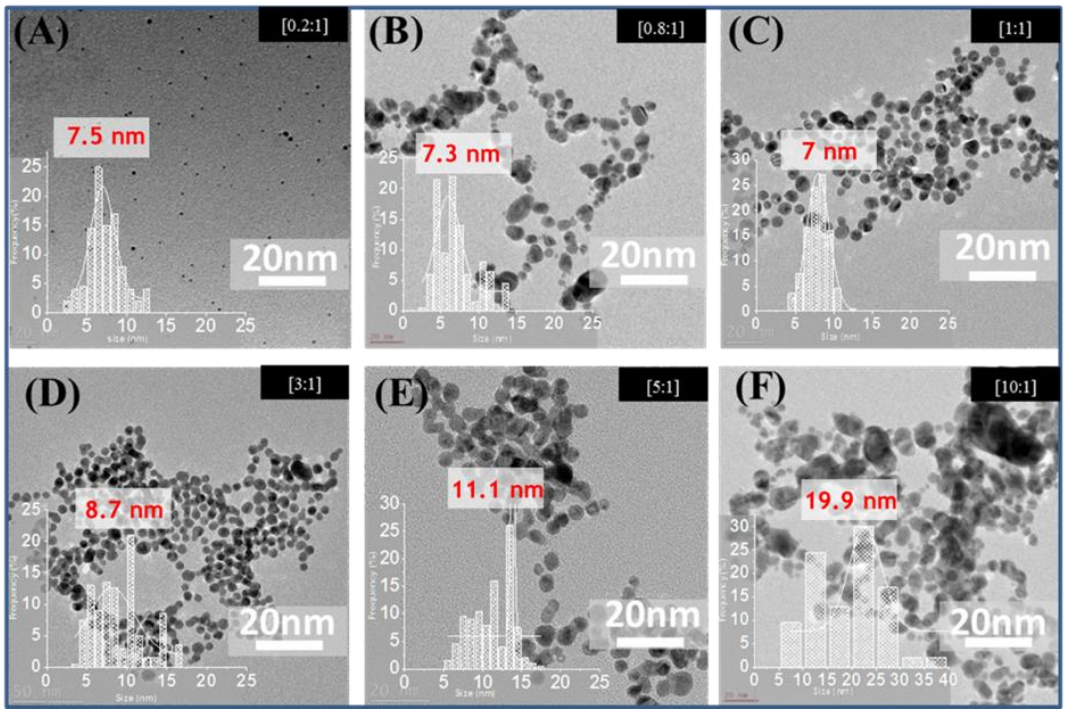

Figure 3.10 TEM images and respective particle size distributions of AuNP synthesized by $NaBH_4$ reduction in the presence of different amounts of citric acid ($C_6H_8O_7$) Citric Acid/Au ratio: from (A) [0.2:1] to (F) [10:1]. The inset in each image shows the particle size distribution for respective samples fitted by a Gaussian curve.

Gold nanoparticles synthesized with a variable ratio of Isocitric acid: Au **Figure 3.11** exhibit the similar behavior of those with citric acid. The ratio 1:1 yields the smallest gold nanoparticles with an average size of 7.6 nm. Higher or Lower ratio lead to bigger nanoparticles.

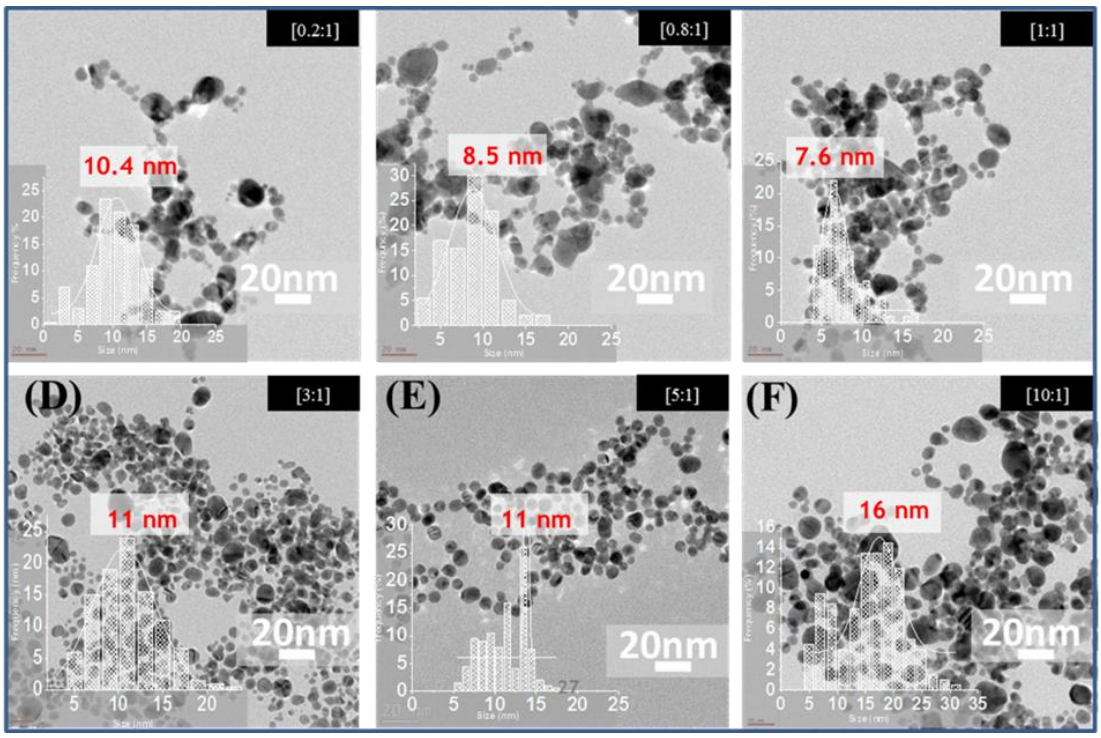

Figure 3.11 TEM images and respective particle size distributions of AuNP synthesized by $NaBH_4$ reduction in the presence of different amounts of Isocitric acid ($C_6H_8O_7$) Isocitric acid/Au ratio: from (A) [0.2:1] to (F) [10:1]. The inset in each image shows the particle size distribution for respective samples fitted by a Gaussian curve.

To complete the study with tri-carboxylate stabilizers, TEM of trimesic acid at different ratio was analyzed **Figure 3.12**. The TEM image shows very well dispersed nanoparticles with an average size of 5 nm. As the results obtained with the other ligands, the smaller one was obtained with a 1:1 ratio.

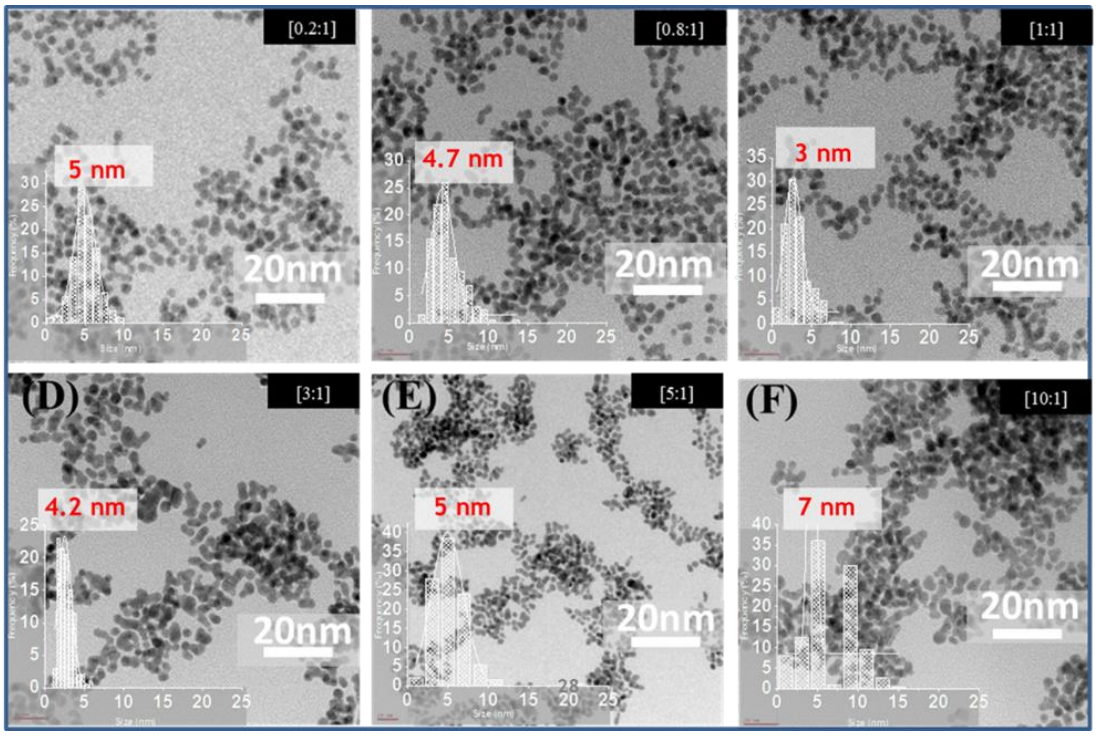

Figure 3.12 TEM images and respective particle size distributions of AuNP synthesized by NaBH4 reduction in the presence of different amounts of trisemic acid ($C_9H_6O_6$) Trimesic Acid/Au ratio: from (A) [0.2:1] to (F) [10:1]. The inset in each image shows the particle size distribution for respective samples fitted by a Gaussian curve.

To conclude about the tri-carboxylate ligands, the TEM results show:

I. The smaller nanoparticles were obtained with an optimum ratio of 1:1 for the 4 stabilizers.

II. The basic form allows the formation of much smaller size comparing to the acidic form. It can be explained by the high affinity of the basic anionic ligand L^- comparing to the acidic neutral form LH acting for the stabilization of the cationic gold Au^{x+} before the total reduction.

III. Changing the structure of the ligand with the same molecular formula don't affect the size of the nanoparticles (citric acid and isocitric acid).

IV. The utilization of rigid ligand (trimesic acid) affords to smaller Au nanoparticles.

The effect of the structure on the Au-NPS size was also revealed for the dicarboxylate ligands. 4 ligands were used at a different ratio from 0.2:1 to 10:1: sodium succinate ($C_4H_4Na_2O_4$), sodium glutarate($Na_2C_5H_6O_4$), phthalic acid ($C_6H_4(COOH)_2$) and tartaric acid ($C_4H_6O_6$) (**Figure 3.13, Figure 3.14, Figure 3.15 and Figure 3.16**). Transmission electron microscope (TEM) images of the gold particles prepared with different ratios show an optimum ratio between 0.2:1 and 1:1. Increase the ratio (10:1) give bigger Au-NPS with agglomeration and large distribution.

A comparison between the TEM images obtained for dicarboxylates ligand and the tri-carboxylate at different ratio give the following conclusions:

I. As in the case of the tri-carboxylate ligand, the basic form allows the formation of smaller Au-NPS.

II. For the same structure of carbon chain (sodium succinate and sodium glutarate), di-carboxylate ligand gives relatively smaller Au-NPS.

III. A modification of the dicarboxylate ligand structure (more OH groups, a lower alkyl chain, rigid ligand) doesn't have a big effect on the average diameter of Au-NPS.

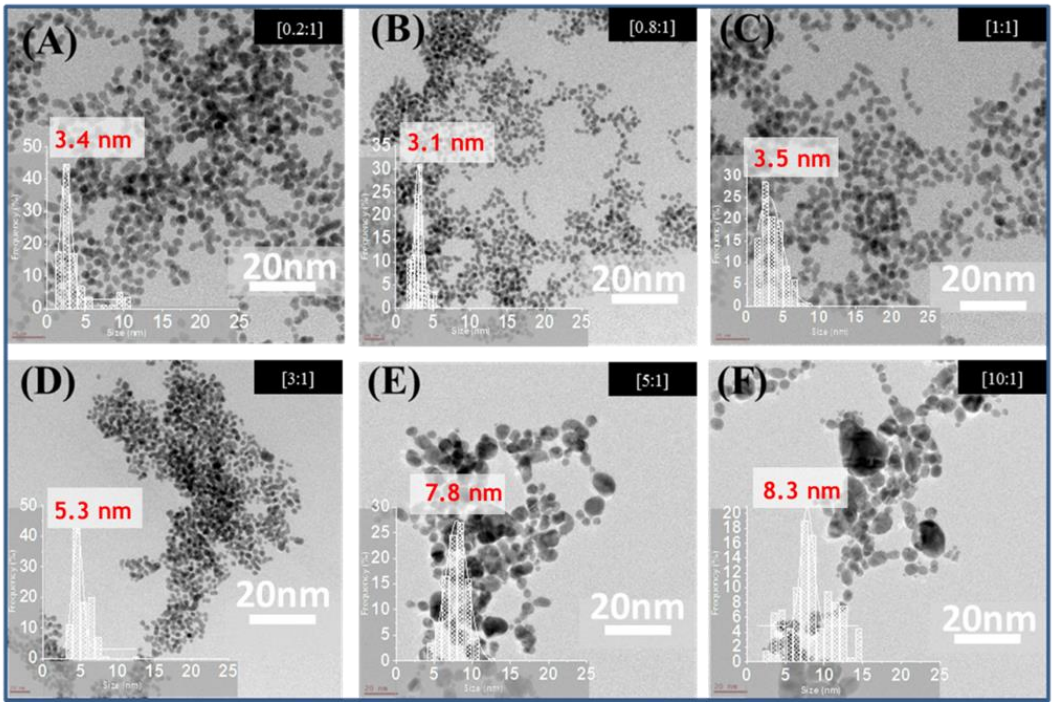

Figure 3.13. TEM images and respective particle size distributions of AuNP synthesized by $NaBH_4$ reduction in the presence of different amounts of sodium succinate ($C_4H_4Na_2O_4$) sodium succinate/Au ratio: from (A) [0.2:1] to (F) [10:1]. The inset in each image shows the particle size distribution for respective samples fitted by a Gaussian curve.

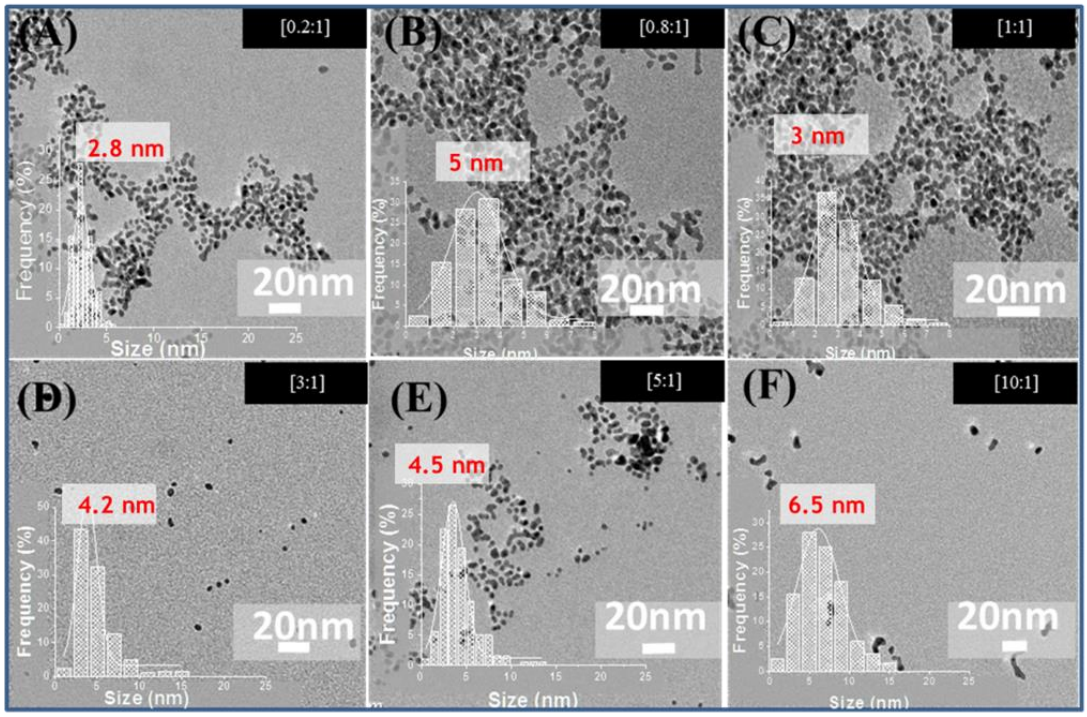

Figure 3.14 TEM images and respective particle size distributions of AuNP synthesized by $NaBH_4$ reduction in the presence of different amounts of sodium glutarate ($Na_2C_5H_6O_4$) Sodium glutarate/Au ratio: from (A) [0.2:1] to (F) [10:1]. The inset in each image shows the particle size distribution for respective samples fitted by a Gaussian curve.

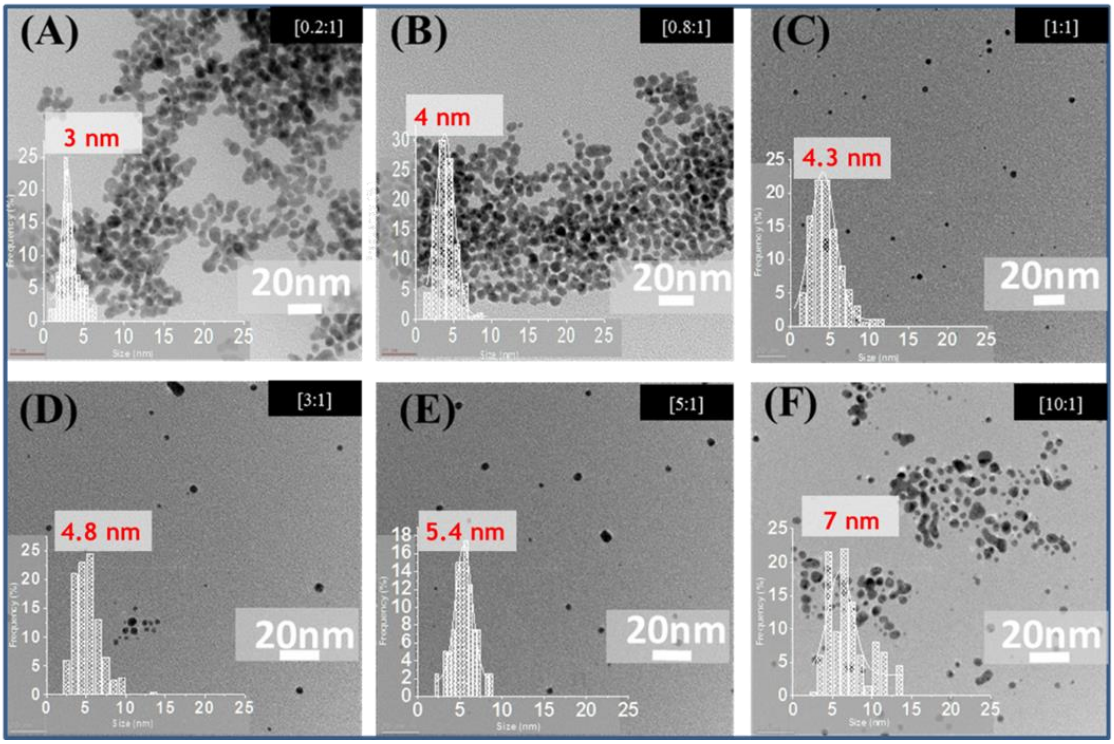

Figure 3.15 TEM images and respective particle size distributions of AuNP synthesized by $NaBH_4$ reduction in the presence of different amounts of phthalic acid (C_6H_4 $(COOH)_2$) Phthalic Acid /Au ratio: from (A) [0.2:1] to (F) [10:1]. The inset in each image shows the particle size distribution for respective samples fitted by a Gaussian curve.

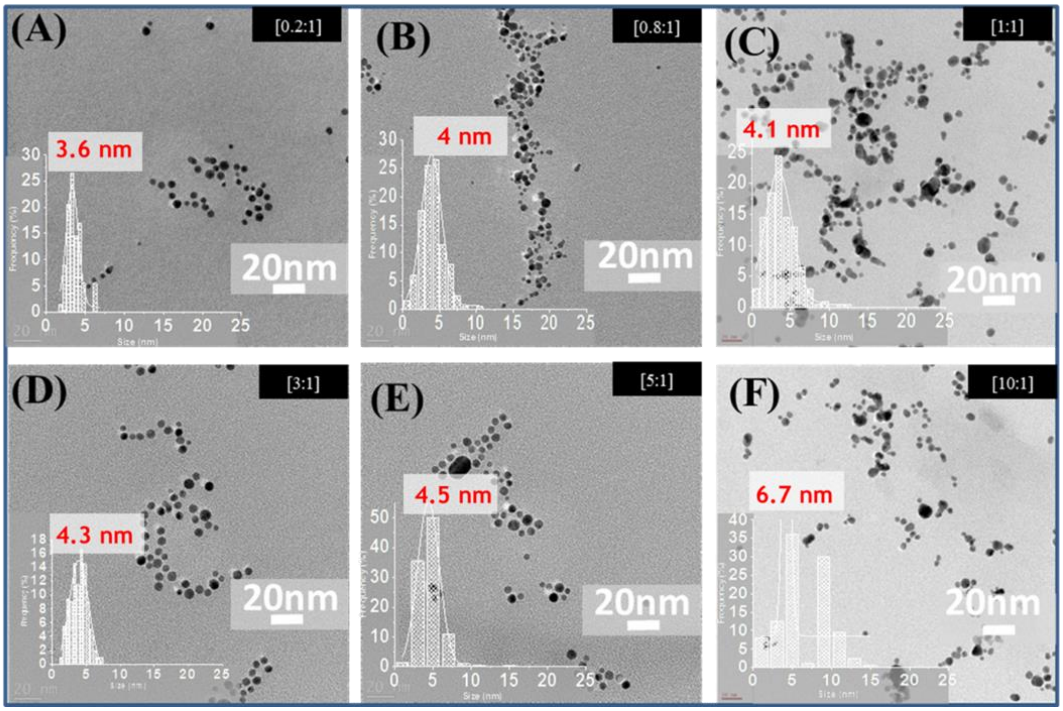

Figure 3.16 TEM images and respective particle size distributions of AuNP synthesized by $NaBH_4$ reduction in the presence of different amounts of Tartaric acid ($C_4H_6O_6$) Tartaric Acid /Au ratio: from (A) [0.2:1] to (F) [10:1]. The inset in each image shows the particle size distribution for respective samples fitted by a Gaussian curve.

For the mono-carboxylate ligand, the effect of the ratios on the particle size was investigated and the particle sizes were easily tuned by a constant amount of $HAuCl_4$ and change the monocarboxylic acid /Au ratio: 0.2:1, 0.8:1, 1:1, 3:1, 5:1, and 10:1. **Figure 3.16, Figure 3.17, Figure 3.18 and**

Figure 3.19, I can conclude the following results;

The size of the noble metal nanoparticles appeared to be dependent on the stabilizing agents' ratios during the chemical reduction process. Larger average Au nanoparticle size was obtained with lower stabilizer ratio. The formation of big nanoparticles was clearly

observed at high or lowers the 1:1 monocarboxylic acid ($NaCH_3COO$), ($C_2H_4O_2$) And (CH_2O_2) /Au.

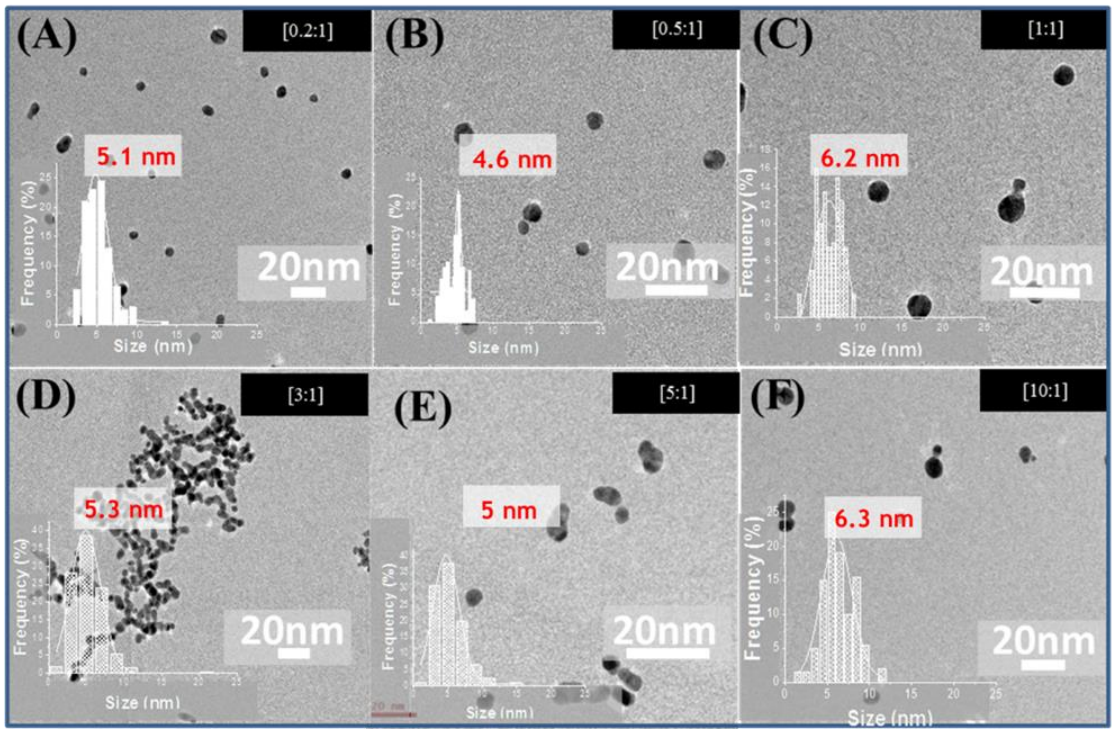

Figure 3.17 TEM images and respective particle size distributions of AuNP synthesized by $NaBH_4$ reduction in the presence of different amounts of sodium acetate ($NaCH_3COO$) Sodium acetate /Au ratio: from (A) [0.2:1] to (F) [10:1]. The inset in each image shows the particle size distribution for respective samples fitted by a Gaussian curve.

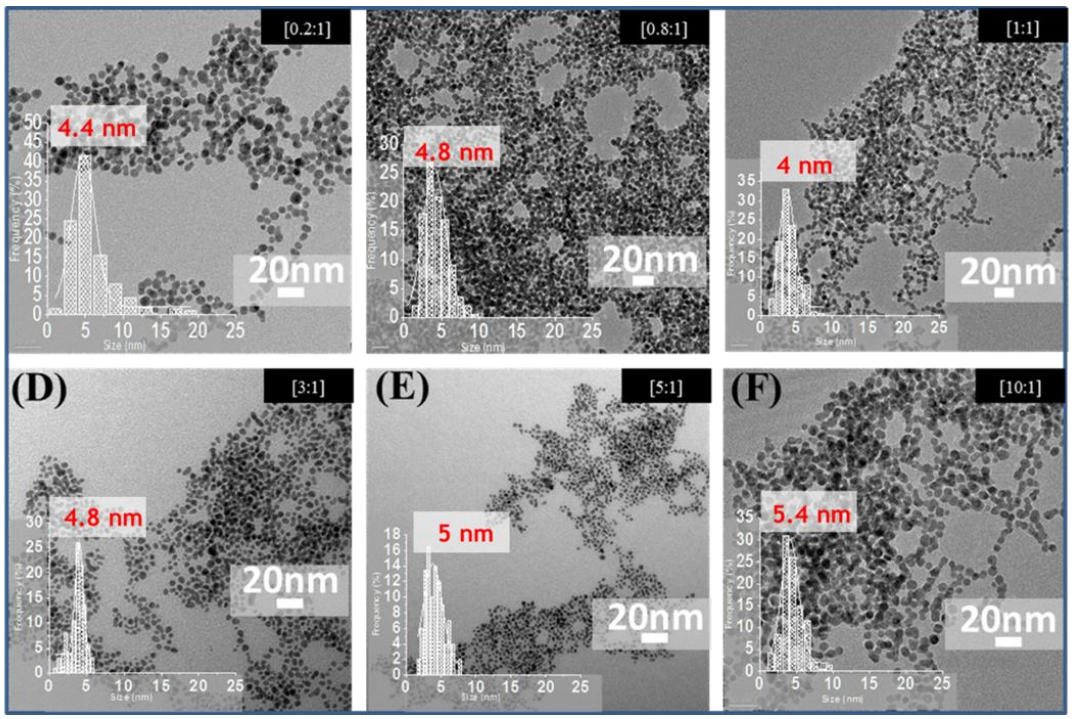

Figure 3.18 TEM images and respective particle size distributions of AuNP synthesized by $NaBH_4$ reduction in the presence of different amounts of Acetic Acid ($C_2H_4O_2$) Acetic Acid/Au ratio: from (A) [0.2:1] to (F) [10:1]. The inset in each image shows the particle size distribution for respective samples fitted by a Gaussian curve.

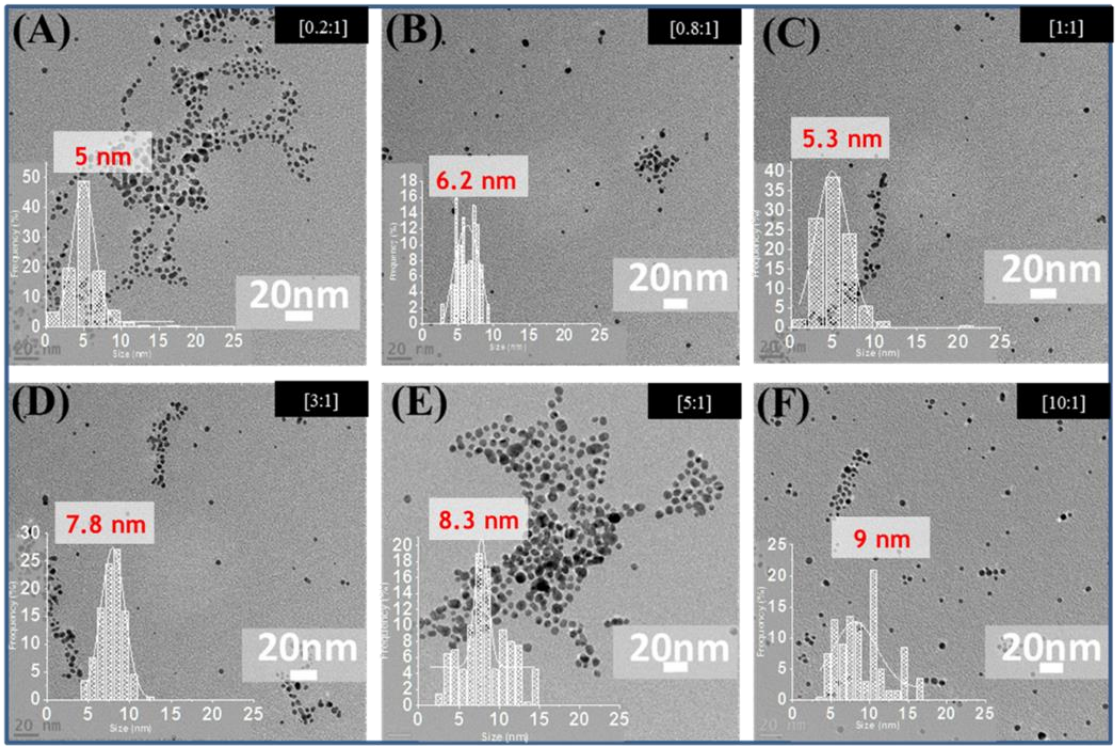

Figure 3.19 TEM images and respective particle size distributions of AuNP synthesized by $NaBH_4$ reduction in the presence of different amounts of Formic Acid (CH_2O_2) Formic Acid /Au ratio: from (A) [0.2:1] to (F) [10:1]. The inset in each image shows the particle size distribution for respective samples fitted by a Gaussian curve.

I would like to summarise the section above with this **Figure 3.20**, the molar ratios of the stabilizers (Tri, Di and Mono) carboxylic acid which are (1,4,5,15,25and 50) × 10^{-4} M. As the ratios of stabilizers/ Au increased from 0.2:1 to 0.8:1, 1:1, 3:1,5:1 and 10:1, suggesting increased the size of the gold nanoparticles as the ligands concentration was higher, as had already been found by Frens[15]. an optimum size from 0.4:1 up to 2:1 stabilizers/Au ratios we found, after this range the size start to increased again. Due to the limitation of the stabilizer to protect the NPs.

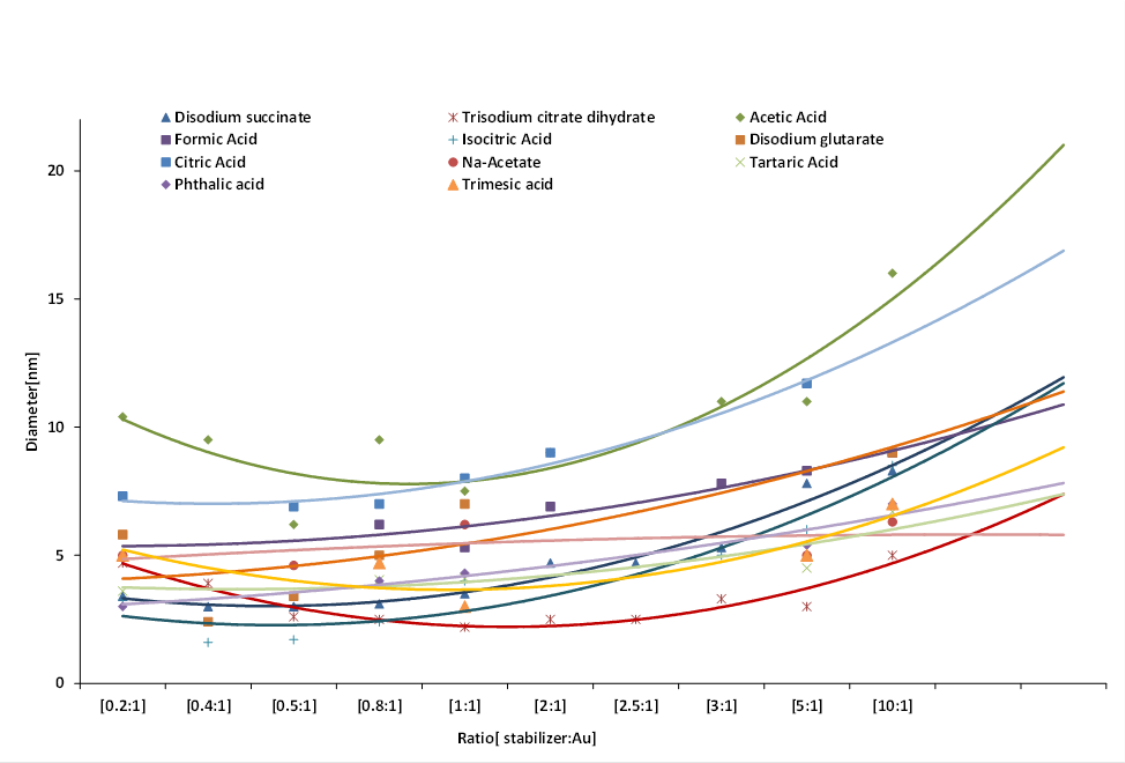

Figure 3.20 Comparison between various stabilizers.

3.3.3 HRTEM and FFT Analysis

HRTEM is a powerful tool for the structural characterizations with atomic resolution. It is coupled with the Fourier analysis. A powerful mathematical tool with various applications in image processing. Because the image in the Fourier, it is easy to examine or process certain frequencies of the image, thus influencing the geometric structure. The Au NPs morphology was investigated by the High-Resolution TEM (HRTEM) and the corresponding Fast Fourier Transform (FFT) images for citrate: Au 1:1 ratio. The results show clearly visible [111] lattice planes of gold (d-111 =2.3 Å) covered the whole particle **Figure 3.21 a**. For another particals, the distances between lattice planes are d-111= 2.3 Å and d-100 = 0.2 Å **Figure 3.21 b**. HRTEM images reveal substantial

differences in morphology of the particles; The Au NPs possess an icosahedral and cuboctahedral shape that is typical for AuNPs. **Figure 3.22** Icosahedron was obviously the major shape detected. Both HRTEM image and FFT pattern **Figure 3.21 and Figure 3.22** confirm the single crystalline nature of the Au NPs.

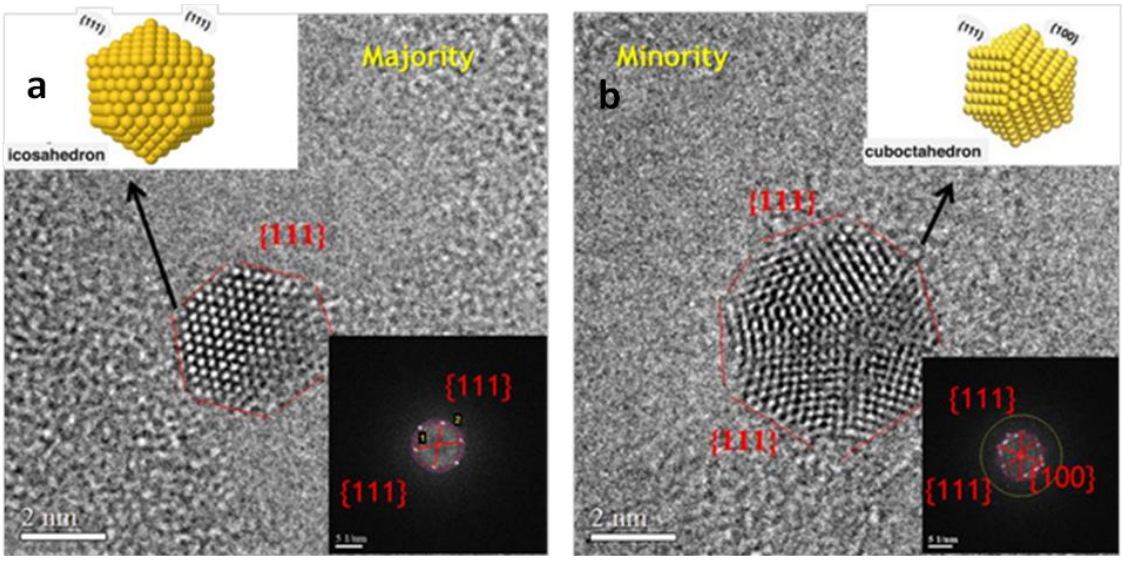

Figure 3.21 FFT investigation the exposed the plane of the Au NPs.

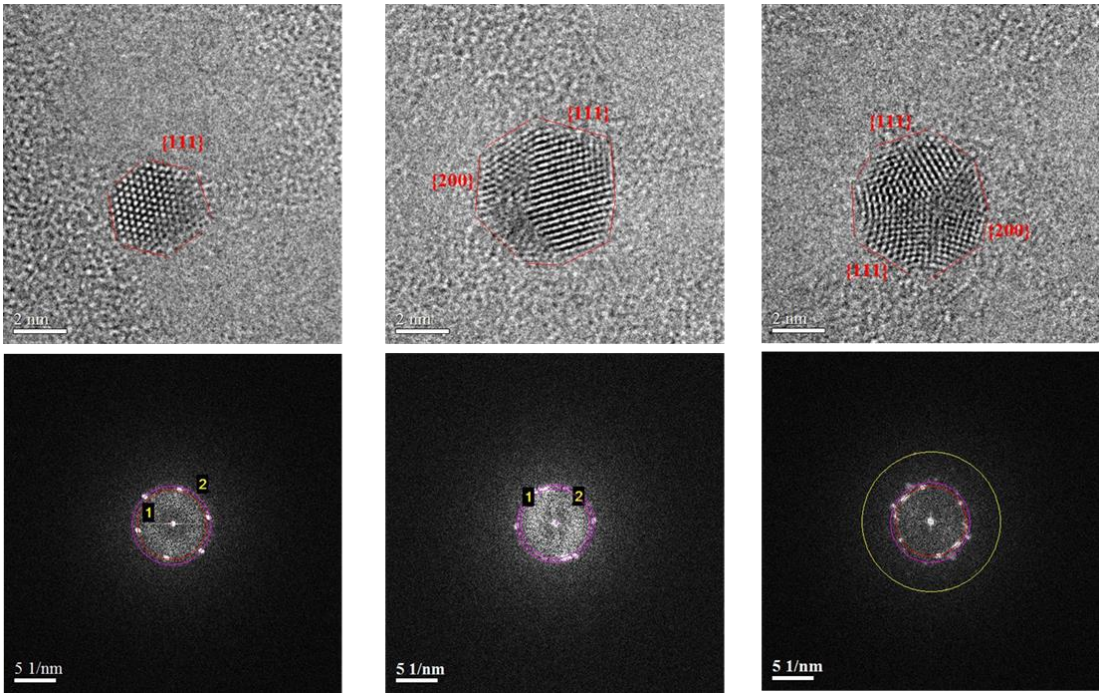

Figure 3.22 FFT investigation that the majority shape of citrate: Au at ratio 1:1.

3.3.4 Effect of post-synthesis heat treatment on size of the Au NPs

In this paragraph we investigate the effect of the temperature on the synthesis of AuNPs. This reaction was done at 5°C: a dilute solution of $HAuCl_4$ (10 mL, 5×10^{-4} M) was added to an aqueous citrate solution (5 mL, 5×10^{-4} M) to make 1;1 Citrate :Au ratio after few second the reducing agent $NaBH_4$ was added and the solution was stirred at 5°C for 60 min. The solution color turn to (red) and the formation of gold nanoparticles was confirmed **Figure 3.23**. The formation of AuNPs was probed by TEM in order to study the growth of the nanoparticle. It was observed that the size of the AuNPs was smaller under this condition **Figure 3.24**. The lower is the temperature (for example 5°C); the smaller is the size of the nanoparticles formed (1nm) **Figure 3.25** compared to the size of gold nanoparticles when we prepare it at 25°C (2.2nm) **Figure 3.25 Right**.

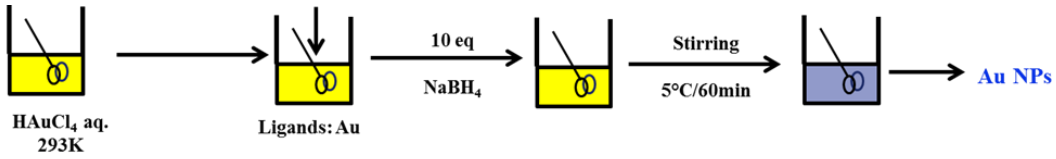

Figure 3.23 Experimental scheme for the synthesis of gold nanoparticles at 5°c.

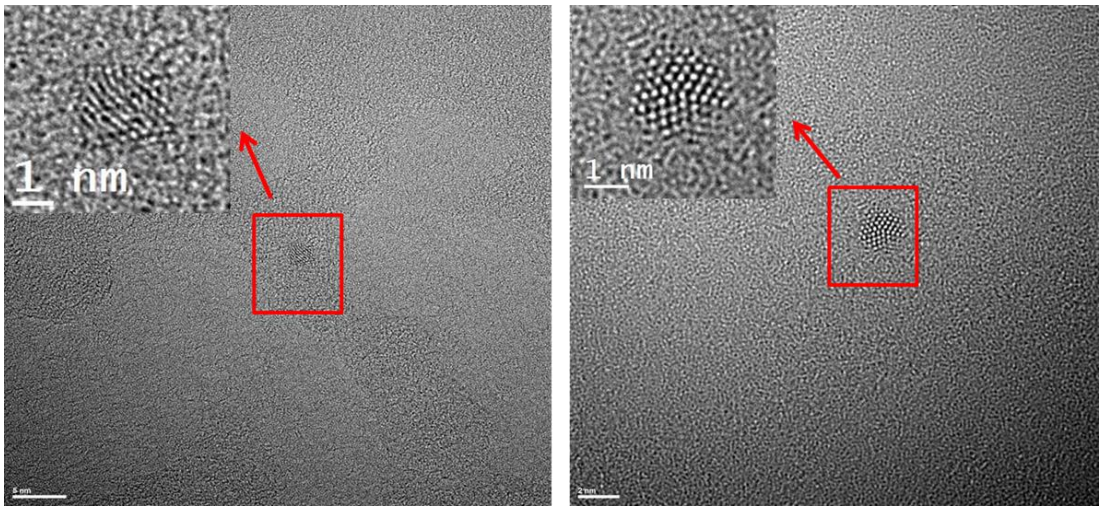

Figure 3.24 TEM and HR-TEM images of Au NPs synthesized at 5°C in the presence of Sodium Citrate.

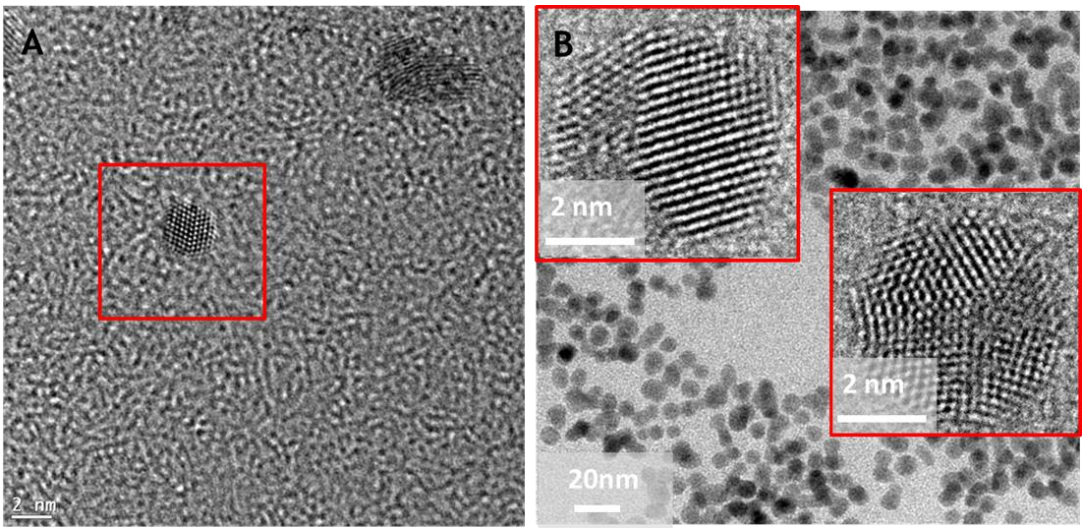

Figure 3.25 TEM and HR-TEM images of Au NPs synthesized at 5°C (left) and at 25°C (Right) in the presence of Sodium Citrate.

3.4 Conclusions

In conclusion, by using the UV-vis technique is complementary to TEM characterization. we are able to detect the morphology (size and shape) of NPs, the molar ratios of the stabilizers increased from 0.2:1 to 0.8:1, 1:1, 3:1,5:1 and 10:1, suggesting increased the size of the gold nanoparticles as the ligands concentration was higher. An optimum size from 0.4:1 up to 2:1 stabilizers/Au ratios we found, after this range the size start to increase again. Due to the limitation of the stabilizer to protect the NPs. The UV-vis spectra display their maximum absorbance peaks and their dependence on the NPs sizes.

The following chapter will discuss the nature of the interactions between citrate (and other carboxylate ligands) and the AuNPs in terms of the mode of coordination at the surface, and the formal oxidation state of Au when interacting with negatively charged carboxylate ligands (i.e., LL in the Green formalism)[82].

Chapter 4.

The Binding Mode of Citrate in The Stabilization Of Gold Nanoparticles

The binding mode of citrate and other carboxylate-containing "ligands" (glutarate, acetate) to gold nanoparticles is crucial for understanding their stabilizing role. Carbon-13 and sodium-23 Solid-state MAS NMR combined with computational modeling (DFT), XPS and TEM measurements are used to provide a detailed picture of the coordination mode of citrate and other carboxylate-containing ligands to gold nanoparticles (AuNPs). The binding between the carboxylate group and the AuNP surface occurs in different modes: mono-carboxylate bidentate (M_1-η^2-μ^2), pseudo mono-carboxylate bidentate with a freely rotating oxygen (M_2-η^2-μ^2) and dicarboxylate bidentate (D-η^2-μ^2). The three modes are simultaneously present at low ratios of citrate to gold, and the pseudo mono-carboxylate bidentate (M_2-η^2-μ^2) mode is favorited at high citrate: gold ratios. The calculated ^{13}C chemical shifts of analogous carboxylate-gold binding modes found in the organometallic literature are in qualitative agreement with the experimental data. XPS confirms that the surface AuNP atoms are predominantly in the zero oxidation state even after coordination of the citrate, although trace amounts of $Au^{\delta+}$ are observed. ^{23}Na NMR experiments suggest that Na^+ ions are present near the gold surface, indicating that the carboxylate binding occurs in an LL type interaction.

4.1 Introduction

The lab-scale synthesis of stable colloidal gold solutions dates as far back as the seminal work reported by Faraday in 1857,[83] and the interest in understanding their properties[84] and exploring their diverse applications[71b, 85] continues to grow. Traditionally, gold was considered to be an inactive catalytic metal, until work by Haruta[71a] demonstrated that decreasing the size of gold nanoparticles (AuNPs) increased their activity towards CO oxidation. Over the last two to three decades, gold has garnered immense interest not only in catalysis[71] but also in various other physical and biological fields.

The citrate-based reduction of gold[86] is now one of the most common methods for synthesizing monodisperse AuNPs for a wide range of applications.[78b] Citrate anions were found to act both as good reducing agents and as an efficient stabilizing agent.[87] The use of citrate as a stabilizer is not restricted to gold or other metals[79] but includes a wide range of materials.[80]

Despite the widespread use of AuNPs, and although it is known that the region surrounding the AuNP becomes negatively charged due to the anionic carboxylate groups. a detailed understanding of the interactions between the Au surface and the citrate ligand still is still elusive. A clear understanding of the chemical and physical interactions between various “ligands” and gold surfaces is indispensable not only for the mechanistic study of catalytic activity at the metal surface but also for biological interactions and potential toxicity effects. Previous work on the citrate-based synthesis of AuNPs has focused on three aspects: reduction of Au(III) complex ions,[88] nucleation and

growth kinetics,[78a, 89] and the mode of the metal stabilizer interaction on the surface.[90] However, the nature of the binding modes between the citrate anion and the gold nanoparticle, once reduced by $NaBH_4$, remains unknown at the molecular level.

Thus far, the stabilization of gold by citrate and the interactions which occur at the interface have been studied by physical methods such as atomic force microscopy (AFM),[90a] scanning tunnelling microscopy (STM),[90b] electroanalytical methods,[91] and more recently by different Fourier transform infrared (FTIR) techniques and associated theoretical modeling.[90c, 90d, 92] Scanning probe microscopy studies investigated the mode of coordination of citrate to gold surfaces and suggested that the citrate anion lies flat on the gold surface and that the interaction involves all three of its carboxylate groups.[43] However, subsequent FTIR studies indicate that the citrate groups are bound to the gold surface by coordination of the carboxylate ligands in a monodentate mode,[90d, 93] a bridging bidentate mode,[92a] or possibly through a combination of both mono- and bridging bidentate coordination modes via one of the carboxylate groups.[90c] To date, the conditions that favour a specific mode of coordination have not been addressed.

Solid-state NMR (SSNMR) has been used successfully to study adsorbed molecules on gold nanoparticles[94] including thiolates,[95] phosphines,[96] carbenes,[97] CO[98] and amines.[99] Solution NMR has been used to study capping groups on nanoparticles,[100] including the decomposition of citrate when the latter is used as a reducing agent.[101] However, determining the binding of carboxylates, which have two equivalent oxygen atoms in the ionized form, is more complex in comparison. Thus far, predicting the binding mode of carboxylates on AuNPs remains unclear and SSNMR has yet to be used to probe the surface binding interactions for this class of AuNPs.

4.2 Aim of this chapter

Here we determine the nature of the interaction between citrate (and other carboxylate-containing ligands) and AuNPs in terms of the modes of coordination at the surface, and the formal oxidation state of Au when interacting with these negatively charged carboxylate ligands (i.e., LL^- in the Green formalism[82]). We achieve this by combining ^{13}C cross polarization magic angle spinning (CP/MAS), ^{23}Na MAS, and low-temperature SSNMR, high-resolution transmission electron microscopy (HRTEM) and density functional theory (DFT) calculations.

4.3 Experimental details

4.3.1 Materials

All chemicals were reagent grade, purchased from Sigma-Aldrich, and were used without further purification. Tetrachloroaurate trihydrate ($HAuCl_4 \cdot 3H_2O$), trisodium citrate dihydrate ($Na_3C_6H_5O_7 \cdot 2H_2O$), Trimesic acid ($C_9H_6O_6$), disodium glutarate ($Na_2C_5H_6O_4$), Sodium Succinate ($C_4H_4Na_2O_4$), Methyl acetate ($CH_3COOCH_3$) and sodium acetate ($NaCH_3COO$) were used as stabilizers and sodium borohydride ($NaBH_4$) was used as a reducing agent. All reactions were done in aqueous media using deionized water (Millipore Milli-Q system, 18.2 MΩ-cm). All glassware was treated with aqua-regia (3:1, HCl/HNO_3) during washing.

4.3.2 AuNP synthesis

100 mL of 0.1 M aqueous stock solutions of trisodium citrate and chloroauric acid were prepared separately by dissolving the required amounts of $Na_3C_6H_5O_7 \cdot 2H_2O$ or $HAuCl_4 \cdot 3H_2O$, respectively. The final concentration of gold chloride in all of the reaction mixtures was 5×10^{-4} M. 0.25 mL aliquots of the chloroauric acid stock solution were placed in separate 100 mL round bottom flasks equipped with a stir bar to which the required amount of trisodium citrate stock solution was added to reach the desired citrate:Au ratio of between 0.2:1 to 30:1. Necessary amounts of water were then added so that the reaction mixture volume measured 47.5 mL. Within approximately 2 min, 2.5 mL of freshly prepared 0.1 M aqueous sodium borohydride solution was added and the resultant solution was maintained under stirring conditions (600 rpm) for 1 hour. Stable solutions were obtained for all reactions with the exception of when the citrate: Au ratio was 30:1, where spontaneous precipitation was observed after the initial reduction of gold ions, and the 20:1 ratio where slow precipitation was observed over an extended period of time. The gold nanoparticle solutions synthesized with citrate: Au ratios below 20:1 exhibited a localized surface plasmon resonance peak (λ_{max}) at ca. 520 nm. The gold nanoparticles thus obtained at this stage were characterized by TEM and solid state NMR.

4.4 Results and discussion

A series of gold nanoparticles were prepared with different citrate:Au ratios, with 1:1 to 5:1 yielding AuNPs with average diameters of approximately 2-3 nm and a desirable

narrow size distribution (**Figure 4.1a**). Spherical aberration correction allows nanoparticle facets to be clearly observed in HRTEM images (**Figure 4.1b**). Shows the 13C CP/MAS NMR spectrum of crystalline bis(trisodium citrate) undecahydrate (hereafter referred to simply as, 'sodium citrate'). The peaks at 46 ppm and 48 ppm correspond to the two CH_2 carbons, the peak at 75 ppm is assigned to the quaternary carbon, with three peaks in the carboxylate region at 178, 181, and 183 ppm. When citrate is adsorbed on AuNPs with different citrate:Au ratios, the HRTEM and 13C CP/MAS NMR spectra have the following distinct features:

Particles prepared with a citrate:Au ratio of 0.2:1 have a broad particle size distribution centered at a diameter of 4.7 nm (**Figure 4.2a**) and a calculated maximum coverage, ($\theta_{(cal)}$), of the nanoparticle by the citrate of 0.75. On certain occasions (probably linked to data acquisition time) it was possible using HRTEM to observe nanoparticles having a uniform thin surrounding layer (**Figure 4.1c**). The low contrast of this layer indicates it is likely carbonaceous material that therefore originated from the sodium citrate used during the synthesis. The thickness of this layer is ca. 0.58 nm, which interestingly is comparable with the dimensions of the sodium citrate salt formula unit. The ^{13}C CP/MAS NMR show, in addition to peaks that occur at the same position as those of crystalline bis(trisodium citrate) undecahydrate, three new peaks in the carboxylate region spanning the chemical shift range from 162 – 167 ppm (**Figure 4.3**).

- Particles prepared with a citrate:Au ratio of 1:1 (**Figure 4.1a and Figure 4.3**) have a narrow particle size distribution centered around a diameter of 2.2 nm and $\theta_{(cal)}$ of 2.1. The band of peaks at 162-167 ppm in the ^{13}C CP/MAS NMR spectrum is replaced by a single narrow peak at 167 ppm.

- Particles prepared with a citrate:Au ratio of 5:1 (**Figure 4.1a and Figure 4.3**) have a size distribution centred around a diameter of 3 nm, and a $\theta_{(cal)}$ of 13.0. Here, we observe that the relative intensity of the peak at 167 ppm has diminished, which can be attributed to a relative increase in the contribution from bulk sodium citrate which is now present in excess.

- At the very high citrate:Au ratio of 20:1 (**Figure 4.1a and Figure 4.3**), the HRTEM images show a layer that is ca. 1.1 nm thick (**Figure 4.1a and Figure 4.3**) around the AuNP, nearly twice that observed for lower citrate:Au ratios.

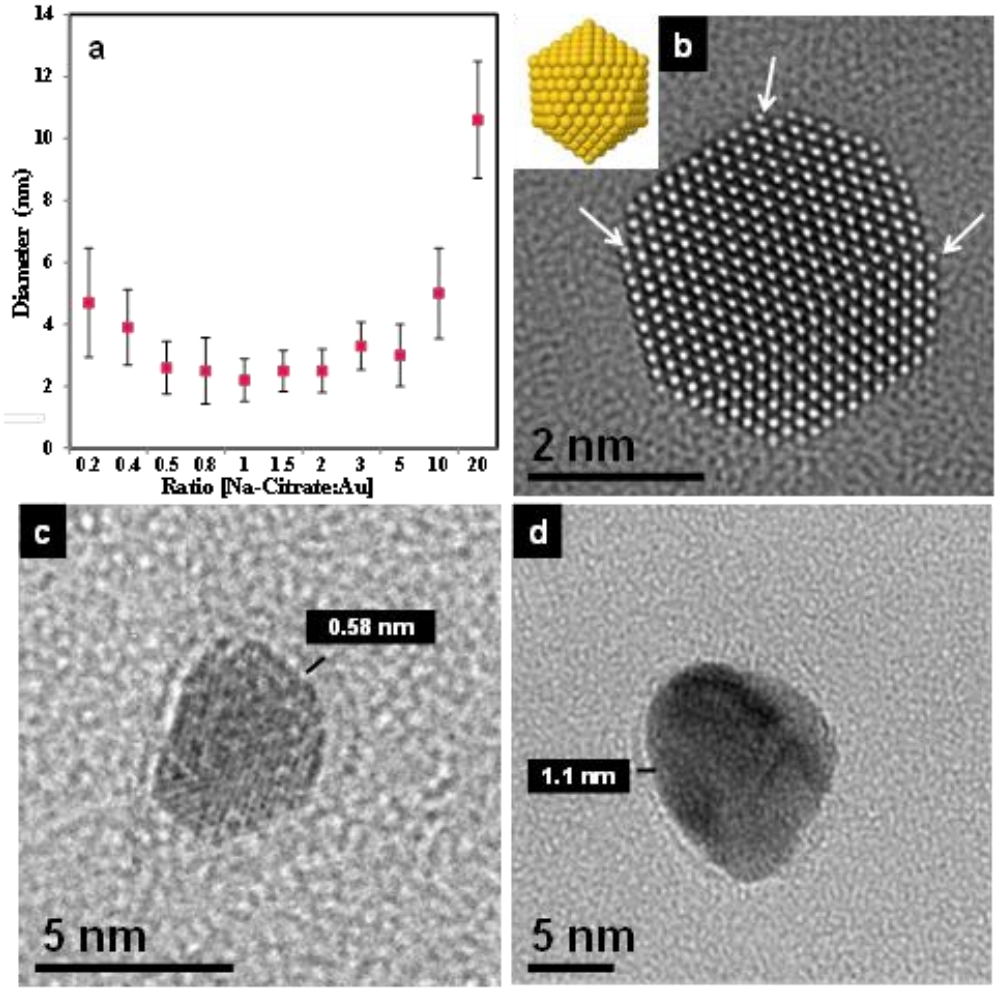

Figure 4.1 (A) Average gold nanoparticle size along with the standard deviation as a function of the sodium citrate: gold ratio. (B) HRTEM image of a gold nanoparticle synthesized by $NaBH_4$ reduction in the presence of citrate with a 1:1 citrate: Au ratio. White arrows indicate surface defect sites. HRTEM images of AuNP with carbonaceous layers of different thickness when synthesized with (C) 0.2:1 and (D) 20:1 citrate: Au ratios.

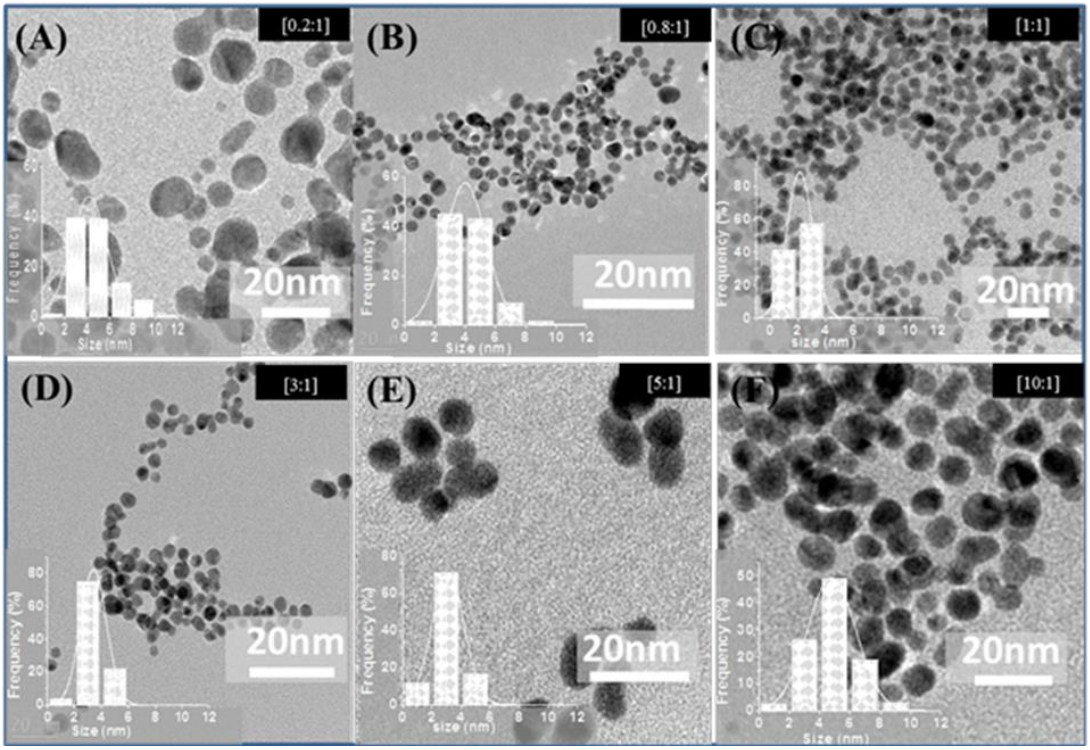

Figure 4.2 TEM images of AuNP synthesized by $NaBH_4$ reduction in the presence of different amounts of citrate with respect to a constant amount of $HAuCl_4$. Citrate/Au ratio: from (A) [0.2:1] to (F) [10:1]. The inset in each image shows the particle size distribution for respective samples fitted by a Gaussian curve.

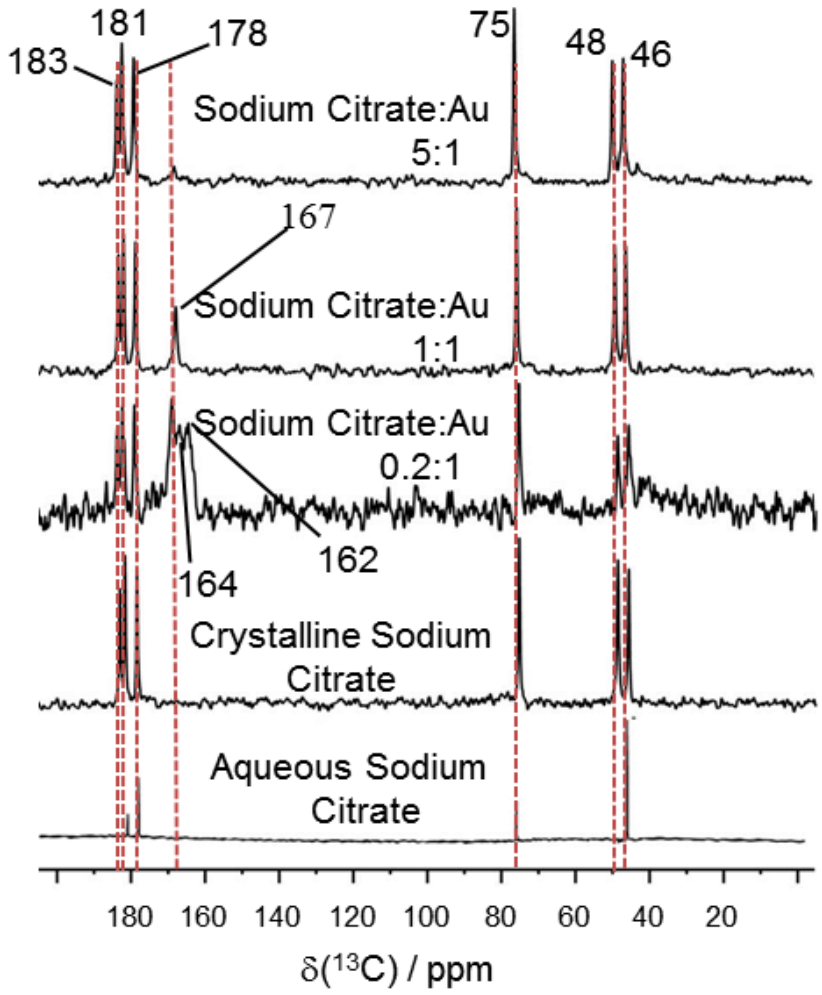

Figure 4.3 One-dimensional (1D) 13C CP/MAS NMR spectra of (A) citrate: Au with different ligand: gold ratios. (number of scans = 50 000 to 100 000, repetition delay = 5 s, contact time = 2 ms, exponential line broadening = 80 Hz).

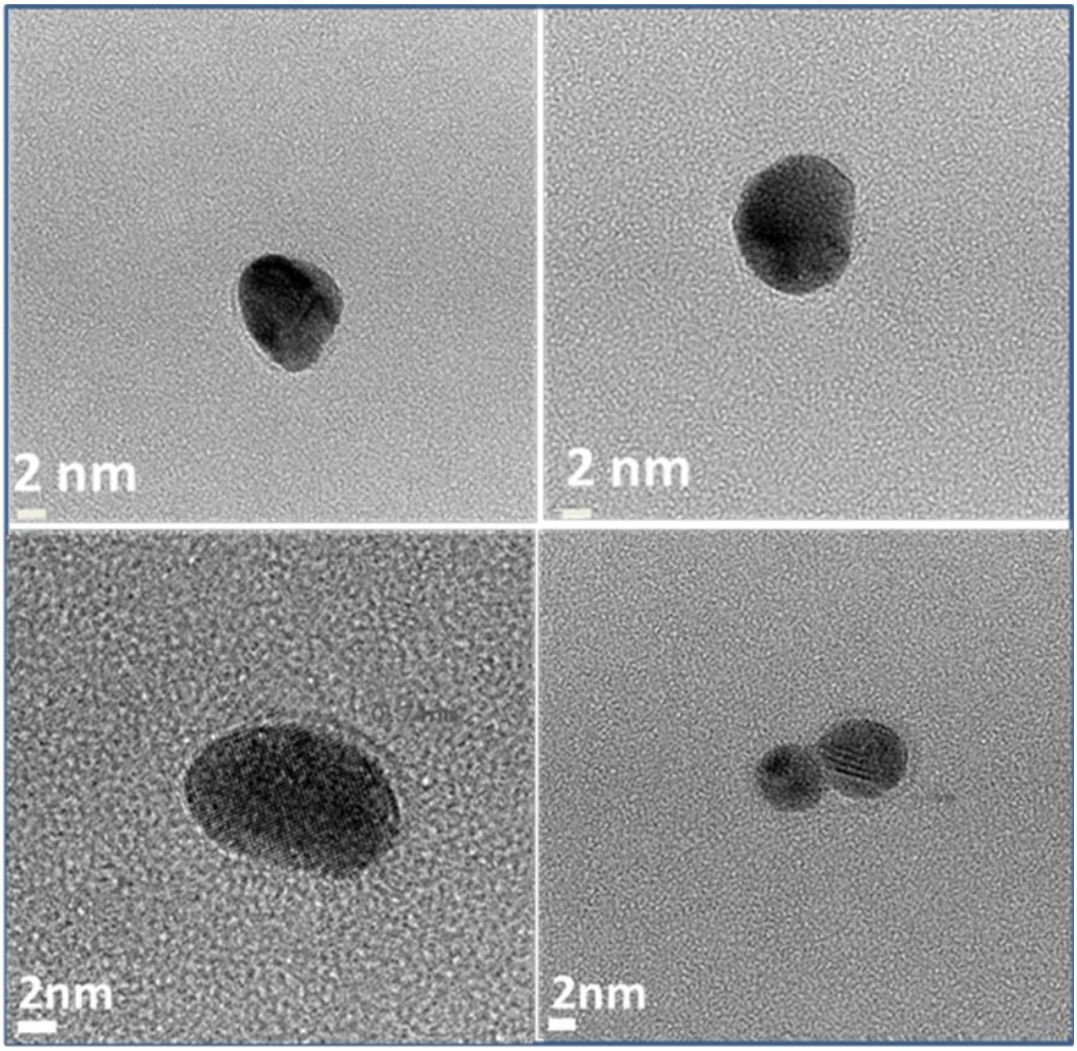

Figure 4.4 HRTEM images of selected AuNP that show a thin layer around them, and synthesized with a citrate to gold ratio of 0.2:1. The low contrast layer surrounding the AuNP is a carbonaceous material, confirmed by energy-dispersive X-ray spectroscopy (EDS), and is derived from the trisodium citrate added as a stabilizer during synthesis.

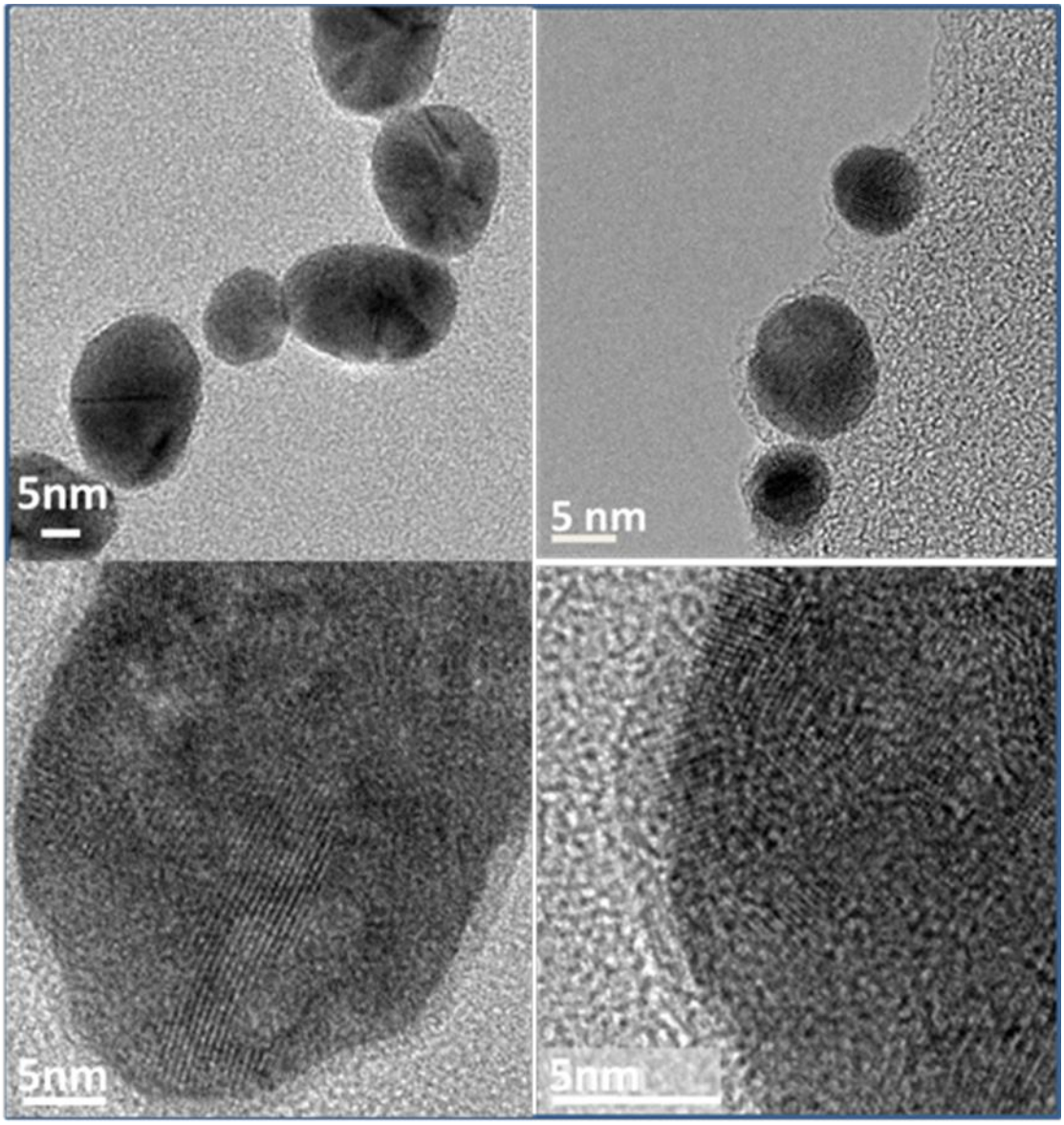

Figure 4.5 HRTEM images of AuNP samples synthesized with a citrate to gold ratio of 20:1. The presence of a layer of carbonaceous material can be clearly observed.

Due to the remarkably high resolution obtained with a spherical aberration (Cs) correction to the HRTEM images, interesting structural details become visible. The faceted structure of the nanoparticle is evident and further we can clearly observe that although the facts are atomically flat, there are a number of surface steps and vacant sites at vertices, as indicated by the arrows in **Figure 4.1b** that could potentially influence the mode of binding of the "surface ligand" in the vicinity.

To complement the SSNMR and HRTEM observations, DFT calculations of systems containing carboxylate groups and various Au surface models were undertaken. We studied the behavior of the interactions of the carboxylate in acetate (Ac), succinate (Sc) and glutarate (Gt) **Figure 4.6**.

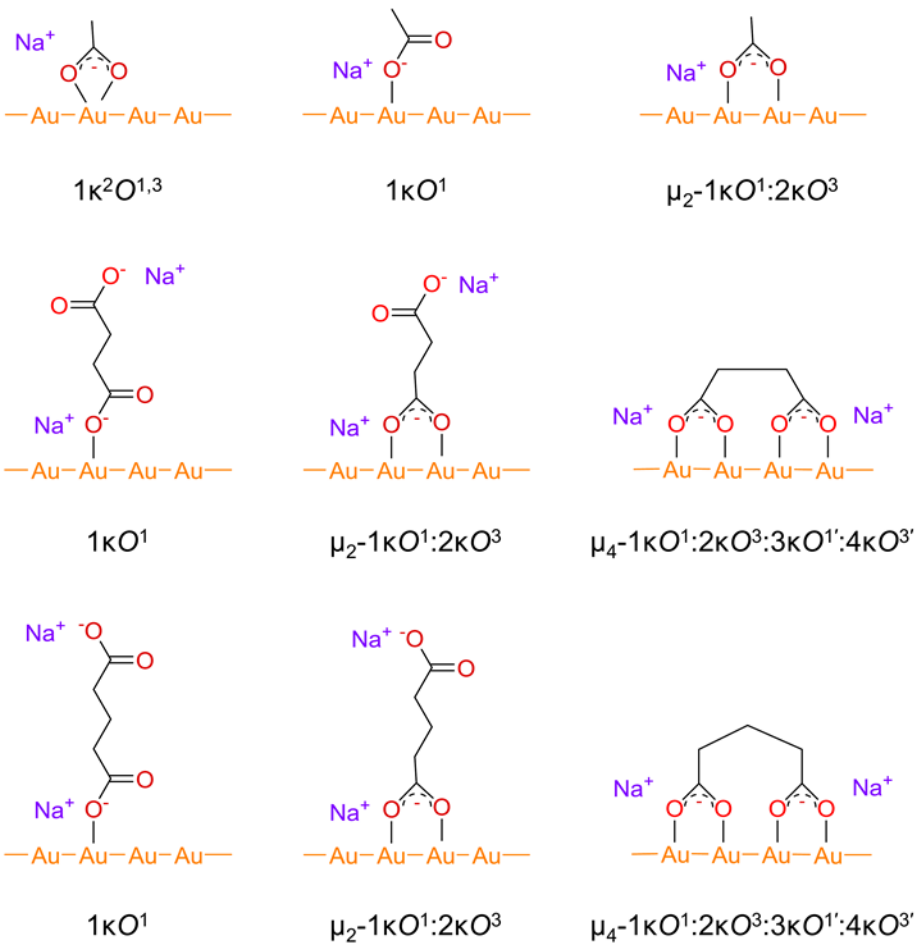

Figure 4.6 Schematic representations of the possible modes of coordination of (top) sodium acetate:Au, (middle) sodium succinate:Au, and (bottom) sodium glutarate:Au.

In this framework, coordination of Sc to the Au surface mimics the coordination of the middle and terminal carboxylates of citrate, while coordination of Gt mimics the two terminal carboxylates of citrate.

When one Ac anion is placed near either of the Au(111) or (100) surfaces,[102] the geometry optimized Ac is consistently found to bridge two Au surface atoms, with each carboxylate oxygen interacting with one Au (i.e., *syn,syn*-η^1:η^1:μ^2, hereafter 'μ^2'), as in **Figure 4.7a and b.** Additionally, the non-H acetate atoms, which lie essentially in a

plane, are nearly normal to the respective Au surface planes. The μ^2 mode was found independently of the initial coordination mode. The acetate binding energy, E_{Bind}, is calculated to be −30.5 kcal/mol for Ac on the Au(100) surface and −17.1 kcal/mol for Au(111), indicating stronger binding to Au(100),

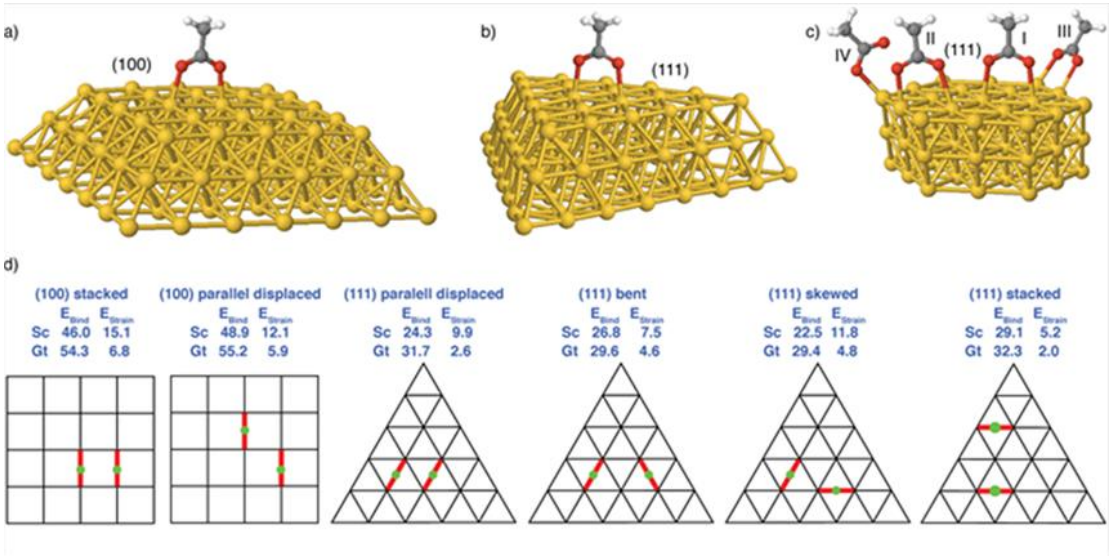

Figure 4.7 DFT-optimized ligand geometries for a single acetate anion interacting with (a) the Au(100) and (b) the Au(111) model surfaces, and of four acetate anions interacting with an Au(111) model surface. In (a) and (b) the acetate is bound in a μ^2 fashion, while in (c) the 4 acetates are found in a variety of coordination modes (both μ^2 and κ^1). In (d), a cartoon representation of the possible coordination modes of succinate (Sc) and glutarate (Gt) to the Au(100) and Au(111) model surfaces is given. The total binding energy, EBind, and the strain energy, EStrain, calculated relative to the binding of two isolated acetate anions are reported in kcal/mol. The single carboxylate units are represented as a thick red line and a green circle.

in rough accord with that found in an earlier theoretical study of the formate adsorption on Au_{20}.[103] The rather low Ac binding energy is due to the inclusion of solvent effects, which substantially stabilize the isolated Ac anion. As the acetate/Au interaction is μ^2, the average Au-O interaction energy is half the above values (ca. −10-15 kcal/mol in water).

Based on these results, for Gt and Sc we only explored geometries presenting μ^2 coordinated carboxylates. The representations in **Figure 4.7d** indicate that Sc and Gt can assume two conformations on Au(100), corresponding to a perfectly stacked or to a parallel-displaced disposition of the two carboxylates, while at least four different dispositions of the carboxylates are possible on the Au(111). The 3D representations of all optimized geometries show that in all cases both carboxylates interact with the surface via a μ^2 coordination geometry, with Au-O distances in the 2.2-2.4 Å range. The E_{Bind} of the carboxylates is in the 25-55 kcal/mol range, which is substantially below the experimentally determined Au-O bond energy in AuO (3 eV ≈ 290 kJ/mol), and the computationally determined Au-O dissociation energy of O_2 on an Au surface,[104] which underscores that the Au-O interactions occurring on the AuNP surfaces are weak compared to covalent interactions.

Comparing Sc and Gt with Ac, our calculations suggest that Gt binding is roughly 3-7 kcal/mol stronger than Sc binding on both surfaces, which suggests that binding of citrate through the terminal carboxylates should be favored over binding through one terminal and the central carboxylate. Nevertheless, the relatively small difference in the binding energy of Sc and Gt to a specific surface, particularly Au(111), suggests that the two and three methylene bridges are flexible enough to adapt to the AuNP surface environment, as determined by coordination of other carboxylates and/or counterions.

To understand if binding of the two carboxylate groups of Sc and Gt results in a strain on the carboxylate skeleton, we calculated the strain energy, E_{Strain}, which was found to be low, indicating that binding of dicarboxylates only requires a limited conformational adaptation of the dicarboxylate skeleton, and thus should be favored relative to binding via a single carboxylate.

As higher loading levels may favor other binding modes,[93] we modelled the coordination of up to four Ac on Au(111). Consistent with the results for Sc and Gt, the bridging bidentate coordination mode is retained if two Ac anions coordinate next to each other. However, with four Ac anions on the small surface fragment shown in **Figure 3c**, other coordination modes are observed. Figure 3c shows a wide variation in Au-O binding motifs for Ac on Au(111), with ligands binding at the edge in a κ^1 fashion (Ac IV in **Figure 4.7**), and in a μ^2 fashion. We note that the monodentate mode was observed particularly at surface edges. It is possible that AuNP surface defects, such as the step edges and vacancies observed in the HRTEM images (highlighted in **Figure 4.1**) could contribute towards such alternative binding modes.[105]

We find that the largest energy cost to binding multiple neighbors is associated with the edge acetate anion in the μ^2 motif (III in **Figure 4.7**), which is about 9 kcal/mol greater than for the other acetate ligands on this Au(111) surface. The additional energy required to bind four Ac anions next to each other as in **Figure 4.7c**, calculated as the total binding energy of four Ac minus four times the binding energy of an isolated Ac, is +20.3 kcal/mol. This energy cost is clearly related to electrostatic repulsion between the Ac anions, but which is much higher in the gas phase, and suggests an important role of the solvent and Na^+ counterions in neutralizing the excess negative Au surface charge.

In summary, DFT calculations predict that at very low loading levels the Ac anion is likely to coordinate in a μ^2 fashion to regular Au surfaces via the two oxygen atoms of the carboxylate. Moving to dicarboxylates, DFT calculations suggest that Sc and Gt can effectively coordinate to both Au(100) and Au(111), with the three methylene spacer favoring Gt coordination. Extrapolating these results to citrate coordination, DFT calculations suggest that citrate will weakly bind to the Au nanoparticle, preferentially via μ^2 binding of the terminal carboxylates.

Based on several model molecular structures and known crystal structures, it is found that the Au-O interaction for a carboxylate group produces a ^{13}C shielding effect on the order of 15 - 30 ppm. This is consistent with the observations made via the ^{13}C SSNMR experiments in **Figure 4.3**. We also find that the bidentate but non-bridging coordination mode will likely lead to a more modest deshielding effect (relative to the parent sodium salt) on the order of a few ppm at Au-O distances considered relevant for an interaction, and this is inconsistent with experimental observations.

We thus arrive at the schematic structures presented in **Figure 4.6**. The following simple interpretations are used to assign the ^{13}C SSNMR spectra: where the surface coverage is lower, the peaks in the spectra can be attributed to monocarboxylate monodentate at 167 ppm and bridging bidentate mono- at 162 ppm and di-carboxylate at 164 ppm. At higher surface coverage the broad band (3 peaks) becomes a single narrow peak at 167 ppm, due to a mode which gives closer packing with the monodentate surface-coordinated carboxylates linked to Au. This agrees with recent IR results of Park and Shumaker-Parry,[49] who showed that citrate can adsorb on the Au surface via 1 or 2 oxygen atoms. However, the difference between bridging and chelating modes could not

be spectrally distinguished with FTIR. NMR experiments as a function of pH also support this conclusion.

In addition to the binding mode, the carbon-13 SSNMR spectra also allow us to deduce the three-dimensional structure of the citrate at the AuNP surface. Generally, small changes in structure lead to notable changes in the shifts of all the carbons (e.g. see appendices for spectra of the two known forms of crystalline sodium citrate). Since in the AuNP samples all the carbon shifts are identical to those measured for bis(trisodium citrate) undecahydrate we conclude that the citrate backbone retains that structure and hydration arrangement when bound to the NP surface, and only the carboxylate groups interacting directly with the gold surface are different.

To confirm the carboxylate–Au interaction, additional SSNMR experiments were done with: (a) different dicarboxylate-containing species (namely sodium glutarate and sodium succinate) as well as a monocarboxylate system (sodium acetate), (b) low temperature (^{13}C CP/MAS NMR) at different citrate:Au ratios, and (c) ^{23}Na MAS NMR. At low ligand:Au ratios (0.2:1), peaks in the range 162-168 ppm were observed in the ^{13}C CP/MAS NMR spectrum of NPs with glutarate or succinate, as for the analogous sodium citrate results.

To confirm the carboxylate–Au interaction, additional SSNMR experiments were done with:

a) Different Tri -carboxylate-containing species (tri sodium citrate- trimesic acid), di-carboxylate-containing species (namely sodium glutarate and sodium succinate) as well as a mono-carboxylate system (sodium acetate and Methyl acetate),

b) Variation in the pH of citrate: Au at the ratio of 1:1 and

c) Low temperature (^{13}CCP/MAS NMR) at different citrate: Au ratios.

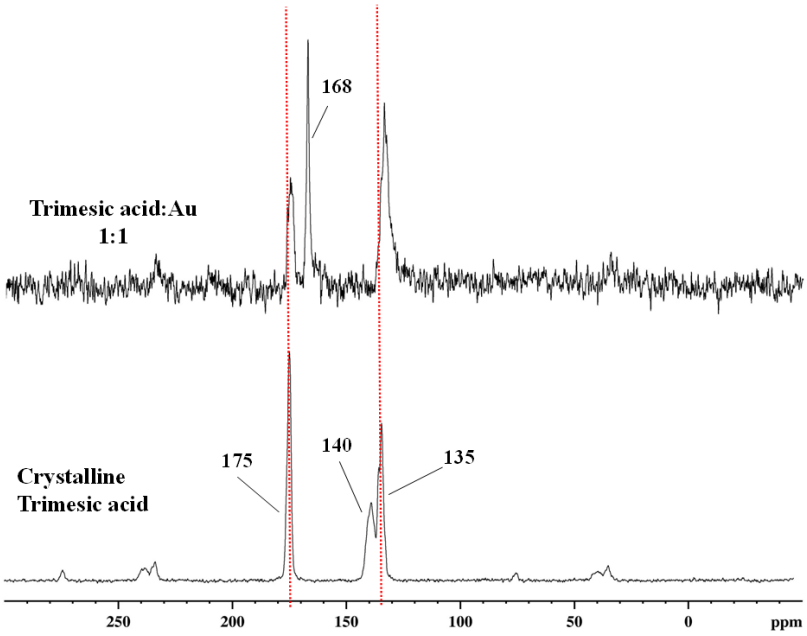

Figure 4.8 ^{13}C CP/MAS NMR spectra of Trimesic acid: gold 1:1 ratio. (number of scans = 50 000 to 100 000, repetition delay = 5 s, contact time = 2 ms, exponential line broadening = 80 Hz).

These new peaks in the same spectral region were also detected with the Trimesic acid system, which is another tri-carboxylate-containing ligand **Figure 4.8**. A series of gold nanoparticles were prepared with different Trimesic acid: Au ratios (ranging from 0.2:1 to 10:1). Amongst them, the ratios between 1:1 and 5:1 yielded the smallest AuNPs, with average diameters of approximately 3-5 nm, and a desirable narrow size distribution **Figure 4.9**. AuNPs synthesized with Trimesic acid: Au ratios above or below this level exhibited larger average particle diameters and broader size distributions

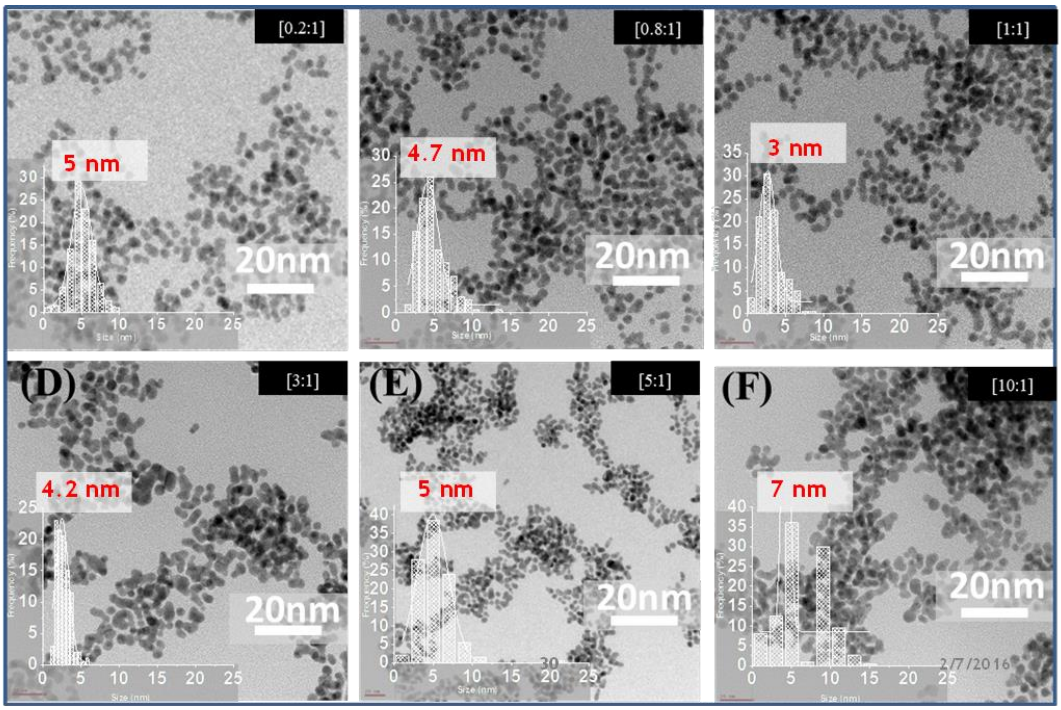

Figure 4.9 TEM images of AuNP synthesized by NaBH4 reduction in the presence of different amounts of Trimesic acid with respect to a constant amount of $HAuCl_4$. Trimesic acid /Au ratio: from (A) [0.2:1] to (F) [10:1]. The inset in each image shows the particle size distribution for respective samples fitted by a Gaussian curve.

We begin by considering sodium glutarate, which was used to stabilize small AuNPs at the low glutarate: Au ratio of 0.2:1 **Figure 4.10**.

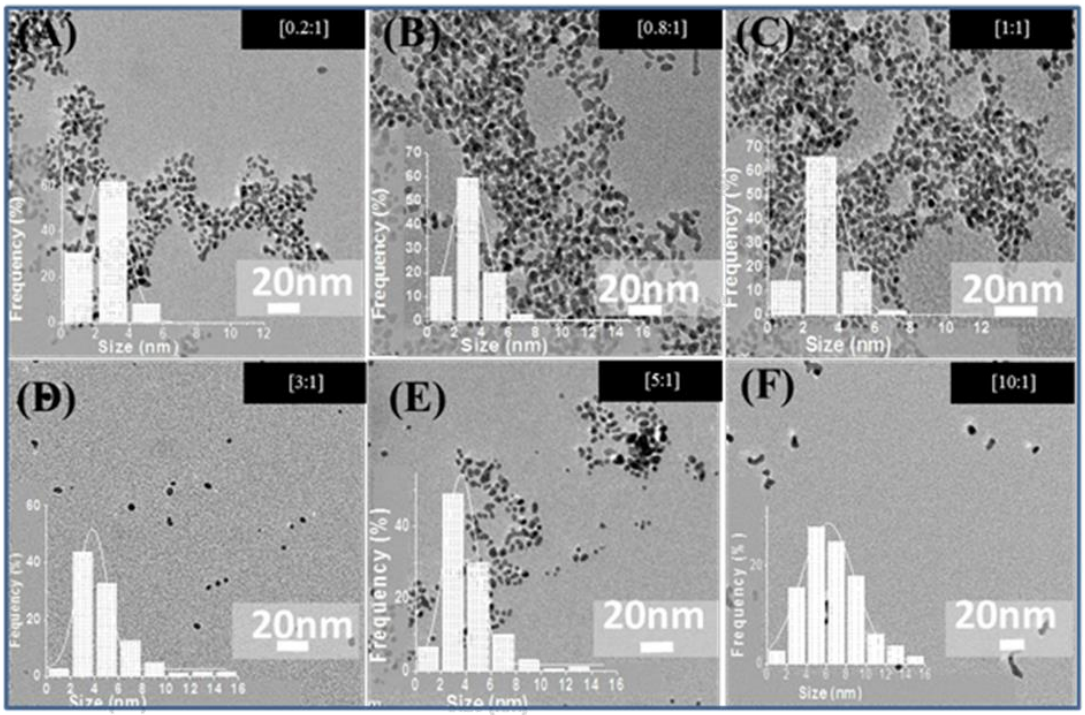

Figure 4.10 TEM images and respective particle size distributions (inset) of AuNP synthesized by NaBH4 reduction in the presence of different amounts of glutarate with respect to a constant amount of HAuCl4. Glutarate/Au ratio: from (A) [0.2:1] to (F) [10:1].

The ^{13}C CP/MAS NMR spectrum of crystalline sodium glutarate shows 3 peaks: one at 24 ppm (CH_2-***C***H_2-CH_2), one at 41 ppm (CH_2-***C***H_2-COO^-), and one at 183 ppm (3 carboxylates, ***C***OO^-) **Figure 4. 11**. When interacting with Au at low ligand: Au ratios (0.2:1), new peaks in the range 162-168 ppm were observed, which is analogous to the above results with sodium citrate **Figure 4.3**. These new peaks in the same spectral

region were also detected with systems containing sodium succinate, which is another di-carboxylate-containing ligand **Figure 4. 12.**

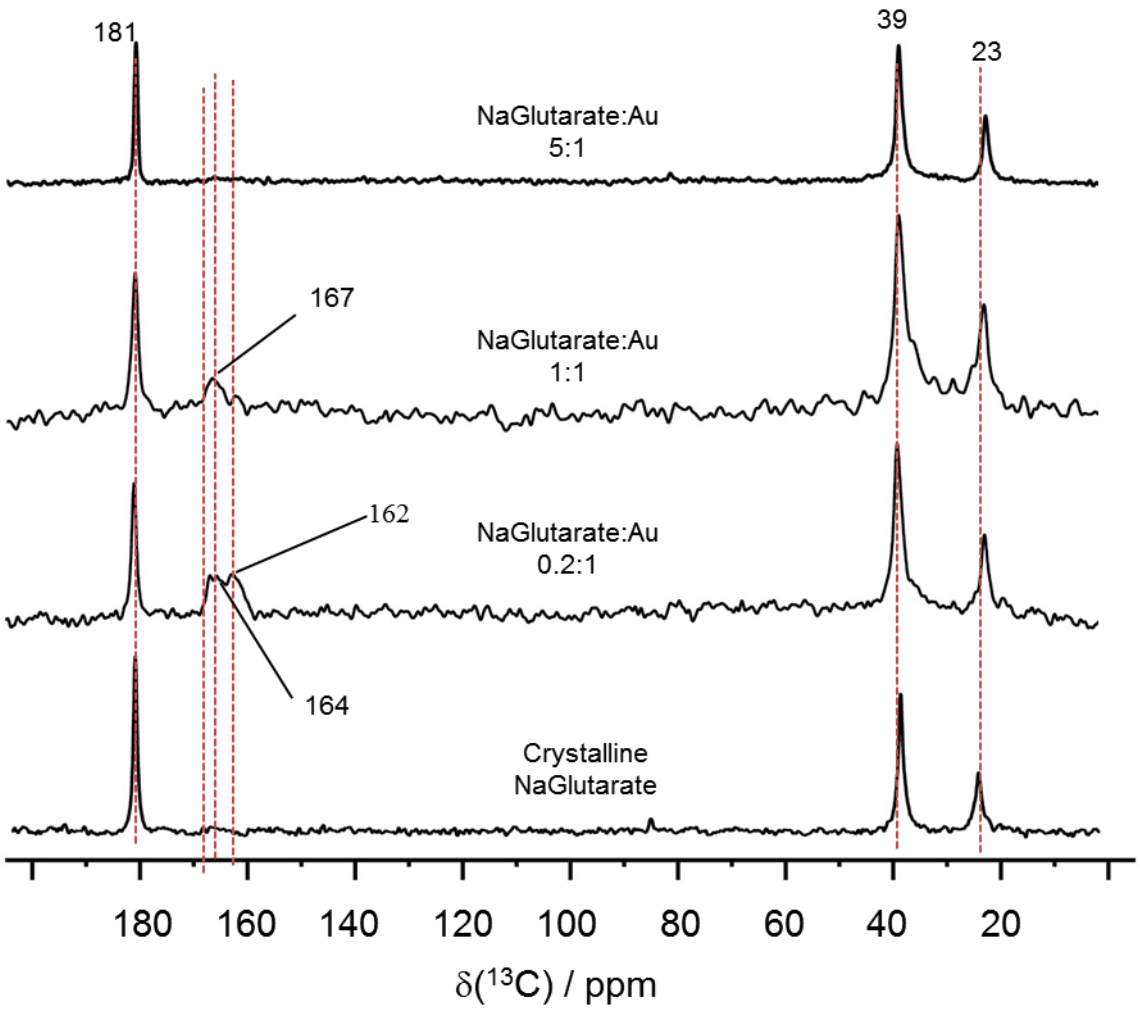

Figure 4. 11 ^{13}C CP/MAS NMR spectra of Glutarate: gold with different ligand: gold ratios. (number of scans = 50 000).

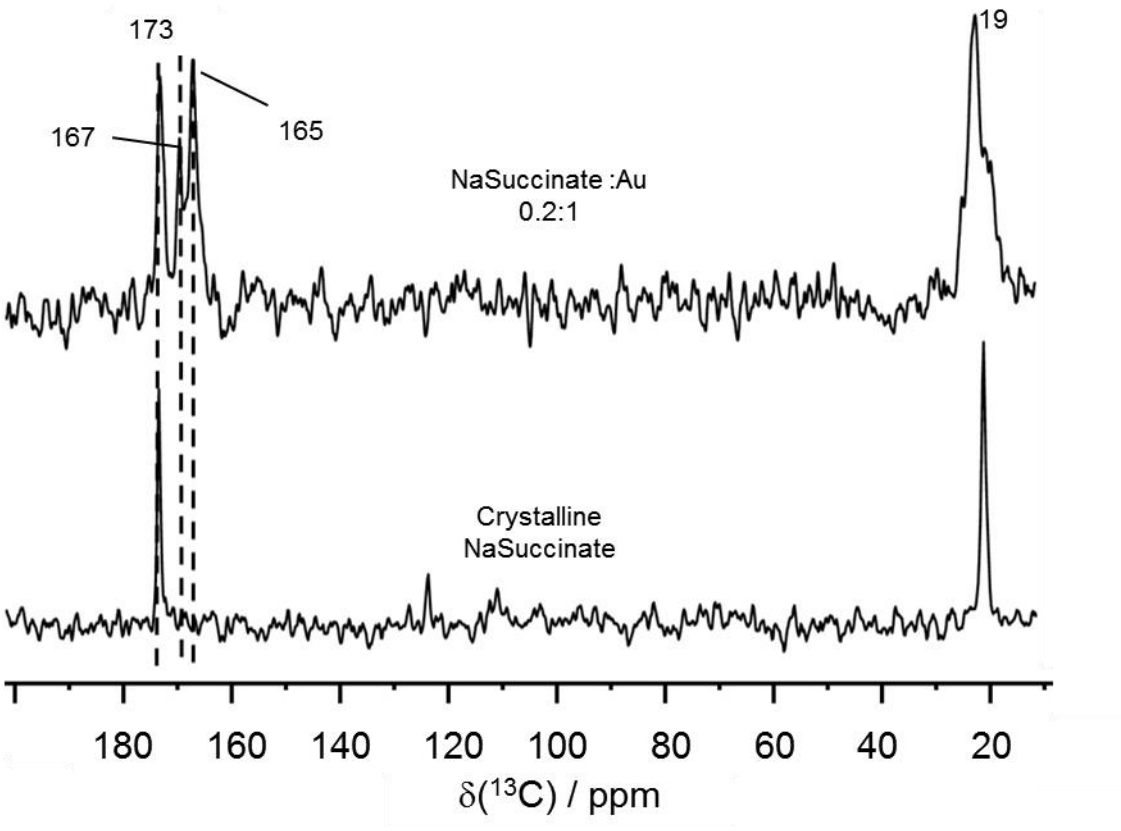

Figure 4. 12 ^{13}C CP/MAS NMR spectra of succinate/Au 0.2:1 (number of scans = 50 000 to 100 000, repetition delay = 5).

We conclude that the peaks at 162 ppm and 164 ppm can be assigned to a mono-carboxylate bidentate (M_1-η^2-μ^2) and di-carboxylate bidentate (D-η^2-μ^2) interactions respectively **Figure 4.6**. The narrow peak at 167 ppm is attributed to pseudo mono-carboxylate bidentate with a freely rotating oxygen (M_2-η^2-μ^2) **Figure 4.6**. By increasing the amount of the ligand species (sodium citrate, sodium glutarate and sodium succinate) to a 1:1 ratio with the AuNP, the (M_2-η^2-μ^2) mode of binding is favoured. Particles stabilized with sodium acetate, provide further insight regarding the binding mode using SSNMR **Figure 4.13.** The AuNP diameter distributions for these particles are shown in **Figure 4. 14.**

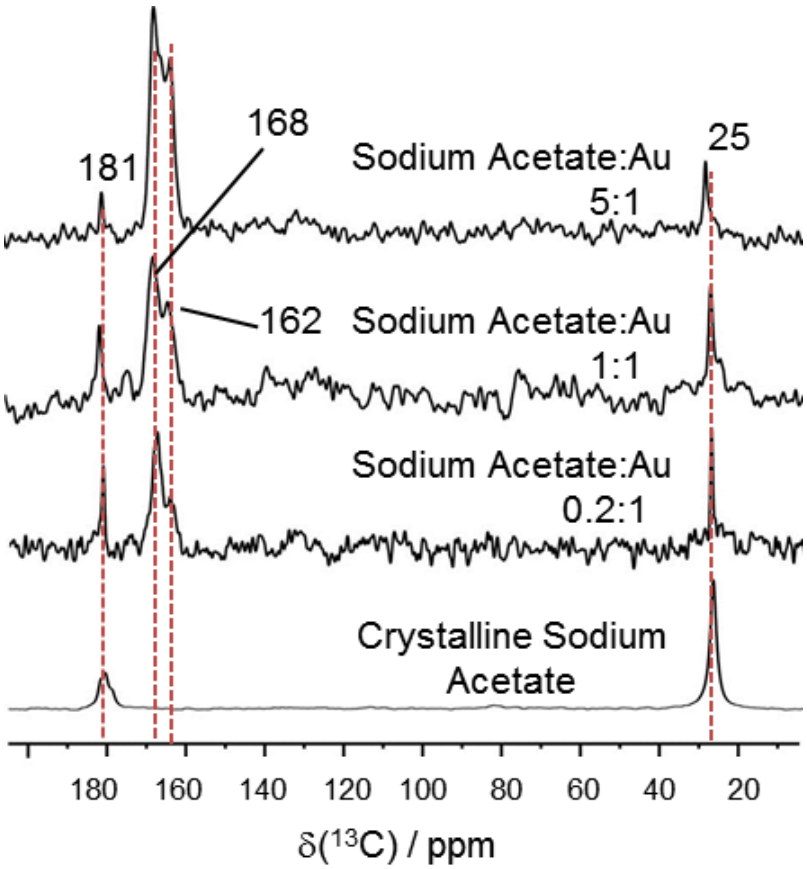

Figure 4.13 One-dimensional (1D) ^{13}C CP/MAS NMR spectra of acetate: Au systems having different ligand: Au ratios. (number of scans = 50 000 to 100 000).

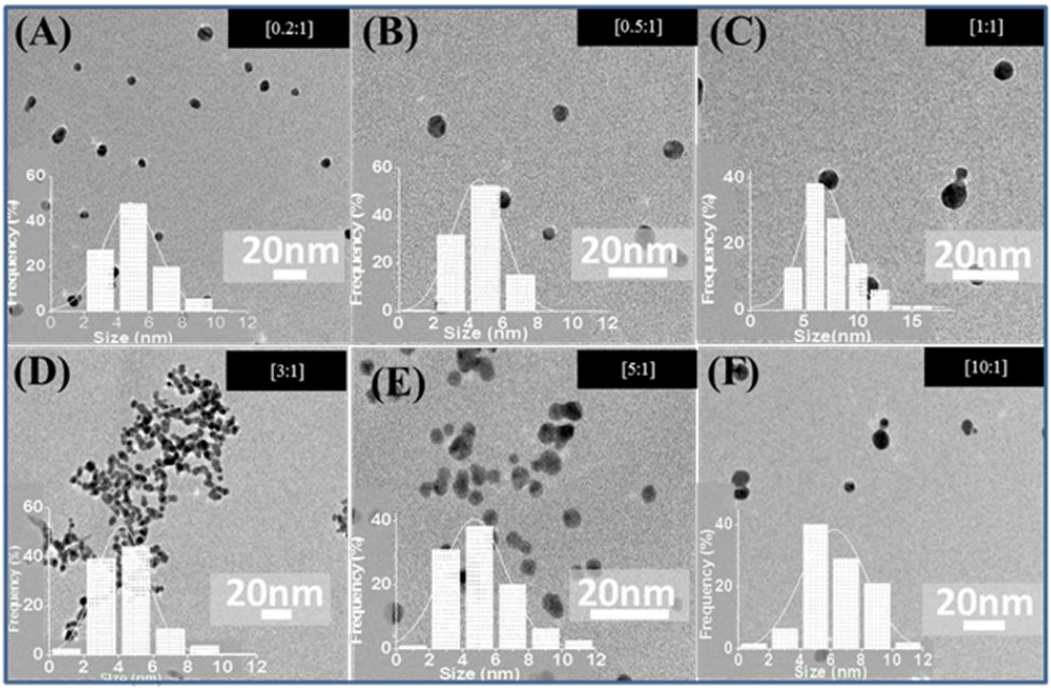

Figure 4. 14 TEM images and respective particle size distributions (inset) of AuNP synthesized by $NaBH_4$ reduction in the presence of different amounts of acetate with respect to a constant amount of HAuCl4. Sodium acetate/Au ratio: from (A) [0.2:1] to (F) [10:1].

The ^{13}C CP/MAS NMR spectrum of crystalline sodium acetate shows the contribution of the methyl and carboxylate carbons at 25 ppm and 181 ppm, respectively. After coordination, and as with the citrate and glutarate ligands, new resonances appear at 168 and 162 ppm, which are tentatively assigned as belonging to a mono-carboxylate bidentate (M_1-η^2-μ^2) and pseudo mono-carboxylate bidentate with freely rotating oxygen (M_2-η^2-μ^2), respectively. The third peak at 164 ppm see with citrate attributed previously

to the di-carboxylate bidentate (D-η^2-μ^2) coordination mode is necessarily absent, as acetate contains a single carboxylate. By increasing the sodium acetate to gold ratio, the intensity of both NMR signals remains roughly constant. The new resonances confirm again the mixed coordination of the carboxylate group onto the AuNP surface; however, here the mixed coordination modes coexist at both low and high ratios, likely due to the absence of significant steric effects and a facility of exchange between bound and free acetate.

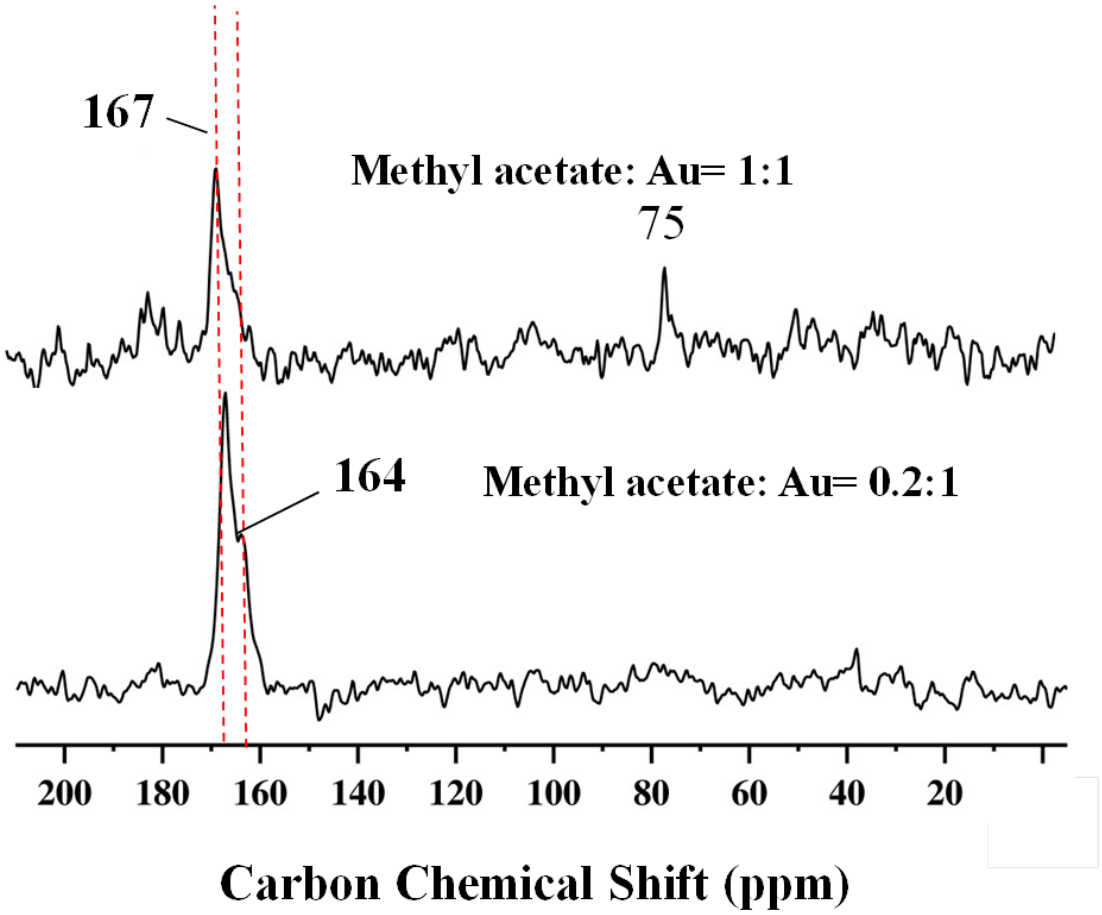

Figure 4. 15 One-dimensional (1D) 13C CP/MAS NMR spectra of Methyl acetate: Au systems having different ligand: Au ratios. (number of scans = 50 000 to 100 000).

To investigate more, we done the ^{13}C CP/MAS NMR spectra of Methyl acetate, We overcome with this conclusion; When is adsorbed on AuNPs with different Methyl acetate: Au (1:1and 0.2:1) ratios, the spectra have the following distinct features:

The ^{13}C CP/MAS NMR show in addition to crystalline Methyl acetate, one new peak in the carboxylate region spanning the chemical shift at 164 ppm and one peak correspond to free ligand at 75ppm **Figure 4. 15**.

- For Methyl acetate: Au ratio of 1:1, the band of the peak in the 164 ppm range in the ^{13}C CP/MAS NMR spectrum is still at the same position **Figure 4.3**. It seems that all the ligand coordinates to AuNPs surface. This is the same case with acetate **Figure 4.13**.

As a further probe of the ligand-AuNP interaction, experiments were done as a function of pH for sodium citrate stabilized particles. After the synthesis of the AuNP, which required the addition of 10 equivalents of sodium borohydride, the pH of the solution was measured to be 9. This value is considerably higher than the three pKa values of sodium citrate (pKa_1 = 3.14, pKa_2 = 4.75 and pKa_3 = 6.39), indicating that all carboxylate (COO^-) groups are deprotonated. The pH of the AuNP solution was then adjusted to either pH = 6 or pH = 3 by adding the required amount of 0.1 M hydrochloric acid, HCl *aq* after synthesis. Transmission electron microscopy (TEM) results show a dramatic increase in AuNP diameter, from 2.2 nm at pH = 9 to 5.0 nm and 7.6 nm for pH = 6 and 3**Figure 4. 16**.

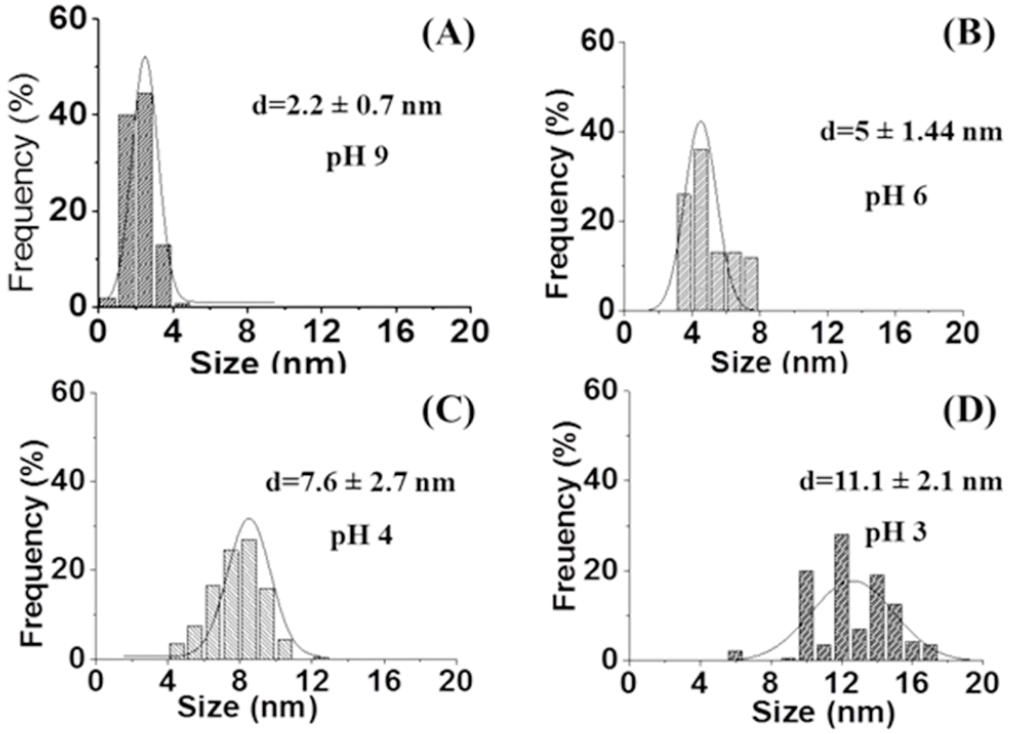

Figure 4. 16 Histograms of particle size distributions calculated from TEM images show a significant increase in the average nanoparticle size with a decrease in the solution pH from 2.2 nm at pH = 9 to 5.0, 7.6 and 11.1 nm at pH = 6, 4 and 3, respectively. This increase in particle size with respect to decreasing pH confirms that the basic form of citrate (R-COO-) is able to effectively restrict the growth of nanoparticles and hence is a better stabilizer than the acidic form (R-COOH).

This increase in particle diameter confirms that the deprotonated form of citrate (R-COO^-) is a better stabilizer than the forms which are either partially or fully protonated (i.e., contain R-COOH). The ^{13}C CP/MAS NMR spectra **Figure 4. 17** of citrate on AuNPs with a citrate: Au ratio of 1:1 and with different pH values support this hypothesis. When the fully deprotonated form of citrate is lost, the characteristic peak of

citrate coordinated to the AuNP at 167 ppm is absent, which we interpret as direct evidence for the elimination of the Au-O interaction. Based upon this, we can speculate that at pH = 9, one carboxylate group of the citrate interacts with the AuNP surface, while the other two are engaged in an ionic interaction with Na^+. We also note that at lower pH values, the ^{13}C NMR peaks of free citrate are shifted to the higher field because the carboxylate groups have been protonated.[106] These same shifts were also recorded for aqueous sodium citrate in liquid state ^{13}C NMR at variable pH **Figure 4. 18**. The above experiments provide direct proof of the role of the carboxylate anion in controlling the size of the gold nanoparticles and highlight that the stabilization ability of the fully deprotonated form is greater than the protonated form.

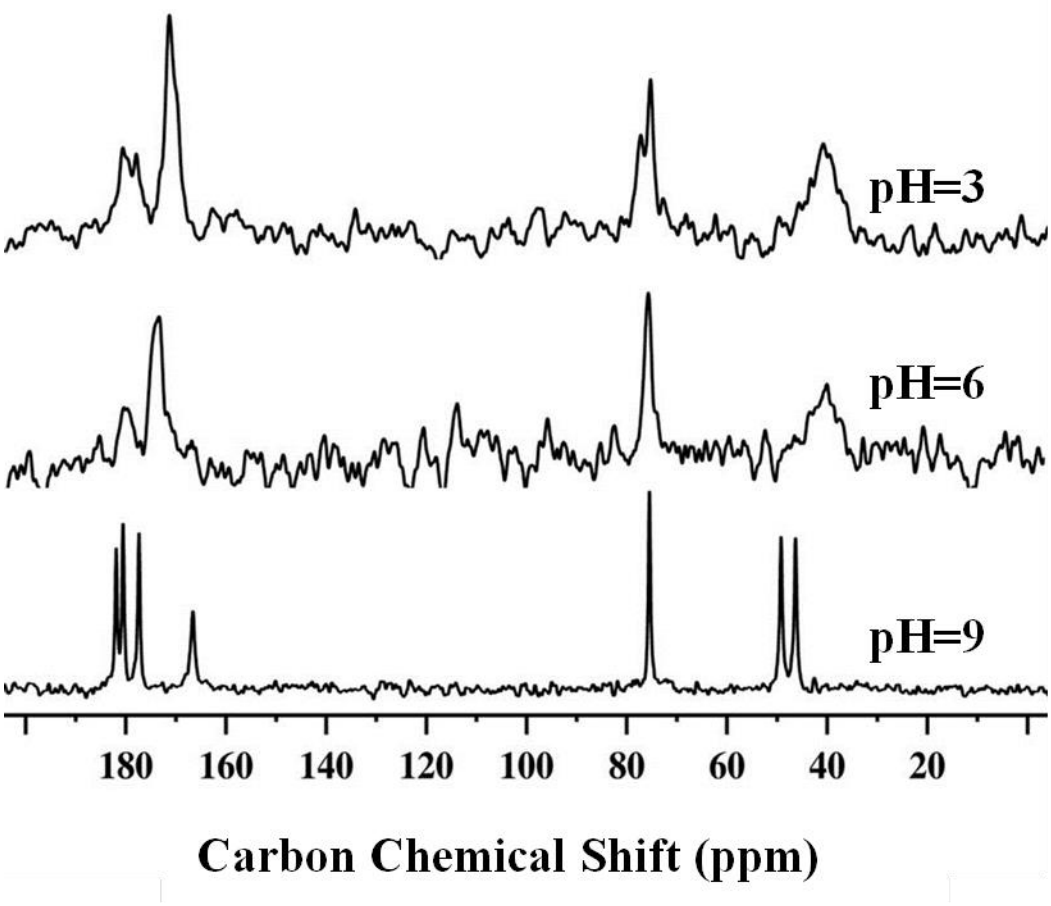

Figure 4. 17 One-dimensional (1D) 13C CP/MAS NMR spectra of the citrate:Au ratio is maintained at 1:1, while the system pH is varied (number of scans = 50 000 to 100 000).

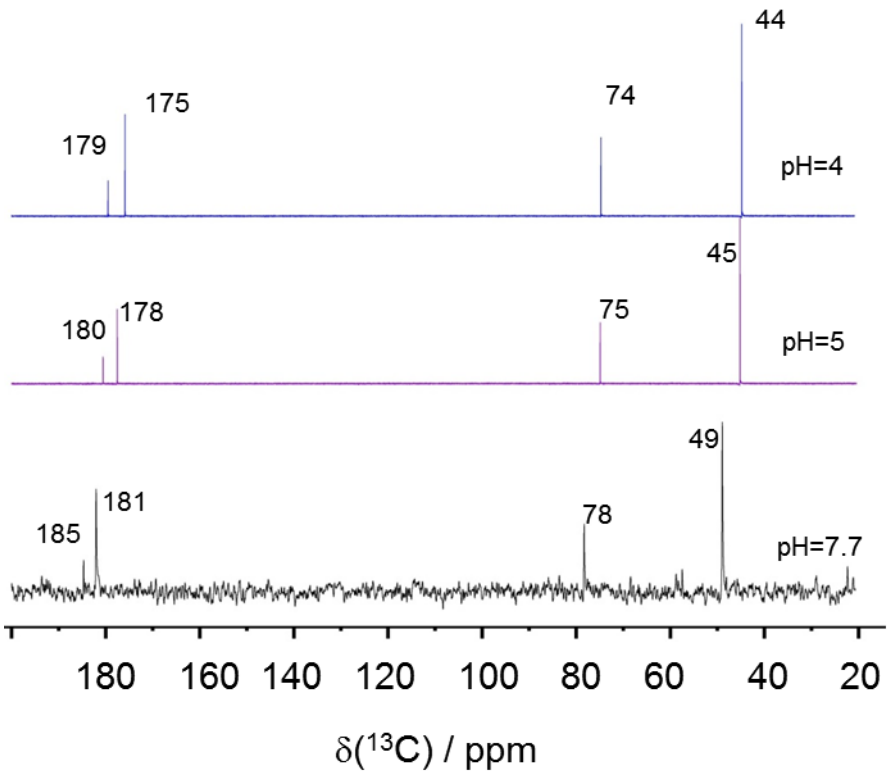

Figure 4. 18 The liquid ^{13}C NMR spectra of an aqueous sodium citrate solution with different pH values show that the resonances shift to the higher field (i.e., lower chemical shifts) because the carboxylate groups of the citrate anion become progressively protonated as the pH is lowered.

To confirm this interpretation, ^{13}C CP/MAS NMR spectra were recorded at 100 K (**Figure 4.19**). For the sodium citrate to Au ratio of 1:1 and 0.2:1 (appendices), the single peak at 167 ppm at RT is replaced by three resonances at 163, 165 and 167 ppm (**Figure 4.19**) at 100 K. This indicates that decreased temperatures reduce the accessible conformations for the carboxylate ligand and the three modes of coordination discussed above all make measurable contributions to the ^{13}C spectrum (i.e., M_1-η^2-μ^2, D-η^2: η^2:μ^2

and M_2-η^2-μ^2). At low citrate:Au ratios (i.e., 0.2:1) the three peaks corresponding to the binding citrate are still present, but there is an increase in signal intensity at 165 ppm (**Figure 4.3**). The D-η^2:η^2:μ^2 mode is favoured at low temperature.

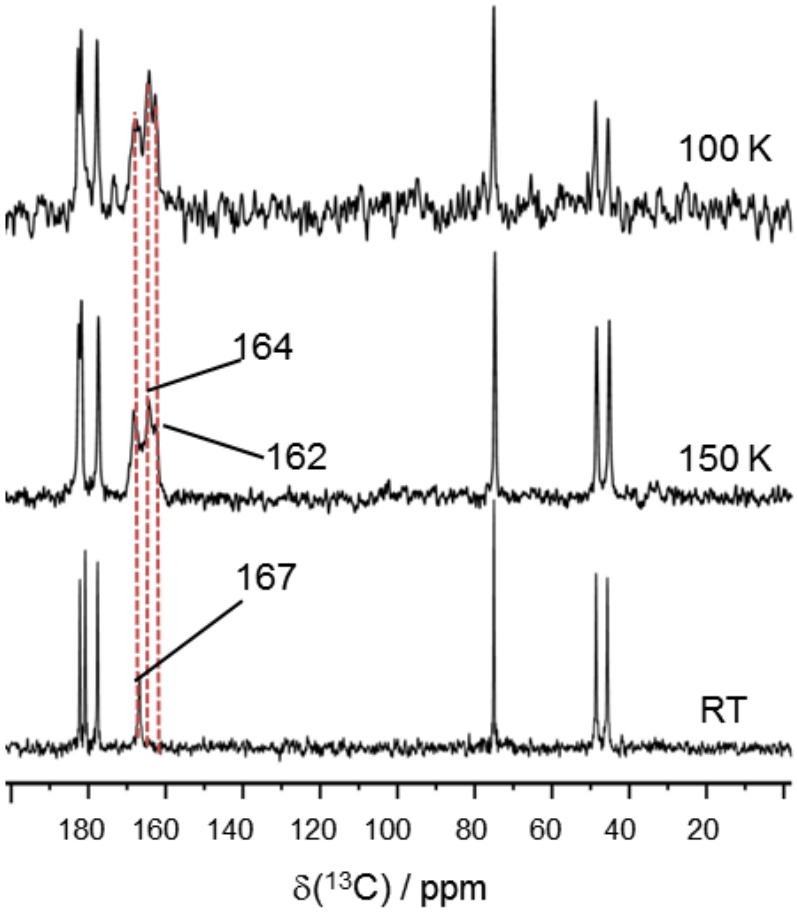

Figure 4.19 The carbonyl region of the 1D ^{13}C CP/MAS spectrum at 298, 150 and 100 K is shown for a citrate:Au ratio of 1:1. The NMR signal was strongly enhanced compared to room temperature, and 1024 scans for the spectra at 100 K and 4096 scans for the spectra at 150 K were acquired for the 1D ^{13}C CP/MAS NMR spectrum shown.

These ligand-stabilized AuNPs were also characterized by ^{13}C CP/MAS[107] at room and low temperature (100K), as well as by ^{23}Na MAS NMR. shows the ^{13}C CP/MAS NMR spectrum of crystalline sodium citrate dihydrate which exhibits peaks at 46 ppm and 48 ppm that correspond to the two CH_2 carbons, the peak at 75 ppm is assigned to the quaternary carbon, with three peaks in the carboxylate region at 178, 181, and 183 ppm[108]. Liquid state ^{13}C NMR of aqueous sodium citrate shows two sharp peaks in the carboxylate region and one peak for the CH_2 moieties.

The low contrast of this layer indicates that it is likely a carbonaceous material that originated from the sodium citrate used during the synthesis. The thickness of this layer is ca. 8.0 Å, which interestingly is comparable with the dimensions of the sodium citrate salt formula unit.[109] The 0.58nm layer observed in the HRTEM images (**Figure 4.1c**) could serve as evidence for the formation of a Sodium citrate layer surrounding the AuNP surface. The ^{13}C CP/MAS NMR show in addition to crystalline sodium citrate, three new peaks in the carboxylate region spanning the chemical shift range from 162 – 167 ppm **Figure 4.3.**

- At the very high citrate: Au ratio of 20:1. The HRTEM images show a layer that is ca 1.1nm thick **Figure 4.1d** around the AuNP that is more than twice that observed for the citrate-stabilized AuNP synthesized at lower citrate: Au ratios.

While it is difficult by energy-dispersive X-ray spectroscopy (EDS) to distinguish carbon on the shell from that of the grid, we could identify the presence of Na within this layer, which strongly supports that it is derived from the sodium citrate used as a

stabilizer **Figure 4.20**. This again indicates the presence of a layer of sodium citrate surrounding the Au surface. However, we expect that the peaks observed in the 162 – 167 ppm range of the ^{13}C solid-state NMR arise only from the carboxylate groups of citrates that are directly interacting with the Au surface within this layer, as discussed and justified below.

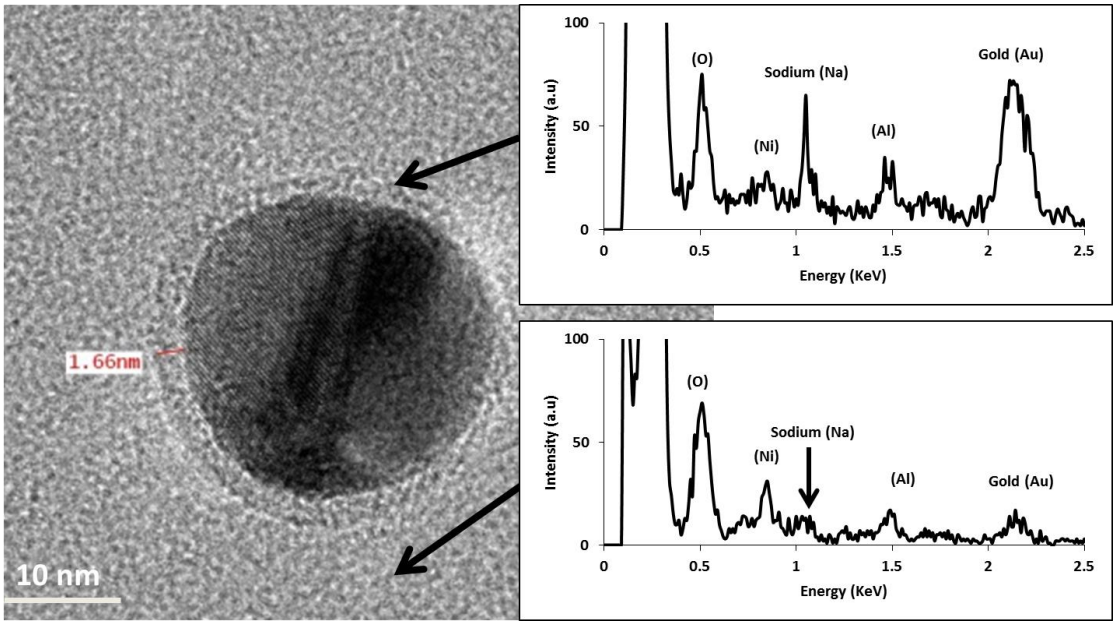

Figure 4.20 TEM/EDX spot analysis of the layer (20:1 citrate: Au ratio). We demonstrate that we have AuNP, O, C, Na, and Ni coming from the grid.

4.4.1 Calculations of 13C magnetic shielding and chemical shifts

4.4.1.1 Models to probe the influence of structural parameters on ^{13}C shielding

Due to the metallic nature of the above model systems containing surface-supported acetate anions, the computational codes available to us could not be used to calculate

magnetic shielding values. However, by considering reasonably similar structures which have been published in the literature and which involve carboxylate – gold interactions, it was thought that a qualitative interpretation of the changes in the ^{13}C shielding values at the carboxylate carbon could be established via these model systems. Upon searching the Cambridge Crystallographic Data Center (CCDC) database, a rather analogous structure, $[Au(O_2CCF_3)P(CH_3)_3]$ was located which could serve as a model for a κ^1 coordination mode (CCDC reference code: FOBXID)[110]. With the fluorine atoms substituted for hydrogen atoms (**Figure 4. 22**), we selected one molecular fragment, relaxed the positions of the newly added hydrogen atoms, and calculated the ^{13}C magnetic shielding at the carbon nuclei. The calculated ^{13}C magnetic shielding at the carboxylate carbon (σ_{iso} = 25.43 ppm) can be used as a reference value in the discussion which follows, where we examine the sensitivity of the ^{13}C magnetic shielding to key structural parameters.

Calculations of Magnetic Shielding Using ADF Software. Using model molecular systems to probe the sensitivity of the ^{13}C magnetic shielding with respect to local geometry changes in a carboxylate group (more completely described in the (appendices), essentially all computational parameters remain as before, except that for magnetic shielding calculations, effects due to the spin-orbit mechanism were included[111]. Specific computational details can also be found in the (appendices).

Calculations Using Periodic Quantum Chemistry Software. Magnetic shielding calculations involving periodic crystal structures as input used the CASTEP software (version 5.5)[112]. Input files were generated using Materials Studio (v. 3.2.0.0), and ultrasoft pseduopotentials[113] were used to describe the core electrons while plane waves

described the valence electrons. As in the above calculations using the ADF computational code, the PBE GGA XC functional was employed. Dispersion effects were included using the approach outlined by Tkatchenko and Scheffler (TS), which has often been applied for crystalline organic systems. The plane wave basis set energy cutoff was set at 700 eV and the k-point spacing was set at 0.05 $Å^{-1}$ in reciprocal space. Crystal structures were taken from a variety of literature sources, as disclosed in the (appendices). Importantly, for all crystalline systems, optimization of the hydrogen positions was performed before calculating the magnetic shielding values.

System	E_{Au} [b] / kJ mol^{-1}	E_{Ac} [c] / kJ mol^{-1}	E_{tot} [d] / kJ mol^{-1}	BSSE [e] / kJ mol^{-1}	B. E. [f] / kJ mol^{-1}
Au(111) + 1 acetate	−15983.85	−4240.00	−20505.84	−2.15	−284.14
Au(100) + 1 acetate	−14025.78	−4239.94	−18555.53	−0.91	−290.72
Au(110) + 1 acetate	−14395.80	−4239.55	−18951.82	−0.68	−317.15
Au(111) + 4 acetates – I [g]	−15983.85	−4240.38	−20504.86	−2.14	−282.77
Au(111) + 4 acetates – II	−15983.85	−4238.57	−20500.98	−3.52	−282.08
Au(111) + 4 acetates – III	−15983.85	−4240.56	−20539.37	−4.44	−319.40
Au(111) + 4 acetates – IV	−15983.85	−4236.18	−20500.54	−5.63	−286.14

Table 4. 1 Calculations of binding energies for acetate anions on Au model surfaces.

[a] Calculations were carried out at the same level of theory as the geometry optimization calculations (i.e., GGA level of DFT, PBE XC functional, all-electron TZ2P basis on ligand atoms, TZ2P basis on Au atoms, but with a frozen core (up to 4*f*), relativistic effects included via the scalar ZORA, and dispersion included via Grimme three parameter correction). For descriptions of the acronyms used and relevant references, see main text.

[b] Bond energy of the relevant gold surface model.

[c] Bond energy of the isolated acetate anion.

[d] Bond energy of the acetate anion and gold surface together.

[e] Basis set superposition error. We note that contrary to the typical expectation, the BSSE is confirmed to be slightly negative for the systems considered herein.

[f] Binding energy, B. E. = $E_{tot} - E_{Au} - E_{Ac} + BSSE$.

[g] Corresponds to acetate 'I'. Although in this system, there a total of four acetates were interacting with the Au(111) surface, for simplicity, the interaction energies between each ligand were ignored. Hence, each acetate ligand was treated in isolation and the E_{tot} values in these rows correspond to only the Au(111) surface and the particular acetate anion (i.e., 'I', 'II', 'III', 'IV') specified in the first column of the row.

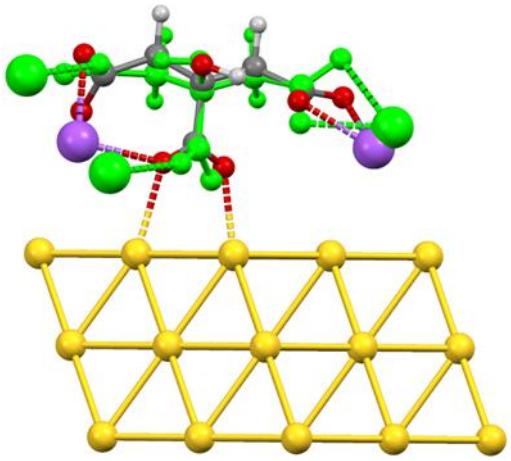

Figure 4. 21 Overlay of the DFT-optimized structure of a citrate anion (including two Na+ counterions) on an Au(111) surface model with the accepted crystal structure of sodium citrate dihydrate (CCDC refcode: UMOGAE). The atomic rmsd between the citrate carbon and oxygen atoms is 0.57 Å, highlighting the conformational similarity between the two citrates. The citrate corresponding to the crystal structure of sodium

citrate dihydrate has been arbitrarily colored green to allow for enhanced visual inspection.

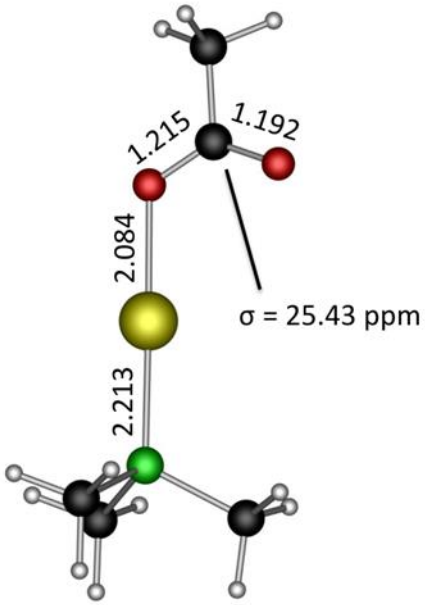

Figure 4. 22 Molecular model for a κ^1 carboxylate-gold interaction, with selected bond distances and the magnetic shielding at the carboxylate carbon indicated. It is based on the crystal structure of [Au(O2CCF3)P(CH3)3] published by Preisenberger et al.,[110] but with the fluorine atoms of the CF3 group replaced by H atoms. Prior to the shielding calculation, the H atomic positions were optimized.

Using the above model as a point of reference, in **Figure 4.23A**, it is seen that reasonably large changes in the Au-O internuclear distance (several tenths of an Å) result in only modest changes in the ^{13}C shielding values of the carboxylate carbon (about +1 ppm of shielding for a +0.1 Å increase in the Au-O distance). This underscores that changes in the Au-O coordination mode itself cannot explain the most significant changes

in the observed ^{13}C chemical shifts upon interacting with the Au surface, which was on the order of 15 to 20 ppm relative to the salt forms. At the same time, it may help explain the subtle effects such as the distribution of the ^{13}C NMR resonances observed experimentally in the region of 162 to 168 ppm.

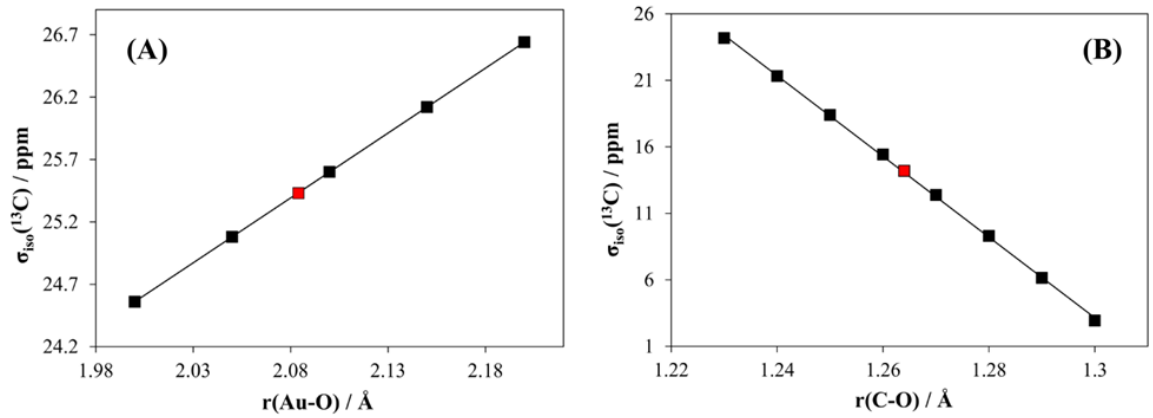

Figure 4.23 Plots highlighting the changes in ^{13}C magnetic shielding as a function of key structural parameters. In (a), the σiso for the carboxylate carbon is seen to be correlated positively with the Au-O distance in the model based on that shown in **Figure 4. 22**. In (b), the σiso of the carboxylate carbon in the acetate anion model is seen to be correlated negatively with the C-O distance. The red squares indicate reference (equilibrium) geometries while the other data points result from calculations using the reference geometries after modifying only the bond distance displayed in the plots. Linear regression fits and Pearson R2 values: for (a), σiso = 10.40(r(Au-O)) + 3.7554, R2 = 1.00; for (b) σiso = −303.4(r(C-O)) + 397.6, R2 = 0.999.

We now consider the importance of the C-O bond distance in determining the ^{13}C magnetic shielding values using an acetate anion as the model (although perhaps a bit crude, we assume for this qualitative example that the two C-O bond distances are

equivalent). Here, even very small changes of 0.01 Å result in substantial changes in the calculated shielding (about a +3 ppm change in σ_{iso} for every −0.01 Å change in the C-O internuclear distance), as seen in **Figure 4.23B**. We note that prior literature accounts using IR spectroscopy observed increased C-O stretching frequencies upon going from the salt forms to the AuNP surface-supported species,[90c] hence changes in the C-O bond length on the order of −0.05 Å are entirely reasonable. Concretely, if we look at the C-O bond lengths in the parent sodium acetate and sodium acetate trihydrate,[114] they are seen to be ca. 1.25 – 1.26 Å, while in the κ^1 coordination model (i.e., initially $[Au(O_2CCF_3)P(CH_3)_3]$, where we subsequently replaced the F atoms with H in the CF_3 moiety) these distances are reduced to about 1.20 Å.[110] Based on the trends established here using model systems, structural changes of this sort could lead to increased σ_{iso} (i.e., decreased δ_{iso} values) of about 15 ppm, in reasonable accord with the experimental findings.

Additionally, these calculations are able to partition the magnetic shielding contributions into diamagnetic, paramagnetic, and spin-orbit mechanisms. The relativistic corrections to the carboxylate ^{13}C magnetic shielding are captured in the spin orbit terms, which are presently calculated to be very small in the Au-containing systems (about 0.1 ppm of the total magnetic shielding for the $[Au(O_2CCH_3)P(CH_3)_3]$ molecular model, **Figure 4. 22**). Due to the very minimal contributions by the spin-orbit mechanism, one may safely ignore relativistic corrections to the ^{13}C magnetic shielding at the carboxylate carbon nuclei. With this in mind, we thought to complement these "gas-phase" calculations with computations that include the translational symmetry found in most crystal structures (i.e., so-called 'periodic codes'). As the periodic codes available

to us do not include relativistic corrections in the computation of magnetic shielding, it was important for us to have first verified the negligible significance of these terms in the system of interest before use.

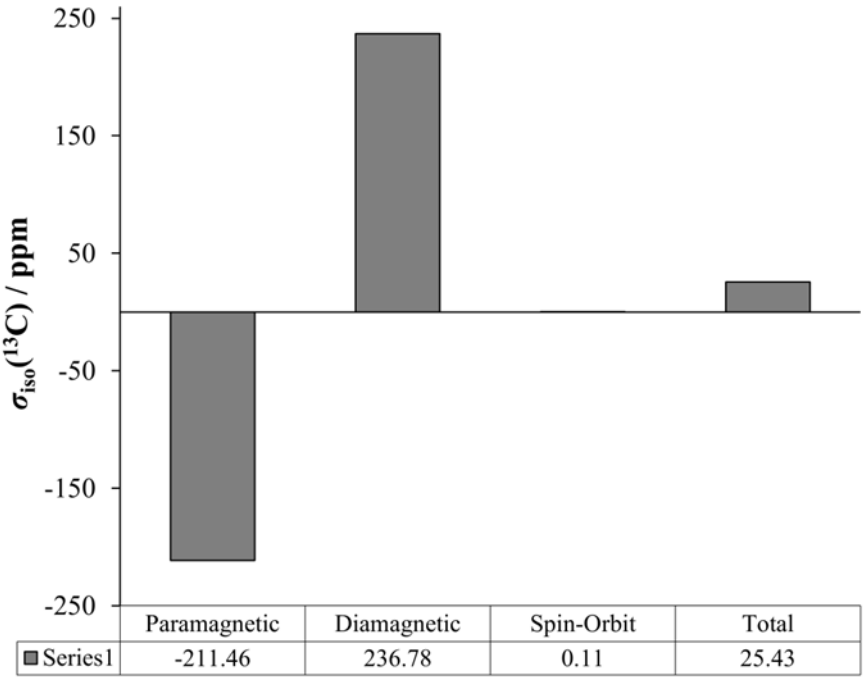

Figure 4.24 Contributions to total isotropic 13C magnetic shielding for the carboxylate carbon in the [Au(O2CCH3)P(CH3)3] molecular model, highlighting the relatively minor effect of the spin-orbit term on total shielding Using Periodic DFT to Probe Changes in 13C Magnetic Shielding.

To calibrate the conversion of quantum chemically calculated magnetic shielding to experimental chemical shifts, we used the accepted crystal structures of sodium acetate trihydrate[3] and sodium citrate dihydrate.[115] These calculated shielding values, when coupled with the experimentally measured ^{13}C shifts as part of the present study, and those found in the literature,[5] lead to the calibration plot below in **Figure 4. 25.**

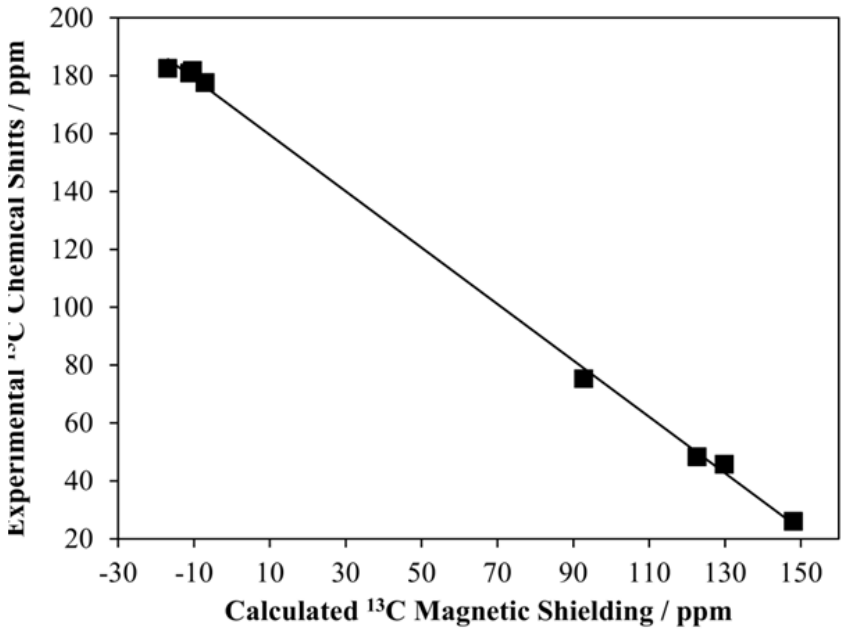

Figure 4. 25 Calibration plot for isotropic magnetic shielding (σiso) vs. isotropic chemical shifts (δiso) for all carbon atoms in the structures of sodium acetate trihydrate and sodium citrate dihydrate. The crystal structures used can be found in the preceding section where the geometrical parameters are disclosed. This calibration curve is subsequently used to generate chemical shift values for similar systems. Linear regression fit and Pearson R2 value: δiso = −0.9738σiso + 169.3, R2 = 0.999.

With this established, we calculate ^{13}C σ_{iso} values for the carboxylate carbon nuclei in the crystal structures of $[Au(O_2CCH_3)P(Ph)_3]$ and $[Au(O_2CCF_3)P(CH_3)_3]$[110, 1166] which again are being used as qualitative models of the surface interactions. Using the shielding/shift relationship established in **Figure 4.22**, we arrive at the predicted chemical shift values, as found **Table 4. 2**.

System	σ_{iso}(^{13}C, calc.) / ppm	δ_{iso}(^{13}C, calc.) / ppm
[Au(O_2<u>C</u>CH_3)P($Ph)_3$]	3.90	165.49
[Au(O_2<u>C</u>CF_3)P($CH_3)_3$] – molecule A	8.88	160.64
[Au(O_2<u>C</u>CF_3)P($CH_3)_3$] – molecule B	15.12	154.57
[Au(O_2<u>C</u>CF_3)P($CH_3)_3$] – molecule C	20.85	148.99

Table 4. 2 Chemical Shifts for Systems Involving Carboxylate – Gold Interactions.

[a] Carbon-13 chemical shift values are determined from the calculated magnetic shielding values according to the relationship established. Structures used for the calculations are given in the sections above. Please note that the crystal structure of [Au(O_2CCF_3)P($CH_3)_3$] possesses three unique molecules in the asymmetric unit (i.e., $Z' = 3$) and we have chosen to distinguish them with the arbitrary labels of 'A', 'B', and 'C'. For comparison, recall that the experimental ^{13}C shift values of the carboxylate carbon nuclei in the sodium citrate dihydrate and sodium acetate salts fell within the range 178 to 183 ppm, as described in the main paper.

From the ensemble of calculations presented here in this additional discussion section, it is clear that increased chemical shielding (i.e., decreased chemical shifts) are expected to be observed when the acetate (and also citrate) ligands bind to the surface of the Au nanoparticle. Although difficult to quantitatively establish, the order of magnitude for the change in the carboxylate ^{13}C shift is seen to range from approximately 15 to 30 ppm, which is in reasonable accord with the experimental observations. Based on the findings from the 'gas-phase' computational software, it is seen that this effect is not so critically due to the presence of the Au atoms, but rather due to a reduction in the C-O bond distance(s) upon coordination with the Au surface. Importantly, this is consistent with the results from IR spectroscopy[90c] which had illustrated an increase in the frequencies of

the various C-O stretching modes upon having a carboxylate group of the citrate anion interacting with the Au nanoparticle.

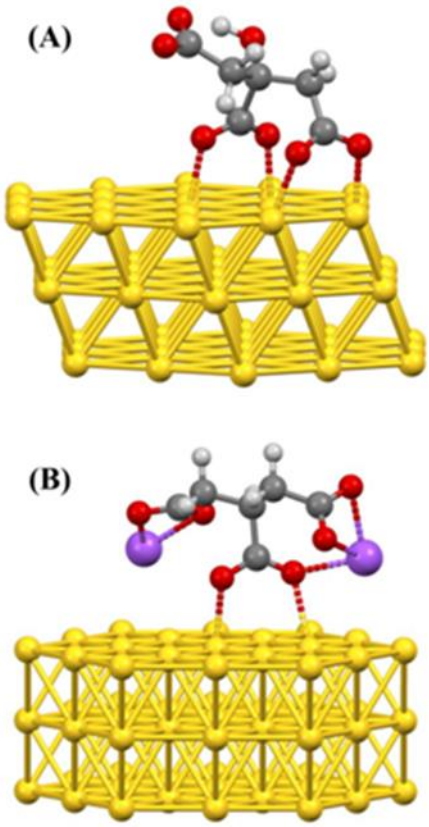

Figure 4. 26 DFT-optimized ligand geometries for a single citrate anion interacting with the Au(111) model surface. In (A), no sodium cations are included, while in (B), two sodium cations are included in the geometry optimization.

To generalise these results for the acetate to the other carboxylate-containing systems considered as part of this study, we arrive at the schematic structures presented in **Figure 4.27.**

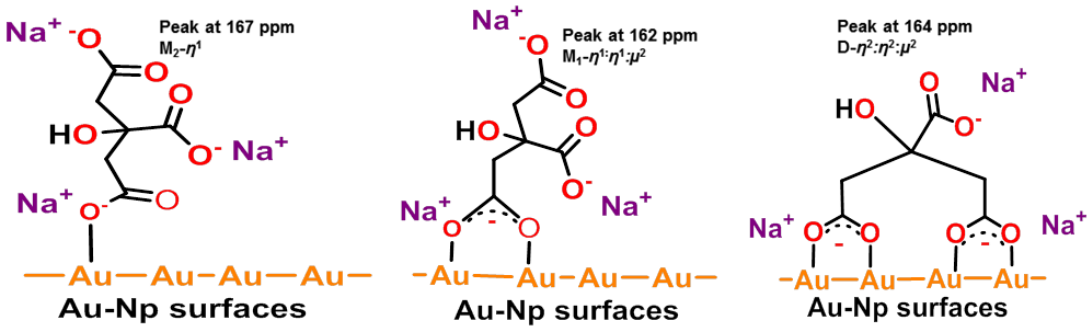

Figure 4.27 Schematic representations of the different modes of coordination of citrate: Au, with their corresponding 13C chemical shifts provided.

The following simple interpretations are used to assign the ^{13}C SSNMR spectra: where the coverage of the surface is lower, the peaks in the ^{13}C SSNMR spectra can be attributed to κ^1 (monodentate, 167 ppm) and μ^2 (bridging bidentate mono- 162 ppm and di-carboxylate 164 ppm) resonances. At higher surface coverage the broad band (3 peaks) becomes a single narrow peak, possibly due to the transition from a μ^2 to a κ^1 mode which allows closer packing in the monodentate surface-coordinated carboxylates linked to Au. This agrees with recent IR results reported by Park and Shumaker-Parry[90c] who showed that citrate can be adsorbed on the Au surface via 1 or 2 oxygen atoms.

However, the difference between bridging and chelating modes could not be spectrally distinguished with FTIR. It is noteworthy to mention here that this could potentially be resolved by NMR because of its sensitivity towards these two kinds of coordination (i.e., κ^1 mode X^-, or μ^2 mode LX^-, respectively).[90c]

We also mention in brief some dispersion-corrected DFT findings regarding a citrate anion interacting with a model Au(111) surface. While the greater conformational freedom of the citrate anion relative to the acetate anion makes conclusive interpretations

rather difficult using quantum chemical methods, we find different local minima for the citrate/Au(111) system depending on whether Na^+ counterions are included. We took as the starting conformation the 'extended' form, with the central carboxylate of the citrate anion directed towards the Au(111) surface.

The only difference is whether Na^+ cations were located proximate to the terminal carboxylates of the citrate. Intriguingly, when Na^+ cations are not present, the geometry optimized structure undergoes a substantial conformational change such that one of the terminal carboxylates interacts with the Au(111) edge **Figure 4.27A**.

However, when including the Na^+ counterions, this conformational change is not seen, and the extended form of the citrate is preserved **Figure 4.27 B**. Importantly, when comparing the heavy atom positions of the geometry optimized citrate on Au(111) displayed in **Figure 4.27B** with the citrate anion structure from the crystal structure of sodium citrate dihydrate,[117] it is seen that the carbon atomic rmsd is only 0.16 Å (if the oxygen atoms are included in the rmsd calculation, this value raises to 0.57 Å. When considering the ^{13}C SSNMR results in **Figure 4.3**, only the carboxylate carbon signals vary between the crystalline form of sodium citrate dihydrate and the citrate which is interacting with the gold nanoparticle. Due to the profound sensitivity of ^{13}C chemical shifts to local structure,[118] we would expect that if the structure in **Figure 4.27A** was realistic, then additional new ^{13}C NMR peaks from the other carbon sites in the citrate should appear, which is contrary to our observations. Likewise, considering the minimal perturbations in the conformation of the citrate seen in **Figure 4.27B** relative to the crystalline structure of sodium citrate dihydrate, it would be expected that no new ^{13}C

peaks outside of the carboxylate region would be observed, which is consistent with our experimental ^{13}C SSNMR observations.

A remaining question concerns the nature of the carboxylate binding interaction, which can be LX or LL, (2 electron donor: L-type ligands and 1electron donor: X-type ligands)[82], is resolved with ^{23}Na NMR. [82] **Figure 4.28** shows the ^{23}Na multiple quantum MAS (MQMAS) NMR spectra of sodium citrate (in black) and citrate:Au (1:1 ratio) (in red). Details of the spectra and the analysis are given in (appendices). The ^{23}Na MQMAS experiment permits to resolve four peaks corresponding to the four crystallographically distinct Na^+ cations in the asymmetric unit cell of bis(trisodium citrate) undecahydrate. Interestingly, the ^{23}Na MQMAS spectrum of citrate:Au (1:1 ratio) shows the same number of ^{23}Na peaks (in addition to the peak at 7.21 ppm which is assigned to NaCl), with the only significant difference being a shift in one of the sodium sites. The structure of bis(trisodium citrate) undecahydrate contains two sodiums that each coordinate only one terminal carboxylate, and two that each coordinate both a central and a terminal carboxylate. Since only one sodium shift changes upon binding this is further clear evidence that binding occurs through a terminal carboxy group, and that the displaced sodium cation remains in the vicinity of the citrate. This strongly suggests that the carboxylate groups act as an LL ligand, as shown in **Figure 4.27**.

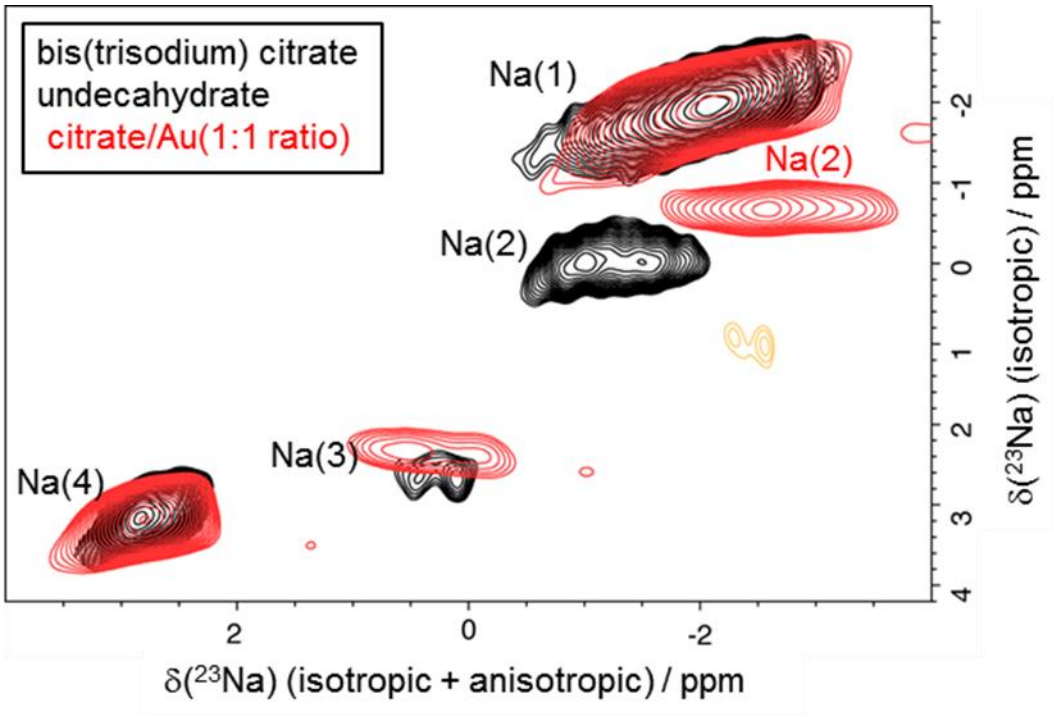

Figure 4.28 ^{23}Na MQMAS NMR spectra of bis(trisodium citrate) undecahydrate (in black) and a system having a citrate:Au ratio of 1:1 (in red) acquired at 21.1 T.

This also supports the conclusion from the carbon spectra above that the structure of the citrate is very similar to that in bis(trisodium citrate) undecahydrate. This also implies that the surface gold atoms interacting with citrate are Au(0).[37] High resolution XPS spectra of the Au 4f core level from a citrate-stabilized AuNP sample, as well as bulk Au, are shown in **Figure 4.29 and Figure 4. 30**, respectively (see Methods and SI for further details). The observed amount of partially charged $Au^{+\delta}$ species in the stabilized sample represents 4% of the total gold species. Importantly, 38 to 51 % of the Au atoms should constitute the AuNP surface for particle diameters between 2 to 3 nm. These results thus indicate that the dominant oxidation state of gold in the citrate-stabilized AuNP sample is Au(0), with minimal charge transfer at the citrate/AuNP interface.

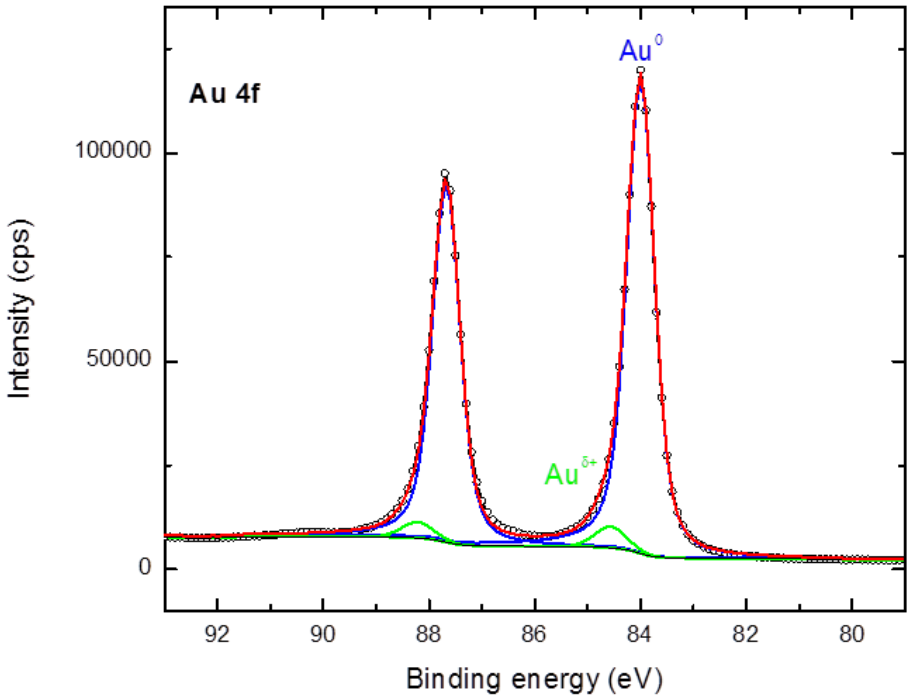

Figure 4.29 XPS spectrum of the Au 4f core levels of citrate stabilized gold nanoparticles synthesized using a 1:1 citrate: Au ratio.

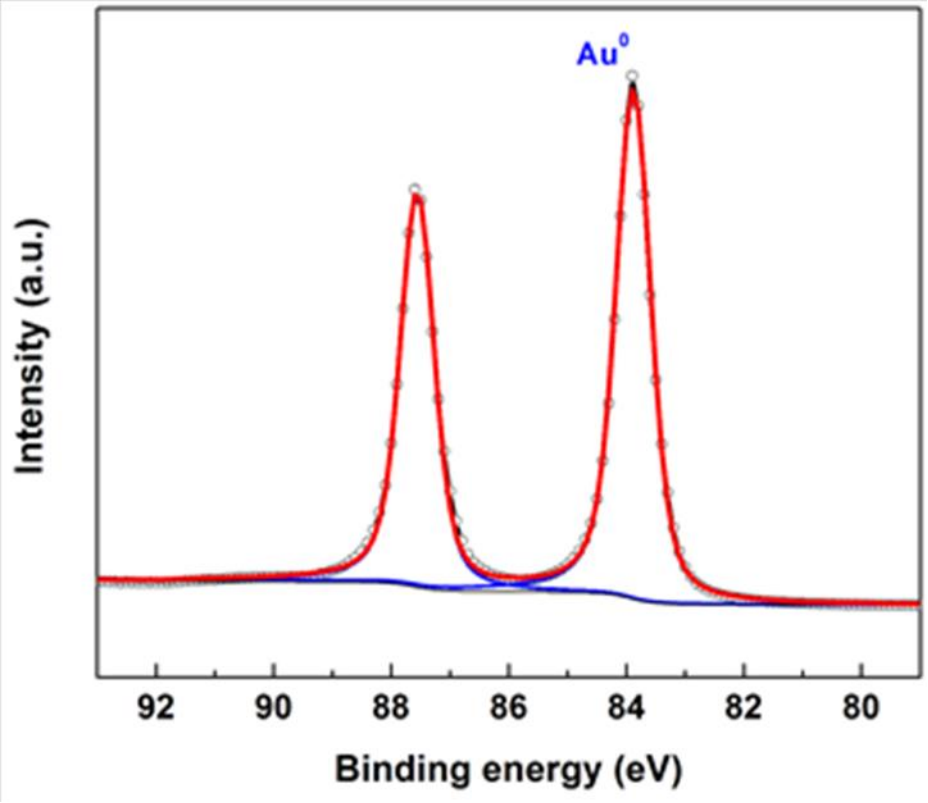

Figure 4. 30 XPS spectrum of the Au 4f core level from bulk Au substrate.

XPS also shows that Na and a very small amount of Cl are present in the sample (**Figure 4. 31**), forming part of the stabilizing layer surrounding the AuNP. No detectable amount of boron was observed, suggesting that anions such as $B(OH)_4^-$ derived from the $NaBH_4$ precursor are not present near the Au surface in the presence of citrate anions.

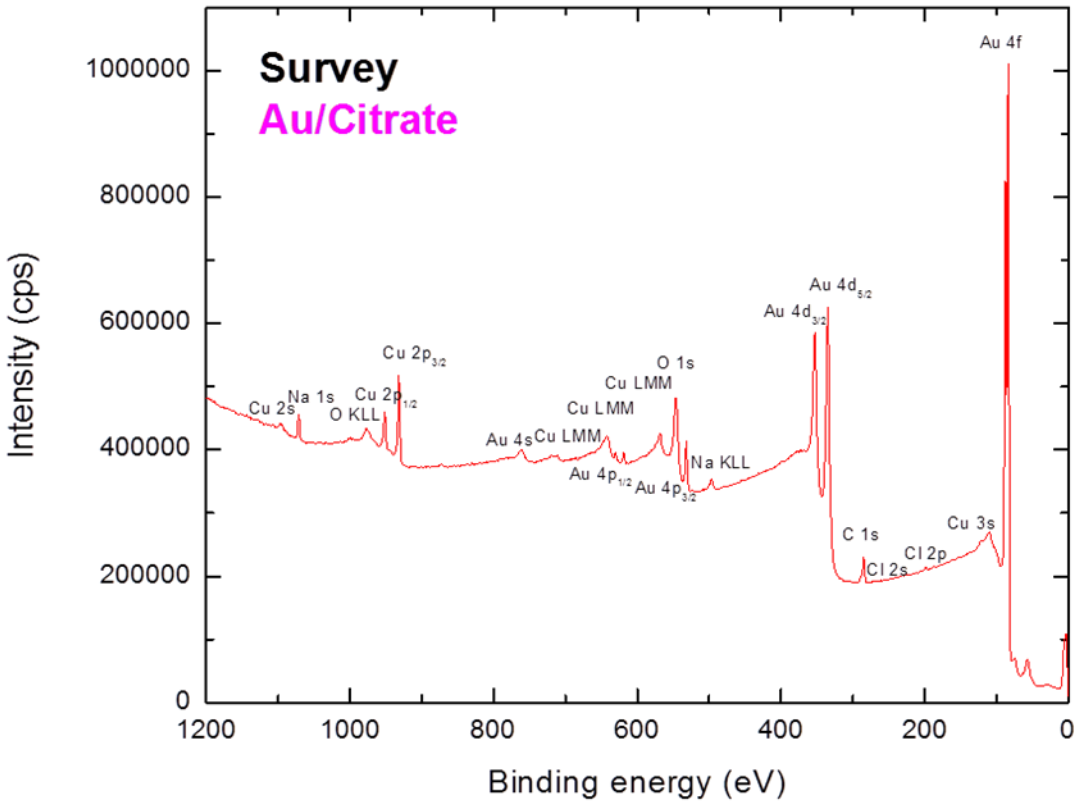

Figure 4. 31 Survey XPS spectrum of a citrate stabilized AuNP sample 1:1 citrate: Au ratio.

In order to get more investigation about the binding mode. We tried to wash the NPs after synthesis **Figure 4. 32** to remove the ligands components along with a maximal recovery of AuNP colloids from the synthesized solution, an optimal centrifugation process was obtained based on tests of centrifugation force 4000 *g* and duration 30 min by following a purification process schematically illustrated in **Figure 4. 32**.

There was a total of four rounds of purification (treatment); the supernatant resulting from the initial centrifugation of 1 mL freshly synthesized AuNPs solution was transferred to a vial and the centrifuged AuNP were immediately dispersed in ultrapure water of its original volume. The composite AuNP solution underwent a second, third

and fourth round of centrifugation by following the same operating procedure as the first round to minimize ligands components and maximize recovery of AuNPs. Then, the AuNPs in all rounds were dried at room temperature to do NMR study.

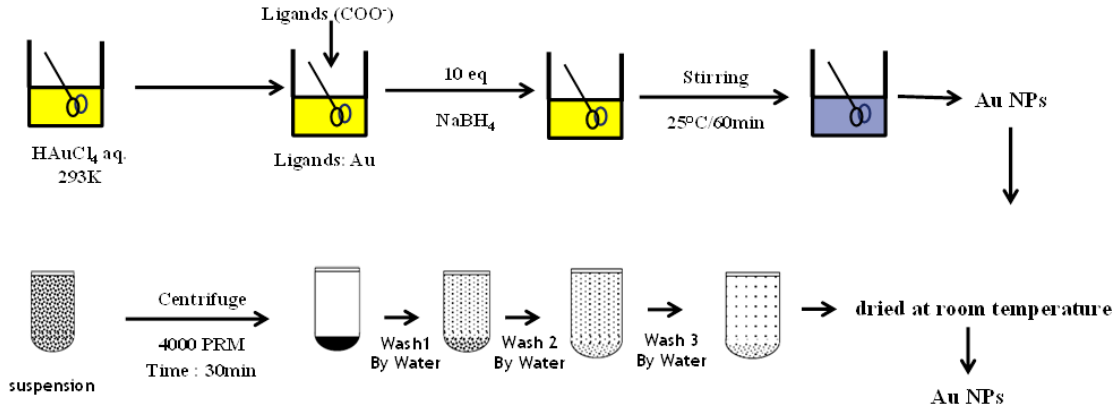

Figure 4. 32 Schematic purification process of gold nanoparticles (post-synthesis).

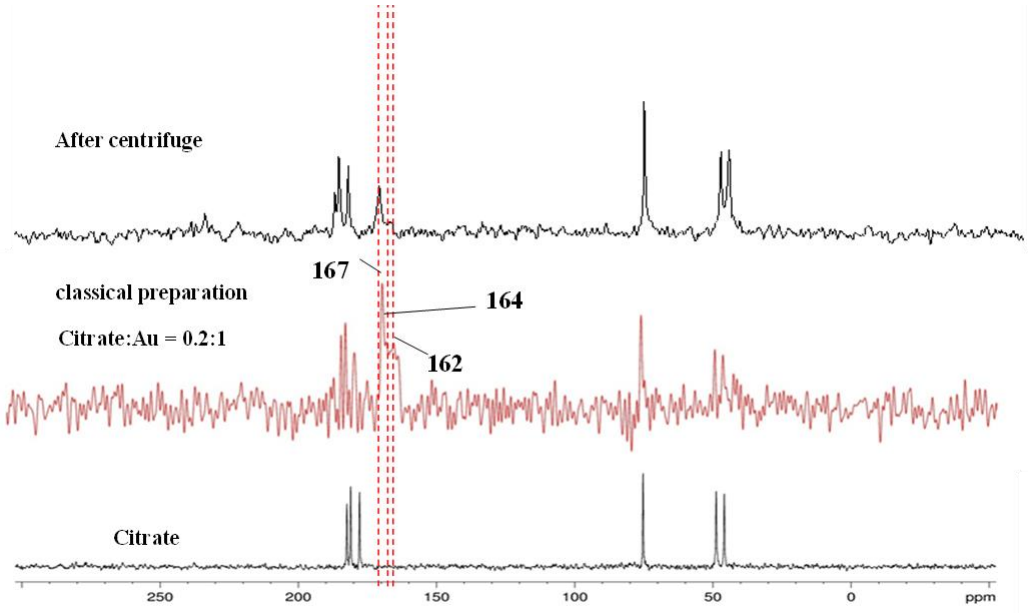

Figure 4. 33 One-dimensional (1D) ^{13}C CP/MAS NMR spectra of citrate:Au at 0.2:1ration before and after centrifuge. (number of scans = 50 000 to 100 000).

To verify whether the interaction of the organic ligand with the gold nanoparticles still remain or not. We clean the gold nanoparticles surface by remove the access of the ligands. We come to this conclusion;

The ^{13}C CP/MAS NMR spectra **Figure 4. 33** of citrate on AuNPs with a citrate: Au ratio of 0.2:1 and with centrifuge system support this hypothesis. When the excess of ligands form AuNPs, the characteristic peak of citrate coordinated to the AuNP at 167 ppm is there, which we interpret as direct evidence for the Au-O interaction. The above experiments provide direct proof of the role of the carboxylate and highlight there stabilization ability on gold nanoparticles.

We conducted a detailed study by IR spectroscopy of the resulting nanostructures. **Figure 4. 34** shows the FTIR spectra of the Au nanoparticles which are prepared by using citrate with various ratios as a stabilizer. The band at 1620 cm^{-1} corresponds to the vibration of the asymmetric υ_{as} (C=O) while one located at 1400 cm^{-1} is characteristic of its symmetrical (C=O) υ_s. The evolution of the first band of 1580 cm^{-1} with the decrease in the amount citrate. It is also observed that decreasing the amount of ligands in the system causes a reduction in the intensity of the vibration band of deformation of the C=O.

This difference clearly shows that the interaction between the citrate and the Au nanoparticle surface is controlled by the COO- anions. The change in IR C=O stretching: symmetric, Asymmetric, shows that the Carbonyl groups are possible functional groups coordinated to the gold nanoparticles surface.

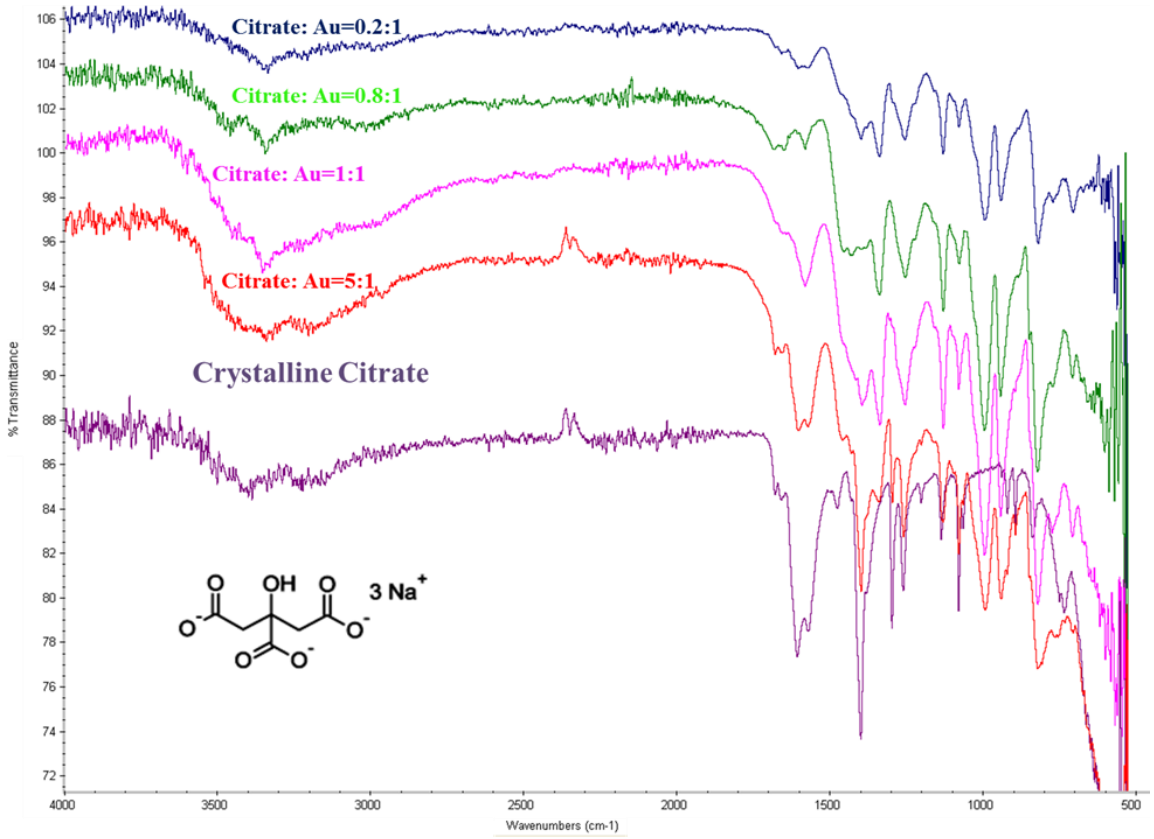

Figure 4. 34 FTIR spectra of AuNP synthesized by NaBH4 reduction in the presence of different amounts of citrate with respect to a constant amount of HAuCl4. Sodium Citrate/Au ratio: 0.2:1, 0.8:1, 1:1 and 5:1.

As shown in **Figure 4. 35 a and b**, respectively. In these images, a few examples are found the stabilizers are a distribution on the Au particles. We can differentiate that by the white color which related to the ligands. The thickness of this color ranges from more than one individual layers.

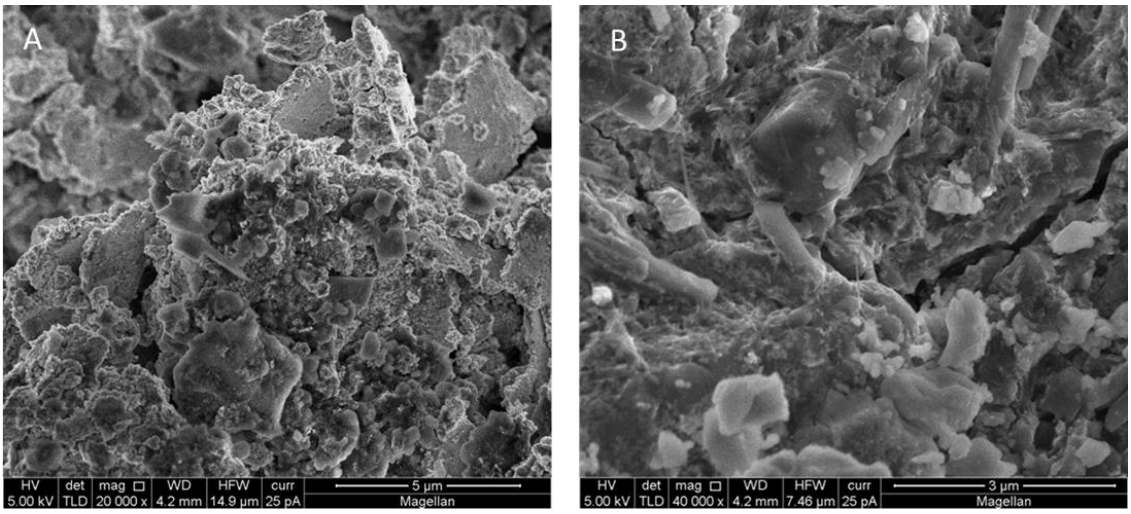

Figure 4. 35 STM images of the surface morphology after deposition of 1:1 citrate/Au ratio.

4.5 Conclusions

In conclusion, by combining SSNMR, TEM, XPS and dispersion-corrected DFT calculations, we determined the structure and mode of interaction of various carboxylate-containing systems with AuNP surfaces. From the NMR data we observe that the interaction involves coordination of one or two carboxylate groups to the surface Au atoms, and that the structure of citrate is the same as in crystalline bis(trisodium citrate) undecahydrate. Guided by DFT calculations, we deduce that the binding between the carboxylate group and the AuNP surface occurs in three different modes: monocarboxylate bidentate (M_1-η^2:η^2:μ^2), pseudo monocarboxylate bidentate (M_2-η^2-μ^2) and dicarboxylate bidentate (D-η^2:η^2:μ^2).

The relative amount of citrate anions with respect to the AuNP is a crucial factor influencing the predominant mode of binding. Based upon our combined computational and experimental results, we tentatively assert that at higher citrate:Au ratios, the M_2-η^2-μ^2 mode is preferred over the bridging bidentate mode. According to our binding energy calculations, the binding interaction for acetate is weak relative to a covalent Au-O bond, and XPS experiments indicate that the AuNP surface atoms are mainly in the zero oxidation state, with a very minor presence of partially charged $Au^{+\delta}$ species. ^{23}Na NMR experiments suggest that Na^+ ions are present near the gold surface, indicating that the carboxylate binding occurs as an LL type interaction ($2e^-$ donor).[82]

Chapter 5.

Gold Base Catalysts

Gold was considered inactive and it was the noble metal less used in homogeneous and heterogeneous catalysis. Gradually gold catalysts appeared in homogeneous catalysis in the selective oxidation of amino alcohol or[119]*amino acids in the synthesis of arenes*[120]*. Until 1986 gold was considered inactive in heterogeneous catalysis. After the pioneering study of Haruta et al*[121]*. showing that the supported gold nanoparticles possess extraordinary properties for the oxidation of carbon monoxide (CO)in presence of hydrogen*[122]*, the number of publications in the field of heterogeneous catalysis on gold has increased considerably.*

Since then gold catalysts have proved active in many heterogeneous catalytic reactions. These reactions involving hydrogen and carbon monoxide, but giving quite different products, can also occure. These include methanol synthesis from syngas [123]*, the reduction of nitrogen oxides*[124,] *the oxidation of methane or volatile organic compounds (VOC) by molecular oxygen"*[125]*. Many investigations agree on the fact that, high catalytic activity is obtained only when gold is present as highly dispersed nano-particles. For this reason, the method of preparation is essential. Many methods proposed in the literature are essentially based on the precipitation of the gold precursor at basic pH on an inorganic oxide. Obtaining nanoparticles is not an easy task because of the tendency of metallic gold to sinter. Therefore, preparing effective catalysts would require an optimum control of many preparation parameters and a deep understanding of the mode of interaction between gold and the support.*

5.1 **Introduction**

Over the last ten years, the ability of gold-based catalysts to catalyze several reactions has been widely studied. Gold catalysts exhibit high activity only when present as dispersed supported nanoparticles [126]. To do this, a lot of preparation methods have been developed, but the most used is deposition - precipitation. This method produces particles having a size less than 3 nm, but problems such as reproducibility or the loss of gold, particularly when using NaOH or Na_2CO_3 as precipitant, are often reported. Meanwhile, the choice of the support is very important because it not only allows stabilizing metallic gold nanoparticles but also to promote the catalytic activity due to the presence of defects in the support. Indeed, such defects can trap the metal nanoparticle and enhance charge transfer between the support and the nanoparticle[127].

After Haruta *et al*[121] first reported that gold can exhibit high catalytic performance in the CO oxidation at sub-ambient temperatures, several investigations were later devoted to the study of the catalytic performance of gold in oxidation reactions such as partial oxidation of propylene to propylene oxide, total oxidation of hydrocarbons, and Improved performance in liquid-phase aerobic epoxidation[122].The complete oxidation of CO is the most studied reaction in the field of gold catalysis. Several factors influence the catalytic activity such as, the method of preparation, the particle size, and shape that are the consequence of the preparation method, the nature of the support, the heat treatment or methods of activation, and the feed composition (presence of water, SO_2, H_2 etc.).

One possible application of gold catalysts is envisaged in the field of combustion of the hydrocarbons and CO at low temperatures. This Chapter is devoted to the preparation, characterization and catalytic behavior of gold catalysts synthesized by the so-called conventional method (deposition – precipitation and co-precipitation). The advantages and disadvantages of these methods will also be discussed. A comprehensive study of the chemistry of gold precursors in solution, the nature of the metal - support interaction, the washing and heat treatment will be undertaken. The catalysts are characterized by X-ray diffraction (XRD), Temperature Programmed Oxidation (TPO) and Transmission Electron Microscopy (TEM). All the catalysts are tested in the total oxidation of the CO and the results will be discussed later.

5.2 Factors influencing the catalytic activity of supported gold catalysts

5.2.1 Effect of method of preparation

The first to have made a detailed study of the effect of the preparation method on the CO oxidation activity of gold-based catalysts were Bamwenda et al[48]. According to the investigators, the catalysts prepared by deposition - precipitation are more active than the catalysts prepared by impregnation and photo - deposition. The activity of these catalysts was shown to be ten times better than that of platinum based catalysts. There is general agreement in the literature on the fact that preparation methods such as deposition - precipitation, co-precipitation and vapor deposition produce very well dispersed catalysts with a particle size of <5 nm, which are very active in the oxidation of CO. However, impregnation leads to poorly dispersed catalysts with particles sizes greater than 10 nm,

which are not active in CO oxidation. A reduction in hydrogen activation treatment followed by oxidation and a further reduction may increase the activity of catalysts[128].

5.2.2 Effect of support the supports used

5.2.2.1 Type nature of support

Many materials have been used as supports for gold catalysts. With regard to the oxidation of CO, the supports were separated by Schubert et al[49, 129]. into two groups: "active" and "inert" carriers. Gold catalysts supported on basic and irreducible oxides such as Al_2O_3, SiO_2, and MgO is less active while those employing reducible oxides as Fe_2O_3, NiOx, CoO_X, TiO_2, are active. It has been proved that the gold catalysts supported on inert oxides show a strong dependence of the catalytic activity with the size of particles[130]. For this system, an oxygen adsorption on the defect sites (edges and corners)[131] of gold particles has been proposed. The increase in the catalytic activity of gold catalysts supported on reducible oxides has been attributed to the ability of these supports to provide oxygen. It is claimed that the reaction is sensitive to the structure of the metal interface - carrier[132] and the heat treatment of the catalysts[133]. The two types of carriers can produce active catalysts for the oxidation of CO, but the mechanism (see Chapter I: Proposed mechanisms) and the factors influencing the activity are different.

5.2.2.2 The effect of metal-support interaction

The primary role of the support is to stabilize and disperse the nanoparticles metal. Yet other effects occur at the interface metal - support. They result in significant changes in catalytic and physicochemical properties of the metal, but also of those of the

support. The definition of the interaction metal - support was proposed by Foger[134]as: The direct influence of the support on the chemisorption and properties of a catalytic metallic phase by stabilizing an unusual metallic structure, or by changing the electronic properties due to the transfer electrons between the metal particles and the carrier or by creating a chemical bond between the metal and the support. The interactions can be classified as weak interaction (WMSI), medium (MMSI) or strong (WSIS). The metals supported on non-reducible oxides (SiO_2, Al_2O_3, MgO etc.) and carbon or graphite has weak interactions. Those in zeolites undergo medium interactions. The metals supported on reducible oxides (especially TiO_2) show strong interactions[135].

Haruta[136] suggests that the great thermal stability of gold catalysts at 300°C is due to the epitaxial contact of gold nanoparticles and the substrate. Contact is made between the densely packed surface of gold (111) and the face (110) of the α- Fe_2O_3, (111) of Co_3O_4, (112) of anatase titania, and (110) of rutile TiO_2. The TEM study showed that gold nanoparticles less than 2 nm, have an angle of contact with the support lower than 90° and a hemispheric morphology. The particles larger than 5 nm have a contact angle greater than 90° and similar hemispherical morphology. The influence of the preparation method on the contact between the gold and the support was explained by Bamwenda et al[48]. Deposition-precipitation leads to hemispheric nanoparticles attached strongly to TiO_2. Whereas, the impregnation and the photo-deposition preparation techniques simply yield spherical particles deposited on the substrate surface. The difference in contact between the gold and the support affects the catalytic properties. As a matter of fact, the catalysts obtained by deposition precipitation have catalytic activity in CO oxidation

(expressed as TOF) about four times greater than that of the catalysts obtained by impregnation and photo deposition.

Radnik *et al*. made an XPS[137] study of gold supported on titania. They reported low values of the gold binding energy. This was attributed to the transfer of electrons from support to the gold particles becoming negatively charged. It is a well-known phenomenon due to metal interactions - strong support (SMSI effect). Grunwaldt et al[138] concluded that the number of gold sites with low coordination differs with the supports because of the different metal-support interactions resulting in different morphologies. This morphology difference causes changes in the influence of interface and the catalytic activity[139].

5.2.3 Particle size

The oxidation of CO does not take place unless gold is dispersed on a support in the form of nanoparticles smaller than 5 nm, which yields extraordinary activity [140,141]. Valden *et al*[142]. have studied the kinetics of the oxidation of CO at low temperature on gold clusters of different sizes supported on titanium thin film. They observed a strong dependence of TOF and the activation energy with the size of the gold clusters. A maximum intrinsic activty was reported for clusters having a size of 3.2 nm **Figure 5.1**. It has been proposed that the sensitivity to the structure of gold catalysts come from the change of the electronic properties of gold clusters according to their size [143].

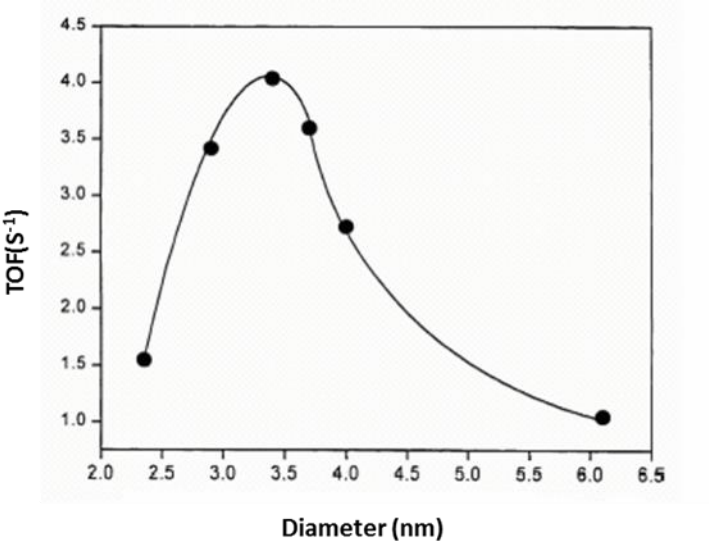

Figure 5.1 Variation of CO oxidation activity as a function of the gold clusters of size from[142].

5.2.4 Particle morphology and interactions metal - media

Haruta[144] studied the influence of the preparation method on the morphology of gold particles. It was shown that deposition - precipitation, co-precipitation, and vapor deposition produce hemispherical particles which are strongly bound to the support by plane faces and which are much more resistant to heat treatment than spherical particles. Haruta[136] suggested that the great thermal stability of gold catalysts supported on titania is due to the epitaxial contact between the nanoparticles and the substrate. The same research group[145] investigated the effect of heat treatment of a mechanical mixture of spherical gold particles of about 5 nm and titania. An increase in the activity of catalysts with the increase of the calcination temperature has been observed. The authors concluded that the nature of the contact of gold resulting in a longer distance interfacial perimeter is responsible for the activity at low temperature. Horvath et al[146], by studying

the system Au / Fe_2O_3, concluded that it is neither the size nor the particle oxidation state of the gold that has to have a very good activity, but that the most important factor is the electronic interaction between the particles and the carrier. Later, Gupta et al[147]. suggested that the catalytic activity of the catalyst Au / Fe_2O_3 for the oxidation of CO is due to the transfer of chemisorption energy from the metal particle to the support thus leading to a localized temperature surge at the metal/support interface, which may act as the sites of higher CO oxidation activity.

5.2.5 Heat treatment

The low melting temperature of gold may cause sintering of the particles while increasing the temperature. The choice of the calcination temperature is very important. The optimum calcination temperature from the literature is 300°C. Park and Lee[52] reported a decrease of the activity of catalysts Au/Fe_2O_3, Au/TiO_2, Au/Al_2O_3 with increasing temperature of calcination. XPS and EXAFS studies showed the evolution of $Au(OH)_3$ to the Au_2O_3 oxide followed by reduction of Au at a higher temperature. The presence of oxidized gold and the easy production of a metal-support interface were observed to be beneficial for the oxidation of CO. Lee e*t al*[54] have shown the importance of the calcining atmosphere for gold-based catalysts supported on oxides of manganese. The air treated catalysts are more active than catalysts treated in hydrogen or vacuum due to a stronger interaction between the oxidized metal and manganese. Maciejewski *et al*[132] did not observe sintering of gold particles when supported on TiO_2 and ZnO up to 600°C. Au/TiO_2 calcined at 500°C and Au/ZnO calcined at 560°C exhibit maximum activity in CO oxidation. Boccuzzi et al[148] reported an increase in particle size (Au/TiO_2) from 2.4 to 10.6 nm with increasing the calcination temperature from 200°C to 600°C for catalysts

prepared by deposition - precipitation. They also found that the increase in temperature causes the different distribution of special sites of corners and edges[149].

5.3 Aim of this chapter

The aim of this Chapter is the synthesis, characterization and testing of a suitable gold catalyst for the oxidation of carbon monoxide (CO). In this Chapter 1wt%, Au/TiO_2 catalyst was prepared by deposition-precipitation. Different synthesis conditions such as pH, ligands, and catalyst pretreatment were investigated in order to find suitable conditions for the preparation of catalyst that would be more active at a lower temperature range (25°C – 300°C). The techniques used for catalyst characterization include TPO, XRD, HRTEM and fixed-bed tubular reactor in order to explain the catalyst surface structure and its suitability in affecting the ligands adsorption and subsequently evaluate the catalytic activity and the interaction with the support (sizes, shapes, oxidation etc.).

5.4 Results and discussions

5.4.1 Supports and catalysts

5.4.1.1 Supports

The support used during this study is TiO_2 (Degussa, P25). The TiO_2 support contains a mixture of both anatase and rutile phases, as determined by the XRD patterns shown in **Figure 5.2**.

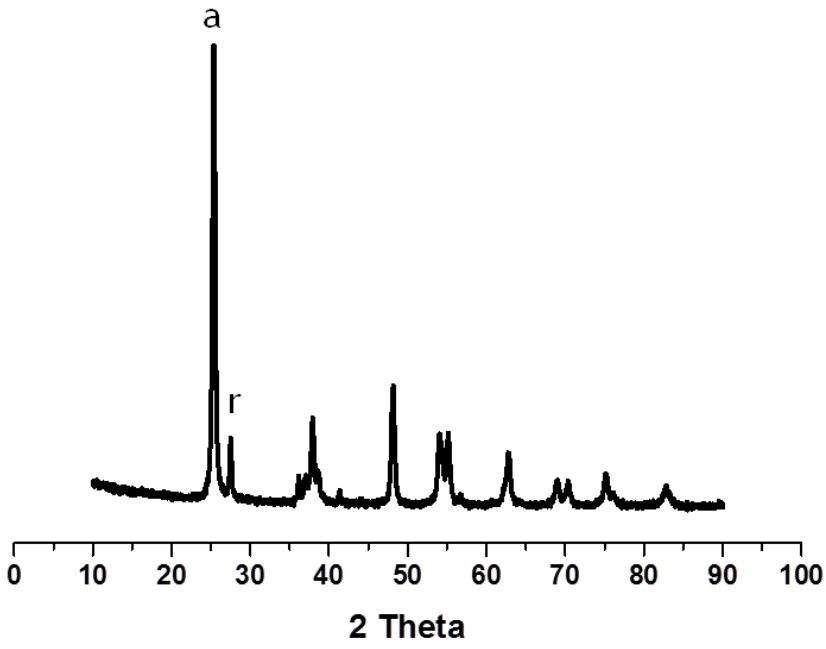

Figure 5.2 XRD patterns of TiO_2 support

The peaks denoted a and r corresponds respectively to the anatase (101) and rutile (110) reflections. The peak at 2θ = 25.4° confirms the TiO_2 anatase structure[150]. Strong diffraction peaks at 25° and 48° indicating TiO_2 in the anatase phase[151]. There is no any spurious diffraction peak found in the sample"besides TiO_2, there are no other crystalline phases". The intensity of XRD peaks of the sample reflects that the formed nanoparticles are crystalline and broad diffraction peaks indicate very small size crystallite.

5.4.1.2 Catalysts

Au supported catalysts were prepared by Deposition – precipitation. The method is to precipitate gold hydroxide on the surface of a support. We used as a precipitating agent,

Sodium hydroxide (NaOH) 0.1 M introduced in large excess. The use of NaOH allows a formation of OH groups **Figure 5.3**[152]. The deposition of $Au(OH)_4^-$ exclusively on the surface of metal oxide support.

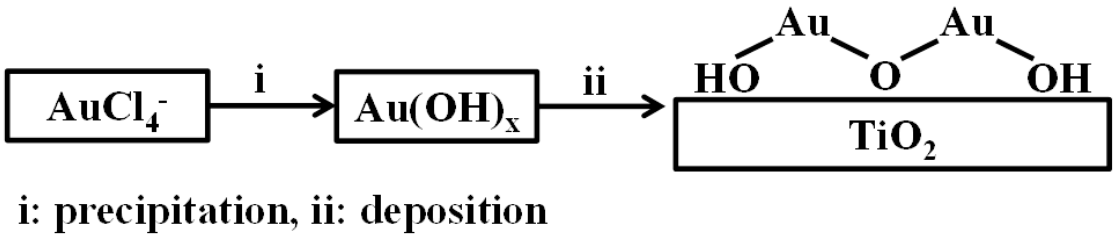

Figure 5.3 deposition-precipitation (DP)

By Nechayev and Nikolenko[153]results as shown in **Figure 5.3**. By deposition precipitation method, the Au precursor is brought out of solution onto a suspension of the support. The pH of the solution is raised in order to precipitate Au, typically as a hydroxide. The surface of the support acts as the nucleating center and this leads to a greater part of the active Au precursor being attached to the support. Thus, when the pH of a solution of gold chloride is from 3to 4, the neutral $AuCl_3 \cdot H_2O$ is the major species. At pH 7, $AuCl(OH)_3^-$ is probably prevalent. At pH 10 and above, the $Au(OH)_4^-$ anion is the dominant species, hydrolyzed species such as $[Au(OH)nCl_{4-n}]^-$ (n = 1-3) react with the surface of the support. This procedure is, in general, applicable to supports with high and medium values of the isoelectric point (point of zero charges = PZC) (Okumura *et al*, 1998). The pzc is the unique value for an oxide and an indicator that the oxide shows acidic or basic properties. For example, the isoelectric point of P-25 TiO_2 is reported to be in the range of 4.5–6.3[154]. The pH values below the PZC of the support generate an oxide, which will be positively charged in water and adhesion of negatively charged

colloid/clusters with good dispersion can then occur, so that anionic species should adsorb by electrostatic attraction at lower pH; neutral species, of course, will not adsorb in this manner.

The connection of negatively charged gold complexes to the positive support matrix takes place **Figure 5.4**. Our idea is to control the pH solution at 9 that mean the hydrolyzed species Au $(OH)_4^-$ react with the surface of TiO_2.this later will enhance the activity of the catalysis.

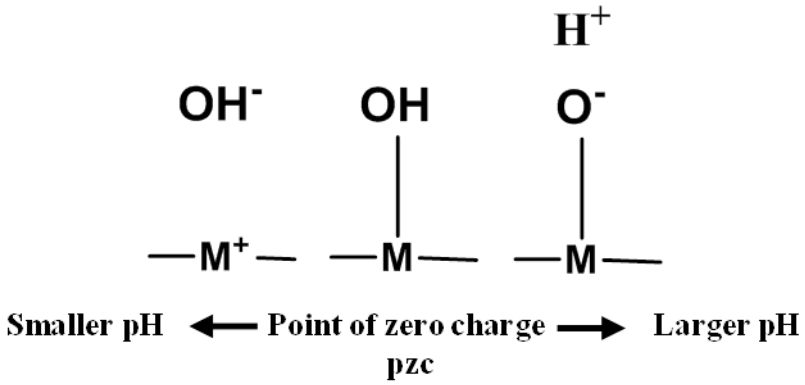

Figure 5.4 Dissociation of the hydroxyl group in aqueous solution and point of zero charges (pzc).

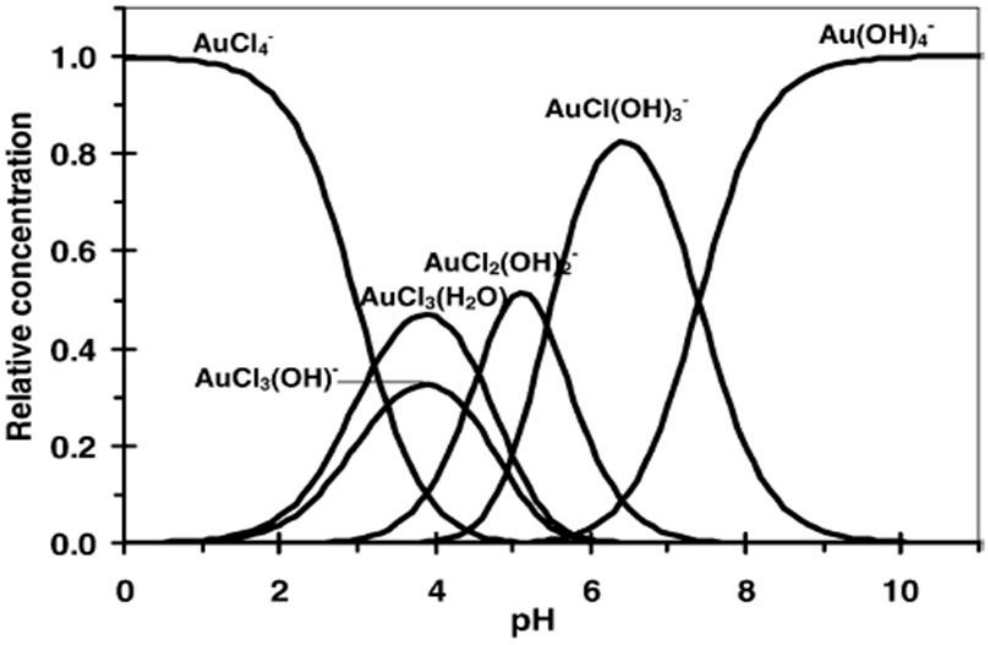

Figure 5.5 Relative equilibrium concentration of gold complexes[155]

At the same protocol we prepare two samples; in the absence of ligands which is used as a reference and in the presence of various ligands (Mono, Di and Try) carboxylic at different Au/ligand ratios.

5.4.2 Preparation of Au/TiO_2 catalysts

5.4.2.1 Materials

All chemicals were reagent grade, purchased from Sigma-Aldrich, and were used without further purification. Tetrachloroaurate trihydrate ($HAuCl_4 \cdot 3H_2O$), trisodium citrate dihydrate ($Na_3C_6H_5O_7 \cdot 2H_2O$), disodium glutarate ($Na_2C_5H_6O_4$), and sodium acetate ($NaCH_3COO$) were used as stabilizers and NaOH (sigma-aldrich, 99.99%) was used as a precipitating agent and TiO_2 (Degussa P-25) was used as support. All reactions

were done in aqueous media using deionized water (Millipore Milli-Q system, 18.2 MΩ-cm). All glassware was washed with aqua-regia (3:1, HCl/HNO_3) solution before catalyst preparation.

5.4.2.2 Synthesis samples preparation in the presence and absence of ligands by deposition precipitation:

The appropriate amounts of Gold(III) chloride hydrate with a concentration of 5×10^{-4} M and TiO_2 were measured in such a way that they make a (1 g per 50 ml of solution). These were mixed with distilled water and stirred with an overhead stirrer for about 20 min. A solution of $HAuCl_4 \cdot 3H_2O$ in 50 ml of distilled water was prepared and added to the support solution in a drop wise manner (approx. 1 drop in 2 seconds). When all the gold solution had been added to the support suspension, the mixture was stirred for about 15 to 20 min. Before precipitation with NaOH solution 0.1 M, which was also added in a drop wise manner at approximately the same dropping rate as that used for the gold solution. The Sodium hydroxide solution was added until pH = 9. The suspension is filtered and the obtained solid is washed with water several times to remove Na^+ and Cl^- ions. The washed precipitate is later dried in an oven at 100°C for 4 hours as shown in **Figure 5.6**.

A similar method (as described above) was used to synthesize this catalyst with the various ligands ($Na_3C_6H_5O_7.2H_2O$, $Na_2C_5H_6O_4$ and $NaCH_3COO$) and different Au/ligand molar ratios (0.2:1,1:1 and 5:1) as shown in **Figure 5.7**.

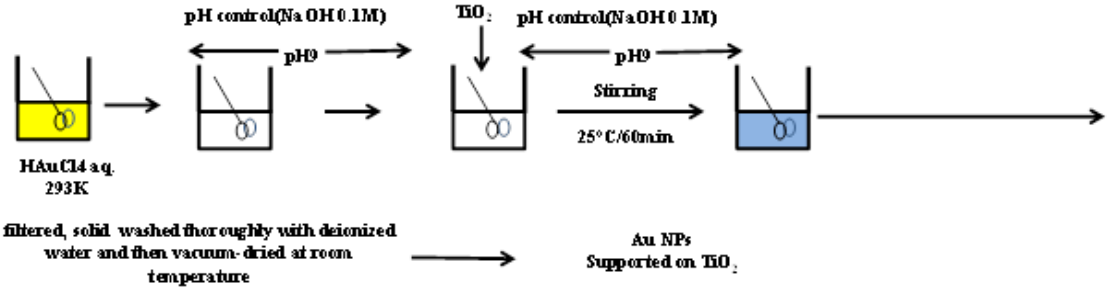

Figure 5.6 Experimental scheme for the synthesis of reference preparation-In the Absence of ligands.

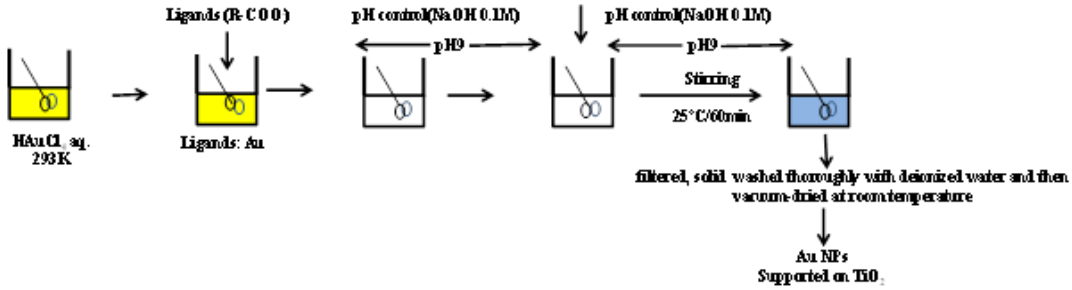

Figure 5.7 Experimental scheme for the synthesis of samples-In the presence of ligands.

5.4.3 Catalyst characterization

5.4.3.1 Transmission Electron Microscopy (TEM)

The catalysts were characterized by TEM to determine the morphology of the solid

and the size of gold crystallites as well as the size distribution of the particles. Two electron microscopes: Titan 80-300 CT and Titan 60-300 ST from FEI Company (Hillsboro, OR) are used to performing the Transmission Electron Microscopy (TEM) study on the synthesized samples. Both microscopes were equipped with X-ray Energy Dispersive Spectrometry (EDS) detectors from Energy-Dispersive X-ray spectroscopy

(EDAX), In Selected area Electron Diffraction (SAED), and TEM-EDS modes to investigate size, crystal structure, and elemental composition of prepared samples. Several Bright fields (BF) mode of the TEM (BF-TEM) micrographs were acquired by setting the microscope at different low magnifications and similarly HRTEM micrographs were obtained by setting the microscope at high image magnifications. The Aberration Corrected Scanning Transmission Electron Microscopy (AC-STEM) analysis was carried out on Titan 60-300 ST to investigate the presence of ligand on the surface of gold nanoparticles (Au-NPs). The Cs-corrector of the microscope was aligned and its spherical aberration coefficient (Cs) reduced to the value of about negative 2 microns. In this way, several AC-TEM micrographs were acquired by setting the objective lens of the microscope in slightly over-focusing condition so that the Au atoms in acquired images exhibit the so called “white-atom” contrast. It is to be noted that the entire TEM datasets were acquired and analyzed by using Digital-Micrograph Software Package of version GMS1.85 from Gatan, Inc.

Microstructure and morphology of the samples before and after the catalytic runs at various temperatures were determined by STEM, the catalyst was deposited onto a holey carbon foil supported on a copper grid. STEM investigations were performed with a CM30ST microscope (FEI; LaB6 cathode, operated at 300 kV, point resolution ~0.2 nm).

The particle sizes were studied with Scanning Transmission Electron Microscopy (STEM). The dry powder was dispersed in ethanol and deposited onto a perforated carbon foil supported on a copper grid. The investigations were performed on a Tecnai F30 microscope (FEI, Eindhoven), the field emission cathode operated at 300 kV).

STEM images obtained with a High Angle Annular Dark Field (HAADF) detector revealed Au particles with bright contrast (Z contrast).

The resulting images were analyzed using Image Pro Analyzer, and at least 100 nanoparticles were evaluated per sample.

As an example, the images of the gold catalysts fresh sample (un calcined) supported on Titanium dioxide are shown in **Figure 5.7**. The citrate: Au molar ratio is 1:1.

The gold particles can be distinguished by a lighter contrast on the surface of the support. As we can see from the pictures, the catalysts prepared by DP exhibit high dispersion and a particle size of about 5 nm. We made some high-resolution images on this sample to study the morphology of gold particles **Figure 5.8**. The crystalline characteristic of gold nanoparticles is shown by the presence of lattice fringes. The measured lattice spacing of 0.23 nm corresponds well to the (111) plane of Au (theoretical value: 0.235 nm).

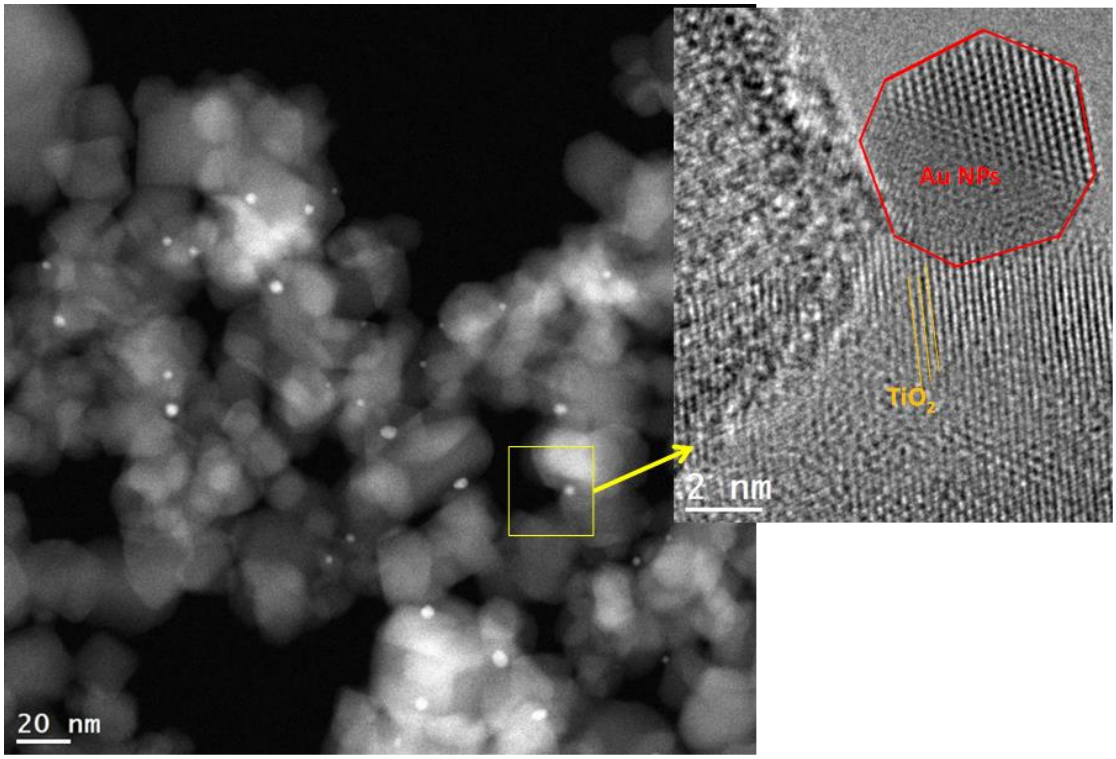

Figure 5.8 High resolution TEM Snapshots of 1:1 ratio of Citrate: gold catalysts supported on Titanium dioxide.

We observe Rhombic dodecahedron shape **Figure 5. 9**. This allowed us to use the model proposed by Robert E. Benfield[156] for calculating the dispersion of particles assuming an Rhombic dodecahedron shape. The atomic site type of the Rhombic dodecahedron is shown in **Figure 5. 9** and their populations are given as functions of cluster edge length m.

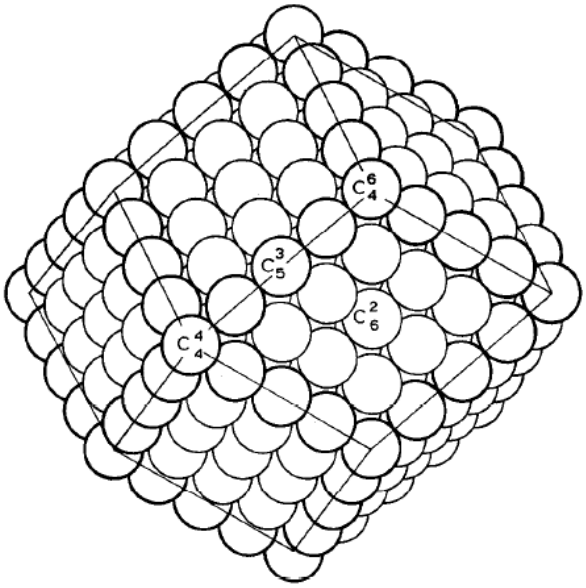

Figure 5. 9 Rhombic dodecahedron with 147 atoms (m = 4), showing the different surface atom sites and their coordination numbers.

The number of surface atoms is taking into account the contact surface of the particle with the carrier and the actual dispersion becomes:

$$\mathbf{D = N_s / N_t}$$ [157]

The Ns and Nt quantities and are determined by the geometric calculations for the cubic face-centered system. Formulae for the populations of different atomic sites in the Rhombic dodecahedron are calculated as a function of the cluster edge length m. The N_t and N_s can be calculated by the following equations:

Rhombic dodecahedron [**Figure 5. 9**]	
Total number of atoms	$(2m - 1)(2m^2 - 2m + 1)$
Number of surface atoms	$12m^2 - 24m + 14$
Number of bulk atoms	$(2m - 3)(2m^2 - 6m + 5)$

Table 5.1 Formulae for the populations of different atomic sites in the Rhombic dodecahedron, as functions of cluster edge length[157,]156.

Based on these calculations, all the results obtained for all catalysts supported on Titanium dioxide characterized by TEM are summarized later.

5.4.3.2 Temperature programmed oxidation (TPO)

In a temperature programmed oxidation (TPO), the sample is exposed to a gas stream containing oxygen (O_2), diluted with an inert gas (N_2) while gradually increasing the temperature.

This technique is used to detect the presence of different oxidizable species having different temperatures and oxidation rates. In this work, the catalyst which is Au/TiO_2 (~ 30 mg) was placed in a U-shaped quartz reactor placed in a furnace then switching valve to select the gas we would like to use for the treatment of the sample, in this work, the pre-treated for the sample was done under 5% O_2 and N_2 95%, the temperature was set up from 25 to 600 °C with a ramp of 5K/min. After that, the sample is cooled down to room

temperature. We monitored the amount of CO_2 formed during TPO using a quadrupole mass spectrometer QMS (m/Ze=44).

The process of removal the ligands in an oxidizing atmosphere is accompanied by CO_2 formation as observed in the TPO experiments **Figure 5.10**. TPO patterns for all Au/TiO2 samples are similar and consist of one broad peak in the same temperature range. Oxygen consumption is attributed to the combustion of the Carboxylic ligands present on the gold surface. The position of the maximum in the TPO profile (ca. 300°C) is observed and this is confirmed that the maximum Carboxylic ligands can be lost from the sample will be at 300°C. However, for the sample in the absence of ligand **Figure 5. 11**, we cannot observe this peak due to that we did not have ligand to burn.

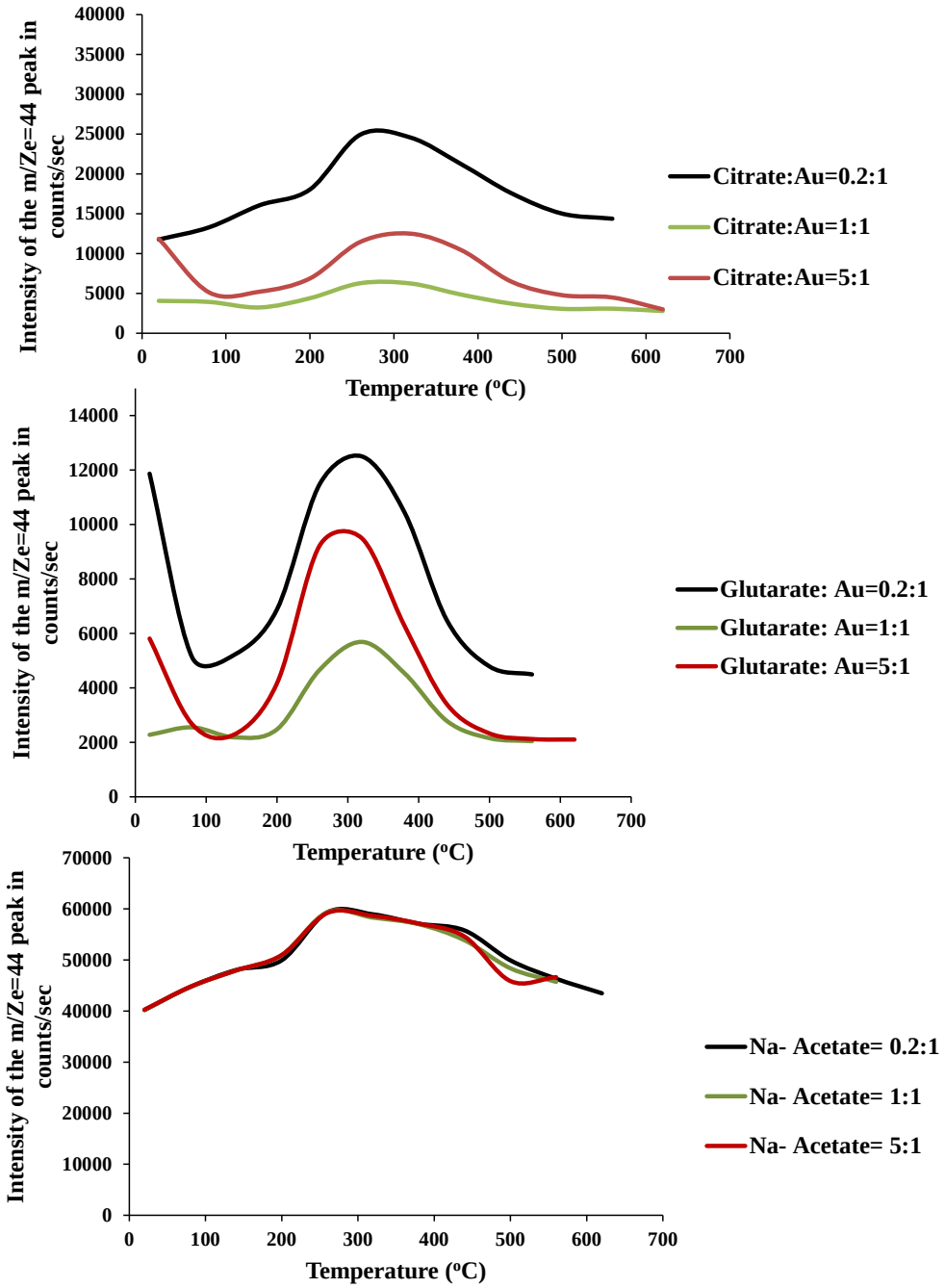

Figure 5.10 Temperature programmed oxidation of deposited Au on Titanium dioxide in the presence of ligands.

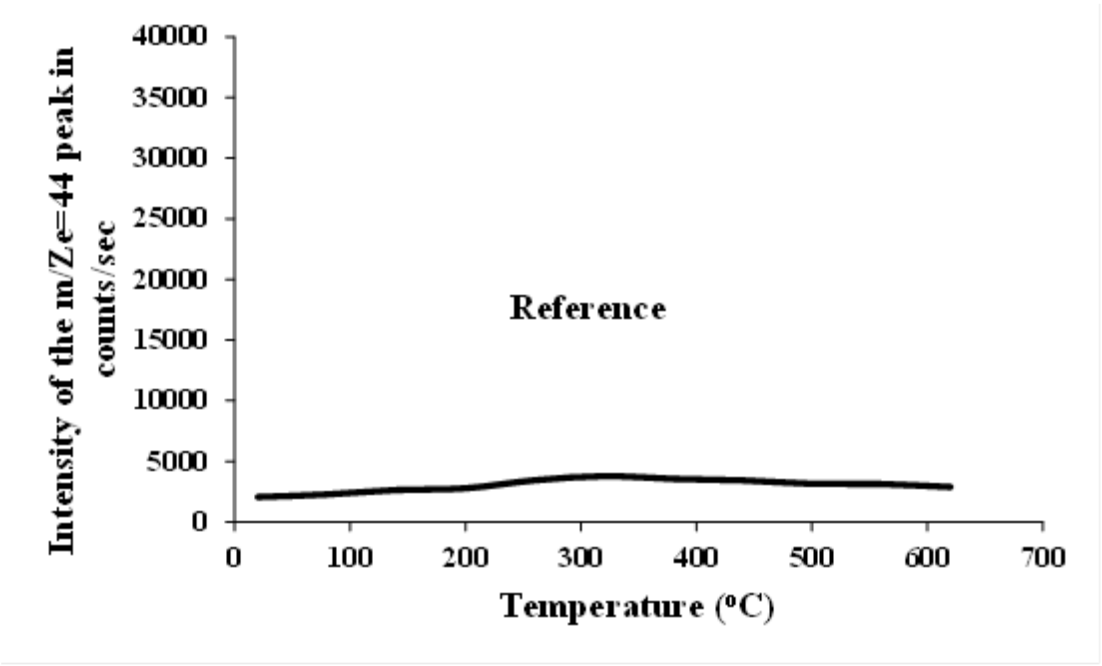

Figure 5. 11 Temperature programmed oxidation of deposited Au on Titanium dioxide in the absence of ligands.

The maximum peak was observed at approximately 320°C for the Citrate and Glutarate, which is the maximum ligand can be lost at this point. The interesting results is that with the mono carboxylic ligand which is Sodium acetate the maximum peak is around 260°C which is confirm that the interaction between the ligand and the gold are very weak compare to others. So, it easy to burn the maximum ligand at 300°C.

5.4.3.3 Inductively coupled plasma spectroscopy (ICP)

Elemental analyses of gold and carbon were conducted at the Analytical Core Lab in KAUST, Saudi Arabia. The gold content was determined by inductively coupled plasma atomic emission spectrometry (ICP-AES) using a Thermo iCap 6500.

Before analysis, 15 mg of the sample was decomposed by an acid mixture of nitric acid and hydrochloric acid (under pressure and high temperature).

Elemental analyses were performed to determine the concentrations of gold, boron, sodium of the synthesized samples; the results of these analyses are presented in **Table 5.2**. The results indicate that the samples particularly Au/TiO_2 is gold rich content.

Sample Labels	Au concentration Wt (%)	B concentration Wt (%)	Na concentration Wt (%)
Au/TiO_2 REFERENCE	0.8	0.02	0.06
$Au_1(citrate)_{0.2}/TiO_2$	0.9	0.01	0.01
$Au_1(citrate)_1/TiO_2$	0.8	0.01	0.04
$Au_1(citrate)_5/TiO_2$	0.8	0.01	0.04
$Au_1(Glutarate)_{0.2}/TiO_2$	0.9	0.01	0.02
$Au_1(Glutarate)_1/TiO_2$	0.9	0.01	0.02
$Au_1(Glutarate)_5/TiO_2$	0.8	0.03	0.1
$Au_1(Sodium\ Acetate)_{0.2}/TiO_2$	1.0	0.02	0.02
$Au_1(Sodium\ Acetate)_1/TiO_2$	0.6	0.01	0.03
$Au_1(Sodium\ Acetate)_5/TiO_2$	0.7	0.01	0.02

Table 5.2 Elemental analyses of Au/TiO_2.

5.4.3.4 CHNS/O analyzer

The total amount of carbon was tentatively determined using a CHNS/O Analyzer Flash 2000 -Thermo Scientific at hot carrier gas extraction method.

	Theoretical calculations	Before Calcination	After pre=treatment at 300°C
Sample name	**%C(Wt)**	**%C(Wt)**	**%C(Wt)**
$Au_1(citrate)_{0.2}/TiO_2$	**0.04**	**0.47**	**0.31**
$Au_1(citrate)_1/TiO_2$	**0.18**	**0.53**	**0.44**
$Au_1(citrate)_5/TiO_2$	**0.89**	**0.76**	**0.34**
$Au_1(Glutarate)_{0.2}/TiO_2$	**0.02**	**0.41**	**0.10**
$Au_1(Glutarate)_1/TiO_2$	**0.11**	**0.50**	**0.28**
$Au_1(Glutarate)_5/TiO_2$	**0.56**	**0.63**	**0.13**
Au_1(Sodium Acetate)$_{0.2}/TiO_2$	**0.01**	**0.27**	**0.04**
Au_1(Sodium Acetate)$_1/TiO_2$	**0.06**	**0.28**	**0.12**
Au_1(Sodium Acetate)$_5/TiO_2$	**0.30**	**0.29**	**0.09**

Table 5.3 Elemental analysis of carbon before and after the pre-treatment at 300°C.

According to our lab her at KAUST, Carbon analysis can be performed using CHNS/O Analyzer if the content is equal or above 0.2 (Wt) %.(for quantification). However, because the samples have less amount of carbon (theoretical calculation), it is important to understand the potential and limitations of this technique.

5.4.3.5 TEM investigations

In a recent paper[50]gold was deposited on TiO_2 and it was shown by structural studies that below 1 nm the gold particles exist in icosahedral symmetry whereas above 1 nm the gold is in fcc cuboctahedral symmetry. This indicates that the geometrical symmetry is also an important factor in developing high activity.

In spite of the catalytic results, there is still no direct evidence available on how gold nanoparticles become active in the catalytic reactions. What we know is that gold species must be in the Nano size diameter range of the supports. All changes in the size of the catalysts are correlated to the catalytic activities of the samples.

In this section, we investigate by scanning transmission electron microscopy (STEM) at different pre-treatment temperatures the average size of gold supported catalysts were obtained by reduction of HAuCl4 metal salt with ligands contained carboxylic group using the method as we detailed before.

5.4.3.5.1 TEM investigations before pretreatment (untreated)

As we explained in chapters three and four the effect of the nature of the ligands ratios and we came with this conclusion; by decreasing a number of ligandsused, the unsupported particle formed is bigger. Indeed, in the presence of a large amount of ligands (excess), increasing the average particles size was faster. However, the good ratio to obtain small gold nanoparticles is 1:1(ligands: Au).

Here, we again proved that; by using the supported particles the size of AuNPs is governed by the ratio between the concentration of carboxylic ligands and the

concentration of gold salt. It is noted that the use of a different concentrated solution of carboxylic ligands leads to the formation and stabilization smaller sizes of particles. Whereas in the presence of low or excess concentration carboxylic ligands, full recovery of the particles by ligands ions is incomplete, this induces so that the particles will tend to aggregate to form larger particles **Figure 5.12.**

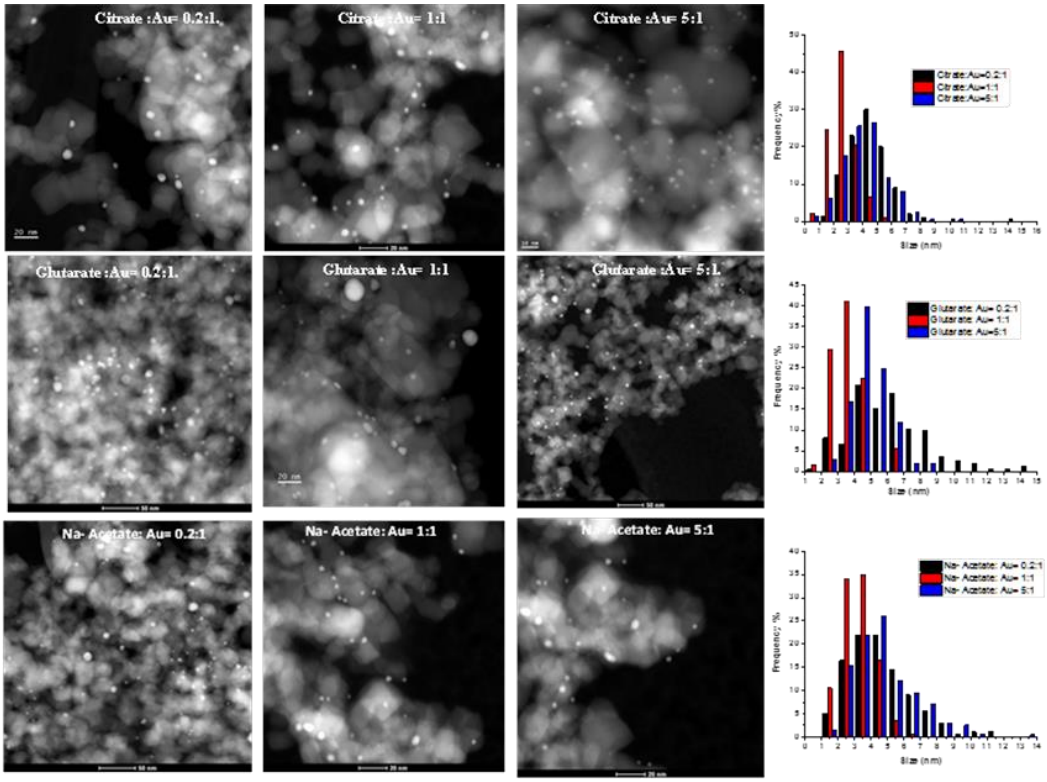

Figure 5.12 (left) STEM images of the 1% Au/TiO_2 fresh samples (untreated) prepared using different ratios of ligands: Citrate, Glutarate, and Na- Acetate. Histograms for the average size for each catalysis at different rations (Right).

5.4.3.5.2 TEM investigations after pretreatment at 300°C

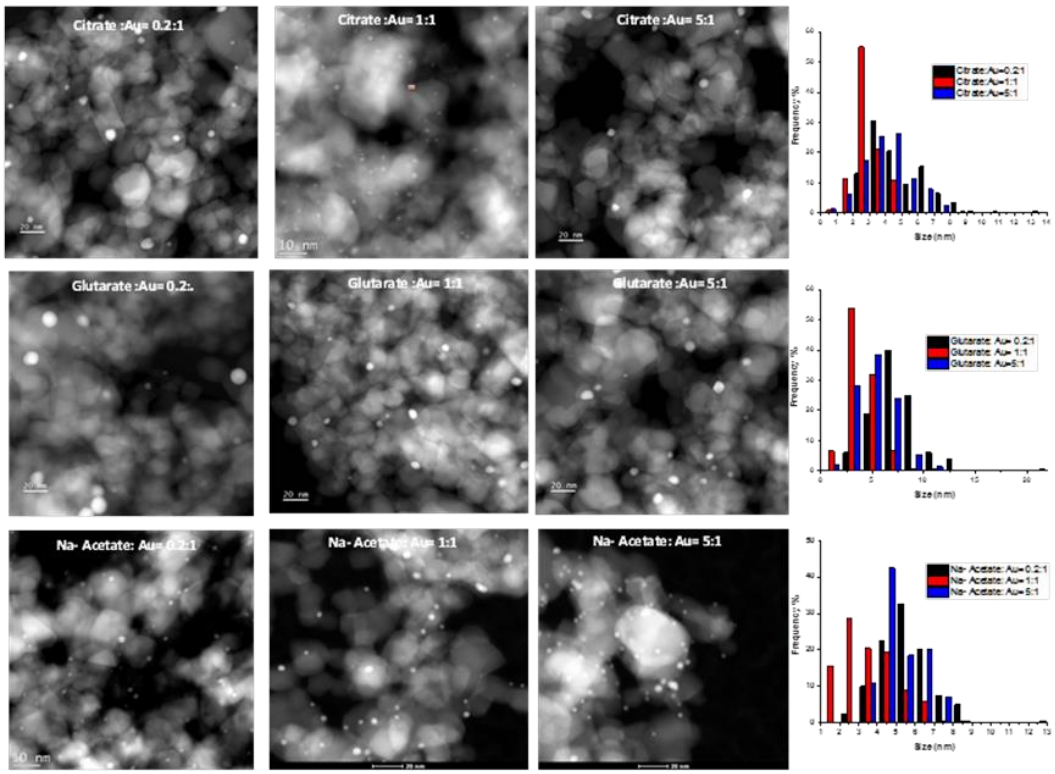

Figure 5.13 (left) STEM images of the 1% Au/TiO_2 samples calcined at 300°C and prepared using different ratios Au/ligands: Citrate, Glutarate, and Na- Acetate. Histograms for the average size for each ligand at different rations (Right).

The treatment at 300°C before the catalytic run, it is important to note that, in these conditions, the particles obtained are very polydispersed in size and shape. The gold nanoparticles increased with mean particle size in the range 4.9–4.1 nm for the Citrate ligand,7.3-5.3 nm for the Glutarate ligand and 5.5-5.3 nm for the Na- Acetate ligand at 0.2:1, 1:1 and 5:1 ligands: Au ratios respectively were obtained according to transmission electron microscopy results. Particle size generally increased slowly with pre-treatment at 300°C temperature. As noticed in **Figure 5.13**. The smaller size of Au/TiO_2 was

obtaining with a ratio 1:1 with all ligands types, this good agreement with unsupported particles. Besides using the TPO, the results shows that the maximum ligand was removed but still some ligand on the surface of gold NPs to protect the gold and keep the size small much they can.

5.4.3.5.3 TEM investigations after reaction at 300°C

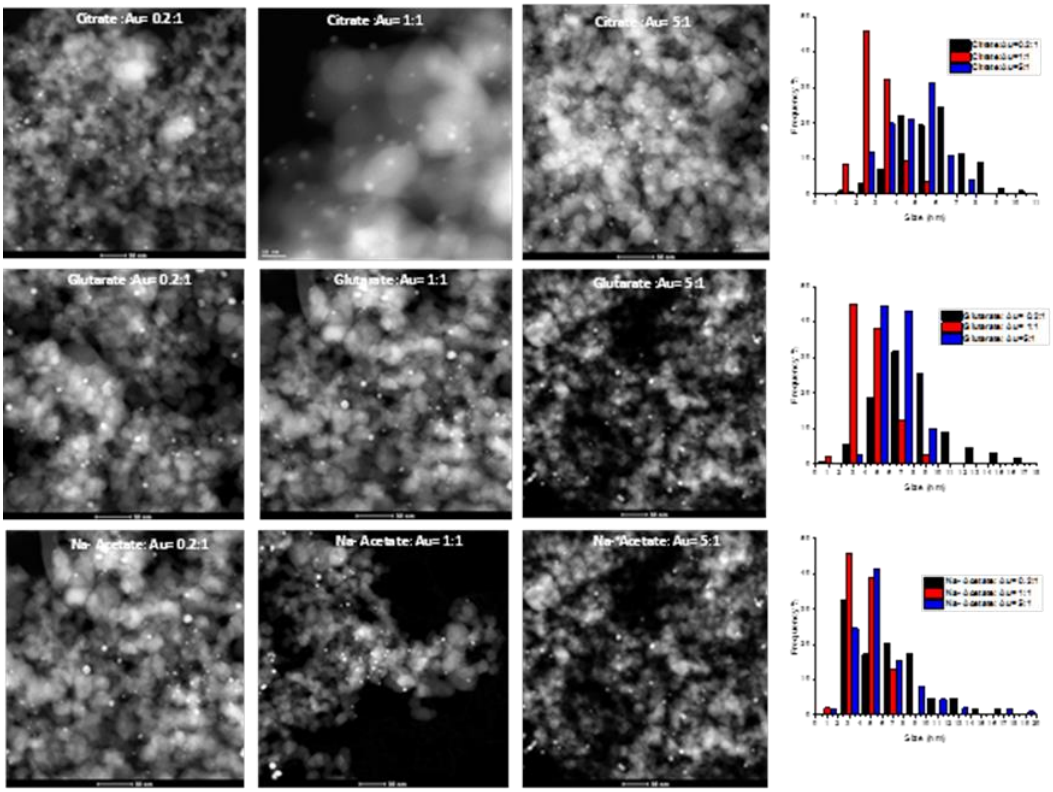

Figure 5.14 (left) STEM images of 1% Au/TiO_2 samples at different ratios of ligands: Citrate, Glutarate, and Na- Acetate. Histograms for the average size for each ligand at different rations (Right). after reaction at 300°C.

5.4.3.5.4 TEM Investigations after reaction at 450°C

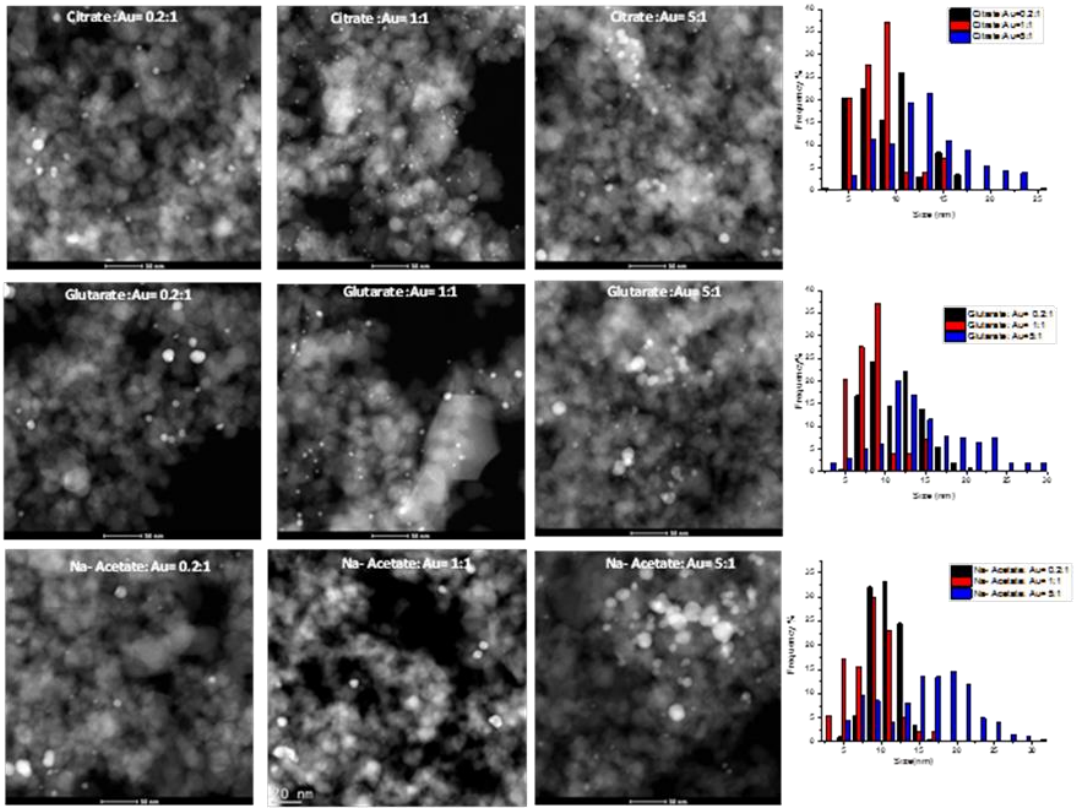

Figure 5.15 (left) STEM images of 1% Au/TiO_2 samples at different ratios of ligands: Citrate, Glutarate, and Na- Acetate. Histograms for the average size for each ligand at different rations (Right). after reaction at 450°C

As shown in **Figure 5.14 and Figure 5.15**. In general, we obtain different sizes of nanoparticles by varying the temperatures (300- 450) °C. Other important points to note are the fallowing;

- The slow increase of crystallite size in the stage of calcination 300°C and after the reaction at 300°C. This indicated that the present of the ligands molecules on the gold

NPs surfaces. Which is confirmed by TPO results Prevent the rapid growth of crystals **Figure 5. 14**.

- Increasing the temperature to 450°C yields more agglomeration as illustrated **Figure 5.15**. Hence, there is a significant change in the mean particle size at a higher temperature. Due to losing the protected agents from the surface of the gold nanoparticles.

Figure 5.16 Shows the STEM images for the samples in the absence of ligand at different pretreatment temperatures. The corresponding mean average particle size shows that the particle size has increased very slightly from 9.2 to 11.0 nm during the heating process across this series of samples that mean the AuNPs immobilized onto TiO_2. These results confirm the role of the ligands to prevent the aggregation of the particles.

In additional from the results reported. We observed that there is no difference of activity as a function of pretreatment temperature.

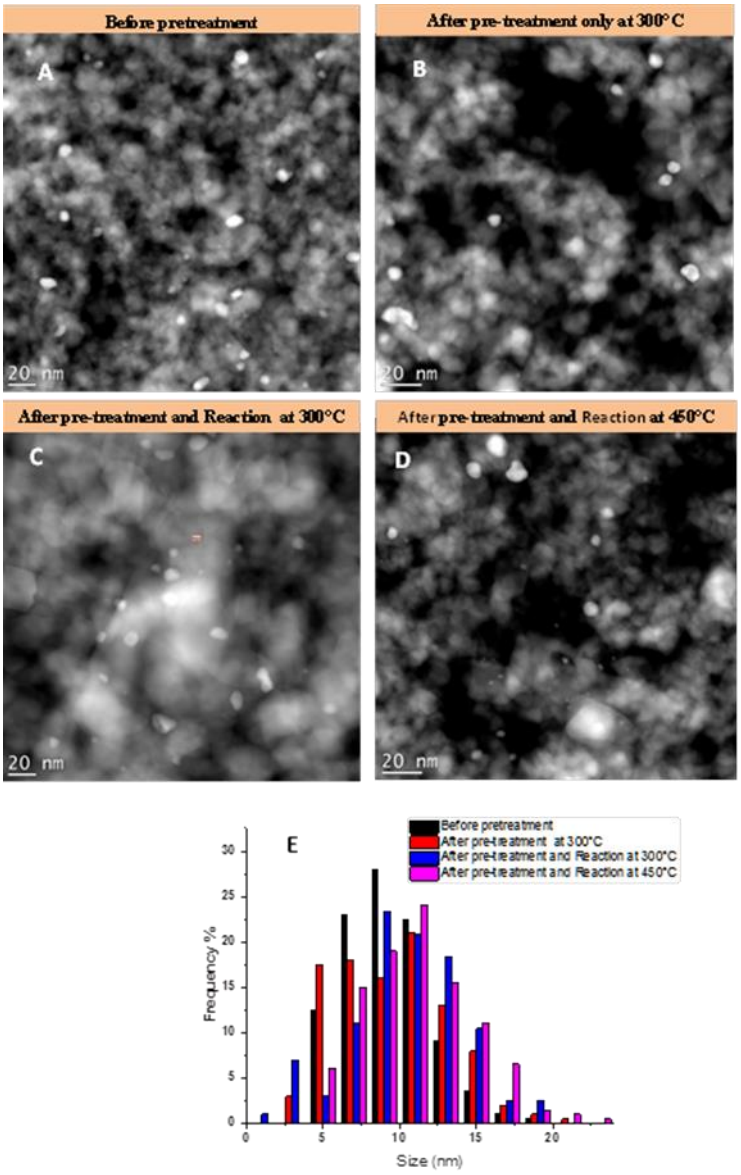

Figure 5.16 TEM images and corresponding histograms of size distributions of the samples in absence of ligands at different pretreatments temperatures: (A) 1% Au/TiO2-untreted, (B) 1%Au/TiO2-300°C before the reaction, (C) 1%Au/TiO2-300 °C after the reaction and (D) 1%Au/TiO2-450°C.(E) Histograms for the average size of the gold nanoparticles at different conditions.

The calculated average sizes of gold nanoparticles were obtaining from TEM, these results confirmed the sintering of gold by increasing the pre-treatment temperature.

	Before Pretreatment	After Pretreatment At 300°C	After pre-treatment and Reaction at 300°C	After pre-treatment and Reaction at 450°C.
Sample Labels	NP size (nm)	NP size (nm)	NP size (nm)	NP size (nm)
Au/TiO_2 REFERENCE	9.2	9.5	10.4	11.0
$Au_1(citrate)_{0.2}/TiO_2$	4.5	4.9	5.9	9.0
$Au_1(citrate)_1/TiO_2$	2.6	2.8	3	8.0
$Au_1(citrate)_5/TiO_2$	3.9	4.1	4.5	12.9
$Au_1(Glutarate)_{0.2}/TiO_2$	6.2	7.3	7.8	11.2
$Au_1(Glutarate)_1/TiO_2$	3.6	3.8	4.3	8.0
$Au_1(Glutarate)_5/TiO_2$	4.8	5.3	6.3	14.8
$Au_1(Sodium\ Acetate)_{0.2}/TiO_2$	4.3	5.5	6.4	10.7
$Au_1(Sodium\ Acetate)_1/TiO_2$	3.2	3.5	4.2	8.5
$Au_1(Sodium\ Acetate)_5/TiO_2$	4.8	5.3	5.8	15.8

Table 5.4 Estimated average size of Au supported on TiO_2

To conclude, the TEM investigation demonstrates the great effect of the nature ligands and depending on the pre-treatment, remarkable differences in the activity results was found.

5.5 Catalytic tests

The complete oxidation of CO is the most studied reaction in the field of Gold catalysis. Several factors influence the catalytic activity such as the method of preparation, particle size, and morphology that are a consequence of the method preparation and heat treatment.

In this part, we present the results of the catalytic test. The most powerful among those supported on Titanium dioxide was selected.

5.5.1 Terms and apparatus

5.5.1.1 Reactor operation

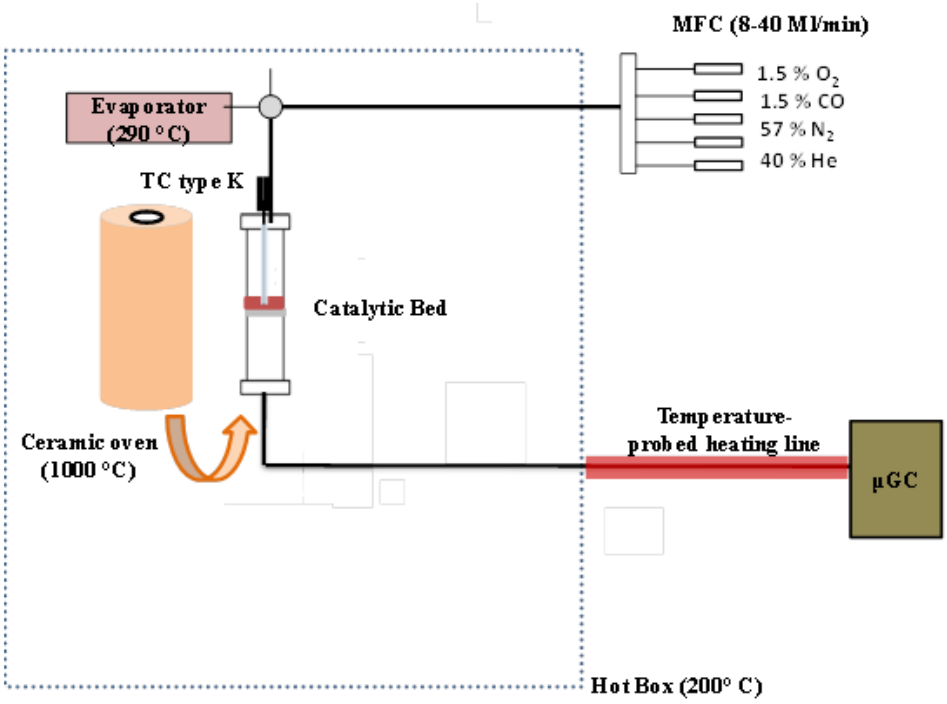

Figure 5.17 Simplified schematic representation of exothermic fixed bed dynamic reactor.

As may be observed in **Figure 5.17** shown, the system consists of an exothermic fixed bed dynamic reactor, with the catalyst bed placed upon a porous plate. The reactor was made from Stainless steel. The flow inside the reactor is up-down, whereby the reactant mixture is fed through the upper part of the reactor and the reaction products are obtained through the lower part.

After passing through a line shut-off valve, the reactant gas streams are fed to the reactor by means of a system of mass flow controllers that provide a known and controlled flow of gases. The present unit is equipped with 5 mass flow controllers. In order to stop the products flowing back through the lines, the controllers are protected with check-valves fitted with Kalretz elastomer seals (elastomeric Teflon).

Gases are introduced into the hot box system that includes an electric forced convection heater that allows the process route to be kept at temperatures of 160ºC, and even 180ºC, to avoid any possible condensation in the system.

This system uses a two-position 6-port valve operated by remote pneumatic control through the computer or by means of the touch screen and allows for selecting from two possible alternatives for the flow path: either towards the reactor or rerouting it towards the system's gas outlet (by-passing the reactor).

When the flow of reactants is directed towards the reactor, it passes through 15 μm sintered filters made of 316 stainless steel, at both the inlet and outlet of the reactor, thereby protecting the arrangement of valves from possible finely-separated catalyst particles.

The reactor was operated with the flow of CO, and O_2 controlled by a flow meter and mass flow controller (Bronkhorst Instrument).

In the course of this investigation, we are planning to conduct experiments in the gas phase at atmospheric pressure and temperatures ranging from 25 to 400°C.

The analysis of the gas fraction at the reactor outlet will be conducted using a Micro-GC.

5.5.1.2 Gas analysis

The gas chromatography is a non-destructive separation technique based on the distribution of sample molecules between a mobile gas phase and a stationary phase within a capillary column. A gaseous product mixture is driven with the "mobile phase", typically helium carrier gas. Column (stationary phase) used to separate these components to the detector that will produce a signal proportional to the amount of each of solutes. Indeed quantitative and qualitative data are obtained by the chromatographic analyzes, only after separation of the different components of the mixture. Under optimal conditions, an electrical signal can be recorded continuously forming what is called the chromatogram. Exploiting this chromatogram provides the concentrations of different gases[159].

μGC chromatograph is a common technique for gas analysis in labs & industry; here we used (μGC3000, SRA instruments). Equipped with 2 analysis modules, each analytical module comprises an injector, a capillary column, and a TCD detector.

The CO oxidation reaction is performed under atmospheric pressure in a fixed bed Stainless steel reactor. The mass of catalyst used is 10 mg diluted in 50 mg of Carborundum fine powder (SiC). The gas mixture contains 1.5 vol.%O_2, 1.5 vol.%CO, N_2 57 vol.% and He 40 vol.% with a total flow of 24 ml/min. The amounts of CO and CO_2 at the reactor outlet are analyzed by μGC. The catalytic test is repeated several times in the temperature range between the ambient to 300°C, 350°C and 450°C to measure the

reproducibility of the experiment. See **Figure 5. 11** for the CO_2, CO, and O_2 micro GC calibration curve.

5.5.1.3 Calibration curve

A GC can separate the compounds, but cannot identify them itself. By calibrating μGC, you can find out at what time various organic compounds are being detected. The area under the curve (automatically calculated by the computer) may be expressed in terms of concentration of the gases, by running some calibration standards at a known concentration.

A calibration curve is simply a graph where the concentration of the gases is plotted along the x-axis and area is plotted along the y-axis. After running each one of the gases on the instrument and getting an area, the points are then plotted on the graph. See **Figure 5.18** the points are then connected with a line. That line represents the calibration curve.

The μGC where is connected by a different mixture of CO, CO_2, and O_2 in inert gas He. In these connections, which consisted of four independent gas lines, the gas flow was adjusted with mass flow controllers (MFC). The gases were mixed after passing the MFCs for bypass measurements, the gas mixing units connected to the μGC. The calibration of the peak areas was performed using calibration gas composition (1.5 % O_2, 1.5 %CO, N_2 57 % and He 40%).

Each concentration gave different peak area. Peak area was then plotted against the concentrations. The Square of correlation coefficients (R^2) of the calibration curves. All gases calibrated show a correlation coefficient close to 1 (between 0.990 and 0.999), thereby confirming the linearity of quantitative curves **Figure 5.18**.

5.5.1.4 Calculations

For example, we estimated the conversion and the reaction rate as;

$$X = \frac{(CO_{in} - CO_{out})}{CO_{in}}$$

$$r\left([mol.g^{-1}sec^{-1}]\right) = \frac{X \times F(CO_{in})[\frac{mol}{sec}] \times 100}{W(g) \times Au(wt\%)}$$

Where: X the conversion, CO_{in} the initial molar fraction of CO at the inlet, CO_{out} the molar fraction of CO at the outlet, r: the intrinsic rate of CO oxidation per gram of Au, $F(CO_{in})$: is the molar flow of CO [mol/ sec] at the inlet of the reactor, W: is the weight of the catalyst in g and Au (wt%): is the loading of Au weight %.

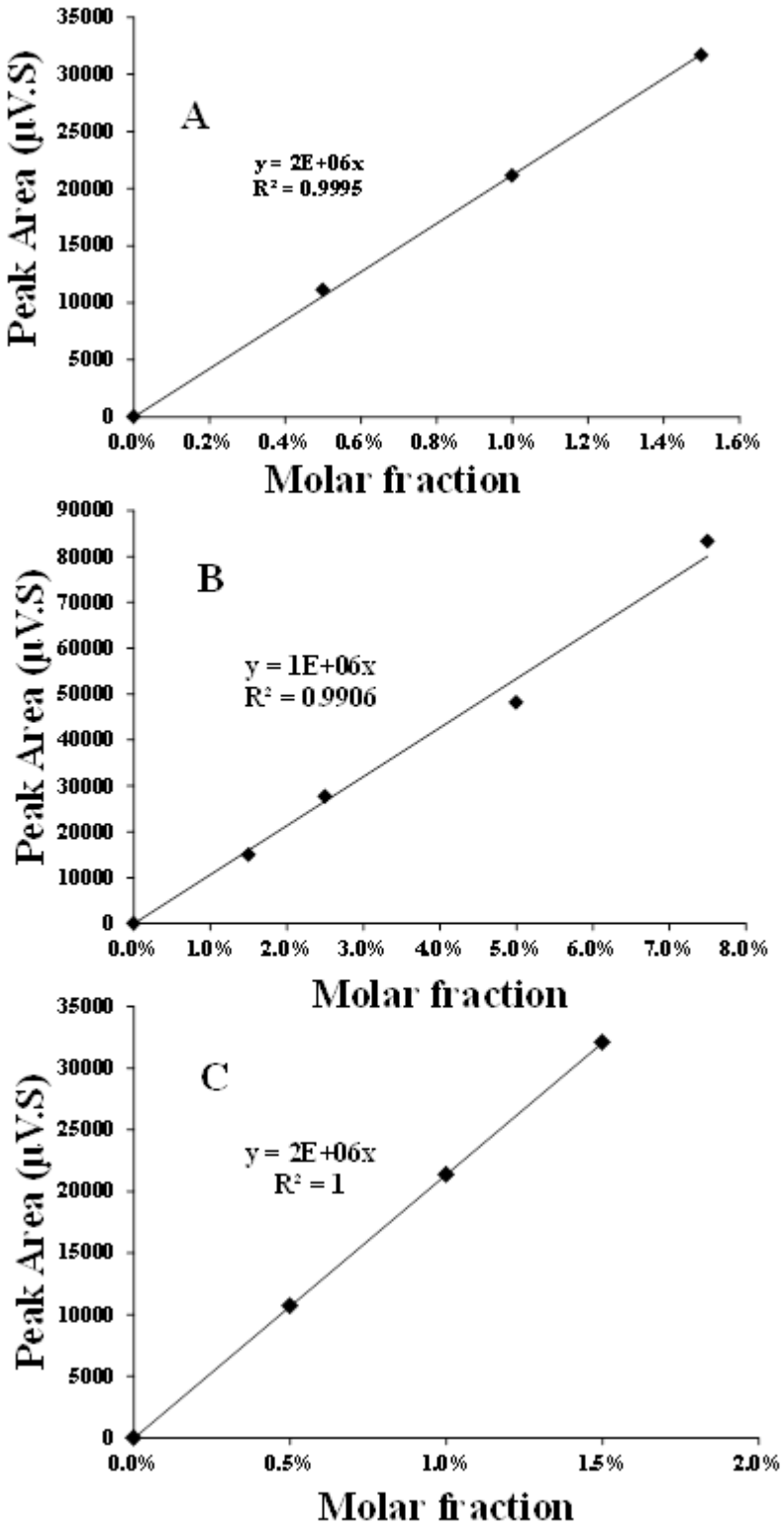

Figure 5.18 Micro GC Calibration curve for the (A) CO, (B) CO_2, and (C) O_2.

5.5.1.5 Calcination (catalyst pretreatment)

The low melting temperature of gold 1063°C may cause sintering of the particles during the reaction or the heat treatment before the reaction. Therefore, the choice of the calcination temperature is very important. The optimum calcination temperature after we did the TPO is 300 ° C **Figure 5.10**. All catalysts are treated with 5%O_2 - He at 300°C for 4 hours. The detailed study of the influence of the calcination atmosphere will be presented in this Section.

5.5.1.6 Reactor loading

The reactor loading process was preceded by thorough cleaning of the reactor with Argon gas to wash out residual gas from the reactor so as to prevent possible impurity formation during catalyst pretreatment and CO oxidation processes. The lower end of the reactor was covered with Glass Wool, 10 mg of catalysis 1% Au/ TiO_2 with 50 mg of Carborundum fine powder(SiC) (sigma > 99%) were added to the reactor and then closed tight. The reactor was then placed inside the furnace to start the catalytic test.

5.5.1.7 Temperature profile used to screen the catalyst

To measure the catalyst activity and product composition, we used the temperature profile shown in **Figure 5.19**. The catalytic test was run for 6 h. The temperature was increased from 25°C to 400°C at a rate of 5 K/min with a step value of 25 degrees. The catalytic acitvity was monitored at each temperature for 30 min. The total flow is 24 ml/min and the molar feed composition is 1.5% O_2, 1.5% CO in N_2 57% and He 40%.

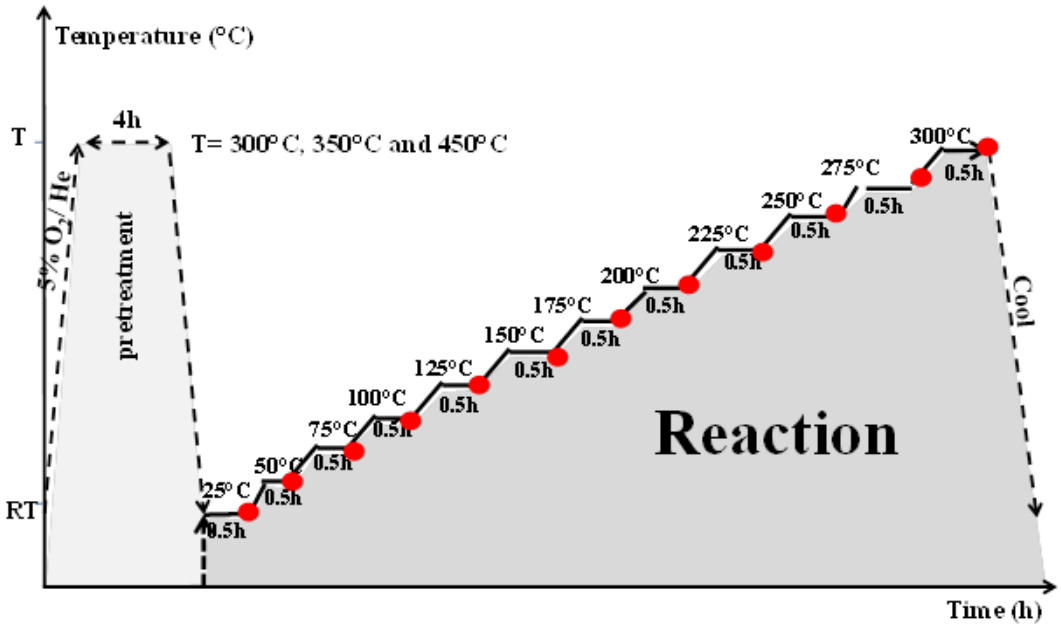

Figure 5.19 Catalytic Screening Protocol

5.5.2 Catalyst pretreatment

5.5.2.1 Study the effect of the pre-treatment temperature

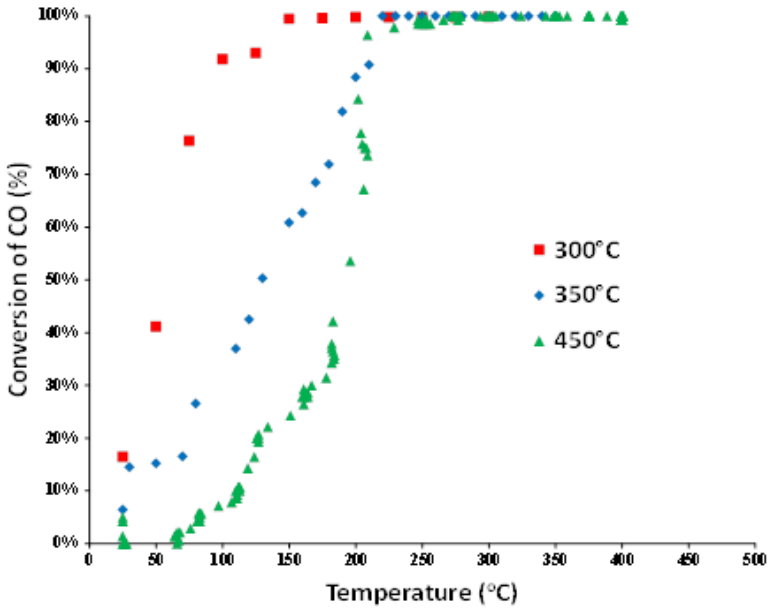

Figure 5.20 CO conversion as a function of temperature for Citrate: Au (0.2:1) ratio catalysts at 1.5%O2, 1.5%CO in N_2 57% and He 40%, total flow is 24ml/min/reactor, reactor loading is ~50mg containing Carborundum fine powder(SiC) mixed respectively with ~10mg Au/TiO_2

All catalysts were tested in the full oxidation reaction of carbon monoxide as shown in **Figure 5.20**. The catalytic tests were repeated several times to ensure reproducibility of the experiments see for example **Figure 5.21** the catalyst activity investigated after pre-treatment at T= 300°C, 350°C, and 450°C temperature.

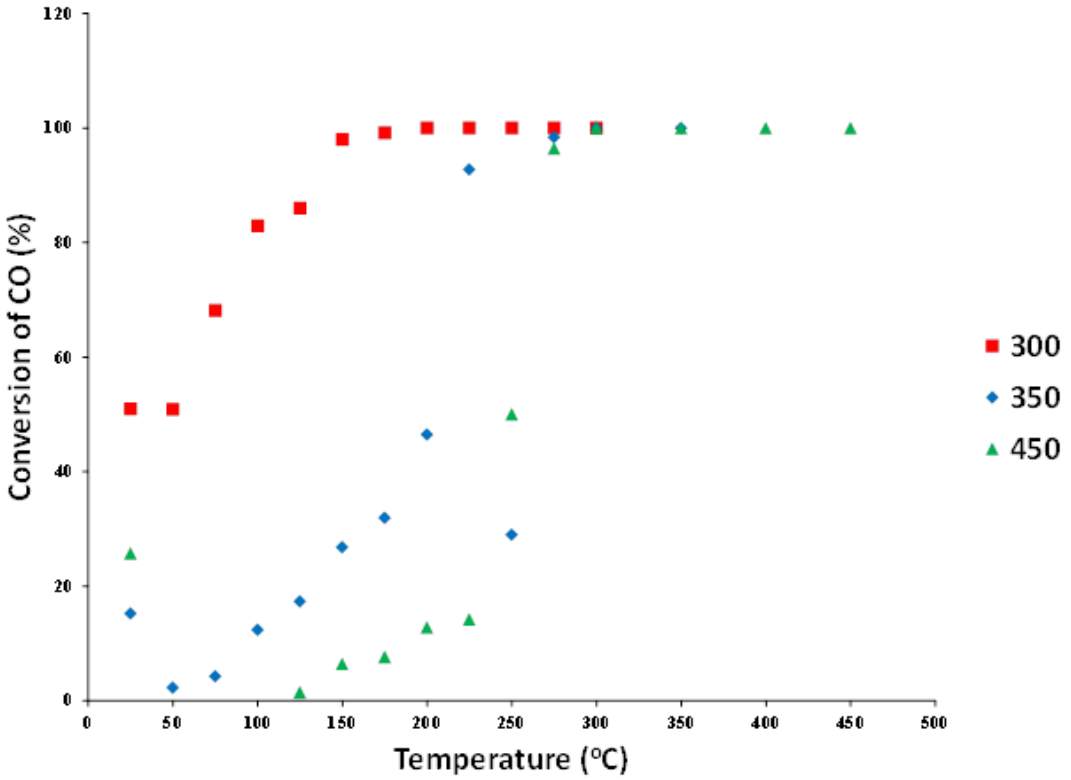

Figure 5.21 CO conversion as a function of temperature for Citrate: Au (5:1) ratio catalysts at 1.5%O2, 1.5%CO in N_2 57% and He 40%, total flow is 24ml/min/reactor, reactor loading is ~50mg containing Carborundum fine powder(SiC) mixed respectively with ~10mg Au/TiO_2

The activities of catalysts loaded with gold to 1 wt%, as determined using ICP **Table 5.2**, and supported on TiO_2 are shown in **Figure 5.20**. This figure shows that pre-treating of the Citrate: Au (1:1) ratio by different temperatures gives different conversion. The above figure also revealed that the optimum temperature for pre-treatment is 300°C which leads to higher CO conversion at lower temperatures. The increase in activity with a decrease in oxidation temperature may arise from the maximal removal of the ligand while avoiding substantial sintering of gold particles.

At temperatures above 300°C, were the maximum of the ligands were removing as proved by TPO. In this case, we lose the size, resulting increase the chance for sintering (Bond and Thompson, 2000) [160].

We can conclude that the observe some activity at a temperature higher than 300°C may, therefore, be arising from the massive increase in metallic gold and sintering[161], in fact, we still see some small particles even after calcination at 450°C [162]as shown in **Figure 5.21.**

However, It is clear that at 300°C seems to be the optimal pre-treatment temperature, as well as the 100% Conversion of CO almost reach at 300°C. However, these results are different for the sample prepared in the absence of ligand. We observe that there is no effect on the pre-treatment temperature on the activity. This can be attributed to the absence of ligand to protect the gold nanoparticles. Based on the literature[121, 140, 163], the most straightforward explanation of this activity is that the activity can be improved by decreasing the size of the particles, this activity can be obtained on catalysts prepared at pH9 [155]. Therefore, we conclude that the CO conversion in the absence of ligand was not affected by the different temperature of the pretreatment as shown in **Figure 5.22**.

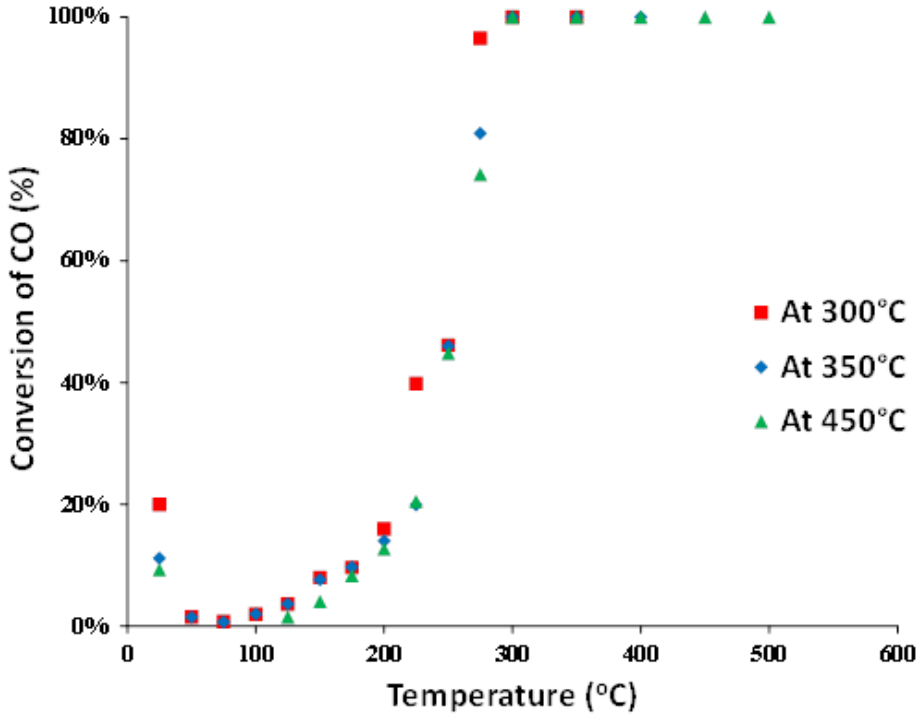

Figure 5.22 CO conversion as a function of temperature for catalysts in the absence of the ligands at 1.5%O2, 1.5%CO in N_2 57% and He 40%, total flow is 24ml/min/reactor, reactor loading is ~50mg containing Carborundum fine powder(SiC) mixed respectively with ~10mg Au/TiO_2

In the light of these results, we would like to confirm using Temperature Programmed Oxidation (TPO) combined with TEM whether the reaction at 300°C is better or not in term of activity.

5.6 Catalytic activity measurement

5.6.1 Catalytic screening at different temperatures

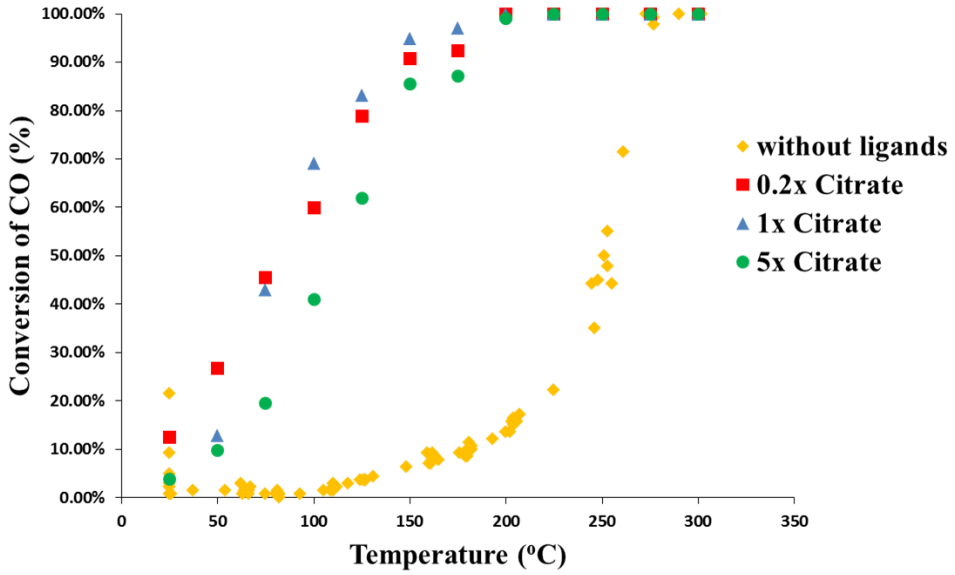

Figure 5.23 CO oxidation over Au/TiO_2 catalysts at different temperatures for Citrate at various ratios: (■) 0.2:1Citrate,: Au; (▲) 1:1 Citrate: Au; (●) 5:1 Citrate,: Au and (◆) without using ligands at 1.5%O_2, 1.5%CO in N_2 57% and He 40%, total flow is 24ml/min/reactor, reactor loading is ~50mg containing Carborundum fine powder(SiC) mixed respectively with ~10mg Au/TiO_2.

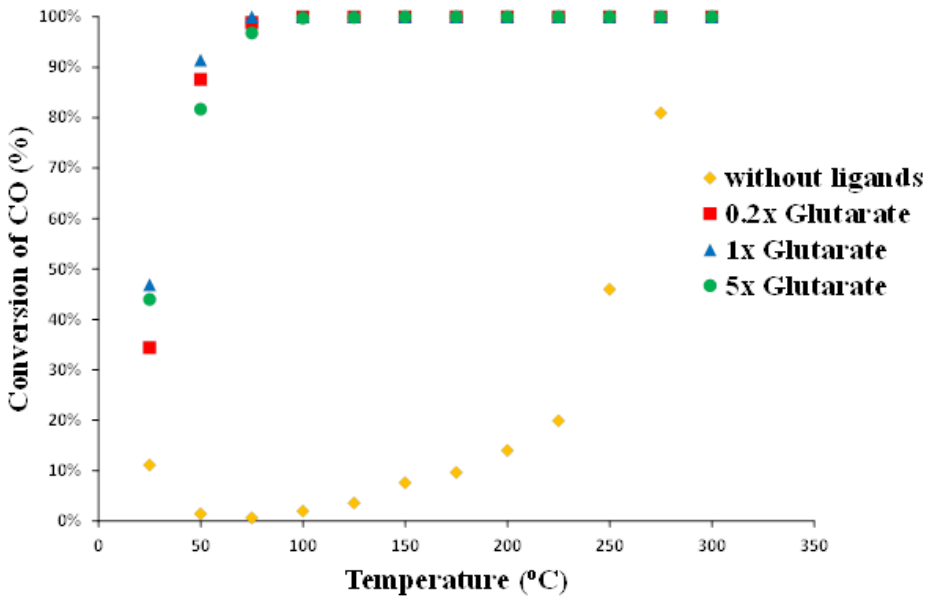

Figure 5.24 CO oxidation over Au/TiO_2 catalysts at different temperatures for Glutarate at various ratios: (■) 0.2:1 Glutarate,: Au; (▲) 1:1 Glutarate: Au; (●) 5:1 Glutarate,: Au and (◆) without using ligands at 1.5%O_2, 1.5%CO in N_2 57% and He 40%, total flow is 24ml/min/reactor, reactor loading is ~50mg containing Carborundum fine powder(SiC) mixed respectively with ~10mg Au/TiO_2

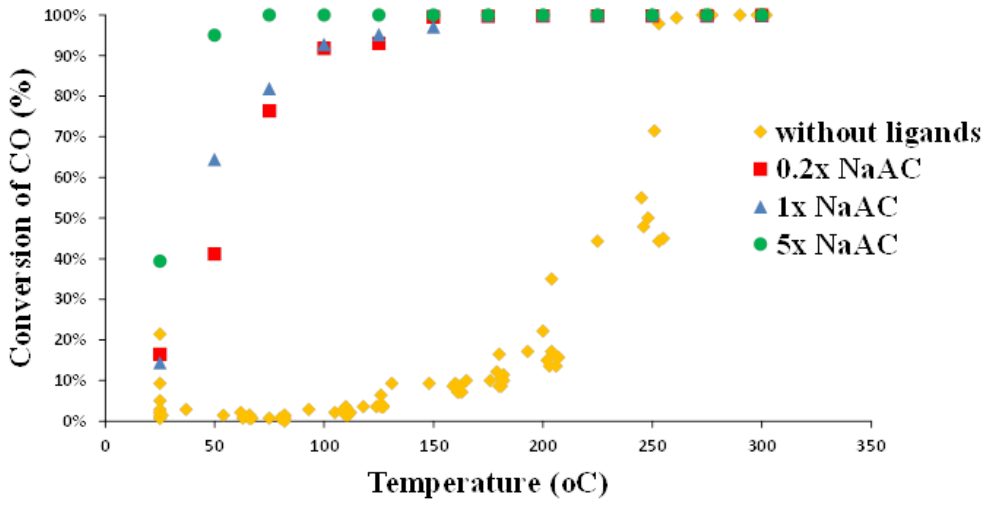

Figure 5.25 CO oxidation over Au/TiO_2 catalysts at different temperatures for Na acetate at various ratios: (■) 0.2:1 Na acetate,: Au; (▲) 1:1 Na acetate: Au; (●) 5:1 Na acetate,: Au and (◆) without using ligands at 1.5%O_2, 1.5%CO in N_2 57% and He 40%, total flow is 24ml/min/reactor, reactor loading is ~50mg containing Carborundum fine powder(SiC) mixed respectively with ~10mg Au/TiO_2.

Figures above shows that in all cases of Au NPs synthesized were first deposit onto the support and then calcined at 300°C for different ligand at various ratios. I will summaries the **Figure 5.23, Figure 5.24 and Figure 5.25** in the following;

- The catalyst prepared in the presence of ligand was generally found to have better activity compared to the reference catalyst. Indeed, significant CO conversion can be achieved at temperatures as low as 50°C, over Au/TiO_2 synthesized in the presence of ligand.

- Maximum conversions of CO over Au/TiO_2 prepared in the presence of ligand was achieved at much lower temperatures. On another hand, for the sample prepared in the

absence of any ligands as a stabilizer, the conversion of CO at 200°C is very small (around 10%) and markedly increased to reach 100% conversion at 250°C.

- When the conversions are high, it means that more reacting molecules are adsorbed on the surface of the catalyst where they are converted into products.

- It has also been demonstrated that thermal treatments of the catalyst at 350°C or higher deactivated the catalyst.

- This treatment is believed to modify the catalyst by removing the hydroxyl groups from the ionic Au species and from the surface of the support. Hydroxyl groups are believed to be crucial for the activity of the catalyst[60, 164]. Thermal treatment also leads to the agglomeration of Au particles which is not desirable for the high activity.

Although the catalytic activity of gold catalysts in the low temperature CO oxidation has been extensively investigated in recent decades, the nature of the active species is still controversial. It has been suggested that the role of the metal oxide is to stabilize the gold nano-particles and that the reaction happens on the gold surface[143b, 144, 165]. Other authors proposed that the reaction takes place at the gold/metal oxide interface and that the metal oxide could act as a source of oxygen[166]. Different researchers, however, proposed that the active species is the metallic gold because they found no proof of the presence of ionic gold species on their active catalysts[57b]. In light of the spectroscopic analysis indicating the presence of ionic gold in the most active catalysts, a few analysts proposed that ionic gold is necessary for high CO oxidation activity although there is no consensus

on whether it is Au^{III} or Au^{I}. Several groups have observed the presence of ionic gold in active catalysts by Mössbauer impact spectroscopy[167], XPS[52], and XANES[164]. Guzman, gates and Minaco *et al.* Have observed the presence of Au^{I} on their active Au/Fe_2O_3 using FTIR[168]. Bond and Thompson[169] suggested in their exhaustive literature survey on gold catalysts that the active site consists of an ensemble of $Au(OH)_3$ and metallic gold. In **Figure 5. 26**, where ionic gold species are believed to be the chemical "*glue"* between the metallic gold species and the support. At high temperature treatment, these species would be reduced to metallic gold and result in the agglomeration of gold on the surface of the support. This hypothesis was confirmed by Costello [170], where they reported that an Au(OH) species is in charge for the adsorption of CO molecule and an oxygen atom would be adsorbed on the surface of the metallic gold particle.

- In this study, we identify the active species responsible for the high activity of gold catalysts. XPS (**chapter 4**) confirm that we have Au^{I}, Au^{0} (the ionic gold to be necessary for high CO oxidation activity).

- Our results show that increase the pH has a significant role to play in activity due to at pH =9 as we approved that by ^{13}CNMR (**chapter 4**), we keep the interaction between the ligands and the gold atoms and later this ligands by protecting the nanoparticles can enhance the catalytic activity.

- At pH = 9 (**Cf. ^{13}C MAS NMR study in chapter 4**), we proved that the interaction between gold atoms and the ligand is optimal. This would protect the nanoparticles

against sintering leading to better catalytic activity. This is in good agreement with the results previously reported by Wolf and Schuth[171].

Removal of Cl^- ions from the catalyst was reported to results in the deposition of small Au particles leading to higher dispersion and improved activity[61,69]. In our study, we think that residual Cl^- ions are almost totally removed during the washing process

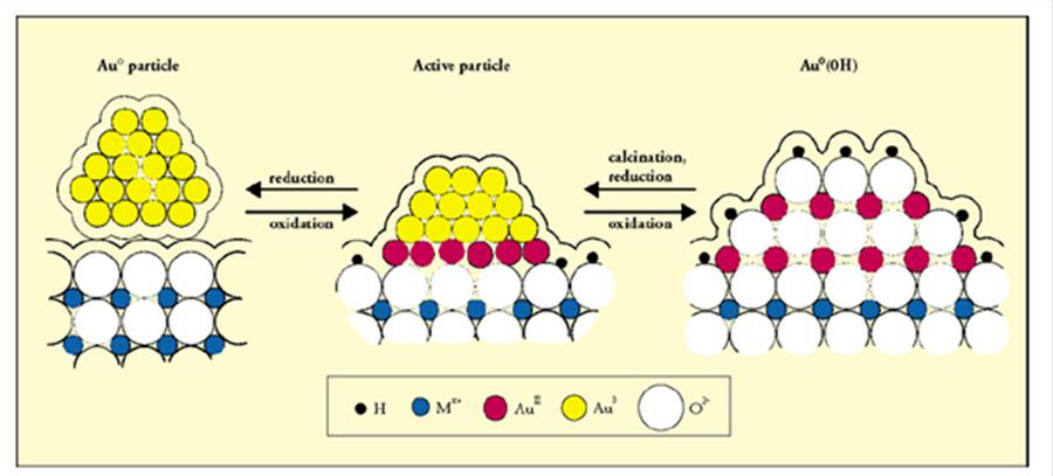

Figure 5. 26 Pictorial representation of supported gold catalyst indicating possible changes under conditions giving oxidation or reduction of the active gold particles[71]

5.7 Conclusion

The studies we have conducted allowed us to show the decisive influence of a number of experimental parameters on the resulting nanostructures.

The Au/TiO_2 catalysts prepared with different ligands and various Au-to-ligand ratios were evaluated for the CO oxidation at 573 K. Thanks to the different results we have obtained, we can conclude that:

1. The TEM images and size distributions of the Au nanoparticles after and before the heat treatments at 300, 350, and 450°C are shown in Table 5.4. The size of Au nanoparticles clearly increases from 2.6 nm before pretreatment to 15.8 after calcination at 450 °C. The mode of pretreatment before use is also important: calcination is frequently used with good results. It is evident that of gold particles grows with the calcination temperature which can be ascribed by more agglomerated crystals.

2. The best ratio to get reliable size is 1:1 with temperature 300°C for pretreatment and catalysis.

3. Additionally, When we have pretreatment temperature at 300°C and we do the reaction between 25°C to 300°C. We observed good activity.

4. The activities are better when we have ligand than if we did not have ligands.

5. The Glutarate seems to be having better effect than the other.

Unfortunately, based only on the present results it will be very hard to clarify the role of the ligands on the catalytic activity. Because we observed the ligands has an affect but we have treated the surface with oxygen so we did not know what is left on the surface.

Appendix1

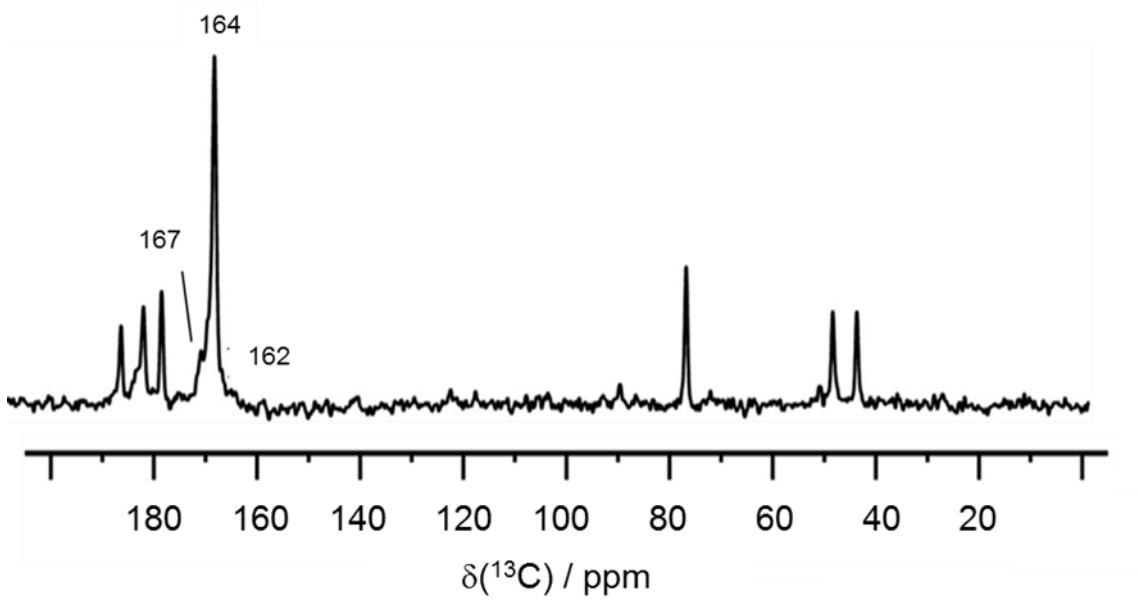

Figure1. Low temperature (100 K) 1D ^{13}C CP/MAS NMR spectrum where the citrate:Au ratio is 0.2:1 acquired at 9.4 T using a pre-cooled system with the probe temperature set at 100 K, an MAS frequency of 10 kHz, and a repetition delay of 5 s.

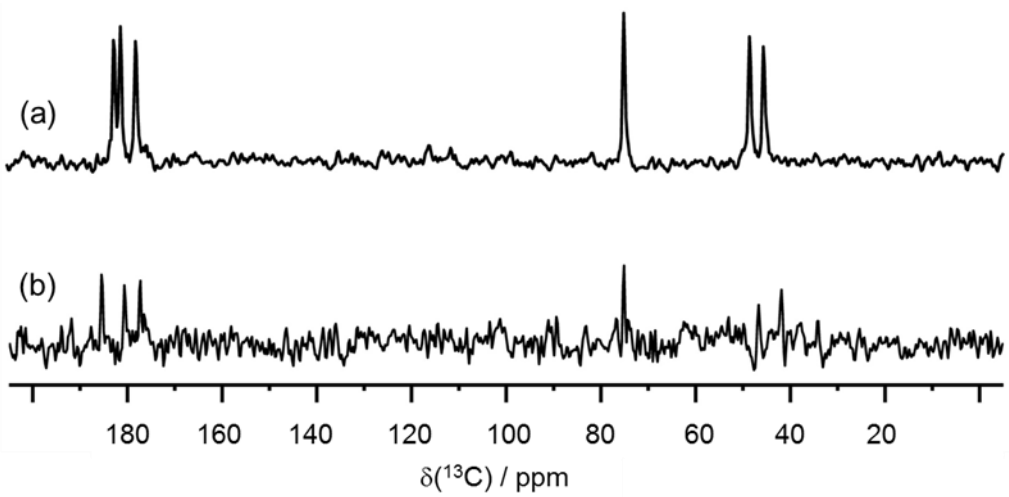

Figure 2. 1D ^{13}C CP/MAS NMR spectra of (a) trisodium citrate dihydrate (CSD code: UMOGAE) and (b). bis(trisodium citrate) undecahydrate (CSD code: FATTID).

Table1. Quadrupolar coupling constant, C_Q, asymmetry parameter, h, and isotropic chemical shifts, d_{iso}, of bis(trisodium citrate) undecahydrate and citrate/Au(1:1 ratio) derived from the ^{23}Na MQMAS NMR spectra.[a]

sodium citrate				citrate/Au(1:1 ratio)		
Sites[b]	$\|C_Q\|$ / MHz[c]	h[c]	d_{iso} / ppm	$\|C_Q\|$ / MHz[c]	h[c]	d_{iso} / ppm
Na(1)	1.00(0.10)	1.00(0.10)	-2.09(0.40)	1.00(0.15)	1.00(0.10)	-2.08(0.58)
Na(2)	1.28(0.03)	0.28(0.06)	-1.03(0.30)	1.23(0.02)	0.80(0.10)	-2.57(0.87)
Na(3)	1.50(0.05)	0.60(0.10)	1.00(0.50)	1.30(0.10)	0.50(0.05)	1.25(0.45)
Na(4)[d]	0.70(0.10)	0.00(0.20)	2.84(0.20)			2.80(0.20)
Na(5)[d]						7.21(0.20)

[a] Error bounds are in parentheses.
[b] There are four crystallographically inequivalent sodium sites in the crystal structure of bis(trisodium citrate) undecahydrate and for citrate:Au (1:1 ratio). $NaCl_{(s)}$ present in both compounds.
[c] The EFG tensor, **V**, can be diagonalized to provide three principal components defined as: $|V_{33}| \geq |V_{22}| \geq |V_{11}|$; quadrupolar coupling constant: $C_Q = eQV_{33}/h$; asymmetry parameter: $\eta_Q = (V_{11} - V_{22})/V_{33}$.
[d] NaCl is observed in the full spectra shown in Figure 13. No second order broadening effects are observed for Na(4) of citrate/Au(1:1 ratio) and NaCl due to negligible EFG at that sodium site.

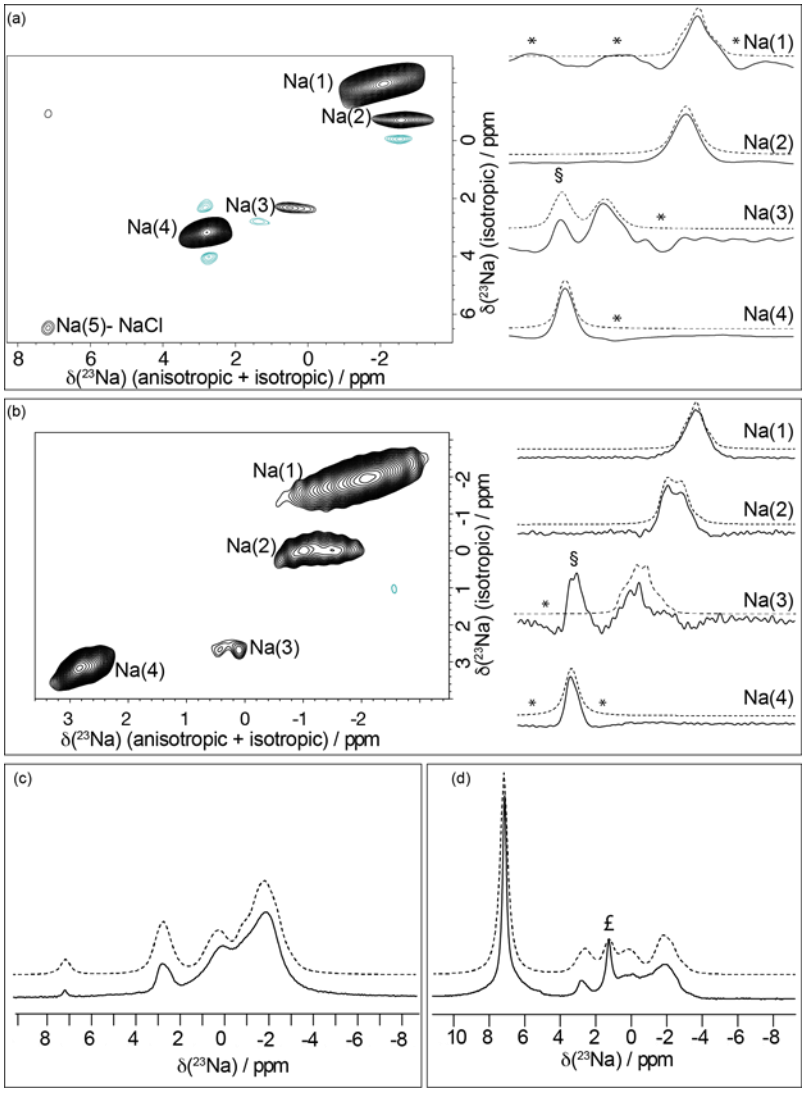

Figure 3. ^{23}Na MQMAS SSNMR spectra (left) acquired at 21.1 T along with the extracted slices (right) of all crystallographically distinct Na sites for (a) citrate/Au (1:1 ratio) and (b) bis(trisodium citrate) undecahydrate. In (a) the full ^{23}Na MQMAS NMR spectrum of citrate:Au (1:1 ratio) is shown to highlight the presence of NaCl at 7.21 ppm. Experimental (black) and simulated (dashed line) 1D ^{23}Na MAS NMR spectra are shown in (c) and (d) for sodium citrate and citrate/Au(1:1 ratio), respectively. All simulated spectra were generated using WSolids.[172] Asterisks show distortions in the slices which are known to happen in MQMAS experiments,[173] while § designates Na(4) observed in the extracted slice containing also the Na(3) signal, and £ designates an impurity. The spectra were appropriately sheared after acquisition using the C_k convention by P. P. Man{Man, 1998 #4420} as well as using the xfshear command in TopSpin and referenced to NaCl(s), d_{iso}(^{23}Na) = 7.21 ppm.

Density Functional Theory (DFT) Calculation Details

Geometry optimizations and binding energy calculations on fixed Au surfaces in vacuo. For calculations involving acetate anions supported on fixed neutral gold nanoparticle surface models *in vacuo*, version 2010.02 of the Amsterdam Density Functional (ADF)[174] DFT software package was used. Au nanoparticle surface models were generated using the crystal structure of bulk gold.[175] Based on prior findings,[176] gold nanoparticles may be modelled using the (111), (100), and to a lesser extent (110) cleavage planes of bulk gold.[177] The typical size of the surfaces used possessed a depth of three layers, with each layer consisting of about 15 – 20 gold atoms. After selecting the surface models, between one and four acetate anions were added with an idealized starting geometry, and then geometry optimized at the generalized gradient approximation (GGA) level of DFT, while the Au atoms were kept fixed. For all optimizations, the exchange-correlation (XC) functional of Perdew, Burke, and Ernzerhof (i.e., PBE) was used.[178] Dispersion effects were included using the three parameter correction developed by Grimme and co-workers[179] which is effective when modelling Au(111)-supported species.[180] To include relativistic effects, the zeroth-order regular approximation (ZORA)[181] was used at the scalar level. All-electron basis sets, which were triple-ζ in the valence and included polarization functions (i.e., TZ2P according to ADF nomenclature), were used for all non-Au atoms. For the Au atoms, a frozen core (up to 4f electrons) TZ2P basis set was used. Due to the metallic nature of the Au surface, geometry optimizations required a density smearing function of width 0.03 Hartree (0.8 eV) to describe the electrons below the highest-occupied molecular orbital. Optimized geometries in Cartesian coordinates, as well as corresponding energies, can be found in the subsequent sections of the Supporting Information, while the binding energy

calculation results using the computational parameters above are in Table 2. In passing, we note that the starting geometry of one acetate anion was allowed to initially be planar with the Au(111) surface model, rather than having both oxygen atoms of the carboxylate group pointing towards the surface. The geometry optimization of this system did not lead to a stable energy minimum geometry. The initial forces were such that the ligand was pushed rather far away (> 3 Å) from the Au(111) surface. When loading 4 acetate anions onto the Au(111) surface, the Au-O internuclear distances ranged from a low of 2.19 Å in one of the acetates binding in a 1κ*O*^{1} fashion, to 2.2 – 2.4 Å for anions binding in a μ_2 fashion.

Table 2. Calculations of binding energies for acetate anions on fixed Au model surfaces *in vacuo*[a]

System (ligand(s) / support)	E_{Au}[b] / kcal mol^{-1}	E_{Ac}[c] / kcal mol^{-1}	E_{tot}[d] / kcal mol^{-1}	BSSE[e] / kcal mol^{-1}	$E_{Bind.}$[f] / kcal mol^{-1}
1 acetate / Au(111)	−3820.23	−1013.38	−4901.01	−0.51	67.91
1 acetate / Au(100)	−3352.24	−1013.37	−4434.88	−0.22	69.48
1 acetate / Au(110)	−3440.68	−1013.28	−4529.59	−0.16	75.80
4 acetates / Au(111) – I[g]	−3820.23	−1013.48	−4900.78	−0.51	67.58
4 acetates / Au(111) – II	−3820.23	−1013.04	−4899.85	−0.84	67.42
4 acetates / Au(111) – III	−3820.23	−1013.52	−4909.03	−1.06	76.34
4 acetates / Au(111) – IV	−3820.23	−1012.47	−4899.75	−1.35	68.39

[a] Calculations were carried out at the same level of theory as the *in vacuo* geometry optimization calculations (GGA DFT, PBE XC functional, all-electron TZ2P basis on ligand atoms, frozen core TZ2P basis on Au atoms (up to 4*f*), relativistic effects included via the scalar ZORA, and dispersion included by the Grimme three parameter correction). For descriptions of the acronyms used and relevant references, see above computational details section. 3D structures can be found in Figure 5(a-c).

[b] Bond energy of the relevant gold surface model.

[c] Bond energy of the isolated acetate anion.

[d] Bond energy of the acetate anion and gold surface together.

[e] Basis set superposition error. We note that contrary to the typical expectation, the BSSE is confirmed to be slightly negative for the systems considered herein. Due to its small magnitude, BSSE corrections were not used in the non-fixed Au surface calculations outlined in the sections below.

[f] Binding energy, $E_{Bind} = -(E_{tot} - E_{Au} - E_{Ac} + BSSE)$.

[g] Corresponds to acetate 'I', as in Figure 3c of the main text. Although in this system, a total of four acetates were interacting with the Au(111) surface, for simplicity, the interaction energies between each ligand were ignored. Hence, each acetate ligand was treated in isolation and the E_{tot} values in these rows correspond to only the Au(111) surface and the particular acetate anion (i.e., 'I', 'II', 'III', 'IV') specified in the first column of the row.

Geometry optimizations and binding energy calculations using large non-fixed Au surfaces. In reality, the Au surface must deform slightly as a result of binding the various ligands. Hence, geometry optimizations of mono- and dicarboxylates coordinating to large non-fixed gold nanoclusters have been performed with the Vienna *ab initio* simulation package (VASP).[182] To this end, 110 Au atom and 85 Au atom clusters were built using the same Au crystal structure denoted above, in order to model the (100) and (111) facets of Au nanoparticles, respectively, as depicted in **Figure 4**. These large clusters were built to model large surfaces by minimizing edge effects on the adsorption of a single carboxylate. In all cases the clusters are composed by three layers of Au atoms.

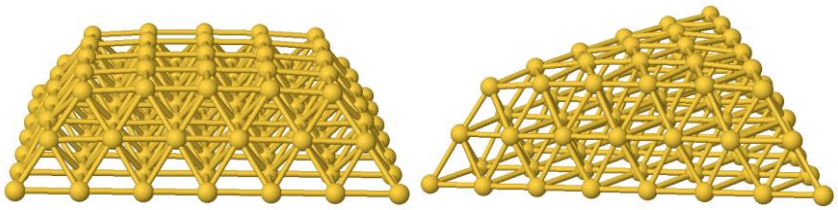

Figure 4. Nanoclusters used to model the Au(100), left, and Au(111), right, surfaces of Au nanoparticles for adsorption of a single acetate, succinate or glutarate anion. Importantly, these surfaces were allowed to deform as a result of their interaction with the various ligands.

Geometry optimizations were performed with the PBE XC functional as implemented in VASP. Plane-wave basis sets with a kinetic energy cutoff of 450 eV describe the valence electrons as defined by the $5d^{10}6s^{1}$ electrons of Au, $2s^{2}2p^{2}$ electrons of C, $1s^{1}$ electron of H and $2s^{2}2p^{4}$ electrons of O. Core electrons were replaced by projector augmented-wave (PAW) relativistic pseudopotentials.[183] The clusters were placed in a cubic box of 30 Å × 30 Å × 30 Å, leaving a distance of at least 10 Å between clusters in

neighboring simulation cells. Relaxation of the atomic positions in the supercell took place until energy differences were smaller than 0.001 eV.

After geometry optimizations, carboxylate binding energies were evaluated with ADF for two reasons. First, in the presence of a charged ligand, periodic boundary conditions can lead to artifacts in the binding energy due to the simulation box presenting a net charge. Indeed, test calculations on acetate binding on a small 55 Au atom cluster indicated the binding energy was converged only with a simulation box having a side of 40 Å. On this basis, larger boxes are expected to be required for the dianionic succinate and glutarate on the large clusters used in this work. Second, ADF allowed solvent (water) effects to be included via a continuum solvation model. Considering that carboxylates are negatively charged, it is expected that a highly polar solvent would reduce remarkably the binding energy of charged ligands. These ADF binding energy calculations were performed with the PBE functional, as before, with the numerical integration parameter set to 5. Scalar relativistic effects were included via the ZORA. A triple-ζ basis set augmented with one polarization function on all atoms (TZP) was used. A dispersion correction was introduced with the empirical Grimme three parameter model, as before. Solvent effects (water) were included with the COSMO continuum solvation model.[184] Radii of 2.223, 1.720, 2.000 and 1.300 Å were used for Au, O, C and H, respectively. Calculations involving the 110 atom cluster mimicking the Au(100) surface were performed in the singlet state, whereas calculations involving the 85 atoms cluster mimicking the Au(111) surface were performed with a total spin density $\alpha - \beta = 1$, and an unrestricted DFT formalism was used. The total binding energy, E_{Bind}, is calculated as in Eq. S1.

$$E_{Bind} = -(E_{tot} - E_{Au} - E_{Carboxylate}); \quad (1)$$

Where E_{tot} is the energy of the Au cluster with the carboxylate-containing anion adsorbed, E_{Au} is the energy of the free Au cluster, and $E_{Carboxylate}$ is the energy of the free carboxylate-containing ligand. As illustrated in the fixed Au surface binding energy calculations, basis set superposition effects were not significant and as such were omitted in this series.

The strain energy, E_{Strain}, for coordination of succinate and glutarate was calculated as in Eq. 2.

$$E_{Strain} = E_{Bind}(Au/Dicarboxylate) - 2E_{Bind}(Au/Acetate); \quad (2)$$

Where $E_{Bind}(Au/Dicarboxylate)$ is the binding energy of succinate or glutarate, and $E_{Bind}(Au/Acetate)$ is the binding energy of acetate. Within this definition, $E_{Strain} = 0$ means that the dicarboxylate binding energy is equal to two times the binding energy of an isolated acetate. In other words, the carbon spacer tethering the two carboxylate groups is not preventing optimal coordination of the dicarboxylate. The ADF-calculated binding energies of all systems are reported in **Table 3**. Pictorial representations of all the geometries with a carboxylate coordinated to the non-fixed Au nanoclusters are in **Figure 5(a-o),** while those pertaining to fixed Au nanoclusters *in vacuo* are in **Figure 6(a-b).** The total ADF bond energies of all the species coordinated to the large non-fixed (100) and (111) Au clusters (**as in Figure 4**) are reported in **Table 4**.

Analysis of the data reported in **Table 3** indicates that both *in vacuo* and in water, binding of the carboxylates to the Au(100) surface is favored by roughly 20 kcal mol^{-1} over binding to the Au(111) surface. In addition, by comparing the *in vacuo* binding

energy calculations of one acetate on various Au surface models in Tables 2 and 3, it is seen that allowing for the Au surface to deform results in binding energies that are enhanced on the order of 10 kcal mol^{-1} for Au(100), but in contrast, the binding energies do not vary significantly between the fixed and non-fixed Au(111) surfaces. This may partially explain the reduced binding energies calculated for acetate on the water-solvated Au(111) surface. Likewise, the larger E_{Bind} of the carboxylates to the Au(100) surface can be related to the lower coordination number of the Au atoms on the (100) surface, 8, relative to the coordination number on the (111) surface, 9. Further, the geometry of the Au(100) surface, with square planar coordinated Au atoms, allows for a greater flexibility of the surface atoms, relative to Au atoms on the (111) surface, with hexa-coordinated Au atoms. Indeed, in the (100) geometries, the distance between the Au atoms involved in binding of the two carboxylates can stretch up to 3.2 Å, from a value of 2.9 Å for an uncoordinated Au(100) surface. In contrast, on the Au(111) surface the distance between the Au atoms involved in binding is only increased to values of around 3.0 Å (see below SI sections for details). In line with previous work, inclusion of solvent effects strongly reduces the binding energy, due to a strong stabilization of the free carboxylates.[185] Analysis of the Hirshfeld charges indicates substantial transfer of electron density from the carboxylates to the Au clusters. In the case of acetate, a total of 0.68e is transferred from the acetate to the Au cluster both for μ_2-acetate coordination to the (100) and (111) surfaces. In the case of succinate, the amount of electron density transferred to the Au clusters is almost the double, in the 1.25-1.35e range.

Table 3. Binding energy and strain energy of carboxylates on large nanoclusters[a]

System (ligand / support)	E_{Bind} (*in vacuo*) / kcal mol^{-1}	E_{Bind} (water) / kcal mol^{-1}	E_{Strain} (water) / kcal mol^{-1}

μ_2-acetate / Au(100)	80.0	30.5	not defined
κ-acetate / Au(100)	71.3	19.4	not defined
μ_4-succinate (stacked) / Au(100)	168.5	46.0	15.1
μ_4-glutarate (stacked) / Au(100)	170.5	54.3	6.8
μ_4-succinate (parallel displaced) / Au(100)	171.2	48.9	12.1
μ_4-glutarate (parallel displaced) / Au(100)	171.2	55.2	5.9
μ_2-acetate / Au(111)	70.4	17.1	not defined
μ_4-succinate (stacked) / Au(111)	153.7	29.1	5.2
μ_4-glutarate (stacked) / Au(111)	151.2	32.3	2.0
μ_4-succinate (parallel displaced) / Au(111)	149.6	24.3	9.9
μ_4-glutarate (parallel displaced) / Au(111)	151.2	31.7	2.6
μ_4-succinate (bent) / Au(111)	150.6	26.8	7.5
μ_4-glutarate (bent) / Au(111)	147.9	29.6	4.6
μ_4-succinate (skewed) / Au(111)	147.4	22.5	11.8
μ_4-glutarate (skewed) / Au(111)	148.9	29.4	4.8

[a] The binding energy is calculated both *in vacuo* and in water using the ADF package. The 3D structures of the various geometries can be found in Figure 5(a-o).

The conformational strain energy, E_{Strain}, was determined to be low, as indicated by comparing the best binding energy of succinate or glutarate with the binding energy of two isolated acetate molecules, as in Eq. S2. If no strain or cooperative effect is in place, according to our definition E_{Strain} should be equal to zero or even negative. The calculated ΔE_{Strain} for succinate on the Au(100) surface, around 15 kcal mol^{-1}, indicates some strain in the coordination of succinate, which is reduced to 6-7 kcal mol^{-1} with the more flexible 3 methylene spacer of glutarate. Similar behaviour is found for succinate and glutarate when coordinating to the Au(111) surface, although a slightly lower ΔE_{Strain} of around 5-12 kcal mol^{-1} is calculated. The lower ΔE_{Strain} of glutarate accounts for the stronger predicted binding of glutarate to the Au surfaces. This allows us to tentatively arrive at the conclusion that one possible binding motif for the citrate would occur preferentially using both terminal carboxylates, rather than one terminal and the central carboxylate.

Pictorial Representations of Optimized Geometries

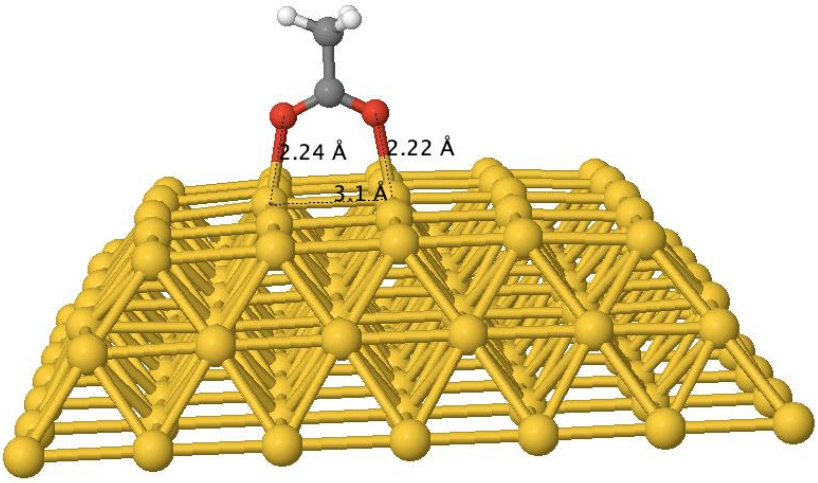

Figure 5a. Optimized geometry of one μ_2 coordinated acetate on an Au(100) model surface, as also depicted in Figure 3a.

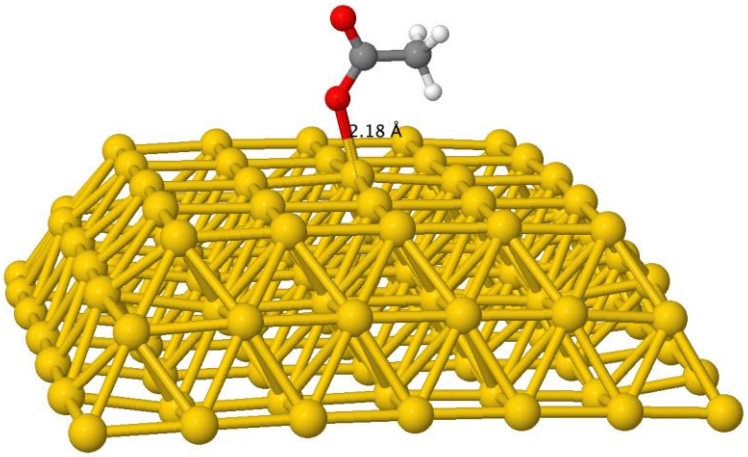

Figure 5b. Optimized geometry of one κ coordinated acetate on an Au(100) model surface.

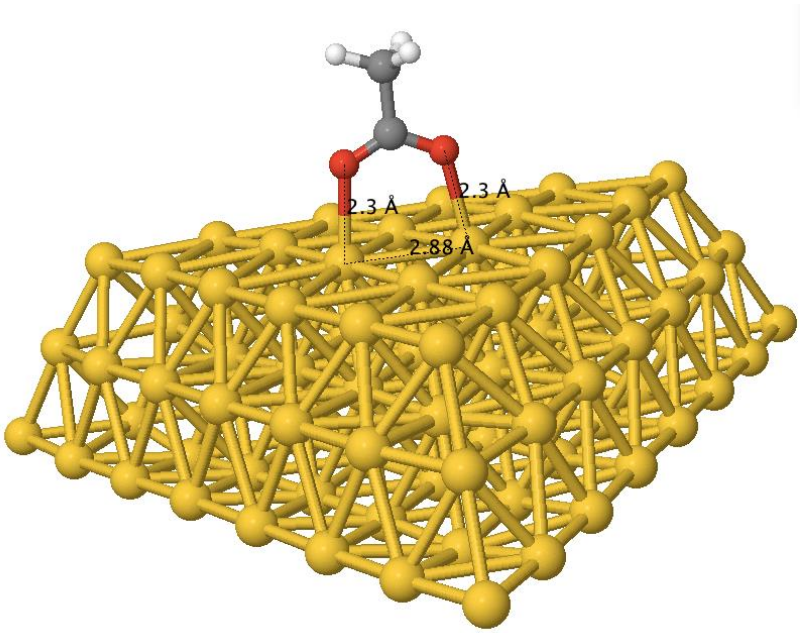

Figure 5c. Optimized geometry of one μ_2 coordinated acetate on an Au(111) model surface, as also depicted in Figure 3b.

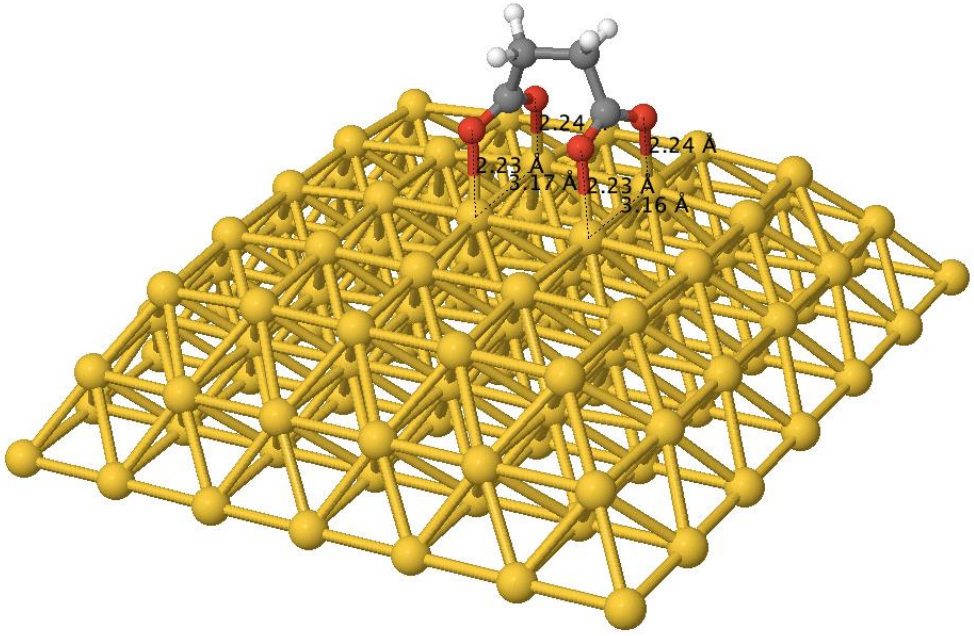

Figure 5d. Optimized geometry of one μ_4 coordinated succinate in the "stacked" conformation on an Au(100) model surface. A schematic of this binding motif can be found in the main manuscript, Figure 3d.

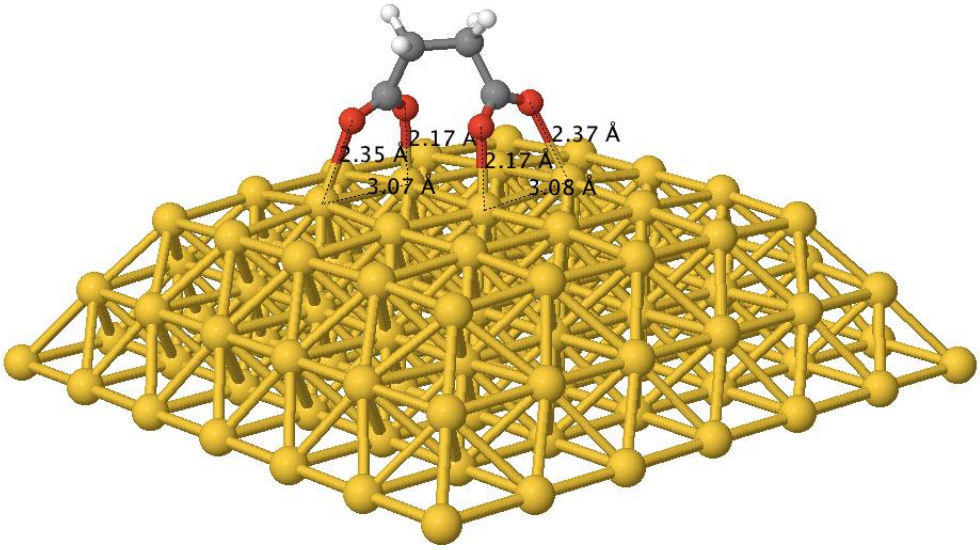

Figure 5e. Optimized geometry of one μ_4 coordinated succinate in the "parallel displaced" conformation on an Au(100) model surface. A schematic of this motif can be found in Figure 3d.

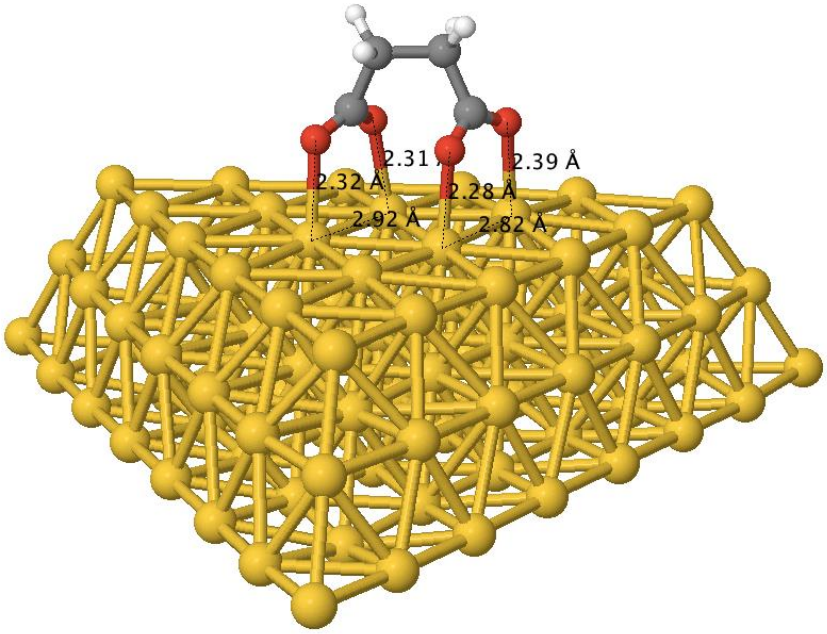

Figure 5f. Optimized geometry of one μ_4 coordinated succinate in the "parallel displaced" conformation on an Au(111) model surface. A schematic of this motif can be found in Figure 3d.

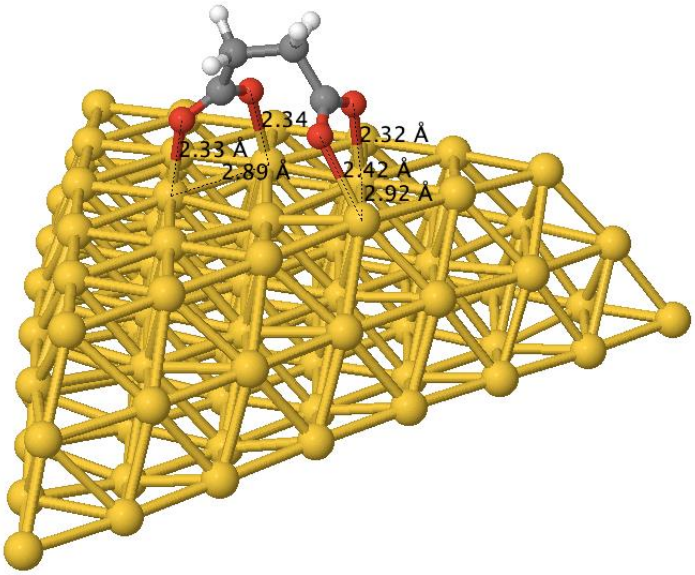

Figure 5g. Optimized geometry of one μ_4 coordinated succinate in the "bent" conformation on an Au(111) model surface. A schematic of this motif can be found in Figure 3d.

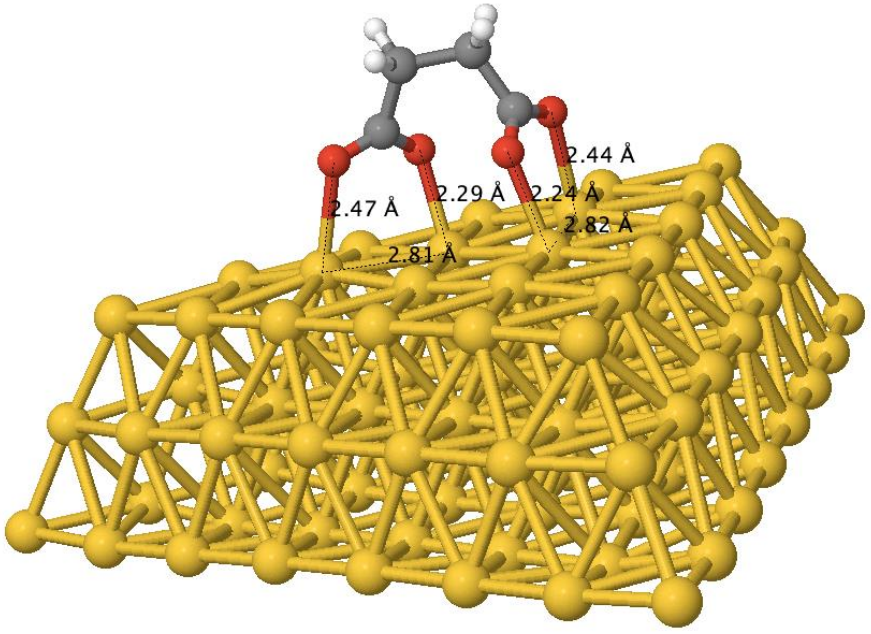

Figure 5h. Optimized geometry of one μ_4 coordinated succinate in the "skewed" conformation on an Au(111) model surface. A schematic of this motif can be found in Figure 3d.

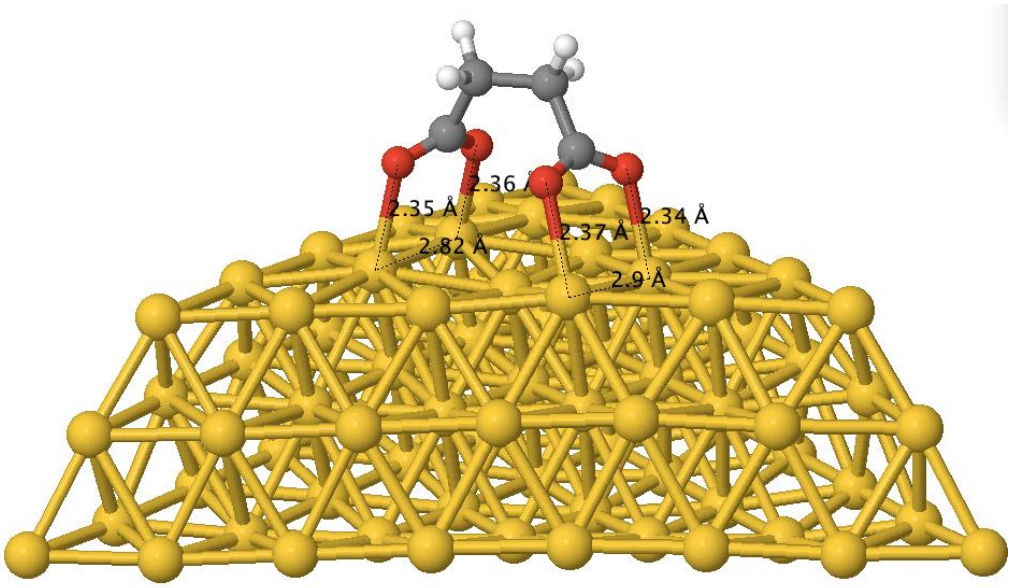

Figure 5i. Optimized geometry of one μ_4 coordinated succinate in the "stacked" conformation on an Au(111) model surface. A schematic of this motif can be found in Figure 3d.

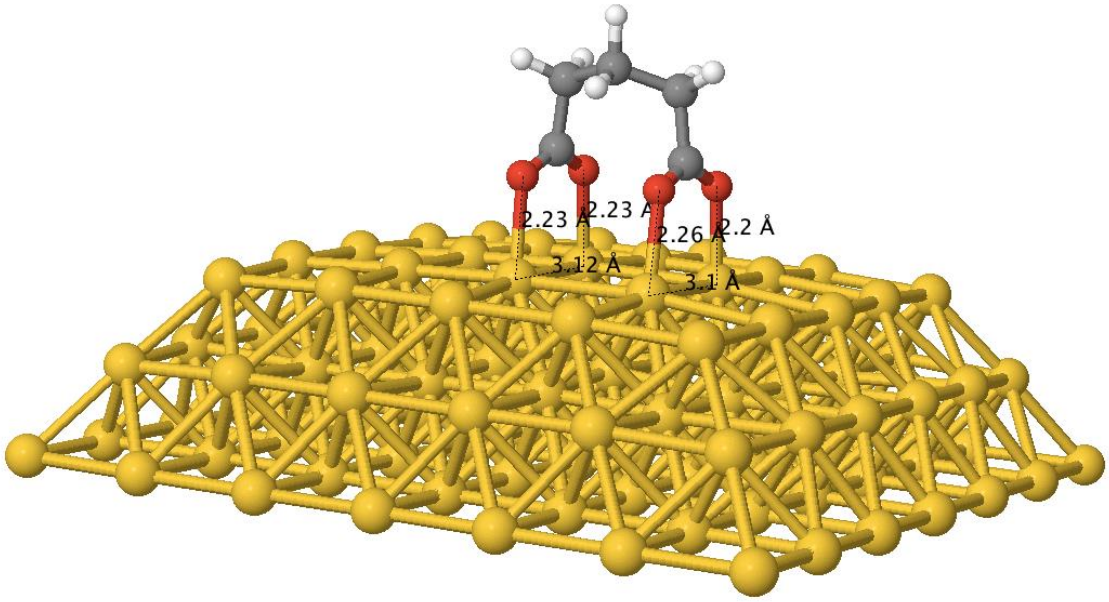

Figure 5j. Optimized geometry of one μ_4 coordinated glutarate in the "stacked" conformation on an Au(100) model surface. A schematic of this motif can be found in Figure 3d.

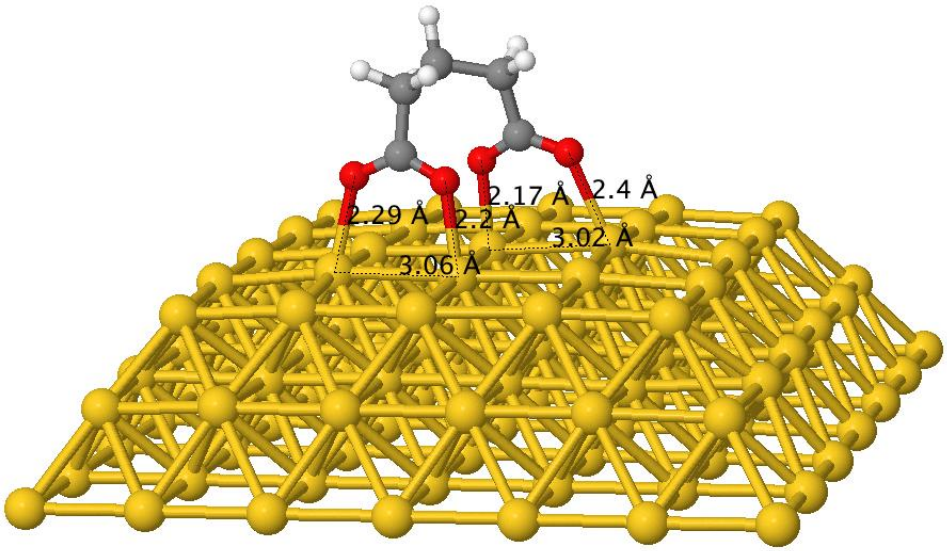

Figure 5k. Optimized geometry of one μ_4 coordinated glutarate in the "parallel displaced" conformation on an Au(100) model surface. A schematic of this motif can be found in Figure 3d.

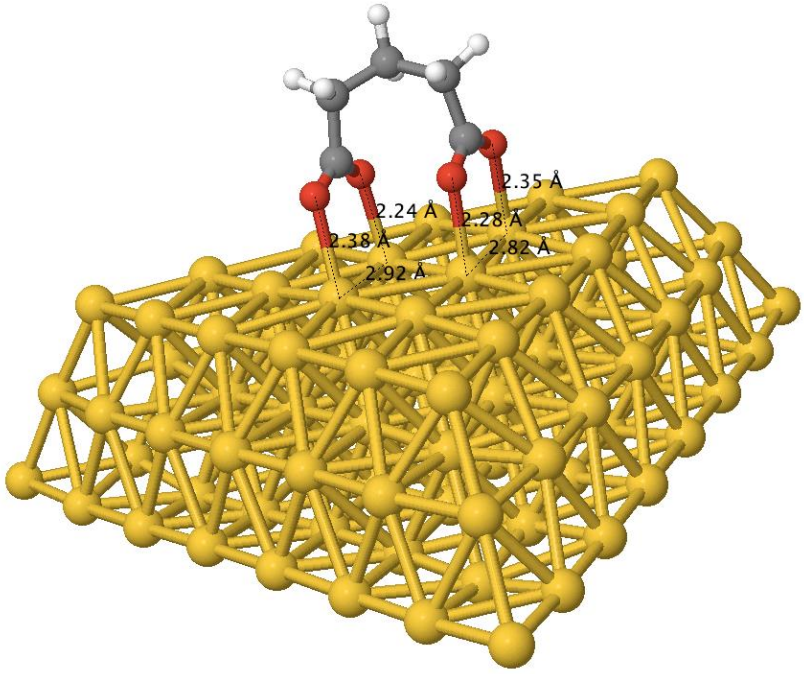

Figure 5l. Optimized geometry of one μ_4 coordinated glutarate in the "parallel displaced" conformation on an Au(111) model surface. A schematic of this motif can be found in Figure 3d.

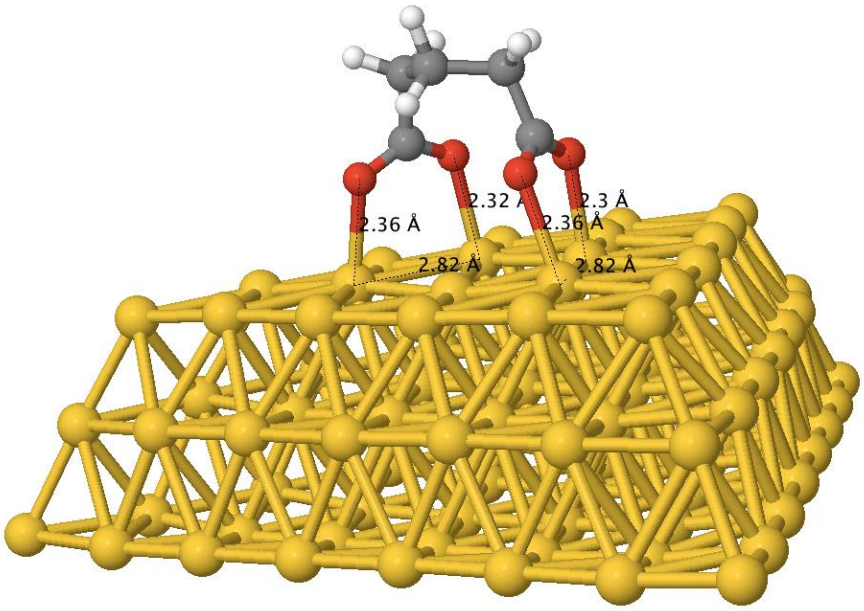

Figure 5m. Optimized geometry of one μ_4 coordinated glutarate in the "bent" conformation on an Au(111) model surface. A schematic of this motif can be found in Figure 3d.

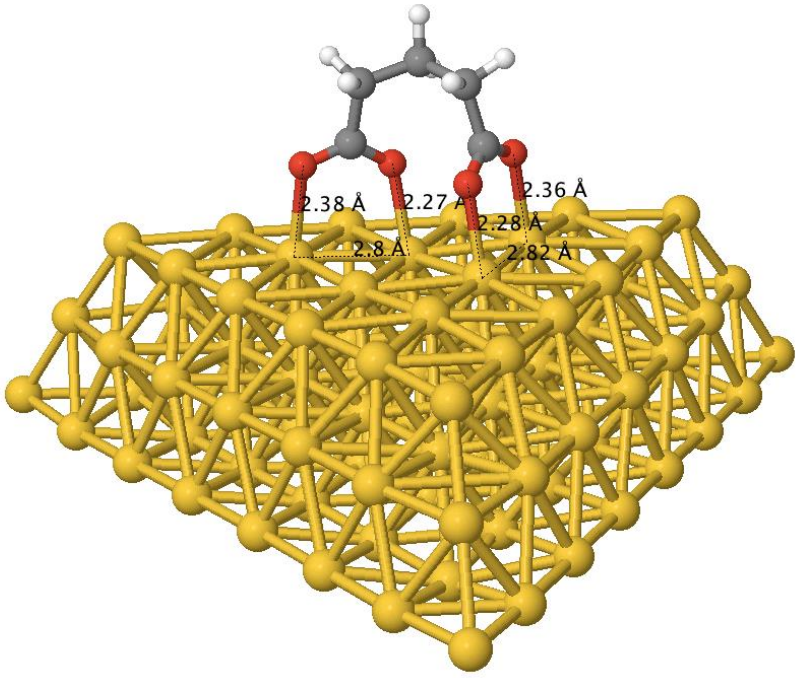

Figure 5n. Optimized geometry of one μ_4 coordinated glutarate in the "skewed" conformation on an Au(111) model surface. A schematic of this motif can be found in Figure 3d.

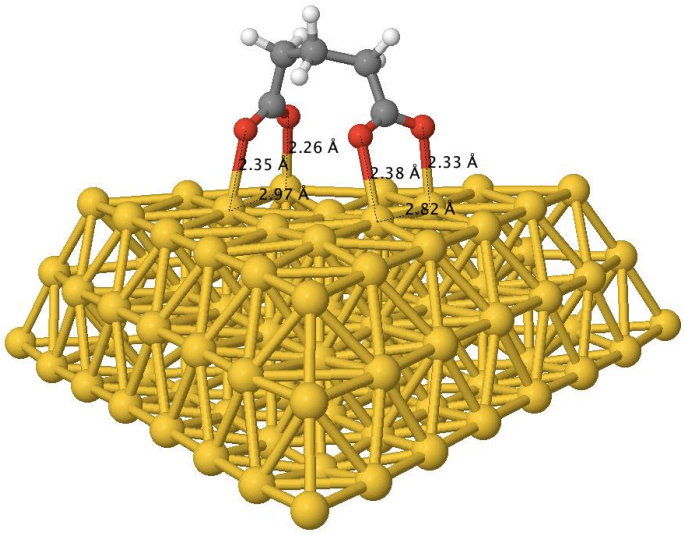

Figure 5o. Optimized geometry of one glutarate in the "stacked" conformation on an Au(111) model surface. A schematic of this motif can be found in Figure 3d.

Table 4. Total bonding energy, relative to spherical spin-restricted atoms, of carboxylates to large non-fixed nanoclusters[a]

System	Bond Energy (*in vacuo*) / kcal mol^{-1}	Bond Energy (water) / kcal mol^{-1}
Au(100) surface model	−7499.5	−7495.5
Au(111) surface model	−5761.3	−5759.2
acetate	−1008.6	−1077.2
succinate	−1787.1	−1980.8
glutarate	−2173.2	−2360.2
μ_2-acetate / Au(100)	−8588.1	−8603.2
κ-acetate / Au(100)	−8579.4	−8592.1
μ_4-succinate (stacked) / Au(100)	−9455.2	−9522.3
μ_4-succinate (parallel displaced) / Au(100)	−9457.9	−9525.2
μ_4-glutarate (stacked) / Au(100)	−9843.2	−9909.9
μ_4-glutarate (parallel displaced) / Au(100)	−9843.9	−9910.8
μ_2-acetate / Au(111)	−6840.3	−6853.5
μ_4-succinate (stacked) / Au(111)	−7702.1	−7769.1
μ_4-glutarate (stacked) / Au(111)	−8085.6	−8151.6

μ_4-succinate (parallel displaced) / Au(111)	−7698.0	−7764.3
μ_4-glutarate (parallel displaced) / Au(111)	−8085.6	−8151.0
μ_4-succinate (bent) / Au(111)	−7699.0	−7766.8
μ_4-glutarate (bent) / Au(111)	−8082.4	−8149.0
μ_4-succinate (skewed) / Au(111)	−7695.9	−7762.5
μ_4-glutarate (skewed) / Au(111)	−8083.4	−8148.8

[a] This is the standard approach for calculating energy in ADF. The 3D structures of the various geometries can be found in Figure 5(a-o).

We additionally tested to see if there was any enthalpic preference for acetate anions to bind at the edges of the Au surface models, as compared to the central regions of the surface (Figure 6(a-c). These binding energy calculations were performed on selected systems. When considering the individual binding energies of the four acetate anions depicted on the Au(111) surface in Figure 3c of the main manuscript, it is found that the 1κ*O*[1] motif occurred only near the surface edges, with the bridging (μ_2) motif occurring in the central regions of the facet. However, the μ_2 motif was also observed to occur at the edges, and additionally, the water-solvated edge acetate anion binding in the μ_2 motif (III in Fig. 3c) was calculated to be 26.4 kcal mol^{-1}, which is about 9 kcal mol^{-1} greater than corresponding binding energies for the other acetate ligands on the Au(111) surface.

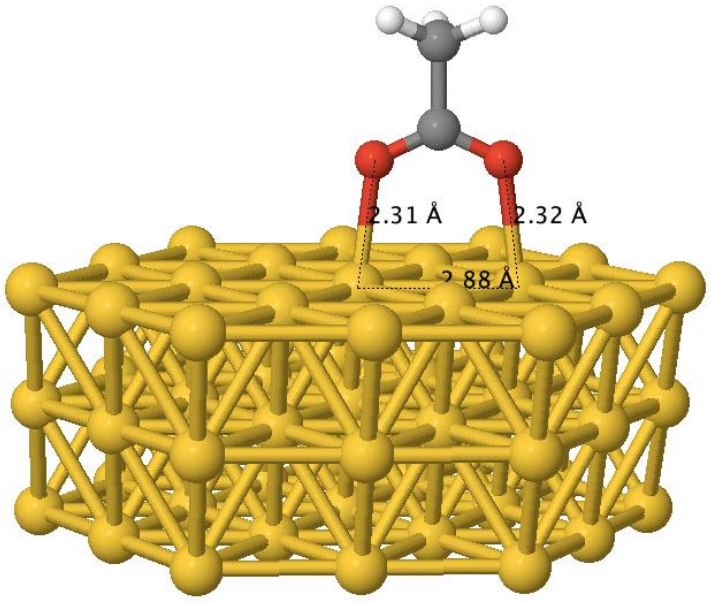

Figure 5a. Optimized geometry of one acetate on a relatively small fixed Au(111) model surface.

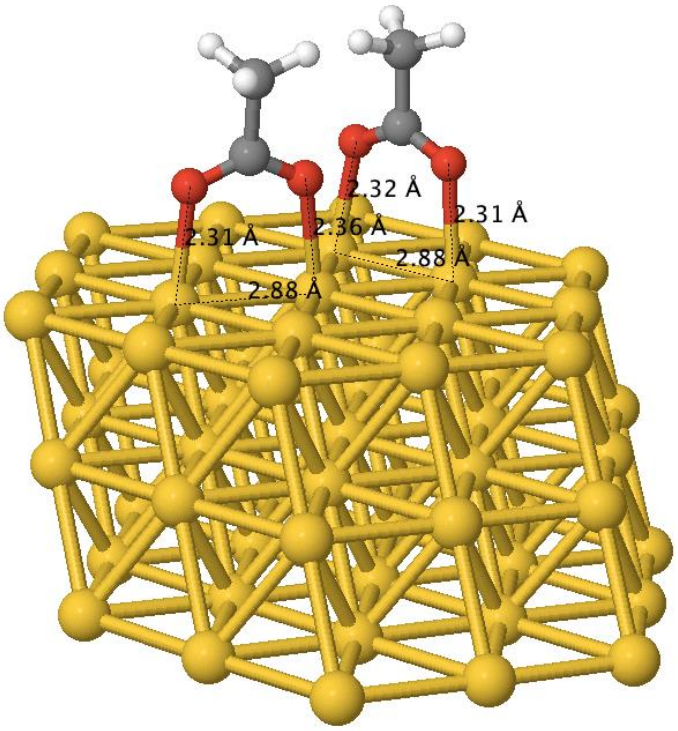

Figure 5b. Optimized geometry of two acetates on a relatively small fixed Au(111) model surface.

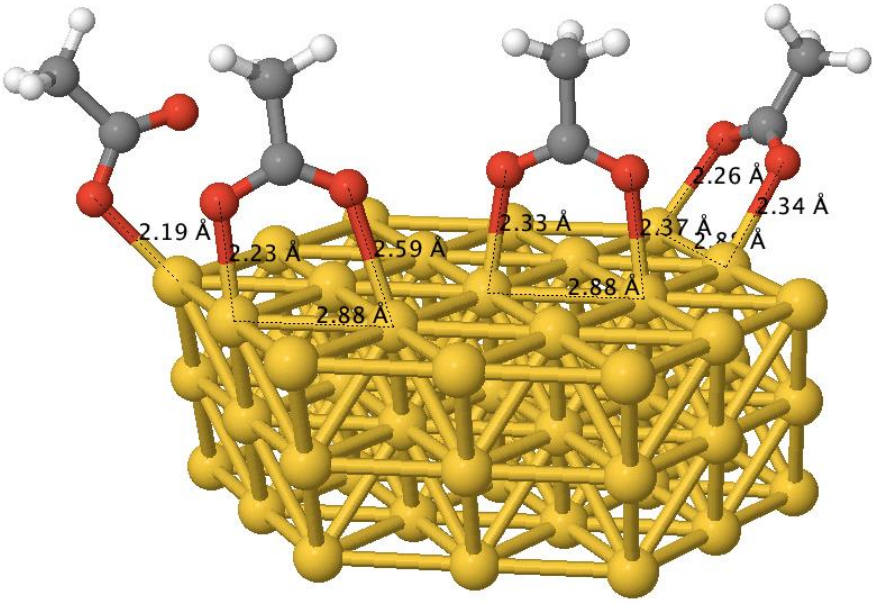

Figure 5c. Optimized geometry of four acetates on a relatively small fixed Au(111) model surface, as also depicted in Figure 3c.

Magnetic shielding calculations for water-solvated ligands on large non-fixed nanoclusters. Magnetic shielding values were calculated with the NMR module of the ADF package using the same computational protocol adopted for the calculation of the binding energies in water. The magnetic shielding was calculated for the carboxylate carbon of the acetate coordinated on the Au(100) surface of the large nanoclusters of Figures S20a and S20b, as representative cases of the κ and μ_2 coordination modes of the carboxylates. As the representative case of the μ_4-mode, we calculated the magnetic shielding of the two carboxylate carbon atoms of succinate coordinated in the stacked and in the parallel-displaced geometries, as in Figures S20d and 20e. The resulting four magnetic shieldings were averaged to a single magnetic shielding value. These shieldings were compared to the magnetic shielding of the carboxylate carbon of water-solvated free acetate. All the calculated shieldings are reported in Table 5.

Table 5. Calculated ^{13}C isotropic magnetic shielding (σ_{iso}) and isotropic chemical shift (δ_{iso}) values[a]

System	$\sigma_{iso}(^{13}C)$ / ppm	$\delta_{iso}(^{13}C)$ / ppm
free acetate	−1.2	0.0
κ-acetate	6.3	−7.5
μ_2-acetate	10.9	−12.1
μ_4-succinate (stacked), carboxylate 1	6.0	−7.2
μ_4-succinate (stacked), carboxylate 2	7.0	−8.2
μ_4-succinate (parallel-displaced), carboxylate 1	7.5	−8.7
μ_4-succinate (parallel-displaced), carboxylate 2	10.3	−11.5
average of succinate carboxylate values	7.7	−8.9
standard deviation of succinate carboxylate values	2.1	−2.1

[a] All bound ligand calculations used the Au(100) surface model as the support. Chemical shifts of bound ligands were calculated as follows: $\delta_{iso} = \sigma_{iso}$(Au/carboxylate) − σ_{iso}(acetate). All calculations included solvent (water) using COSMO.

Magnetic shielding calculations of molecular systems in vacuo using ADF. To better understand the origin of the observed ^{13}C chemical shift changes and the above magnetic shielding calculations as functions of key carboxylate structural parameters, we used model molecular systems to probe the sensitivity of the ^{13}C magnetic shielding with respect to local geometry changes in a carboxylate group. Essentially all computational parameters remain as before, except that effects due to the spin-orbit mechanism were included, as we were interested in seeing the importance of this mechanism upon the calculated ^{13}C isotropic magnetic shielding values when a carboxylate is near an Au atom.[186]

Magnetic shielding calculations using periodic quantum chemistry software. Magnetic shielding calculations involving periodic crystal structures as input used CASTEP (v.5.5).[187] Input files were generated using Materials Studio (v.3.2.0.0), and ultrasoft pseduopotentials[113a] were used to describe the core electrons, while planewaves described

the valence electrons. As in the above calculations using ADF, the PBE GGA XC functional was employed. Dispersion effects were included using the approach outlined by Tkatchenko and Scheffler (TS),[188] which has often been applied for crystalline organic systems. The planewave basis set energy cutoff was set as 700 eV and the *k*-point spacing was set at 0.05 $Å^{-1}$ in reciprocal space. Crystal structures were taken from a variety of literature sources, as disclosed later in the Supporting Information. Importantly, for all crystalline systems, optimization of the hydrogen positions was performed before calculating the magnetic shielding values.

In water continuum solvent, binding to the Au(100) facet is favored by roughly 20 kcal/mol over binding to the Au(111) facet both for Sc and Gt. The larger E_{Bind} of the carboxylates to the Au(100) facet can be related to the lower coordination number of the Au atoms on the (100) facet, 8, relative to the coordination number on the (111) facet, 9. Further, the geometry of the Au(100) facet, with square planar coordinated Au atoms, allows for a greater flexibility of the surface atoms, relative to Au atoms on the (111) surface, with hexa-coordinated Au atoms. Indeed, in the (100) geometries, the distance between the Au atoms involved in binding of the two carboxylates can stretch up to 3.2 Å, from a value of 2.9 Å for a uncoordinated Au(100) surface. In contrast, on the Au(111) surface the distance between the Au atoms involved in binding is only increased to values of around 3.0 Å (appendices).

The conformational strain energy, E_{Strain}, was determined to be low indicating by comparing the best binding energy of Sc or Gt with the binding energy of two isolated Ac molecules, for example, $\Delta E_{Strain}(Sc) = E_{Bind}(Sc) - 2E_{Bind}(Ac)$. If no strain or cooperative effect is in place, according to our definition E_{Strain} should be equal to zero. The calculated ΔE_{Strain} for Sc on the Au(100) facet, around 15 kcal/mol, indicates some strain in the coordination of Sc, which is reduced to 6-7 kcal/mol with the more flexible 3 methylene spacer of Gt. Similar behaviour is found for Sc and Gt when coordinating to the Au(111) facet, although a slightly lower ΔE_{Strain} of around 5-12 kcal/mol is calculated. The lower ΔE_{Strain} of Gt accounts for the stronger predicted binding of Gt to the Au facets. This allows us to tentatively arrive at the conclusion that one possible binding motif for the citrate would occur preferentially using both terminal carboxylates, rather than one terminal and the central carboxylate.

We additionally tested to see if there was any enthalpic preference for Ac anions to bind at the edges of the Au surface models, as compared to the central regions of the surface. These binding energy calculations were performed on selected systems. When considering the individual binding energies of the four acetate anions depicted on the Au(111) surface in Figure 3c of the main manuscript, it is found that the $1\kappa O^1$ motif occurred only near the surface edges, with the bridging (μ_2) motif occurring in the central regions of the facet. However, the μ_2 motif was also observed to occur at the edges, and additionally, the edge acetate anion binding in the μ_2 motif (III in Fig. 3c) was calculated to be 26.4 kcal/mol, which is about 9 kcal/mol greater than corresponding binding energies for the other acetate ligands on the Au(111) surface.

Calculations of Magnetic Shielding Using ADF Software. Using model molecular systems to probe the sensitivity of the ^{13}C magnetic shielding with respect to local geometry changes in a carboxylate group (more completely described in subsequent sections of the appendices), essentially all computational parameters remain as before, except that for magnetic shielding calculations, effects due to the spin-orbit mechanism were included.[186] We note specifically that ^{13}C chemical shift calculations are not possible using the AuNP-containing model systems described in the main manuscript with the computational codes available to us, due to the partial metallic character of the AuNP surface. Hence, to comment upon whether the observed ^{13}C NMR chemical shifts in the range of 162 to 168 ppm are consistent with an Au-O interaction, we chose to look both at rather highly idealized model systems using molecular modelling software, as well as taking crystal structures from the literature where these types of interactions are present (modelled using periodic quantum chemical software, as described directly below.

Calculations Using Periodic Quantum Chemistry Software. Magnetic shielding calculations involving periodic crystal structures as input used the CASTEP software (version 5.5).[187] Input files were generated using Materials Studio (v.3.2.0.0), and ultrasoft pseduopotentials[113a] were used to describe the core electrons, while planewaves described the valence electrons. As in the above calculations using the ADF computational code, the PBE GGA XC functional was employed. Dispersion effects were included using the approach outlined by Tkatchenko and Scheffler (TS),[188] which has often been applied for crystalline organic systems. The planewave basis set energy cutoff was set as 700 eV and the *k*-point spacing was set at 0.05 $Å^{-1}$ in reciprocal space. Crystal

structures were taken from a variety of literature sources, as disclosed later in the appendices. Importantly, for all crystalline systems, optimization of the hydrogen positions was performed before calculating the magnetic shielding values.

Single crystal X-ray crystallography - crystal structure data

CCDC number 1472104 contains the supplementary crystallographic data for this paper, which can be obtained free of charge from The CCDC via www.ccdc.cam.ac.uk/data_request/cif. X-ray diffraction experiments on the crystals obtained from the bottle which was marked as 'sodium citrate dihydrate' were carried out at 170 K on an Agilent CrysAlis PRO diffractometer diffractometer using Mo-Kα radiation (λ = 0.71073 Å). The computational cell refinement, data reduction and absorption correction were processed using Agilent CrysAlis PRO software (CrysAlis PRO, Agilent Technologies, Version 1.171.37.31; cell refinement: CrysAlis PRO, Agilent Technologies, Version 1.171.37.31; data reduction: CrysAlis PRO, Agilent Technologies, Version 1.171.37.31). The structure was solved using Superflip,189 and refined against F^2 in Crystals software.[190] All hydrogen atoms were located geometrically and refined using a riding model. Crystal structure and refinement data are given in **Table 6**.

Table 6. Relevant crystal structure data for bis(trisodium citrate) undecahydrate

Empirical formula	$C_{12}H_{32}Na_6O_{25}$
Formula weight	714.31
Temperature / K	170
Crystal system	orthorhombic

Space group	P b n m
a / Å	6.41860 (12)
b / Å	16.4125 (3)
c / Å	26.2968 (4)
Volume / Å^3	2770.24 (5)
Z	4
ρ_{calc} (g/cm^3)	1.713
μ / mm^{-1}	0.241
F(000)	1480.0
Crystal size / mm	0.1 × 0.1 × 0.1
Radiation	MoKα (λ = 0.71073 Å)
Index Ranges	$-8 \leq h \leq 8$, $-21 \leq k \leq 21$, $-36 \leq l \leq 36$.
2Θ range for data collection / °	3.401 to 29.772
Reflections collected	47401
Unique reflections	3811
R_{int}	0.032
Parameters Refined	239
R_1, wR_2 [I > 2 σ(I)]	0.0264, 0.0667
R_1, wR_2 [all data]	0.0308, 0.0708
Goodness-of-fit on F^2	0.9461
δp_{max}, δp_{min} / e nm^{-3}	0.47, −0.37

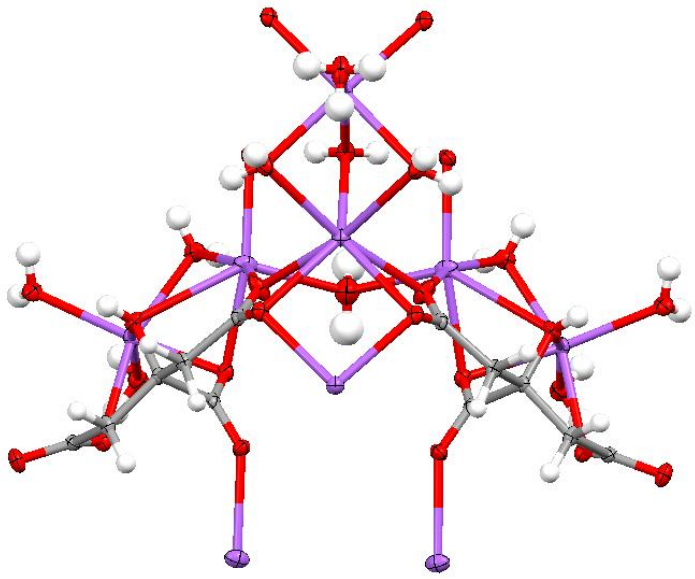

Figure 6. Structure of bis(trisodium citrate) undecahydrate where the oxygen, sodium, carbon and hydrogen atoms are presented in red, purple, grey and white, respectively. Thermal ellipsoids are drawn at 50 % probability.

Appendix 2. XYZ coordinates for free and adsorbed carboxylates on large non-fixed Au(100) and Au(111) nanoclusters

---

--

C2H3O2

C 8.575857 9.701839 11.376778
C 8.593557 9.624426 9.823724
H 8.428308 8.702574 11.815467
H 7.721596 10.328083 11.684599
H 9.497686 10.161989 11.763599
O 9.375745 10.424027 9.226483
O 7.798850 8.783861 9.301752

--

C4H4O4

C 8.537489 11.127948 12.906740
C 7.082281 11.668352 12.691149
C 9.655969 12.187935 12.906751
C 11.110415 11.647471 12.691134
H 8.765408 10.438992 12.079938
H 8.539498 10.526266 13.824526
H 9.428205 12.876642 12.079748
H 9.653844 12.789595 13.824502
O 6.149141 11.020557 13.273115
O 6.915192 12.677125 11.935524
O 12.044734 12.294759 13.273054
O 11.277823 10.638156 11.935315

--

C5H6O4

C 9.515799 11.517072 11.714693
C 11.024858 11.370646 11.359122
C 8.566725 10.555536 10.989082
C 7.181793 10.359560 11.629789
C 6.053421 11.364305 11.254077
H 9.228487 12.569331 11.563984
H 9.456166 11.337124 12.805605
H 6.781754 9.375184 11.325054
H 7.246853 10.322792 12.731133
H 9.090199 9.588734 10.917618
H 8.407414 10.907851 9.956571
O 11.441836 10.238298 10.957965
O 11.751653 12.399967 11.547489
O 5.091250 11.447619 12.084285
O 6.134391 11.967180 10.141781

--

C6H5O7

C 9.056076 9.109221 8.756882

C 7.464369
6.983223 8.836959
C 6.957554
6.493956 7.451663
C 8.844990
7.582764 9.155663
C 10.077480
6.673368 8.858351
C 10.541456
6.129452 7.477769
H 6.721212
7.734153 9.156906
H 10.931344
7.249242 9.254871
H 9.932811
5.792570 9.505013
H 9.456826
8.452496 10.727949
H 7.334070
6.123116 9.512064
O 8.317776
9.653775 7.904513
O 9.959438
9.678515 9.478800
O 7.407300
6.968593 6.373289
O 6.003796
5.638998 7.523085
O 10.411140
4.871882 7.293974
O 11.141380
6.916543 6.685320
O 8.848382
7.670230 10.638283

--

Au100-nanocluster

Au 24.654600
6.614100 4.233399
Au 21.771000
6.602700 4.248600
Au 18.887100
6.591300 4.263999
Au 24.643497
9.497400 4.270999
Au 16.003500
6.580200 4.279200
Au 21.759901
9.486300 4.286400
Au 13.119900
6.568800 4.294400
Au 18.875999
9.474899 4.301600
Au 24.632401
12.381000 4.308800
Au 10.236000
6.557400 4.309800
Au 15.992399
9.463500 4.317000
Au 21.748800
12.369599 4.324000
Au 7.352400
6.546300 4.325000
Au 13.108800
9.452399 4.332200
Au 18.864901
12.358499 4.339400
Au 24.621300
15.264600 4.346600
Au 10.224900
9.441000 4.347400
Au 15.981300
12.347100 4.354600
Au 21.737700
15.253201 4.361800
Au 7.341300
9.429600 4.362800
Au 13.097699
12.335700 4.370000
Au 18.854099
15.242100 4.377000
Au 24.610199
18.148199 4.384201
Au 10.213800
12.324600 4.385200
Au 15.970200
15.230700 4.392400
Au 21.726599
18.136801 4.399600
Au 7.330200
12.313200 4.400400

Au 13.086599
15.219299 4.407600
Au 18.842999
18.125399 4.414801
Au 24.599100
21.031500 4.421999
Au 10.202701
15.208200 4.422801
Au 15.959101
18.114300 4.429999
Au 21.715500
21.020401 4.437200
Au 7.319100
15.196801 4.438200
Au 13.075500
18.102900 4.445400
Au 18.831900
21.008999 4.452600
Au 24.587999
23.915100 4.459800
Au 10.191601
18.091499 4.460599
Au 15.948000
20.997601 4.467800
Au 21.704399
23.903700 4.475000
Au 7.308000
18.080400 4.475800
Au 13.064400
20.986500 4.483000
Au 18.820799
23.892599 4.490200
Au 10.180500
20.975100 4.498400
Au 15.936899
23.881201 4.505600
Au 7.296900
20.963701 4.513600
Au 13.053300
23.869801 4.520800
Au 10.169399
23.858700 4.536000
Au 7.285800
23.847300 4.551400
Au 23.223984
8.018122 6.245224
Au 20.310766
7.807239 6.379106
Au 17.445431
7.833558 6.406558
Au 23.409517
10.931992 6.402833
Au 14.575601
7.822713 6.421996
Au 20.317717
10.901349 6.311934
Au 11.710632
7.776031 6.423161
Au 17.437189
10.885787 6.397212
Au 23.363049
13.796537 6.452411
Au 8.793541
7.961915 6.322016
Au 14.558558
10.874997 6.412686
Au 20.310970
13.781713 6.418818
Au 11.676607
10.866326 6.357759
Au 17.425003
13.769599 6.510005
Au 23.352934
16.666527 6.489796
Au 8.586750
10.873370 6.481549
Au 14.549529
13.759627 6.526107
Au 20.299278
16.660095 6.457509
Au 11.663295
13.747692 6.465714
Au 17.413424
16.645020 6.547394
Au 23.377483
19.530930 6.516060
Au 8.612137
13.738366 6.530582
Au 14.537986
16.634075 6.563415
Au 20.285624
19.541767 6.425450

Au 11.651901
16.625837 6.502513
Au 17.404076
19.531946 6.509706
Au 23.167835
22.445354 6.434104
Au 8.597151
16.608688 6.569618
Au 14.525213
19.520302 6.525037
Au 20.253153
22.630775 6.573171
Au 11.644448
19.507942 6.471711
Au 17.388588
22.584902 6.599530
Au 8.553801
19.473129 6.593850
Au 14.517957
22.573690 6.614421
Au 11.653048
22.597561 6.618548
Au 8.738854
22.390829 6.511411
Au 21.760777
9.454720 8.168185
Au 18.890720
9.403421 8.337931
Au 16.013744
9.392041 8.384069
Au 21.789347
12.323956 8.360295
Au 13.137572
9.381601 8.369205
Au 18.885323
12.308132 8.559453
Au 10.266343
9.410411 8.230453
Au 16.006847
12.278487 8.607161
Au 21.777727
15.199727 8.428041
Au 13.125981
12.286326 8.589625
Au 18.890722
15.186604 8.629008
Au 10.218546
12.278248 8.422969
Au 15.993845
15.174000 8.671982
Au 21.767653
18.076197 8.436541
Au 13.096111
15.164432 8.660675
Au 18.860168
18.066607 8.632976
Au 10.205094
15.154741 8.489391
Au 15.980295
18.069925 8.683430
Au 21.716097
20.948730 8.320543
Au 13.100967
18.043478 8.665670
Au 18.845955
20.975760 8.489521
Au 10.193001
18.030577 8.498002
Au 15.969325
20.962059 8.533300
Au 13.094349
20.952763 8.519892
Au 10.222319
20.903175 8.380433

-
Au111-nanocluster
Au 15.364500
24.866400 5.919250
Au 13.929600
22.365002 5.924250
Au 12.494699
19.863600 5.929001
Au 11.059800
17.362200 5.934000
Au 16.813501
22.373100 5.936501
Au 9.624600
14.860800 5.938999
Au 15.378301
19.871700 5.941249

Au 8.189699
12.359400 5.944000
Au 13.943400
17.370300 5.946250
Au 6.754800
9.858000 5.948750
Au 12.508500
14.868900 5.951250
Au 18.262199
19.879801 5.953500
Au 5.319900
7.356600 5.953750
Au 11.073600
12.367500 5.956250
Au 16.827299
17.378099 5.958500
Au 9.638400
9.866100 5.960999
Au 15.392099
14.876699 5.963500
Au 8.203500
7.364700 5.966000
Au 13.957200
12.375300 5.968501
Au 19.710899
17.386200 5.970749
Au 12.522300
9.873899 5.973500
Au 18.276001
14.884800 5.975750
Au 11.087400
7.372500 5.978251
Au 16.841101
12.383400 5.980750
Au 15.405901
9.882000 5.985750
Au 21.159599
14.892900 5.988000
Au 13.971000
7.380600 5.990499
Au 19.724701
12.391500 5.993000
Au 18.289801
9.890100 5.998001
Au 16.854900
7.388700 6.002749
Au 22.608601
12.399600 6.005250
Au 21.173401
9.898200 6.010249
Au 19.738499
7.396800 6.015000
Au 24.057299
9.905999 6.022500
Au 22.622400
7.404600 6.027500
Au 25.506001
7.412700 6.039751
Au 15.359336
23.087925 8.229706
Au 13.647285
20.743196 8.293743
Au 12.232070
18.299946 8.364321
Au 10.800316
15.853724 8.371512
Au 17.084545
20.752756 8.308323
Au 9.412016
13.382480 8.373937
Au 15.373217
18.178562 8.274549
Au 8.017109
10.926956 8.312985
Au 13.924243
15.699676 8.371325
Au 6.856812
8.265612 8.258944
Au 12.510508
13.234909 8.376179
Au 18.512657
18.317244 8.390961
Au 11.101809
10.732320 8.289368
Au 16.834753
15.707470 8.383589
Au 9.743547
7.955705 8.333543
Au 15.386147
13.223269 8.491729
Au 13.972929
10.718268 8.393473

Au 19.957935
15.879201 8.410721
Au 12.567269
7.951793 8.411674
Au 18.262341
13.250801 8.400719
Au 16.814436
10.726034 8.405438
Au 15.401381
7.934943 8.426373
Au 21.360199
13.416232 8.425007
Au 19.685951
10.756233 8.326212
Au 18.235157
7.968068 8.435839
Au 22.768778
10.968270 8.375463
Au 21.059052
7.988147 8.381681
Au 23.944630
8.312585 8.331544
Au 15.355200
21.338753 10.375483
Au 13.902929
18.938869 10.564735
Au 12.450755
16.525301 10.616735
Au 11.057726
14.096361 10.621601
Au 16.819525
18.947102 10.576965
Au 9.706832
11.624147 10.579285
Au 15.366536
16.504023 10.889181
Au 8.368375
9.158138 10.399700
Au 13.933073
14.061468 10.962210
Au 12.548178
11.590714 10.898740
Au 18.284323
16.541359 10.641465
Au 11.172502
9.102476 10.596196
Au 16.813314
14.069613 10.974674
Au 15.380164
11.571481 10.979532
Au 13.988907
9.052618 10.656230
Au 19.691126
14.120337 10.658516
Au 18.212429
11.606522 10.922985
Au 16.788893
9.060494 10.668260
Au 21.056194
11.656130 10.627720
Au 19.605433
9.126163 10.632760
Au 22.410898
9.197872 10.459473

--
Au100-C2H3O2(μ2)
Au 5.695200
23.122200 4.324000
Au 8.579100
23.139299 4.332000
Au 5.712301
20.238600 4.336600
Au 11.462699
23.156399 4.340000
Au 8.596199
20.255699 4.344600
Au 14.346600
23.173500 4.347800
Au 5.729401
17.354700 4.349200
Au 11.479799
20.272799 4.352400
Au 17.230200
23.190601 4.355800
Au 8.613299
17.371801 4.357200
Au 14.363400
20.289900 4.360400
Au 5.746500
14.471100 4.361800

Au 20.113800
23.207701 4.363800
Au 11.496900
17.388901 4.365000
Au 17.247301
20.307001 4.368400
Au 8.630100
14.488199 4.369600
Au 22.997700
23.224800 4.371600
Au 14.380499
17.406000 4.373000
Au 5.763600
11.587200 4.374400
Au 20.130901
20.324100 4.376200
Au 11.514001
14.505300 4.377600
Au 17.264400
17.423100 4.381000
Au 8.647201
11.604600 4.382200
Au 23.014799
20.341202 4.384200
Au 14.397601
14.522400 4.385600
Au 5.780701
8.703600 4.386800
Au 20.147999
17.440201 4.388800
Au 11.531101
11.621699 4.390200
Au 17.281502
14.539499 4.393400
Au 8.664301
8.720700 4.394800
Au 23.031900
17.457602 4.396800
Au 14.414701
11.638800 4.398200
Au 5.797801
5.820000 4.399400
Au 20.165102
14.556600 4.401400
Au 11.548201
8.737801 4.402800
Au 17.298599
11.655900 4.406000
Au 8.681400
5.837100 4.407400
Au 23.049000
14.573700 4.409400
Au 14.431801
8.754900 4.410600
Au 20.182199
11.672999 4.414000
Au 11.565301
5.854200 4.415400
Au 17.315701
8.772000 4.418600
Au 23.066099
11.690101 4.421800
Au 14.448901
5.871300 4.423200
Au 20.199301
8.789100 4.426600
Au 17.332800
5.888400 4.431200
Au 23.083200
8.806200 4.434400
Au 20.216400
5.905500 4.439000
Au 23.099998
5.922600 4.447000
Au 7.132452
21.709036 6.324765
Au 10.042166
21.938923 6.446306
Au 6.941110
18.801889 6.453209
Au 12.912477
21.938152 6.466405
Au 10.037936
18.827288 6.341888
Au 15.789268
21.936792 6.473169
Au 6.969454
15.939068 6.461643
Au 12.927551
18.858166 6.413256
Au 18.652328
21.970253 6.469709

Au 10.081310
15.928851 6.458690
Au 15.813376
18.866974 6.425034
Au 6.982785
13.038352 6.475287
Au 21.566273
21.792021 6.365456
Au 12.949628
15.948644 6.554139
Au 18.689882
18.875984 6.376476
Au 10.097586
13.083497 6.469950
Au 15.808212
15.964263 6.542623
Au 6.988557
10.174089 6.491077
Au 21.783661
18.881113 6.490618
Au 12.965937
13.097315 6.565789
Au 18.715548
15.998883 6.450191
Au 10.087843
10.183914 6.378757
Au 15.826362
13.113052 6.553445
Au 7.216805
7.266756 6.387628
Au 21.788603
16.015902 6.515149
Au 12.980103
10.185575 6.451113
Au 18.730873
13.112943 6.462796
Au 10.128251
7.074096 6.509266
Au 15.865754
10.209676 6.463646
Au 21.802757
13.134348 6.526991
Au 13.001678
7.105576 6.529682
Au 18.741562
10.234571 6.415417

Au 15.880222
7.143354 6.535069
Au 21.834787
10.269425 6.530416
Au 18.742411
7.142390 6.536133
Au 21.651882
7.356610 6.428717
Au 8.615896
20.257746 8.222999
Au 11.480289
20.364422 8.370280
Au 8.554348
17.383848 8.365765
Au 14.352970
20.380856 8.409174
Au 11.474070
17.484907 8.539592
Au 17.224129
20.350815 8.400797
Au 8.481783
14.505080 8.391441
Au 14.369342
17.526503 8.596329
Au 20.100170
20.319643 8.258466
Au 11.383943
14.520421 8.655337
Au 17.257759
17.442513 8.573061
Au 8.585616
11.629636 8.387244
Au 14.480570
14.539440 8.659228
Au 20.173254
17.448608 8.416416
Au 11.509879
11.558195 8.564219
Au 17.400440
14.558019 8.633487
Au 8.680877
8.755783 8.271209
Au 14.406425
11.550464 8.618378
Au 20.248962
14.575169 8.449330

Au 11.548594
8.678831 8.417340
Au 17.293024
11.669884 8.600651
Au 14.422618
8.693363 8.458353
Au 20.204746
11.699183 8.441675
Au 17.295029
8.760232 8.452209
Au 20.170286
8.826433 8.312477
C 12.972265
14.542383 11.405607
C 13.006810
14.580909 12.921722
H 13.546444
15.483713 13.237691
H 13.572975
13.715405 13.289177
H 11.996105
14.579671 13.339147
O 11.824093
14.532619 10.855456
O 14.118484
14.528274 10.844454

--
Au100-C2H3O2(κ)
Au 24.083815
7.183355 4.073390
Au 21.393997
6.947818 4.270513
Au 18.710493
6.892210 4.381469
Au 24.302999
9.873057 4.287172
Au 16.001654
6.918136 4.397943
Au 21.516230
9.734393 3.926653
Au 13.293409
6.873647 4.412479
Au 18.764179
9.671153 4.075094
Au 24.320101
12.557334 4.411855
Au 10.609394
6.897524 4.341212
Au 15.991232
9.678635 4.150521
Au 21.545383
12.487581 4.087920
Au 7.918235
7.118912 4.163085
Au 13.219101
9.653203 4.104722
Au 18.762135
12.459557 4.148967
Au 24.272289
15.264355 4.453456
Au 10.466683
9.685910 3.990209
Au 15.982250
12.460288 4.139480
Au 21.512177
15.256893 4.192396
Au 7.682109
9.806618 4.376413
Au 13.204816
12.442313 4.199109
Au 18.737038
15.243482 4.152357
Au 24.295763
17.972233 4.480215
Au 10.421097
12.439060 4.144030
Au 15.966280
15.234679 4.163465
Au 21.520506
18.026939 4.154748
Au 7.645924
12.490161 4.496888
Au 13.197765
15.220424 4.198861
Au 18.737761
18.025414 4.203505
Au 24.258026
20.660269 4.424362
Au 10.422571
15.208517 4.250775

Au 15.957100
18.003119 4.205713
Au 21.472031
20.786024 4.064259
Au 7.665491
15.198105 4.535646
Au 13.176989
17.998514 4.243821
Au 18.714823
20.809895 4.198328
Au 24.029024
23.356661 4.287627
Au 10.395097
17.979767 4.206250
Au 15.945439
20.778086 4.283344
Au 21.334270
23.565599 4.472819
Au 7.622684
17.905844 4.565472
Au 13.176886
20.782568 4.222986
Au 18.647318
23.578348 4.576077
Au 10.420372
20.739298 4.116024
Au 15.940369
23.532042 4.596855
Au 7.640366
20.592949 4.509201
Au 13.232922
23.551462 4.603971
Au 10.545582
23.520506 4.533020
Au 7.852150
23.289627 4.368436
Au 22.897593
8.348318 6.281775
Au 20.151844
7.956353 6.586196
Au 17.400040
7.934139 6.625869
Au 23.263763
11.093363 6.601189
Au 14.620774
7.930509 6.638529

Au 20.279942
10.946380 6.213551
Au 11.868804
7.925092 6.635532
Au 17.429783
10.925066 6.317341
Au 23.231918
13.845219 6.660154
Au 9.116182
8.293026 6.361207
Au 14.565113
10.920378 6.335178
Au 20.248760
13.791461 6.340656
Au 11.715656
10.913450 6.265431
Au 17.389500
13.798906 6.411033
Au 23.215870
16.615992 6.692930
Au 8.732861
11.035778 6.678739
Au 14.598426
13.797790 6.455802
Au 20.230028
16.655775 6.376348
Au 11.724981
13.757915 6.390898
Au 17.377157
16.608540 6.446052
Au 23.226580
19.369461 6.703541
Au 8.740081
13.787800 6.733425
Au 14.571444
16.595169 6.477289
Au 20.238140
19.502949 6.309835
Au 11.709766
16.621096 6.422823
Au 17.393700
19.462721 6.420263
Au 22.841764
22.122959 6.452913
Au 8.724826
16.558250 6.770244

Au 14.529122
19.448112 6.436392
Au 20.091654
22.484993 6.756075
Au 11.684466
19.466871 6.353992
Au 17.338814
22.447580 6.796703
Au 8.700507
19.311750 6.779805
Au 14.572820
22.432465 6.809918
Au 11.819298
22.448898 6.800412
Au 9.068189
22.065502 6.524003
Au 21.574514
9.645434 8.357472
Au 18.797840
9.575590 8.492445
Au 16.014507
9.466127 8.536697
Au 21.623741
12.415670 8.512070
Au 13.230383
9.559403 8.523531
Au 18.824026
12.374324 8.512690
Au 10.450636
9.603467 8.421406
Au 16.005760
12.228534 8.540939
Au 21.606300
15.200617 8.552640
Au 13.184211
12.358953 8.557338
Au 18.833279
15.190076 8.572001
Au 10.383209
12.372975 8.570337
Au 15.992167
15.044485 8.768112
Au 21.589615
17.987314 8.573315
Au 13.140767
15.170993 8.616819
Au 18.787390
18.003235 8.596210
Au 10.362494
15.156216 8.613244
Au 15.977742
17.964720 8.628814
Au 21.527288
20.761686 8.485310
Au 13.166759
17.980164 8.632616
Au 18.757622
20.802004 8.618311
Au 10.365451
17.941040 8.631775
Au 15.971436
20.752958 8.633133
Au 13.184660
20.778778 8.649569
Au 10.413416
20.714710 8.544387
C 16.391745
13.356186 11.993829
C 16.219858
14.870145 11.998663
H 15.647963
12.906814 12.665796
H 17.386578
13.119858 12.404081
H 16.308401
12.914056 10.987101
O 16.272099
15.562518 10.871229
O 16.075863
15.462656 13.072559

--
Au111-C2H3O2
Au 9.787124
14.825499 6.062855
Au 12.547881
19.628054 5.994316
Au 11.174559
17.238932 6.056753
Au 25.030666
7.684345 6.134677

Au 23.740763
10.107923 6.052258
Au 23.739305
8.431998 8.425004
Au 22.287355
7.573671 6.055945
Au 20.972944
10.012204 5.644526
Au 19.559908
7.550058 6.053928
Au 20.939907
8.031994 8.477880
Au 18.182756
7.935364 8.523922
Au 22.388029
12.475658 6.047097
Au 22.329430
9.240756 10.599260
Au 22.674128
11.049620 8.475876
Au 21.358171
13.473454 8.512310
Au 19.661894
10.768645 8.161498
Au 20.995026
11.670891 10.656359
Au 19.557848
9.167345 10.660090
Au 18.204966
11.608606 10.721601
Au 16.779839
9.064873 10.676115
Au 19.682564
14.122791 10.663477
Au 18.191921
9.970644 5.735852
Au 16.803228
7.526144 6.102742
Au 15.405260
9.963415 5.751755
Au 14.021810
7.520492 6.098756
Au 15.399693
7.861017 8.539083
Au 12.623406
9.959400 5.738629

Au 12.619268
7.935274 8.511881
Au 11.265359
7.529263 6.033995
Au 9.844715
9.976504 5.588171
Au 8.538630
7.537910 6.006761
Au 9.862847
7.989947 8.445552
Au 7.063601
8.375216 8.363494
Au 21.014814
14.867156 6.086850
Au 19.619507
17.272154 6.078726
Au 18.218220
19.647987 6.012024
Au 19.606707
12.434151 5.729244
Au 18.205397
14.843534 5.737102
Au 16.805897
12.403481 5.659676
Au 18.239805
13.266003 8.265275
Au 16.789858
10.733225 8.273956
Au 15.361036
13.236917 8.299161
Au 13.965642
10.750508 8.310526
Au 15.378186
11.574748 10.818298
Au 20.022404
15.916477 8.522327
Au 18.554092
18.279758 8.489195
Au 16.801058
15.697832 8.296930
Au 18.282532
16.528982 10.661679
Au 16.809805
14.067986 10.806599
Au 15.356238
16.472574 10.794355

Au 13.906649
14.076355 10.741309
Au 15.396278
14.829046 5.646701
Au 14.001531
12.396939 5.655018
Au 12.585507
14.824848 5.656183
Au 11.198018
12.403877 5.637251
Au 12.476873
13.255692 8.198016
Au 16.808104
17.248642 5.723275
Au 15.386050
19.636822 5.567995
Au 13.976068
17.244833 5.624853
Au 15.360641
18.161598 8.120240
Au 13.886959
15.717706 8.193349
Au 12.192578
18.261925 8.482262
Au 10.778626
15.865930 8.499018
Au 12.477109
16.506102 10.664212
Au 13.997748
9.060925 10.679227
Au 12.567700
11.617620 10.803776
Au 11.226444
9.162343 10.644010
Au 11.110612
10.750819 8.137527
Au 9.422215
13.435731 8.491201
Au 8.113195
11.003695 8.426013
Au 9.774896
11.632753 10.635973
Au 8.459535
9.197076 10.545552
Au 11.085732
14.083388 10.667445
Au 16.832787
21.995642 5.977770
Au 16.796257
18.870247 10.621829
Au 17.115299
20.633169 8.421345
Au 15.366963
22.853182 8.333958
Au 13.631618
20.620493 8.405647
Au 15.367554
21.241325 10.522414
Au 13.931945
18.874430 10.620958
Au 7.079602
10.060884 5.982498
Au 5.797095
7.635072 6.055379
Au 8.420747
12.431240 6.007777
Au 15.365896
24.313421 6.020418
Au 13.917945
21.982563 5.956028
C 16.045795
12.894097 15.175194
C 16.074474
12.850873 13.652128
H 15.536331
13.813463 15.493727
H 17.076027
12.938260 15.551661
H 15.530816
12.017756 15.581589
O 15.508872
11.849423 13.102773
O 16.663311
13.828207 13.088411

--
Au100-C4H4O4-stacked
Au 24.654600
6.614100 4.233399
Au 21.771000
6.602700 4.248600

Au 18.887100
6.591300 4.263999
Au 24.643499
9.497400 4.270999
Au 16.003500
6.580200 4.279200
Au 21.759899
9.486300 4.286400
Au 13.119900
6.568800 4.294400
Au 18.875999
9.474899 4.301600
Au 24.632401
12.381000 4.308800
Au 10.236000
6.557400 4.309800
Au 15.992399
9.463500 4.317000
Au 21.748800
12.369599 4.324000
Au 7.352400
6.546300 4.325000
Au 13.108800
9.452399 4.332200
Au 18.864901
12.358500 4.339400
Au 24.621300
15.264600 4.346600
Au 10.224900
9.441000 4.347400
Au 15.981300
12.347100 4.354600
Au 21.737700
15.253201 4.361800
Au 7.341300
9.429600 4.362800
Au 13.097699
12.335700 4.370000
Au 18.854099
15.242100 4.377000
Au 24.610199
18.148199 4.384201
Au 10.213800
12.324600 4.385200
Au 15.970200
15.230700 4.392400
Au 21.726599
18.136801 4.399600
Au 7.330200
12.313200 4.400400
Au 13.086599
15.219299 4.407600
Au 18.842999
18.125399 4.414801
Au 24.599100
21.031500 4.421999
Au 10.202701
15.208200 4.422801
Au 15.959101
18.114300 4.429999
Au 21.715500
21.020401 4.437200
Au 7.319100
15.196801 4.438200
Au 13.075500
18.102900 4.445400
Au 18.831900
21.008999 4.452600
Au 24.587999
23.915100 4.459800
Au 10.191601
18.091499 4.460599
Au 15.948000
20.997601 4.467800
Au 21.704399
23.903700 4.475000
Au 7.308000
18.080400 4.475800
Au 13.064400
20.986500 4.483000
Au 18.820799
23.892599 4.490200
Au 10.180500
20.975100 4.498400
Au 15.936899
23.881201 4.505600
Au 7.296900
20.963701 4.513600
Au 13.053300
23.869801 4.520800
Au 10.169399
23.858700 4.536000

Au 7.285800
23.847300 4.551400
Au 23.226137
8.015793 6.256160
Au 20.326851
7.792580 6.391478
Au 17.474035
7.777184 6.400049
Au 23.449476
10.923745 6.406136
Au 14.575059
7.740023 6.399375
Au 20.318867
10.895181 6.296403
Au 11.679220
7.707113 6.423797
Au 17.412724
10.894643 6.411608
Au 23.443964
13.802336 6.461462
Au 8.774870
7.930028 6.331563
Au 14.553156
10.931444 6.477826
Au 20.336906
13.784961 6.400892
Au 11.688025
10.872251 6.346601
Au 17.416019
13.765404 6.532391
Au 23.398258
16.681150 6.495645
Au 8.528342
10.829244 6.472160
Au 14.551183
13.764361 6.721203
Au 20.315720
16.674009 6.443670
Au 11.684565
13.752822 6.481676
Au 17.405910
16.644989 6.530595
Au 23.384739
19.540483 6.522086
Au 8.534390
13.737673 6.492062
Au 14.543285
16.588406 6.642856
Au 20.288221
19.546516 6.429797
Au 11.674244
16.611021 6.514596
Au 17.413021
19.550562 6.499825
Au 23.169504
22.448050 6.448740
Au 8.538766
16.650150 6.554873
Au 14.527203
19.528431 6.508578
Au 20.260923
22.637402 6.579101
Au 11.643371
19.515106 6.459293
Au 17.401834
22.623711 6.606944
Au 8.539138
19.496227 6.608411
Au 14.522284
22.633518 6.618245
Au 11.645218
22.635378 6.626125
Au 8.734625
22.396463 6.523614
Au 21.767414
9.477287 8.165298
Au 18.886658
9.382832 8.314297
Au 16.000280
9.245072 8.321726
Au 21.893406
12.334395 8.337707
Au 13.131216
9.228788 8.304096
Au 19.056067
12.296294 8.530348
Au 10.262596
9.400834 8.189210
Au 16.207743
12.121317 8.664170
Au 21.881884
15.205734 8.400622

Au 12.963303
12.139068 8.577131
Au 19.050779
15.196388 8.595702
Au 10.046089
12.272522 8.342287
Au 16.156553
15.291837 8.676339
Au 21.781776
18.075632 8.438054
Au 12.875664
15.292290 8.723266
Au 18.866915
18.074707 8.609965
Au 10.024551
15.148825 8.415383
Au 15.991645
18.198223 8.668925
Au 21.714708
20.948025 8.332620
Au 13.093928
18.174856 8.642148
Au 18.844191
20.986246 8.494704
Au 10.180232
18.027061 8.467602
Au 15.970796
21.045822 8.511787
Au 13.103083
21.036249 8.501122
Au 10.242951
20.914461 8.380828
C 15.856098
13.748095 11.352560
C 13.139269
13.565525 11.332520
C 15.226393
13.861912 12.745351
C 13.746817
13.385335 12.727560
H 13.668301
12.326331 12.992187
H 15.303397
14.906538 13.058810
H 15.793380
13.235980 13.444615
H 13.167004
13.977014 13.449852
O 15.816205
12.589326 10.818763
O 13.198810
14.751386 10.860883
O 16.302246
14.827643 10.849302
O 12.700417
12.514466 10.765990

--

Au100-C4H4O4-parallel-displaced

Au 24.654600
6.614100 4.233399
Au 21.771000
6.602700 4.248600
Au 18.887100
6.591300 4.263999
Au 24.643499
9.497400 4.270999
Au 16.003500
6.580200 4.279200
Au 21.759899
9.486300 4.286400
Au 13.119900
6.568800 4.294400
Au 18.875999
9.474899 4.301600
Au 24.632401
12.381000 4.308800
Au 10.236000
6.557400 4.309800
Au 15.992399
9.463500 4.317000
Au 21.748800
12.369599 4.324000
Au 7.352400
6.546300 4.325000
Au 13.108800
9.452399 4.332200
Au 18.864901
12.358500 4.339400
Au 24.621300
15.264600 4.346600

Au 10.224900
9.441000 4.347400
Au 15.981300
12.347100 4.354600
Au 21.737700
15.253201 4.361800
Au 7.341300
9.429600 4.362800
Au 13.097699
12.335700 4.370000
Au 18.854099
15.242100 4.377000
Au 24.610199
18.148199 4.384201
Au 10.213800
12.324600 4.385200
Au 15.970200
15.230700 4.392400
Au 21.726599
18.136801 4.399600
Au 7.330200
12.313200 4.400400
Au 13.086599
15.219299 4.407600
Au 18.842999
18.125399 4.414801
Au 24.599100
21.031500 4.421999
Au 10.202701
15.208200 4.422801
Au 15.959101
18.114300 4.429999
Au 21.715500
21.020401 4.437200
Au 7.319100
15.196801 4.438200
Au 13.075500
18.102900 4.445400
Au 18.831900
21.008999 4.452600
Au 24.587999
23.915100 4.459800
Au 10.191601
18.091499 4.460599
Au 15.948000
20.997601 4.467800
Au 21.704399
23.903700 4.475000
Au 7.308000
18.080400 4.475800
Au 13.064400
20.986500 4.483000
Au 18.820799
23.892599 4.490200
Au 10.180500
20.975100 4.498400
Au 15.936899
23.881201 4.505600
Au 7.296900
20.963701 4.513600
Au 13.053300
23.869801 4.520800
Au 10.169399
23.858700 4.536000
Au 7.285800
23.847300 4.551400
Au 23.224764
8.018559 6.256365
Au 20.320076
7.793122 6.389556
Au 17.462828
7.777728 6.413170
Au 23.431786
10.924963 6.414558
Au 14.576324
7.763296 6.421356
Au 20.325413
10.897635 6.310259
Au 11.698234
7.749652 6.418176
Au 17.444937
10.847391 6.376369
Au 23.421495
13.787126 6.461830
Au 8.786558
7.945309 6.332174
Au 14.545510
10.896984 6.427217
Au 20.340506
13.776611 6.408180
Au 11.705324
10.902518 6.396685

Au 17.432713
13.757224 6.453547
Au 23.415178
16.674299 6.498242
Au 8.562000
10.838424 6.477032
Au 14.536938
13.778703 6.625983
Au 20.325537
16.666414 6.444496
Au 11.666412
13.748339 6.476674
Au 17.417448
16.641171 6.556793
Au 23.400063
19.539665 6.521397
Au 8.539131
13.714880 6.501482
Au 14.553953
16.611071 6.658186
Au 20.280708
19.547009 6.420556
Au 11.642373
16.624411 6.465755
Au 17.390074
19.491180 6.559328
Au 23.166872
22.446409 6.444158
Au 8.507345
16.643339 6.558273
Au 14.548896
19.494736 6.539762
Au 20.258631
22.637371 6.580811
Au 11.641157
19.529327 6.448464
Au 17.402315
22.600790 6.596913
Au 8.513711
19.500278 6.610624
Au 14.520989
22.624504 6.615975
Au 11.643684
22.642218 6.626482
Au 8.737026
22.395315 6.521037

Au 21.766554
9.457869 8.176900
Au 18.892029
9.387462 8.334422
Au 16.012486
9.290614 8.349561
Au 21.821157
12.326811 8.355397
Au 13.143044
9.306402 8.339452
Au 18.926029
12.303279 8.516218
Au 10.272839
9.403282 8.214971
Au 16.071781
12.127611 8.564267
Au 21.907583
15.203363 8.409425
Au 13.076486
12.234889 8.677612
Au 19.097420
15.188711 8.611042
Au 10.125560
12.280347 8.385693
Au 16.244179
15.042876 8.607725
Au 21.822483
18.077795 8.426133
Au 12.814102
15.297232 8.608488
Au 18.940594
18.070135 8.624943
Au 9.975467
15.150139 8.417462
Au 16.026905
18.110432 8.784413
Au 21.718498
20.939386 8.324075
Au 13.032143
18.191748 8.615275
Au 18.844398
20.986687 8.488682
Au 10.142402
18.024797 8.447375
Au 15.966518
21.023453 8.509410

Au 13.099955
21.045263 8.491100
Au 10.237439
20.905106 8.378337
C 14.900608
15.761553 12.703792
C 15.532102
16.124134 11.357018
C 14.179016
14.392066 12.678310
C 13.545848
14.084828 11.318518
H 14.229863
16.577408 12.995299
H 15.718607
15.715256 13.439783
H 14.850847
13.564708 12.932268
H 13.367607
14.405585 13.423743
O 15.468078
17.318830 10.948397
O 16.080271
15.120753 10.772916
O 13.592607
12.900544 10.874597
O 13.023791
15.115794 10.762348

--
Au111-C4H4O4-parallel-displaced
Au 9.772268
14.827286 5.991395
Au 12.530064
19.631987 5.950583
Au 11.148580
17.246487 6.004130
Au 25.052404
7.668474 6.112872
Au 23.746696
10.086935 6.020354
Au 23.766354
8.422741 8.410871
Au 22.300901
7.568740 6.037252
Au 20.975689
10.003160 5.606225
Au 19.565838
7.552163 6.035339
Au 20.953199
8.044029 8.451197
Au 18.188921
7.957142 8.500957
Au 22.389946
12.457287 6.007845
Au 22.331697
9.236912 10.577628
Au 22.683514
11.030081 8.443789
Au 21.373602
13.453974 8.462319
Au 19.669981
10.746396 8.157259
Au 20.995430
11.660583 10.636575
Au 19.563234
9.156038 10.667397
Au 18.194374
11.587171 10.758242
Au 16.783136
9.017456 10.686616
Au 19.758078
14.136261 10.633126
Au 18.191587
9.970695 5.733716
Au 16.805197
7.526788 6.080176
Au 15.405752
9.961429 5.723742
Au 14.018263
7.520262 6.056420
Au 15.397394
7.861177 8.505458
Au 12.617007
9.953372 5.660599
Au 12.604328
7.935294 8.458677
Au 11.253627
7.531182 5.984229
Au 9.834535
9.974717 5.551636

Au 8.519248
7.536855 5.970652
Au 9.846112
8.008603 8.401243
Au 7.043310
8.384578 8.340639
Au 21.020931
14.856608 6.029347
Au 19.622335
17.272198 6.011827
Au 18.219240
19.658041 5.950768
Au 19.605066
12.423079 5.719450
Au 18.206766
14.836157 5.709970
Au 16.802311
12.402011 5.684070
Au 18.276049
13.234838 8.267638
Au 16.796293
10.697408 8.292966
Au 15.403772
13.182667 8.359862
Au 13.971436
10.686165 8.240512
Au 15.362449
11.496437 10.795084
Au 20.047449
15.909353 8.446740
Au 18.571478
18.295158 8.416683
Au 16.865358
15.679370 8.252766
Au 18.382196
16.565096 10.592248
Au 16.904129
14.081329 10.734240
Au 15.403928
16.469255 10.793612
Au 13.889760
14.015261 10.751586
Au 15.396370
14.824119 5.671076
Au 14.002857
12.394377 5.661572

Au 12.587370
14.824599 5.731522
Au 11.196887
12.402169 5.650330
Au 12.506862
13.218595 8.215259
Au 16.804140
17.246361 5.703824
Au 15.374769
19.627329 5.649202
Au 13.969412
17.232689 5.754132
Au 15.391960
18.101845 8.178930
Au 13.963824
15.642529 8.327106
Au 12.218389
18.240154 8.424168
Au 10.751577
15.871825 8.436532
Au 12.435735
16.509745 10.623062
Au 13.981800
8.988190 10.657260
Au 12.540566
11.551885 10.675488
Au 11.198451
9.116642 10.612806
Au 11.107341
10.723433 8.095166
Au 9.424398
13.419626 8.413898
Au 8.104923
10.999235 8.385171
Au 9.754775
11.629194 10.587318
Au 8.429983
9.200018 10.532182
Au 11.026165
14.100923 10.601728
Au 16.812553
22.005516 5.912973
Au 16.847034
18.894413 10.584130
Au 17.102348
20.632942 8.358886

Au 15.365907
22.849926 8.303679
Au 13.665692
20.594000 8.349675
Au 15.365150
21.224251 10.493369
Au 13.924358
18.865273 10.597075
Au 7.061787
10.050517 5.952720
Au 5.763975
7.622301 6.053387
Au 8.412206
12.422970 5.948593
Au 15.344606
24.342003 6.022010
Au 13.914091
21.991352 5.909690
C 15.615140
14.664395 14.984012
C 16.108995
15.104109 13.595497
C 15.183046
13.178530 14.972920
C 14.695156
12.771681 13.575734
H 14.787237
15.324522 15.260887
H 16.427666
14.805658 15.713541
H 16.006565
12.508671 15.248130
H 14.361534
13.025544 15.690957
O 15.696910
16.214962 13.149096
O 16.860107
14.251904 13.009493
O 15.149683
11.687428 13.094597
O 13.907687
13.612076 13.022685

--
Au111-C4H4O4-bent

Au 9.762139
14.810765 5.960189
Au 12.524714
19.613285 5.920042
Au 11.134897
17.230255 5.967406
Au 25.026323
7.705021 6.066992
Au 23.716940
10.119131 6.042524
Au 23.741348
8.405092 8.387661
Au 22.280746
7.589020 6.007755
Au 20.962395
10.012941 5.553229
Au 19.548412
7.563231 6.022276
Au 20.930285
8.002577 8.433725
Au 18.165167
7.886700 8.501348
Au 22.333347
12.467522 6.112095
Au 22.305376
9.158837 10.575854
Au 22.666573
11.015238 8.499187
Au 21.340843
13.436415 8.622561
Au 19.659201
10.728489 8.091802
Au 20.948208
11.561248 10.688246
Au 19.532282
9.095852 10.640641
Au 18.135956
11.517813 10.716968
Au 16.743031
9.005278 10.647904
Au 19.581970
13.963545 10.752619
Au 18.182911
9.971082 5.610256
Au 16.793316
7.542545 6.076874

Au 15.400803
9.960193 5.665582
Au 14.009872
7.521406 6.056003
Au 15.373446
7.825127 8.507811
Au 12.620547
9.951914 5.652586
Au 12.588278
7.929239 8.458221
Au 11.255740
7.527288 5.969268
Au 9.839365
9.967416 5.522438
Au 8.522212
7.527976 5.936520
Au 9.829315
8.022534 8.366641
Au 7.017262
8.361347 8.296915
Au 20.940079
14.830431 6.230742
Au 19.556709
17.222782 6.254493
Au 18.204206
19.586170 6.181922
Au 19.593761
12.421849 5.553932
Au 18.187059
14.823302 5.623713
Au 16.794714
12.393620 5.511604
Au 18.293600
13.209425 8.125905
Au 16.815815
10.685698 8.211306
Au 15.380722
13.161428 8.138178
Au 13.994051
10.674361 8.247946
Au 15.306503
11.481936 10.771139
Au 19.851013
15.808432 8.682314
Au 18.436426
18.171974 8.704261

Au 16.870178
15.686935 8.206873
Au 18.190639
16.431759 10.941478
Au 16.757839
13.951979 10.507057
Au 15.285044
16.425720 10.696501
Au 13.850903
13.976619 10.742073
Au 15.384217
14.813989 5.570792
Au 13.990001
12.383637 5.564796
Au 12.580178
14.811802 5.718244
Au 11.193445
12.394402 5.620703
Au 12.507949
13.206286 8.211601
Au 16.788925
17.225670 5.642236
Au 15.381906
19.599483 5.611547
Au 13.960609
17.220039 5.693249
Au 15.363618
18.108273 8.173880
Au 13.964018
15.634974 8.267789
Au 12.171760
18.230474 8.387120
Au 10.699324
15.858319 8.403500
Au 12.364064
16.479673 10.570082
Au 13.945234
8.987048 10.662883
Au 12.497478
11.532374 10.715686
Au 11.162891
9.098199 10.609723
Au 11.124678
10.716261 8.081465
Au 9.400594
13.396894 8.385937

Au 8.099507
10.969233 8.343027
Au 9.716036
11.604311 10.559557
Au 8.396783
9.172318 10.496031
Au 11.000785
14.065724 10.576277
Au 16.839788
21.938347 6.037069
Au 16.679350
18.879517 10.761005
Au 17.060621
20.594049 8.519462
Au 15.324430
22.832199 8.333469
Au 13.625731
20.584383 8.331554
Au 15.237354
21.228027 10.543971
Au 13.801983
18.867516 10.594114
Au 7.062213
10.037197 5.910792
Au 5.771663
7.611652 5.976724
Au 8.409611
12.409865 5.910540
Au 15.390699
24.272202 6.002206
Au 13.935039
21.954329 5.886178
C 16.009638
15.082128 14.888298
C 16.415937
15.758432 13.559158
C 15.808791
13.551003 14.808844
C 15.142000
13.058413 13.512136
H 15.076921
15.562400 15.207391
H 16.790560
15.279506 15.636909
H 16.757406
13.009794 14.913994
H 15.160583
13.242551 15.645531
O 15.493620
16.437502 13.003477
O 17.604162
15.579126 13.128130
O 15.642945
11.995584 13.020698
O 14.191270
13.759853 13.051651

--
Au111-C4H4O4-skewed
Au 9.767530
14.834266 5.961452
Au 12.532243
19.647169 5.930511
Au 11.150908
17.255047 5.956662
Au 25.044086
7.670284 6.127798
Au 23.747496
10.094582 6.043478
Au 23.758997
8.428370 8.426185
Au 22.295721
7.574562 6.050316
Au 20.978769
10.011310 5.633050
Au 19.564770
7.559161 6.059904
Au 20.952858
8.055387 8.474062
Au 18.187790
7.983212 8.526188
Au 22.386286
12.467023 6.029285
Au 22.341225
9.254837 10.602077
Au 22.673603
11.038106 8.459902
Au 21.351759
13.456800 8.483721
Au 19.659767
10.760441 8.161854

Au 21.000299
11.673923 10.661875
Au 19.576542
9.178047 10.688414
Au 18.201492
11.606312 10.786765
Au 16.792805
9.091320 10.700449
Au 19.716356
14.129885 10.646784
Au 18.195885
9.975341 5.665056
Au 16.806032
7.547018 6.095535
Au 15.398905
9.967944 5.710610
Au 14.023162
7.530461 6.082248
Au 15.404704
7.929484 8.523571
Au 12.615591
9.959932 5.695552
Au 12.620651
7.973996 8.497411
Au 11.262917
7.523902 6.020535
Au 9.839985
9.979662 5.644809
Au 8.530938
7.538144 5.970362
Au 9.859120
8.038187 8.414949
Au 7.055913
8.406708 8.350069
Au 21.015980
14.862972 6.051852
Au 19.621861
17.272831 6.031967
Au 18.228188
19.660246 5.969736
Au 19.600529
12.430682 5.728216
Au 18.203228
14.841269 5.700451
Au 16.796619
12.408845 5.650312
Au 18.238951
13.231459 8.273311
Au 16.801519
10.691034 8.206729
Au 15.363974
13.202224 8.262625
Au 13.955097
10.711198 8.263142
Au 15.398150
11.546610 10.702806
Au 20.048334
15.916065 8.476669
Au 18.566292
18.286659 8.437725
Au 16.841997
15.669857 8.257775
Au 18.346197
16.551140 10.610743
Au 16.848841
14.070279 10.725062
Au 15.395432
16.489908 10.798448
Au 13.868741
14.066861 10.625864
Au 15.392021
14.834027 5.593546
Au 13.996403
12.400423 5.610727
Au 12.581321
14.829947 5.657128
Au 11.192597
12.404126 5.677567
Au 12.491760
13.223652 8.212219
Au 16.805336
17.250402 5.718677
Au 15.381405
19.637276 5.671037
Au 13.970673
17.247072 5.699828
Au 15.389480
18.099838 8.178824
Au 13.928200
15.681655 8.230819
Au 12.186876
18.276829 8.387811

Au 10.748258
15.884955 8.387237
Au 12.405353
16.552795 10.564789
Au 13.999477
9.069818 10.688859
Au 12.568252
11.598444 10.935043
Au 11.213120
9.157203 10.653531
Au 11.130557
10.755511 8.181231
Au 9.422722
13.426188 8.396614
Au 8.100604
11.010796 8.392993
Au 9.765451
11.657757 10.609353
Au 8.453093
9.226406 10.544243
Au 10.994092
14.141811 10.573602
Au 16.827818
22.014368 5.932952
Au 16.838791
18.900230 10.597769
Au 17.093941
20.625853 8.368338
Au 15.356880
22.850574 8.304658
Au 13.644780
20.614477 8.350336
Au 15.360383
21.231707 10.497085
Au 13.912168
18.877884 10.575115
Au 7.065332
10.042812 5.946943
Au 5.777826
7.603380 6.082378
Au 8.396901
12.428644 5.955914
Au 15.355208
24.350990 6.026318
Au 13.920839
22.003334 5.910318
C 15.394114
14.459455 14.957137
C 15.883966
14.864503 13.561260
C 14.290595
13.364804 14.941963
C 13.613686
13.134060 13.580166
H 15.053832
15.364384 15.472087
H 16.263550
14.063354 15.499362
H 14.673471
12.392179 15.274003
H 13.493430
13.653726 15.643616
O 15.734259
16.054686 13.176392
O 16.427479
13.891174 12.919411
O 13.272838
11.958334 13.275620
O 13.467228
14.190493 12.872058

--
Au111-C4H4O4-stacked
Au 9.785762
14.865911 6.028841
Au 12.549773
19.636065 5.937213
Au 11.169193
17.266869 6.020068
Au 24.966154
7.669244 6.184852
Au 23.689499
10.088764 6.028184
Au 23.698900
8.454529 8.480986
Au 22.221294
7.584298 6.158015
Au 20.942068
10.009554 5.656085
Au 19.505661
7.588379 6.263329

Au 20.905207
8.043133 8.631759
Au 18.123526
8.088864 8.749645
Au 22.366453
12.473877 6.033610
Au 22.321148
9.328460 10.673297
Au 22.647699
11.062741 8.466585
Au 21.323408
13.488235 8.478653
Au 19.659512
10.771495 8.203657
Au 20.998623
11.751908 10.681002
Au 19.568434
9.275554 10.837496
Au 18.145285
11.715582 10.699398
Au 16.706326
9.205273 10.945544
Au 19.633480
14.182359 10.612874
Au 18.184238
9.986067 5.649120
Au 16.783600
7.593393 6.262909
Au 15.412409
9.979056 5.601180
Au 14.023446
7.586603 6.188983
Au 15.380385
8.052814 8.668343
Au 12.621889
9.978319 5.600246
Au 12.579994
7.977320 8.560629
Au 11.281003
7.558655 6.038570
Au 9.864447
10.021856 5.648520
Au 8.552499
7.579581 5.908037
Au 9.827593
8.062386 8.391707

Au 7.041608
8.420252 8.253620
Au 20.989664
14.865518 6.036985
Au 19.582863
17.268396 6.004711
Au 18.203115
19.649876 5.941797
Au 19.599966
12.428859 5.595300
Au 18.208128
14.836353 5.555424
Au 16.809200
12.408466 5.427772
Au 18.287912
13.240359 8.152446
Au 16.831356
10.696651 8.205335
Au 15.451594
13.241454 8.008868
Au 13.980224
10.699682 8.105433
Au 15.286194
11.731469 10.426975
Au 19.967806
15.928001 8.451059
Au 18.532457
18.306606 8.431253
Au 16.905935
15.724949 8.066528
Au 18.214603
16.560675 10.601056
Au 16.742891
14.161188 10.577105
Au 15.350986
16.550432 10.870444
Au 13.884308
14.175096 10.977355
Au 15.401001
14.839828 5.481730
Au 14.004090
12.408020 5.511749
Au 12.612277
14.830773 5.809380
Au 11.220109
12.436629 5.731607

Au 12.604338
13.230813 8.353782
Au 16.800825
17.256914 5.508291
Au 15.376782
19.637667 5.523576
Au 13.980434
17.235050 5.686017
Au 15.403537
18.133072 8.083334
Au 14.005876
15.662992 8.362401
Au 12.226233
18.278746 8.428439
Au 10.710170
15.953491 8.470025
Au 12.437933
16.579889 10.634512
Au 13.891016
9.247671 10.690168
Au 12.467914
11.742299 10.866935
Au 11.124836
9.232827 10.640017
Au 11.160229
10.814496 8.188383
Au 9.369847
13.505056 8.443241
Au 8.107690
11.042866 8.326842
Au 9.668283
11.719308 10.589543
Au 8.372061
9.268840 10.477023
Au 11.001245
14.194201 10.612215
Au 16.823906
22.004044 5.896144
Au 16.782171
18.933022 10.578546
Au 17.086395
20.651850 8.348638
Au 15.377925
22.895935 8.262089
Au 13.691520
20.616869 8.325829
Au 15.349568
21.299719 10.472760
Au 13.922305
18.930885 10.593290
Au 7.087677
10.096674 5.869260
Au 5.804011
7.660080 5.938652
Au 8.420399
12.482250 5.939592
Au 15.360630
24.331871 5.922899
Au 13.917808
21.999512 5.896549
C 14.633449
11.818641 14.889665
C 13.958899
12.357439 13.617933
C 16.167679
11.786214 14.798972
C 16.750467
11.152534 13.518212
H 14.217193
10.825597 15.091369
H 14.351969
12.484997 15.721665
H 16.569750
12.804848 14.853743
H 16.560982
11.218884 15.658772
O 13.004686
11.659138 13.155919
O 14.439506
13.441086 13.145139
O 17.707361
11.806959 12.995651
O 16.234013
10.062079 13.100939

Au100-C5H6O4-stacked

Au 24.654600
6.614100 4.233399
Au 21.771000
6.602700 4.248600

Au 18.887100
6.591300 4.263999
Au 24.643499
9.497400 4.270999
Au 16.003500
6.580200 4.279200
Au 21.759899
9.486300 4.286400
Au 13.119900
6.568800 4.294400
Au 18.875999
9.474899 4.301600
Au 24.632401
12.381000 4.308800
Au 10.236000
6.557400 4.309800
Au 15.992399
9.463500 4.317000
Au 21.748800
12.369599 4.324000
Au 7.352400
6.546300 4.325000
Au 13.108800
9.452399 4.332200
Au 18.864901
12.358500 4.339400
Au 24.621300
15.264600 4.346600
Au 10.224900
9.441000 4.347400
Au 15.981300
12.347100 4.354600
Au 21.737700
15.253201 4.361800
Au 7.341300
9.429600 4.362800
Au 13.097699
12.335700 4.370000
Au 18.854099
15.242100 4.377000
Au 24.610199
18.148199 4.384201
Au 10.213800
12.324600 4.385200
Au 15.970200
15.230700 4.392400
Au 21.726599
18.136801 4.399600
Au 7.330200
12.313200 4.400400
Au 13.086599
15.219299 4.407600
Au 18.842999
18.125399 4.414801
Au 24.599100
21.031500 4.421999
Au 10.202701
15.208200 4.422801
Au 15.959101
18.114300 4.429999
Au 21.715500
21.020401 4.437200
Au 7.319100
15.196801 4.438200
Au 13.075500
18.102900 4.445400
Au 18.831900
21.008999 4.452600
Au 24.587999
23.915100 4.459800
Au 10.191601
18.091499 4.460599
Au 15.948000
20.997601 4.467800
Au 21.704399
23.903700 4.475000
Au 7.308000
18.080400 4.475800
Au 13.064400
20.986500 4.483000
Au 18.820799
23.892599 4.490200
Au 10.180500
20.975100 4.498400
Au 15.936899
23.881201 4.505600
Au 7.296900
20.963701 4.513600
Au 13.053300
23.869801 4.520800
Au 10.169399
23.858700 4.536000

Au 7.285800
23.847300 4.551400
Au 23.228851
8.018741 6.256025
Au 20.336321
7.793417 6.391004
Au 17.485292
7.772412 6.390574
Au 23.453619
10.928051 6.410699
Au 14.566294
7.747268 6.388261
Au 20.328697
10.899508 6.299836
Au 11.670753
7.730075 6.413997
Au 17.430059
10.894579 6.388126
Au 23.428368
13.804487 6.459846
Au 8.773990
7.949636 6.333267
Au 14.568028
10.891335 6.430794
Au 20.318548
13.787498 6.399096
Au 11.711275
10.903622 6.383051
Au 17.383234
13.767879 6.588498
Au 23.388332
16.680582 6.496533
Au 8.554637
10.850547 6.476186
Au 14.566588
13.747437 6.715703
Au 20.304569
16.673176 6.447861
Au 11.739334
13.754978 6.538510
Au 17.394772
16.624117 6.558785
Au 23.386162
19.538933 6.524847
Au 8.559885
13.730409 6.507254
Au 14.533452
16.612629 6.581151
Au 20.290695
19.545010 6.430385
Au 11.653437
16.612373 6.503251
Au 17.418564
19.542444 6.496244
Au 23.168051
22.445885 6.447518
Au 8.546663
16.633402 6.560649
Au 14.529312
19.541214 6.504743
Au 20.260605
22.636993 6.579808
Au 11.636209
19.516346 6.456908
Au 17.401854
22.625437 6.605246
Au 8.535490
19.490362 6.604701
Au 14.519238
22.643639 6.624984
Au 11.645127
22.636293 6.628029
Au 8.738111
22.392954 6.521751
Au 21.774118
9.478419 8.170171
Au 18.889534
9.389767 8.306616
Au 16.011822
9.202873 8.306504
Au 21.876854
12.335902 8.337620
Au 13.136971
9.229897 8.310860
Au 19.030779
12.299831 8.532936
Au 10.269547
9.410112 8.201519
Au 16.157005
12.063874 8.624023
Au 21.844975
15.203750 8.399719

Au 13.055384
12.122677 8.656528
Au 18.994539
15.197364 8.612302
Au 10.118262
12.281192 8.377653
Au 16.076080
15.326981 8.724619
Au 21.777519
18.076216 8.438949
Au 12.953259
15.298855 8.697598
Au 18.864042
18.076300 8.615427
Au 10.065042
15.150806 8.432978
Au 15.984285
18.220585 8.659085
Au 21.717991
20.948782 8.335022
Au 13.087820
18.190962 8.620699
Au 18.846062
20.985683 8.491098
Au 10.171623
18.032068 8.471536
Au 15.973063
21.055500 8.509826
Au 13.100179
21.040327 8.500473
Au 10.236732
20.910877 8.382939
C 14.758167
12.257739 11.367560
C 14.455293
15.267865 11.446022
C 14.824320
12.514939 12.878865
C 14.420832
15.067175 12.961993
C 13.923159
13.663412 13.354036
H 15.875081
12.694807 13.145562
H 12.908561
13.510365 12.963515
H 15.430514
15.239923 13.359250
H 13.740431
15.819483 13.386178
H 14.510221
11.578270 13.369422
H 13.864174
13.625955 14.452793
O 15.883124
12.055243 10.804489
O 13.598757
12.271352 10.843626
O 15.606682
15.206758 10.902473
O 13.323824
15.441513 10.888558

--
Au100-C5H6O4-parallel-displaced
Au 24.654600
6.614100 4.233399
Au 21.771000
6.602700 4.248600
Au 18.887100
6.591300 4.263999
Au 24.643499
9.497400 4.270999
Au 16.003500
6.580200 4.279200
Au 21.759899
9.486300 4.286400
Au 13.119900
6.568800 4.294400
Au 18.875999
9.474899 4.301600
Au 24.632401
12.381000 4.308800
Au 10.236000
6.557400 4.309800
Au 15.992399
9.463500 4.317000
Au 21.748800
12.369599 4.324000
Au 7.352400
6.546300 4.325000

Au 13.108800
9.452399 4.332200
Au 18.864901
12.358500 4.339400
Au 24.621300
15.264600 4.346600
Au 10.224900
9.441000 4.347400
Au 15.981300
12.347100 4.354600
Au 21.737700
15.253201 4.361800
Au 7.341300
9.429600 4.362800
Au 13.097699
12.335700 4.370000
Au 18.854099
15.242100 4.377000
Au 24.610199
18.148199 4.384201
Au 10.213800
12.324600 4.385200
Au 15.970200
15.230700 4.392400
Au 21.726599
18.136801 4.399600
Au 7.330200
12.313200 4.400400
Au 13.086599
15.219299 4.407600
Au 18.842999
18.125399 4.414801
Au 24.599100
21.031500 4.421999
Au 10.202701
15.208200 4.422801
Au 15.959101
18.114300 4.429999
Au 21.715500
21.020401 4.437200
Au 7.319100
15.196801 4.438200
Au 13.075500
18.102900 4.445400
Au 18.831900
21.008999 4.452600
Au 24.587999
23.915100 4.459800
Au 10.191601
18.091499 4.460599
Au 15.948000
20.997601 4.467800
Au 21.704399
23.903700 4.475000
Au 7.308000
18.080400 4.475800
Au 13.064400
20.986500 4.483000
Au 18.820799
23.892599 4.490200
Au 10.180500
20.975100 4.498400
Au 15.936899
23.881201 4.505600
Au 7.296900
20.963701 4.513600
Au 13.053300
23.869801 4.520800
Au 10.169399
23.858700 4.536000
Au 7.285800
23.847300 4.551400
Au 23.223509
8.020516 6.254781
Au 20.330009
7.780582 6.391432
Au 17.474319
7.764560 6.392964
Au 23.441568
10.930045 6.406017
Au 14.558208
7.767502 6.391806
Au 20.322725
10.906823 6.292427
Au 11.680238
7.750601 6.420059
Au 17.419676
10.894022 6.393642
Au 23.389988
13.804359 6.449976
Au 8.782537
7.953899 6.334909

Au 14.563114
10.890265 6.439658
Au 20.269396
13.805608 6.451158
Au 11.714693
10.893868 6.394125
Au 17.398005
13.776603 6.610551
Au 23.352001
16.677656 6.488758
Au 8.570903
10.861141 6.473053
Au 14.570882
13.748642 6.612670
Au 20.253584
16.640881 6.508043
Au 11.689463
13.729345 6.483260
Au 17.407553
16.635160 6.561814
Au 23.380281
19.532726 6.523257
Au 8.569754
13.743157 6.522975
Au 14.531789
16.641329 6.523723
Au 20.287483
19.532373 6.421767
Au 11.620508
16.634459 6.481963
Au 17.408306
19.550243 6.497612
Au 23.165751
22.443428 6.444760
Au 8.554955
16.624847 6.576238
Au 14.518853
19.550270 6.515166
Au 20.257635
22.644892 6.578809
Au 11.640712
19.518919 6.469794
Au 17.394781
22.634562 6.607339
Au 8.545490
19.481144 6.604192

Au 14.510489
22.621433 6.620914
Au 11.647590
22.615936 6.631281
Au 8.739930
22.389492 6.523429
Au 21.756683
9.479649 8.163244
Au 18.883610
9.355865 8.301400
Au 16.008261
9.197219 8.321939
Au 21.862949
12.334972 8.339403
Au 13.139306
9.295148 8.332875
Au 19.010813
12.239954 8.537251
Au 10.265306
9.416336 8.216549
Au 16.119223
12.056549 8.611414
Au 21.804220
15.201668 8.419598
Au 13.068062
12.267285 8.660522
Au 18.903812
15.182453 8.783111
Au 10.133238
12.281963 8.397451
Au 15.891897
15.367449 8.621506
Au 21.768450
18.074928 8.442579
Au 12.962630
15.239282 8.618137
Au 18.854389
18.110256 8.624962
Au 10.119997
15.153172 8.460644
Au 15.975106
18.249775 8.666023
Au 21.705997
20.945395 8.323970
Au 13.092113
18.091846 8.630922

Au 18.843515
21.007212 8.483679
Au 10.183990
18.030499 8.499022
Au 15.971115
21.072084 8.521761
Au 13.096172
20.984249 8.521163
Au 10.226473
20.906456 8.394321
C 14.903450
12.651722 12.886227
C 14.779995
12.411310 11.382835
C 15.231855
14.113310 13.254466
C 16.646992
14.612781 12.923254
C 16.920237
14.896289 11.440091
H 15.689531
11.986491 13.271852
H 13.949251
12.373070 13.351311
H 16.797552
15.580338 13.432520
H 17.425850
13.936710 13.302132
H 15.093275
14.204567 14.343404
H 14.495026
14.781679 12.786693
O 13.616199
12.456809 10.877782
O 15.889962
12.186668 10.791064
O 18.115295
14.829772 11.023010
O 15.872303
15.226101 10.783076

--
Au111-C5H6O4-parallel-displaced
Au 16.192625
9.379516 5.119478
Au 11.399867
6.594462 5.053566
Au 13.792767
7.975207 5.109430
Au 6.484521
23.184290 5.133976
Au 6.430619
20.434757 5.004381
Au 7.271492
21.891121 7.399033
Au 8.930261
21.903671 5.000243
Au 8.874152
19.125082 4.715930
Au 11.323075
20.577839 5.009671
Au 9.892871
20.862188 7.433020
Au 12.339468
19.579557 7.463560
Au 6.415553
17.700502 5.035427
Au 8.106312
20.484797 9.578407
Au 6.904057
19.097418 7.444661
Au 6.815226
16.339411 7.499136
Au 9.663333
17.813654 7.229746
Au 8.022084
17.726662 9.662994
Au 10.557837
19.223068 9.638462
Au 10.509348
16.397432 9.785419
Au 13.051552
17.978045 9.622426
Au 7.884498
14.950360 9.676812
Au 11.304810
17.782316 4.747190
Au 13.732653
19.216509 5.046755
Au 13.726791
16.402077 4.744912

Au 16.154753
17.835016 5.052658
Au 14.812128
18.261177 7.479686
Au 16.145603
15.019246 4.766957
Au 17.175323
16.793695 7.484885
Au 18.539633
16.447464 5.017641
Au 18.544783
13.616358 4.617586
Au 20.900837
15.080544 5.009536
Au 19.534567
15.373243 7.447684
Au 21.771505
13.652991 7.391767
Au 6.418600
14.941146 5.073113
Au 6.442403
12.154448 5.064926
Au 6.477346
9.387635 5.042055
Au 8.859555
16.348127 4.784146
Au 8.870834
13.567932 4.749815
Au 11.300799
14.979186 4.679945
Au 9.635859
14.976738 7.340143
Au 12.151493
16.453030 7.284604
Au 12.129155
13.567682 7.384442
Au 14.594065
15.051329 7.322331
Au 13.003573
15.081375 9.783545
Au 6.747781
13.551956 7.504053
Au 6.845395
10.765028 7.492664
Au 9.606191
12.148388 7.254393
Au 7.876188
12.162858 9.670712
Au 10.411442
13.527919 9.727396
Au 10.504808
10.725468 9.698874
Au 12.963442
12.125403 9.905466
Au 11.316620
12.176257 4.691803
Au 13.732985
13.591680 4.745651
Au 13.756427
10.780839 4.782911
Au 16.157082
12.188808 4.785108
Au 14.584183
12.129658 7.360832
Au 8.889842
10.771399 4.715651
Au 8.937009
7.988215 4.630034
Au 11.353288
9.368055 4.705330
Au 9.666996
9.283554 7.158072
Au 12.158033
10.694748 7.276843
Au 12.387894
7.627655 7.525065
Au 14.826262
8.974788 7.556807
Au 13.036343
9.269161 9.701354
Au 15.449751
16.569605 9.669757
Au 15.382510
13.596007 9.843974
Au 17.767523
15.061192 9.655872
Au 17.055902
13.609552 7.191493
Au 17.176548
10.461211 7.534777
Au 19.531563
11.906716 7.456133

Au 17.785576
12.182627 9.691793
Au 20.136711
13.637602 9.568027
Au 15.433053
10.695408 9.736932
Au 6.509458
6.657550 5.062808
Au 8.058458
9.395620 9.668397
Au 6.932172
8.011495 7.488048
Au 7.350799
5.226616 7.446698
Au 9.968206
6.304621 7.482852
Au 8.158375
6.632751 9.625789
Au 10.584340
7.949905 9.682784
Au 20.916702
12.174603 5.031255
Au 23.241974
13.645723 5.077655
Au 18.561703
10.788793 5.049344
Au 6.618057
3.903964 5.176481
Au 9.037300
5.222275 5.063819
C 11.263598
13.032234 14.139670
C 11.356409
12.789993 12.626703
C 10.784710
14.445514 14.506117
C 11.773849
15.569452 14.139800
C 11.851660
15.776285 12.624422
H 12.246461
12.812000 14.581935
H 10.547567
12.290726 14.530446
H 11.437409
16.513741 14.588687
H 12.777786
15.328353 14.517614
H 10.619823
14.481874 15.595047
H 9.816948
14.644451 14.020258
O 10.404305
13.324137 11.959364
O 12.329771
12.108491 12.200180
O 12.839598
15.201951 12.051374
O 10.919335
16.451426 12.094307

Au111-C5H6O4-bent

Au 16.194748
9.380325 5.087186
Au 11.409567
6.585818 5.044527
Au 13.793692
7.973274 5.091089
Au 6.506746
23.188164 5.134230
Au 6.434953
20.435499 5.002668
Au 7.271112
21.883522 7.399572
Au 8.941919
21.895758 5.002866
Au 8.879931
19.125807 4.697152
Au 11.328555
20.563635 5.032692
Au 9.883709
20.831467 7.444582
Au 12.324209
19.550400 7.508054
Au 6.418913
17.700579 5.024614
Au 8.087626
20.482786 9.592267
Au 6.897717
19.094650 7.441335

Au 6.817492
16.333595 7.484616
Au 9.625540
17.800377 7.215201
Au 8.006580
17.726229 9.667584
Au 10.525083
19.188044 9.664260
Au 10.487116
16.375736 9.821610
Au 13.005821
17.920959 9.675450
Au 7.911227
14.944650 9.645460
Au 11.302216
17.774967 4.742263
Au 13.727869
19.207109 5.091547
Au 13.715863
16.395569 4.804150
Au 16.141859
17.831585 5.093676
Au 14.782341
18.231014 7.531793
Au 16.134457
15.020943 4.777050
Au 17.148911
16.770433 7.514735
Au 18.525448
16.453327 5.032581
Au 18.534721
13.622247 4.624009
Au 20.892794
15.091921 5.008685
Au 19.509624
15.340306 7.438818
Au 21.775856
13.642290 7.373966
Au 6.434972
14.942956 5.037381
Au 6.451290
12.150822 5.043758
Au 6.468139
9.394736 5.035543
Au 8.857363
16.352629 4.661337

Au 8.864564
13.559745 4.663805
Au 11.298142
14.973331 4.668445
Au 9.566518
14.974229 7.197111
Au 12.087258
16.429220 7.336071
Au 12.119489
13.573545 7.323386
Au 14.554484
15.057049 7.359580
Au 12.964200
15.035520 9.883293
Au 6.779813
13.551227 7.469386
Au 6.851905
10.770485 7.492333
Au 9.588768
12.147299 7.196118
Au 7.933118
12.172341 9.648856
Au 10.422356
13.568539 9.623273
Au 10.527764
10.760210 9.803205
Au 12.993233
12.120918 9.833693
Au 11.313761
12.173764 4.654519
Au 13.731178
13.588678 4.717817
Au 13.751642
10.781795 4.783285
Au 16.153475
12.191859 4.769651
Au 14.581446
12.129008 7.341391
Au 8.889197
10.769012 4.658474
Au 8.946549
7.997728 4.705207
Au 11.351580
9.373738 4.733323
Au 9.680157
9.326079 7.217870

Au 12.132460
10.713863 7.313043
Au 12.402728
7.596031 7.511452
Au 14.844538
8.958885 7.522040
Au 13.069160
9.237052 9.665652
Au 15.413675
16.524672 9.711448
Au 15.390842
13.599657 9.840553
Au 17.774292
15.053374 9.673202
Au 17.032152
13.611459 7.193326
Au 17.194397
10.453900 7.505630
Au 19.534767
11.913411 7.438340
Au 17.793310
12.176091 9.670396
Au 20.149921
13.632130 9.561868
Au 15.462298
10.664867 9.701193
Au 6.515270
6.662852 5.019657
Au 8.060935
9.394392 9.676772
Au 6.964328
8.011763 7.454620
Au 7.366984
5.226680 7.419982
Au 9.970553
6.296922 7.460084
Au 8.169891
6.640424 9.608531
Au 10.598433
7.950724 9.668705
Au 20.911552
12.184617 5.007435
Au 23.233006
13.655032 5.044269
Au 18.562550
10.791170 5.029083
Au 6.611467
3.913394 5.157559
Au 9.034137
5.231281 5.021056
C 11.424290
12.223656 14.107524
C 11.577851
11.827602 12.634136
C 10.531761
13.466013 14.317677
C 11.224575
14.834646 14.130322
C 11.424180
15.236653 12.663661
H 12.420155
12.385455 14.542833
H 10.954021
11.369941 14.615708
H 10.592151
15.605557 14.589125
H 12.202317
14.833584 14.632659
H 10.160822
13.433024 15.351918
H 9.648296
13.399138 13.667001
O 12.729372
11.985914 12.118759
O 10.520296
11.392128 12.075047
O 12.579967
15.037680 12.170562
O 10.396316
15.718619 12.083512

-
Au111-C5H6O4-skewed
Au 16.187992
9.397826 5.102355
Au 11.408684
6.588260 5.054589
Au 13.792518
7.980736 5.102366
Au 6.506664
23.179989 5.137698

Au 6.436777
20.431694 5.011574
Au 7.273768
21.874697 7.408391
Au 8.946502
21.893620 5.022871
Au 8.882578
19.114788 4.766717
Au 11.335977
20.565441 5.049682
Au 9.888236
20.814478 7.458607
Au 12.335466
19.541842 7.519898
Au 6.412105
17.696018 5.032186
Au 8.096696
20.463894 9.594480
Au 6.910687
19.083017 7.449759
Au 6.815135
16.328873 7.485576
Au 9.669588
17.767456 7.270702
Au 8.018210
17.699581 9.673066
Au 10.540477
19.174427 9.679913
Au 10.502065
16.353266 9.882894
Au 13.019126
17.903904 9.682570
Au 7.890866
14.928047 9.645958
Au 11.309807
17.771088 4.800261
Au 13.736294
19.207666 5.105613
Au 13.724041
16.392294 4.808264
Au 16.146473
17.831371 5.098703
Au 14.800836
18.235504 7.544286
Au 16.140753
15.017481 4.773001
Au 17.156422
16.770367 7.518111
Au 18.529888
16.454805 5.041530
Au 18.544666
13.626818 4.615064
Au 20.895267
15.092232 5.014948
Au 19.521307
15.355559 7.454029
Au 21.775137
13.650577 7.385936
Au 6.415303
14.937305 5.047638
Au 6.435420
12.146665 5.040217
Au 6.461795
9.381104 5.030018
Au 8.859732
16.342516 4.793297
Au 8.869089
13.555871 4.741317
Au 11.297962
14.973696 4.688320
Au 9.631953
14.937154 7.316105
Au 12.145064
16.398624 7.359612
Au 12.131861
13.525656 7.333241
Au 14.582245
14.995089 7.369481
Au 12.978544
15.007816 9.882382
Au 6.752213
13.542564 7.467849
Au 6.832392
10.746947 7.467499
Au 9.624035
12.091563 7.247207
Au 7.864011
12.146753 9.619438
Au 10.428837
13.490080 9.677583
Au 10.548059
10.699861 9.799850

Au 13.023385
12.106446 9.755890
Au 11.314514
12.169545 4.653529
Au 13.729218
13.587841 4.726470
Au 13.751437
10.777431 4.731210
Au 16.162376
12.193885 4.673527
Au 14.641509
12.080730 7.241598
Au 8.889051
10.761455 4.718559
Au 8.941679
7.993530 4.690532
Au 11.351076
9.367419 4.695858
Au 9.702950
9.275174 7.223891
Au 12.176676
10.660769 7.279450
Au 12.400716
7.609586 7.529459
Au 14.828768
8.986765 7.541947
Au 13.065144
9.245043 9.713181
Au 15.420133
16.508034 9.703959
Au 15.394433
13.576095 9.881056
Au 17.773823
15.044693 9.678966
Au 17.063536
13.591524 7.180456
Au 17.195864
10.449430 7.530562
Au 19.544594
11.906914 7.459946
Au 17.804752
12.178541 9.695721
Au 20.153481
13.640679 9.578432
Au 15.455496
10.690756 9.726458

Au 6.516029
6.652903 5.018863
Au 8.057537
9.379574 9.658406
Au 6.916294
7.996464 7.468489
Au 7.345593
5.227186 7.422292
Au 9.965165
6.290146 7.463245
Au 8.158608
6.629272 9.610923
Au 10.602430
7.902845 9.697590
Au 20.913609
12.186537 5.017710
Au 23.234070
13.661527 5.063710
Au 18.564756
10.797807 5.049256
Au 6.624801
3.902986 5.158161
Au 9.035862
5.230801 5.017068
C 10.526082
12.424745 14.078129
C 10.417639
12.162880 12.573118
C 10.281040
13.879141 14.493998
C 11.421355
14.869097 14.179048
C 11.575018
15.251200 12.699824
H 11.522467
12.075865 14.393388
H 9.805530
11.752384 14.570686
H 11.225850
15.803386 14.724143
H 12.378853
14.458790 14.528148
H 10.127201
13.895382 15.586146
H 9.350902
14.240040 14.032812

O 10.043643
13.170279 11.888005
O 10.702528
11.002810 12.156355
O 12.602939
14.754756 12.119526
O 10.701176
16.027937 12.213639

Au111-C5H6O4-stacked
Au 16.189383
9.381408 5.091677
Au 11.404713
6.598334 5.080202
Au 13.788489
7.972386 5.115445
Au 6.502649
23.157888 5.098640
Au 6.443817
20.416805 4.993503
Au 7.254665
21.891281 7.399589
Au 8.945347
21.889044 5.041620
Au 8.877690
19.124739 4.665595
Au 11.332842
20.569273 5.098778
Au 9.888641
20.868744 7.497414
Au 12.287187
19.468012 7.557684
Au 6.422783
17.689775 5.068560
Au 8.051570
20.493322 9.599053
Au 6.868353
19.096399 7.466086
Au 6.836161
16.333120 7.547274
Au 9.631714
17.846222 7.216371
Au 8.001966
17.728767 9.699758
Au 10.467555
19.184673 9.709252
Au 10.490161
16.353378 9.805601
Au 13.008706
17.920729 9.793624
Au 7.963675
14.939766 9.721918
Au 11.302708
17.789442 4.700012
Au 13.724312
19.214483 5.094614
Au 13.730243
16.410395 4.708402
Au 16.140326
17.833860 5.097702
Au 14.700426
18.127178 7.523032
Au 16.154987
15.026309 4.654862
Au 17.190720
16.834694 7.515038
Au 18.527658
16.463074 5.028132
Au 18.537918
13.623994 4.636683
Au 20.886303
15.086017 4.962488
Au 19.542334
15.382245 7.426373
Au 21.757433
13.644770 7.346200
Au 6.436461
14.932581 5.131526
Au 6.468895
12.152308 5.135689
Au 6.490958
9.397306 5.097633
Au 8.861238
16.355574 4.719333
Au 8.883334
13.574193 4.759626
Au 11.305197
14.989182 4.662024
Au 9.638357
15.021061 7.305491

Au 12.149950
16.510006 7.262515
Au 12.092541
13.570639 7.216832
Au 14.617944
15.029871 7.188503
Au 12.943096
14.964655 9.567024
Au 6.830677
13.544263 7.566007
Au 6.889603
10.764394 7.570994
Au 9.589952
12.157328 7.255961
Au 8.011293
12.156361 9.742826
Au 10.472659
13.530893 9.769823
Au 10.521976
10.749618 9.953997
Au 12.965224
12.097513 9.933632
Au 11.319391
12.178817 4.668306
Au 13.741553
13.597076 4.631974
Au 13.753975
10.787080 4.780586
Au 16.159796
12.191227 4.693879
Au 14.589052
12.128728 7.279821
Au 8.898296
10.774776 4.686827
Au 8.946557
7.996904 4.661368
Au 11.357665
9.386199 4.795841
Au 9.680716
9.312105 7.211926
Au 12.142275
10.742357 7.404631
Au 12.379792
7.644232 7.547206
Au 14.832853
8.942280 7.537599
Au 13.041269
9.267668 9.733482
Au 15.403002
16.420132 9.627384
Au 15.391980
13.525147 9.705576
Au 17.801989
15.036585 9.618509
Au 17.045086
13.571177 7.168118
Au 17.227154
10.383170 7.503242
Au 19.562845
11.869699 7.416575
Au 17.838118
12.122951 9.634893
Au 20.158466
13.616111 9.545383
Au 15.461475
10.634540 9.660263
Au 6.518560
6.670002 5.080094
Au 8.099163
9.378626 9.724734
Au 6.961649
8.005751 7.518034
Au 7.355309
5.205112 7.454141
Au 9.962962
6.311115 7.495042
Au 8.181859
6.613371 9.634229
Au 10.591642
7.965922 9.721271
Au 20.907139
12.188779 4.964037
Au 23.236614
13.659177 5.057896
Au 18.563400
10.782506 5.015642
Au 6.623755
3.924180 5.142901
Au 9.040590
5.227830 5.073909
C 14.018529
14.345989 13.879321

C	14.098516	13.560159	12.562609
C	12.630427	14.863407	14.291501
C	12.408913	16.369665	14.044282
C	12.138709	16.739668	12.579596
H	14.742449	15.167930	13.782069
H	14.432303	13.676113	14.650292
H	11.517675	16.689064	14.606261
H	13.268333	16.951405	14.403340
H	12.487432	14.684752	15.367438
H	11.856862	14.287068	13.765219
O	13.033769	13.016459	12.125607
O	15.256883	13.537336	12.029468
O	13.005867	17.500973	12.017064
O	11.077797	16.260614	12.080981

Appendix 3. XYZ coordinates for adsorbed acetates on small fixed Au nanoclusters *in vacuo* (ADF)

Fixed-Au111-1 acetate

[bond energy: −7.81027219 Ha]

Au	0.000000	0.000000	-8.144000
Au	-4.072000	4.072000	-8.144000
Au	0.000000	-4.072000	-4.072000
Au	-4.072000	0.000000	-4.072000
Au	0.000000	0.000000	-4.072000
Au	4.072000	0.000000	-4.072000
Au	-8.144000	4.072000	-4.072000
Au	-4.072000	4.072000	-4.072000
Au	0.000000	4.072000	-4.072000
Au	-4.072000	-4.072000	0.000000
Au	0.000000	-4.072000	0.000000
Au	4.072000	-4.072000	0.000000
Au	-8.144000	0.000000	0.000000
Au	-4.072000	0.000000	0.000000
Au	0.000000	0.000000	0.000000
Au	-4.072000	4.072000	0.000000
Au	0.000000	-4.072000	4.072000
Au	-4.072000	0.000000	4.072000
Au	0.000000	-2.036000	-6.108000
Au	-4.072000	2.036000	-6.108000
Au	0.000000	2.036000	-6.108000
Au	-4.072000	-2.036000	-2.036000
Au	0.000000	-2.036000	-2.036000
Au	4.072000	-2.036000	-2.036000
Au	-8.144000	2.036000	-2.036000
Au	-4.072000	2.036000	-2.036000

Au 0.000000 2.036000 -2.036000
Au -4.072000 - 2.036000 2.036000
Au 0.000000 - 2.036000 2.036000
Au -4.072000 2.036000 2.036000
Au -2.036000 0.000000 -6.108000
Au 2.036000 0.000000 -6.108000
Au -6.108000 4.072000 -6.108000
Au -2.036000 4.072000 -6.108000
Au -2.036000 - 4.072000 -2.036000
Au 2.036000 - 4.072000 -2.036000
Au -6.108000 0.000000 -2.036000
Au -2.036000 0.000000 -2.036000
Au 2.036000 0.000000 -2.036000
Au -6.108000 4.072000 -2.036000
Au -2.036000 4.072000 -2.036000
Au -2.036000 - 4.072000 2.036000
Au 2.036000 - 4.072000 2.036000
Au -6.108000 0.000000 2.036000
Au -2.036000 0.000000 2.036000
Au -2.036000 2.036000 -8.144000
Au -2.036000 - 2.036000 -4.072000
Au 2.036000 - 2.036000 -4.072000
Au -6.108000 2.036000 -4.072000
Au -2.036000 2.036000 -4.072000
Au 2.036000 - 2.036000 -4.072000
Au -6.108000 2.036000 0.000000
Au -2.036000 - 2.036000 0.000000
Au 2.036000 - 2.036000 0.000000
Au -6.108000 2.036000 0.000000
Au -2.036000 2.036000 0.000000
Au -2.036000 - 2.036000 4.072000
O 1.489431 1.391929 1.080202
C 2.614259 1.713532 0.584657
O 3.138692 1.353676 -0.514120
C 3.433375 2.701756 1.413924
H 3.208539 2.586636 2.479644
H 4.503320 2.570916 1.218890
H 3.143273 3.716155 1.103298

Fixed-Au111-2 acetates

[bond energy: −9.45941763 Ha]

Au 0.000000 0.000000 -8.144000
Au -4.072000 4.072000 -8.144000
Au 0.000000 - 4.072000 -4.072000
Au -4.072000 0.000000 -4.072000
Au 0.000000 0.000000 -4.072000

Au 4.072000 0.000000 -4.072000
Au -8.144000 4.072000 -4.072000
Au -4.072000 4.072000 -4.072000
Au 0.000000 4.072000 -4.072000
Au -4.072000 -4.072000 0.000000
Au 0.000000 -4.072000 0.000000
Au 4.072000 -4.072000 0.000000
Au -8.144000 0.000000 0.000000
Au -4.072000 0.000000 0.000000
Au 0.000000 0.000000 0.000000
Au -4.072000 4.072000 0.000000
Au 0.000000 -4.072000 4.072000
Au -4.072000 0.000000 4.072000
Au 0.000000 -2.036000 -6.108000
Au -4.072000 2.036000 -6.108000
Au 0.000000 2.036000 -6.108000
Au 4.072000 -2.036000 -6.108000
Au -8.144000 2.036000 -6.108000
Au -4.072000 2.036000 -6.108000
Au 0.000000 2.036000 -6.108000
Au -4.072000 -2.036000 -2.036000
Au 0.000000 -2.036000 -2.036000
Au 4.072000 -2.036000 -2.036000
Au -8.144000 2.036000 -2.036000
Au -4.072000 2.036000 -2.036000
Au 0.000000 2.036000 -2.036000
Au -4.072000 -2.036000 2.036000
Au 0.000000 -2.036000 2.036000
Au 4.072000 -2.036000 2.036000
Au -8.144000 2.036000 2.036000
Au -4.072000 2.036000 2.036000
Au 0.000000 2.036000 2.036000
Au -4.072000 -4.072000 0.000000
Au 0.000000 -4.072000 0.000000
Au 4.072000 -4.072000 0.000000
Au -8.144000 0.000000 0.000000
Au -4.072000 0.000000 0.000000
Au 0.000000 0.000000 0.000000
Au -4.072000 4.072000 0.000000
Au 0.000000 -4.072000 4.072000
Au -4.072000 0.000000 4.072000
Au 0.000000 -2.036000 -6.108000
Au -4.072000 2.036000 -6.108000
Au 0.000000 2.036000 -6.108000
Au 4.072000 -2.036000 -6.108000
Au -8.144000 2.036000 -6.108000
Au -4.072000 2.036000 -6.108000
Au 0.000000 2.036000 -6.108000
Au -4.072000 -2.036000 -2.036000
Au 0.000000 -2.036000 -2.036000
Au 4.072000 -2.036000 -2.036000
Au -8.144000 2.036000 -2.036000
Au -4.072000 2.036000 -2.036000
Au 0.000000 2.036000 -2.036000
Au -4.072000 -2.036000 2.036000
Au 0.000000 -2.036000 2.036000
Au 4.072000 -2.036000 2.036000
Au -8.144000 2.036000 2.036000
Au -4.072000 2.036000 2.036000
Au 0.000000 2.036000 2.036000
Au -4.072000 -4.072000 0.000000
Au 0.000000 -4.072000 0.000000
Au 4.072000 -4.072000 0.000000
Au -8.144000 0.000000 0.000000
Au -4.072000 0.000000 0.000000
Au 0.000000 0.000000 0.000000
Au -4.072000 4.072000 0.000000
Au 0.000000 -4.072000 4.072000
Au -4.072000 0.000000 4.072000
Au 0.000000 -2.036000 -6.108000
Au -4.072000 2.036000 -6.108000
Au 0.000000 2.036000 -6.108000
Au 4.072000 -2.036000 -6.108000
Au -8.144000 2.036000 -6.108000
Au -4.072000 2.036000 -6.108000
Au 0.000000 2.036000 -6.108000
Au -4.072000 -2.036000 -2.036000
Au 0.000000 -2.036000 -2.036000
Au 4.072000 -2.036000 -2.036000
Au -8.144000 2.036000 -2.036000
Au -4.072000 2.036000 -2.036000
Au 0.000000 2.036000 -2.036000
Au -4.072000 -2.036000 2.036000
Au 0.000000 -2.036000 2.036000
Au 4.072000 -2.036000 2.036000
Au -8.144000 2.036000 2.036000
Au -4.072000 2.036000 2.036000
Au 0.000000 2.036000 2.036000
Au -4.072000 -4.072000 0.000000
Au 0.000000 -4.072000 0.000000
Au 4.072000 -4.072000 0.000000
Au -8.144000 0.000000 0.000000
Au -4.072000 0.000000 0.000000
Au 0.000000 0.000000 0.000000
Au -4.072000 4.072000 0.000000
Au 0.000000 -4.072000 4.072000
Au -4.072000 0.000000 4.072000
Au 0.000000 -2.036000 -6.108000
Au -4.072000 2.036000 -6.108000
Au 0.000000 2.036000 -6.108000
Au 4.072000 -2.036000 -6.108000
Au -8.144000 2.036000 -6.108000
Au -4.072000 2.036000 -6.108000
Au 0.000000 2.036000 -6.108000
Au -4.072000 -2.036000 -2.036000
Au 0.000000 -2.036000 -2.036000
Au 4.072000 -2.036000 -2.036000
Au -8.144000 2.036000 -2.036000
Au -4.072000 2.036000 -2.036000
Au 0.000000 2.036000 -2.036000
Au -4.072000 -2.036000 2.036000
Au 0.000000 -2.036000 2.036000
Au 4.072000 -2.036000 2.036000
Au -8.144000 2.036000 2.036000
Au -4.072000 2.036000 2.036000
Au 0.000000 2.036000 2.036000
Au -4.072000 -4.072000 0.000000
Au 0.000000 -4.072000 0.000000
Au 4.072000 -4.072000 0.000000
Au -8.144000 0.000000 0.000000
Au -4.072000 0.000000 0.000000
Au 0.000000 0.000000 0.000000
Au -4.072000 4.072000 0.000000
Au 0.000000 -4.072000 4.072000
Au -4.072000 0.000000 4.072000
Au 0.000000 -2.036000 -6.108000
Au -4.072000 2.036000 -6.108000
Au 0.000000 2.036000 -6.108000
Au 4.072000 -2.036000 -6.108000
Au -8.144000 2.036000 -6.108000
Au -4.072000 2.036000 -6.108000
Au 0.000000 2.036000 -6.108000
Au -4.072000 -2.036000 -2.036000
Au 0.000000 -2.036000 -2.036000
Au 4.072000 -2.036000 -2.036000
Au -8.144000 2.036000 -2.036000
Au -4.072000 2.036000 -2.036000
Au 0.000000 2.036000 -2.036000
Au -4.072000 -2.036000 2.036000
Au 0.000000 -2.036000 2.036000
Au 4.072000 -2.036000 2.036000
Au -8.144000 2.036000 2.036000
Au -4.072000 2.036000 2.036000
Au 0.000000 2.036000 2.036000
Au -4.072000 -4.072000 0.000000
Au 0.000000 -4.072000 0.000000
Au 4.072000 -4.072000 0.000000
Au -8.144000 0.000000 0.000000
Au -4.072000 0.000000 0.000000
Au 0.000000 0.000000 0.000000
Au -4.072000 4.072000 0.000000
Au 0.000000 -4.072000 4.072000
Au -4.072000 0.000000 4.072000
Au 0.000000 -2.036000 -6.108000
Au -4.072000 2.036000 -6.108000
Au 0.000000 2.036000 -6.108000
Au 4.072000 -2.036000 -6.108000
Au -8.144000 2.036000 -6.108000
Au -4.072000 2.036000 -6.108000
Au 0.000000 2.036000 -6.108000
Au -4.072000 -2.036000 -2.036000
Au 0.000000 -2.036000 -2.036000
Au 4.072000 -2.036000 -2.036000
Au -8.144000 2.036000 -2.036000
Au -4.072000 2.036000 -2.036000
Au 0.000000 2.036000 -2.036000
Au -4.072000 -2.036000 2.036000
Au 0.000000 -2.036000 2.036000
Au 4.072000 -2.036000 2.036000
Au -8.144000 2.036000 2.036000
Au -4.072000 2.036000 2.036000
Au 0.000000 2.036000 2.036000

Au -6.108000 - 2.036000 0.000000
Au -2.036000 - 2.036000 0.000000
Au 2.036000 - 2.036000 0.000000
Au -6.108000 2.036000 0.000000
Au -2.036000 2.036000 0.000000
Au -2.036000 - 2.036000 4.072000
O 1.538609 1.492708 0.979948
C 2.651070 1.810247 0.465888
O 3.192468 1.392446 -0.605580
C 3.468678 2.867067 1.215669
H 2.978976 3.148978 2.154033
H 4.476198 2.476571 1.409425
H 3.568814 3.750269 0.570103
O 1.041942 - 0.548855 3.476952
C 0.572777 0.602252 3.728857
O -0.546507 1.104442 3.405440
C 1.496875 1.512875 4.537652
H 0.939158 2.351743 4.965432
H 2.001936 0.934958 5.320930
H 2.258858 1.900260 3.848641

Fixed-Au111-4 acetates

[bond energy: −12.56919286 Ha]

Au 0.000000 0.000000 -8.144000
Au -4.072000 4.072000 -8.144000
Au 0.000000 - 4.072000 -4.072000
Au -4.072000 0.000000 -4.072000
Au 0.000000 0.000000 -4.072000
Au 4.072000 0.000000 -4.072000
Au -8.144000 4.072000 -4.072000
Au -4.072000 4.072000 -4.072000
Au 0.000000 4.072000 -4.072000
Au -4.072000 - 4.072000 0.000000
Au 0.000000 - 4.072000 0.000000
Au 4.072000 - 4.072000 0.000000
Au -8.144000 0.000000 0.000000
Au -4.072000 0.000000 0.000000
Au 0.000000 0.000000 0.000000
Au -4.072000 4.072000 0.000000
Au 0.000000 - 4.072000 4.072000
Au -4.072000 0.000000 4.072000
Au 0.000000 - 2.036000 -6.108000
Au -4.072000 2.036000 -6.108000
Au 0.000000 2.036000 -6.108000
Au -4.072000 - 2.036000 -2.036000
Au 0.000000 - 2.036000 -2.036000

Au 4.072000 - 2.036000 -2.036000
Au -8.144000 2.036000 -2.036000
Au -4.072000 2.036000 -2.036000
Au 0.000000 2.036000 -2.036000
Au -4.072000 - 2.036000 2.036000
Au 0.000000 - 2.036000 2.036000
Au -4.072000 2.036000 2.036000
Au -2.036000 0.000000 -6.108000
Au 2.036000 0.000000 -6.108000
Au -6.108000 4.072000 -6.108000
Au -2.036000 4.072000 -6.108000
Au -2.036000 - 4.072000 -2.036000
Au 2.036000 - 4.072000 -2.036000
Au -6.108000 0.000000 -2.036000
Au -2.036000 0.000000 -2.036000
Au 2.036000 0.000000 -2.036000
Au -6.108000 4.072000 -2.036000
Au -2.036000 4.072000 -2.036000
Au -2.036000 - 4.072000 2.036000
Au 2.036000 - 4.072000 2.036000
Au -6.108000 0.000000 2.036000
Au -2.036000 0.000000 2.036000
Au -2.036000 2.036000 -8.144000
Au -2.036000 - 2.036000 -4.072000
Au 2.036000 - 2.036000 -4.072000
Au -6.108000 2.036000 -4.072000
Au -2.036000 2.036000 -4.072000
Au 2.036000 2.036000 -4.072000
Au -6.108000 - 2.036000 0.000000
Au -2.036000 - 2.036000 0.000000
Au 2.036000 - 2.036000 0.000000
Au -6.108000 2.036000 0.000000
Au -2.036000 2.036000 0.000000
Au -2.036000 - 2.036000 4.072000
O 1.489735 1.440830 1.063987
C 2.636986 1.718127 0.606002
O 3.194146 1.343001 -0.469010
C 3.455750 2.678520 1.480745
H 3.222448 2.507084 2.538471
H 4.527746 2.558324 1.284008
H 3.161133 3.705600 1.221476
O 0.680104 - 0.382812 3.912132
C 0.095304 - 0.174637 5.001241
O -0.869016 - 0.837378 5.539139
C 0.509455 1.060455 5.806120
H -0.257293 1.828797 5.619437

H 0.510443 0.840770 6.881898
H 1.487746 1.426057 5.474311
O 1.710419 5.554404 -4.101648
C 2.914340 5.142429 -4.124923
C 3.977385 6.249029 -4.057310
H 4.204142 6.435407 -2.997199
H 3.599757 7.178913 -4.500144
H 4.898559 5.922542 -4.554578
O 3.361543 3.961469 -4.165825
O -2.854198 2.551106 5.475755
C -3.516439 1.898694 6.293196
C -3.527952 2.319096 7.777741
H -4.538505 2.654226 8.056503
H -3.276164 1.455673 8.408960
H -2.811044 3.131559 7.945839
O -4.256363 0.852377 6.078627

Fixed-Au110-1 acetate

[bond energy: −7.21841372 Ha]

Au 4.072000 0.000000 0.000000
Au 0.000000 4.072000 0.000000
Au 4.072000 0.000000 4.072000
Au 0.000000 4.072000 4.072000
Au 0.000000 2.036000 2.036000
Au 4.072000 2.036000 2.036000
Au 2.036000 0.000000 2.036000
Au 2.036000 4.072000 2.036000
Au 2.036000 2.036000 0.000000
Au 2.036000 2.036000 4.072000
Au 0.000000 2.036000 -2.036000
Au 2.036000 0.000000 -2.036000
Au 0.000000 4.072000 -4.072000
Au -2.036000 4.072000 -2.036000
Au 2.036000 4.072000 -2.036000
Au 2.036000 2.036000 -4.072000
Au 4.072000 0.000000 -4.072000
Au 4.072000 -2.036000 -2.036000
Au 4.072000 2.036000 -2.036000
Au 4.072000 -2.036000 2.036000
Au -2.036000 4.072000 2.036000
Au 6.108000 0.000000 -2.036000
Au 6.108000 0.000000 2.036000
Au 6.108000 -2.036000 0.000000
Au 6.108000 -4.072000 -2.036000
Au 6.108000 -2.036000 -4.072000
Au 6.108000 -4.072000 2.036000

Au 6.108000 - 2.036000 4.072000
Au 8.144000 - 2.036000 -2.036000
Au 8.144000 - 2.036000 2.036000
Au 0.000000 6.108000 -2.036000
Au 0.000000 6.108000 2.036000
Au -2.036000 6.108000 0.000000
Au -2.036000 8.144000 -2.036000
Au -2.036000 6.108000 -4.072000
Au -2.036000 8.144000 2.036000
Au -2.036000 6.108000 4.072000
Au -4.072000 6.108000 -2.036000
Au -4.072000 6.108000 2.036000
Au 0.000000 2.036000 6.108000
Au 2.036000 0.000000 6.108000
Au 0.000000 4.072000 8.144000
Au -2.036000 4.072000 6.108000
Au 2.036000 4.072000 6.108000
Au 2.036000 2.036000 8.144000
Au 4.072000 0.000000 8.144000
Au 4.072000 - 2.036000 6.108000
Au 4.072000 2.036000 6.108000
Au 6.108000 0.000000 6.108000
Au 6.108000 - 4.072000 6.108000
Au 6.108000 - 2.036000 8.144000
Au 8.144000 - 2.036000 6.108000
Au 0.000000 6.108000 6.108000
Au -2.036000 8.144000 6.108000
Au -2.036000 6.108000 8.144000
Au -4.072000 6.108000 6.108000
O 5.420317 3.807856 2.028037
C 4.999441 5.006595 1.983586
O 3.800739 5.427977 1.989013
C 6.080073 6.074747 1.880212
H 6.393923 6.133900 0.828523
H 5.690108 7.049652 2.189888
H 6.950505 5.788052 2.480599

Fixed-Au100-1 acetate

[bond energy: −7.06739334 Ha]

Au 0.000000 0.000000 0.000000
Au 4.072000 0.000000 0.000000
Au 0.000000 4.072000 0.000000
Au 4.072000 4.072000 0.000000
Au 0.000000 0.000000 4.072000
Au 4.072000 0.000000 4.072000
Au 0.000000 4.072000 4.072000

Au 4.072000 4.072000 4.072000
Au 0.000000 2.036000 2.036000
Au 4.072000 2.036000 2.036000
Au 2.036000 0.000000 2.036000
Au 2.036000 4.072000 2.036000
Au 2.036000 2.036000 0.000000
Au 2.036000 2.036000 4.072000
Au 0.000000 -2.036000 -2.036000
Au 0.000000 2.036000 -2.036000
Au 0.000000 -2.036000 2.036000
Au 2.036000 0.000000 -2.036000
Au 0.000000 0.000000 -4.072000
Au 2.036000 -2.036000 -4.072000
Au 0.000000 4.072000 -4.072000
Au 2.036000 4.072000 -2.036000
Au 2.036000 -4.072000 -2.036000
Au 2.036000 -2.036000 -4.072000
Au 4.072000 0.000000 -4.072000
Au 4.072000 -2.036000 -2.036000
Au 4.072000 2.036000 -2.036000
Au 4.072000 -2.036000 2.036000
Au 4.072000 4.072000 -4.072000
Au 0.000000 6.108000 -2.036000
Au 0.000000 6.108000 2.036000
Au 2.036000 6.108000 0.000000
Au 2.036000 6.108000 -4.072000
Au 2.036000 6.108000 4.072000
Au 4.072000 6.108000 -2.036000
Au 4.072000 6.108000 2.036000
Au 0.000000 2.036000 6.108000
Au 0.000000 2.036000 6.108000
Au 2.036000 0.000000 6.108000
Au 0.000000 0.000000 8.144000
Au 2.036000 2.036000 8.144000
Au 0.000000 4.072000 8.144000
Au 2.036000 4.072000 6.108000
Au 2.036000 2.036000 8.144000
Au 4.072000 0.000000 8.144000
Au 4.072000 2.036000 6.108000
Au 4.072000 4.072000 8.144000
Au 0.000000 6.108000 6.108000
Au 2.036000 6.108000 8.144000
Au 4.072000 6.108000 6.108000
O 6.323852 2.412761 2.125476

C 6.863333 3.293622 2.863198
O 6.317048 4.076157 3.702557
C 8.373234 3.443286 2.694657
H 8.794377 4.072532 3.484972
H 8.842580 2.452444 2.694186
H 8.564875 3.904289 1.716010

Appendix 4. XYZ coordinates for small molecules *in vacuo* (ADF)

H-optimized $CH_3COOAuP(CH_3)_3$
[bond energy: −4.09590766 Ha]

O 11.141190 0.697630 5.527980
C 11.140660 1.679300 7.587900
H 11.337793 -3.119181 2.003603
Au 11.983170 -0.238940 3.867980
C 11.821480 0.981680 6.493570
C 12.427950 -2.989340 1.998230
P 12.841260 -1.228230 2.084060
O 12.950770 0.680580 6.729600
H 12.848407 -3.455209 1.093682
H 12.835777 -3.490011 2.887200
C 14.583930 -1.197550 1.925810
C 12.259220 -0.477200 0.563260
H 14.904932 -1.716632 1.008882
H 14.946440 -0.159989 1.891315
H 15.057852 -1.680982 2.792225
H 10.801213 0.924544 8.314795
H 11.840598 2.338308 8.114179
H 10.250986 2.251115 7.283235
H 12.672375 -0.978688 -0.327120
H 11.161256 -0.512478 0.521605
H 12.562758 0.579808 0.554301

-

Fully optimized $CH_3COOAuP(CH_3)_3$
(reference against $1\kappa^2O^{1,3}$ model)
[bond energy: −4.12006997 Ha]

O 10.944084 0.519557 5.570273
C 11.069228 1.541666 7.704516
H 11.407210 -3.214858 1.861862
Au 11.868414 -0.315465 3.934978
C 11.785125 0.960238 6.491336
C 12.487424 -3.025895 1.928167
P 12.774461 -1.225596 2.123841
O 13.014873 0.913168 6.416983

H 12.985930 -3.401465 1.022814
H 12.877776 -3.551031 2.810260
C 14.596660 -1.059793 2.068126
C 12.216561 -0.522021 0.524816
H 15.003904 -1.530423 1.161099
H 14.862675 0.005643 2.085395
H 15.028831 -1.534742 2.959210
H 10.537221 0.736531 8.231533
H 11.793742 2.005491 8.381499
H 10.315235 2.275589 7.389424
H 12.733821 -1.010737 -0.313914
H 11.132261 -0.666258 0.423235
H 12.426578 0.555926 0.510948

$1\kappa^2O^{1,3}$ $CH_3COOAuP(CH_3)_3$ model
(reference against above)
[bond energy: −4.10897347 Ha]

H 11.380831 -3.163815 1.917164
Au 12.026776 -0.288000 3.781024
C 12.471556 -3.038400 1.911274
P 12.884866 -1.277291 1.997104
H 12.891929 -3.510075 1.009051
H 12.876721 -3.537458 2.802208
C 14.627536 -1.246610 1.838854
C 12.302826 -0.526260 0.476304
H 14.964879 -1.755384 0.920590
H 14.985929 -0.207432 1.817498
H 15.096713 -1.735305 2.704630
H 12.745568 -1.005194 -0.411749
H 11.207814 -0.595885 0.419130
H 12.572843 0.539033 0.481858
C 10.912339 0.930751 5.902425
O 10.157899 0.328484 5.072751
O 12.175842 0.974950 5.748628
C 10.293263 1.586016 7.121772
H 10.919817 2.409726 7.480368
H 9.279459 1.936525 6.898319
H 10.223960 0.834367 7.921435

Fully optimized acetate
[bond energy: −1.61575422 Ha]

O 10.579237 0.519015 5.623248
C 11.149092 1.545185 7.706688
C 11.556396 0.878154 6.340979

O 12.796774 0.772237 6.124594
H 10.617869 0.803024 8.324732
H 12.023756 1.918768 8.260274
H 10.444386 2.371299 7.520037

Appendix 5. Crystal structure data for periodic systems with Au-O motifs, after H-atom optimization in CASTEP

Sodium Acetate Trihydrate (CCDC refcode: NAACET01)

[energy: −31808.38232 eV]

*C*2/*c*, *a* = 12.353 Å, *b* = 10.466 Å, *c* = 10.401 Å, $\alpha = \gamma = 90°$, $\beta = 111.69°$, *V* = 1249.5 Å^3, *Z* = 8

coordinates in *a*,*b*,*c* crystal frame

Na 0.088030 0.428700 0.421310
C 0.325900 0.561520 0.421500
C 0.394230 0.566980 0.574910
O 0.262250 0.466410 0.372890
O 0.336460 0.653490 0.349290
O 0.350840 0.211120 0.384280
O 0.880050 0.417280 0.404260
O 0.000000 0.597620 0.250000
O 0.000000 0.262580 0.250000
H 0.486377 0.586554 0.595835
H 0.362160 0.647036 0.619406
H 0.384870 0.479047 0.626646
H 0.042284 0.653616 0.208236
H 0.048150 0.206989 0.216148
H 0.330961 0.300705 0.395844
H 0.281228 0.181949 0.303698
H 0.867726 0.324126 0.406097
H 0.825008 0.442811 0.310900

Bis(trisodium citrate) undecahydrate (CCDC refcode: FATTID)

[energy: −85121.372937 eV]

Pnma, *a* = 16.459 Å, *b* = 26.426 Å, *c* = 6.435 Å, $\alpha = \gamma = \beta = 90°$, *V* = 2798.9 Å^3, *Z* = 8

coordinates in *a*,*b*,*c* crystal frame

H 0.340125 0.135405 0.262411
H 0.365320 0.092648 0.458835
H 0.245456 0.078966 0.091447
H 0.283000 0.034106 0.268304

H 0.254893 0.053555 0.640693
H 0.264320 0.220551 0.181186
H 0.109785 0.220241 0.240690
H 0.161199 0.250000 0.739427
H 0.096663 0.250000 0.927746
H 0.394700 0.059671 0.834123
H 0.418765 0.055967 0.066568
H 0.415077 0.012977 0.417493
H 0.496389 0.021375 0.287142
H 0.435707 0.153497 0.994325
H 0.515241 0.184082 0.014845
H -0.006455 0.153235 0.945193
H 0.049837 0.115331 0.067645
C 0.341300 0.167130 0.564500
C 0.322900 0.123370 0.419700
C 0.236100 0.101890 0.414600
C 0.233400 0.061200 0.243300
C 0.154400 0.031820 0.223500
C 0.175100 0.144750 0.366300
O 0.411520 0.186510 0.548100
O 0.289550 0.182630 0.690500
O 0.088460 0.053300 0.265200
O 0.158880 0.986980 0.158200
O 0.118010 0.152840 0.489700
O 0.187920 0.169130 0.201000
O 0.213590 0.080020 0.610100
O 0.299500 0.250000 0.153300
O 0.074500 0.250000 0.216900
O 0.103600 0.250000 0.774000
O 0.424090 0.078180 0.944000
O 0.440400 0.006710 0.281300
O 0.455800 0.187600 0.024500
O 0.044900 0.132710 0.934200
Na 0.433870 0.250000 0.295100
Na 0.374130 0.250000 0.823800
Na 0.066080 0.075060 0.628700
Na 0.168240 0.167700 0.834900

[Au(O$_2$CCH$_3$)P(Ph)$_3$] (CCDC refcode: CILYAX)

[energy: −33005.83098 eV]

*P*2$_1$2$_1$2$_1$, *a* = 11.088 Å, *b* = 12.050 Å, *c* = 13.839 Å, *α* = *β* = *γ* = 90°, *V* = 1849.03 Å^3, *Z* = 4

coordinates in *a*,*b*,*c* crystal frame

H 0.372285 -0.066035 0.166734

H 0.238526 -0.220210 0.212931
H 0.158151 -0.231229 0.375863
H 0.205770 -0.089068 0.496502
H 0.338019 0.069906 0.452949
H 0.331219 0.316592 0.351480
H 0.359991 0.419530 0.499280
H 0.531813 0.379034 0.608031
H 0.678698 0.232391 0.557516
H 0.647524 0.125382 0.409690
H 0.523629 0.276865 0.111658
H 0.395866 0.404438 0.011576
H 0.175280 0.400877 0.024602
H 0.076374 0.280498 0.144849
H 0.199134 0.156922 0.247167
H -0.578520 0.970241 0.672145
H -0.494952 1.052862 0.587456
H -0.515989 1.099209 0.707455
C 0.884700 0.031000 0.197100
C 1.001000 -0.025300 0.162600
C 0.361800 0.013000 0.305500
C 0.335000 -0.069900 0.239700
C 0.261300 -0.155700 0.265000
C 0.215800 -0.161400 0.356500
C 0.241900 -0.083100 0.423400
C 0.317300 0.006400 0.399500
C 0.484700 0.211300 0.371200
C 0.407800 0.295600 0.397400
C 0.425100 0.355400 0.480300
C 0.520900 0.333600 0.540600
C 0.601100 0.251600 0.512300
C 0.582900 0.190000 0.429200
C 0.368600 0.209100 0.186800
C 0.425900 0.276600 0.119700
C 0.353200 0.349300 0.063800
C 0.228100 0.346600 0.071400
C 0.174200 0.282100 0.136700
C 0.244300 0.209900 0.194600
O 0.791000 -0.000600 0.152300
O 0.883900 0.093300 0.264300
P 0.460500 0.125600 0.266000
Au 0.632200 0.064100 0.205700

[Au(O$_2$CCF$_3$)P(CH$_3$)$_3$] (CCDC refcode: FOBXID)

[energy: −93129.35323 eV]

$P2_1/n$, a = 9.759 Å, b = 11.362 Å, c = 27.183 Å, $\alpha = \gamma = 90°$, $\beta = 99.35°$,

V = 2974.05 Å^3, Z = 12, Z' = 3
coordinates in *a*,*b*,*c* crystal frame

C 0.909600 - 0.178400 0.074600
C 0.853300 - 0.300800 0.079000
C 0.580200 0.265700 0.090300
C 0.540700 0.386600 0.072200
C 0.320900 1.086400 0.242100
C 0.269600 1.147800 0.282900
C 1.002900 0.334700 0.156300
C 0.938300 0.324100 0.050400
C 1.207600 0.267700 0.102100
C 0.652100 - 0.156000 0.219000
C 0.771000 0.017600 0.290200
C 0.938100 - 0.099000 0.228200
C 0.526900 0.894600 0.071800
C 0.307200 0.736900 0.074500
C 0.265700 0.958000 0.021000
O 0.894000 - 0.108100 0.109600
O 0.958500 - 0.156300 0.038100
O 0.651200 0.264800 0.132700
O 0.536200 0.184400 0.064400
O 0.234900 1.061400 0.206100
O 0.440600 1.059900 0.250900
F 0.793100 - 0.316300 0.117200
F 0.773000 - 0.329300 0.041000
F 0.960900 - 0.375900 0.084600
F 0.450000 0.392400 0.033100
F 0.478000 0.449700 0.104800
F 0.649400 0.454300 0.069200
F 0.354500 1.189300 0.319500
F 0.149500 1.179100 0.277300
F 0.222200 1.062100 0.312600
P 1.030700 0.246900 0.103800
P 0.771600 - 0.032100 0.227400
P 0.351000 0.891900 0.077700
Au 0.965260 0.061670 0.106580
Au 0.713870 0.111240 0.172540
Au 0.293170 0.978970 0.144210
H 1.043413 0.424070 0.153183
H 0.891578 0.339566 0.157671
H 1.055157 0.294721 0.191039
H 0.968494 0.417241 0.051465
H 0.962566 0.282526 0.016384
H 0.826651 0.318039 0.050531
H 1.231959 0.362124 0.101752

H 1.270435
0.228373 0.135149
H 1.238002
0.226517 0.068997
H 0.682225 -
0.220189 0.249099
H 0.546510 -
0.124294 0.219904
H 0.656889 -
0.198156 0.183095
H 0.792564 -
0.056893 0.316016
H 0.853130
0.083200 0.300102
H 0.669965
0.056527 0.293103
H 0.955736 -
0.164453 0.258364
H 0.940665 -
0.142283 0.192392
H 1.020663 -
0.032704 0.234136
H 0.540749
0.850289 0.036956
H 0.562398
0.986091 0.070848
H 0.591270
0.850510 0.103194
H 0.338595
0.698029 0.041016
H 0.362151
0.691350 0.107488
H 0.195528
0.724440 0.073260
H 0.295070
0.912192 -0.011337
H 0.152739
0.954535 0.019199
H 0.297950
1.050314 0.02021

REFERENCES

1. Faraday, M., The Bakerian lecture: experimental relations of gold (and other metals) to light. *Philosophical Transactions of the Royal Society of London* **1857**, 145-181.

2. Neuroscience and nanotechnologies: opportunities and uncertainties. *Royal Society & Royal Academy of Engineering* **2008**.

3. Reibold, M.; Paufler, P.; Levin, A. A.; Kochmann, W.; Patzke, N.; Meyer, D. C., Materials: Carbon nanotubes in an ancient Damascus sabre. *Nature* **2006,** *444* (7117), 286-286.

4. Gorin, D. J.; Toste, F. D., Relativistic effects in homogeneous gold catalysis. *Nature* **2007,** *446* (7134), 395-403.

5. (a) Schwerdtfeger, P.; Dolg, M.; Schwarz, W. E.; Bowmaker, G. A.; Boyd, P. D., Relativistic effects in gold chemistry. I. Diatomic gold compounds. *The Journal of chemical physics* **1989,** *91* (3), 1762-1774; (b) Schwerdtfeger, P.; Boyd, P. D.; Brienne, S.; Burrell, A. K., Relativistic effects in gold chemistry. 4. Gold (III) and gold (V) compounds. *Inorganic Chemistry* **1992,** *31* (16), 3411-3422.

6. Puddephatt, R. J., Modern Supramolecular Gold Chemistry.Gold-Metal Interactions and Applications. Edited by A. Laguna. *Angewandte Chemie International Edition* **2009,** *48* (20), 3560-3560.

7. Dietzel, P. D. C.; Jansen, M., Synthesis and crystal structure determination of tetramethylammonium auride. *Chemical Communications* **2001,** (21), 2208-2209.

8. Bartlett, N., Relativistic effects and the chemistry of gold. *Gold Bulletin* **1998,** *31* (1), 22-25.

9. Walker, J., http://www.fourmilab.ch/documents/golden_glow/ **2006**.

10. Cotton, S. A., *Chemistry of precious metals*. Blackie Academic & Professional: London; New York, 1997.

11. R.H, B., The chemistry of the Lycurgus Cup', Proc 7th Internat. Cong. Glass, comptes rendus 2. **1965,** *223* (1), 13.21.

12. Sabine, E., On the Evidence of the Existence of the Decennial Inequality in the Solar-Diurnal Magnetic Variations, and Its Non-Existence in the Lunar-Diurnal Variation, of the Declination at Hobarton. *Philosophical Transactions of the Royal Society of London* **1857,** *147*, 1-8.

13. (a) Graham, T., Liquid Diffusion Applied to Analysis. *Philosophical Transactions of the Royal Society of London* **1861,** *151*, 183-224; (b) Kahn, R. L., Serum Diagnosis for Syphilis. *In Colloid Chemistry; Alexander, J., Ed.; The Chemical Catalog Co.: New York* **1928,** *II*, 757; (c) Hauser, E. A., Aurum potabile. *Journal of Chemical Education* **1952,** *29* (9), 456; (d) Brown, D. H.; Smith, W. E., The chemistry of the gold drugs used in the treatment of rheumatoid arthritis. *Chemical Society Reviews* **1980,** *9* (2), 217-240; (e) Hyatt, A. D.; Eaton, B., *Immuno-gold electron microscopy in virus diagnosis and research*. CRC Press: 1992.

14. Turkevich, J.; Stevenson, P. C.; Hillier, J., *Disc. Faraday Soc.* **1951,** *11* (null), 55.

15. Frens, G., Controlled nucleation for the regulation of the particle size in monodisperse gold suspensions. *Nature* **1973,** *241* (105), 20-22.

16. (a) Kreibig, U.; Vollmer, M., *Optical properties of metal clusters*. Springer: 1995; (b) Mock, J. J.; Barbic, M.; Smith, D. R.; Schultz, D. A.; Schultz, S., Shape effects in plasmon resonance of individual colloidal silver nanoparticles. *The Journal of Chemical Physics* **2002,** *116* (15), 6755-6759.

17. Kelly, K. L.; Coronado, E.; Zhao, L. L.; Schatz, G. C., The Optical Properties of Metal Nanoparticles: The Influence of Size, Shape, and Dielectric Environment. *The Journal of Physical Chemistry B* **2002,** *107* (3), 668-677.

18. (a) Feynman, The Wonders That Await a Micro-Microscope. *Saturday Review* **1960**, 45-47; (b) Feynman, R. P., There"s Plenty of Room at the Bottom. *Engineering and Science* **1960**, 22-36.

19. Janot, R.; Guérard, D., Ball-milling: the behavior of graphite as a function of the dispersal media. *Carbon* **2002,** *40* (15), 2887-2896.

20. (a) Asoh, H.; Arai, F.; Ono, S., Site-selective chemical etching of silicon using patterned silver catalyst. *Electrochemistry Communications* **2007,** *9* (4), 535-539; (b) Buckmaster, R.; Hanada, T.; Kawazoe, Y.; Cho, M.-w.; Yao, T.; Urushihara, N.; Yamamoto, A., Novel Method for Site-Controlled Surface Nanodot Fabrication by Ion Beam Synthesis. *Nano Letters* **2005,** *5* (4), 771-776; (c) Shen, H.; Cheng, B.; Lu, G.; Ning, T.; Guan, D.; Zhou, Y.; Chen, Z., Enhancement of optical nonlinearity in periodic gold nanoparticle arrays. *Nanotechnology* **2006,** *17* (16), 4274.

21. Swihart, M. T., Vapor-phase synthesis of nanoparticles. *Current Opinion in Colloid & Interface Science* **2003,** *8* (1), 127-133.

22. (a) Li, Y.; Park, C.-W., Particle size distribution in the synthesis of nanoparticles using microemulsions. *Langmuir* **1999,** *15* (4), 952-956; (b) Bandyopadhyaya, R.; Kumar, R.; Gandhi, K., Simulation of precipitation reactions in reverse micelles. *Langmuir* **2000,** *16* (18), 7139-7149; (c) Singh, R.; Durairaj, M. R.; Kumar, S., An Improved Monte Carlo Scheme for Simulation of Synthesis of Nanoparticles in Reverse Micelles. *Langmuir* **2003,** *19* (15), 6317-6328.

23. Sun, Y.; Xia, Y., Large-Scale Synthesis of Uniform Silver Nanowires Through a Soft, Self-Seeding, Polyol Process. *Advanced Materials* **2002,** *14* (11), 833-837.

24. Kim, F.; Connor, S.; Song, H.; Kuykendall, T.; Yang, P., Platonic Gold Nanocrystals. *Angewandte Chemie International Edition* **2004,** *43* (28), 3673-3677.

25. Kawasaki, H.; Nishimura, K.; Arakawa, R., Influence of the Counterions of Cetyltrimetylammonium Salts on the Surfactant Adsorption onto Gold Surfaces and the Formation of Gold Nanoparticles. *The Journal of Physical Chemistry C* **2007,** *111* (6), 2683-2690.

26. Hiramatsu, H.; Osterloh, F. E., A Simple Large-Scale Synthesis of Nearly Monodisperse Gold and Silver Nanoparticles with Adjustable Sizes and with Exchangeable Surfactants. *Chemistry of Materials* **2004,** *16* (13), 2509-2511.

27. (a) Abdelmoti, L. G.; Zamborini, F. P., Potential-Controlled Electrochemical Seed-Mediated Growth of Gold Nanorods Directly on Electrode Surfaces. *Langmuir* **2010,** *26* (16), 13511-13521; (b) Rodríguez-Sánchez, L.; Blanco, M. C.; López-Quintela, M. A., Electrochemical Synthesis of Silver Nanoparticles. *The Journal of Physical Chemistry B* **2000,** *104* (41), 9683-9688.

28. Yin, B.; Ma, H.; Wang, S.; Chen, S., Electrochemical Synthesis of Silver Nanoparticles under Protection of Poly(N-vinylpyrrolidone). *The Journal of Physical Chemistry B* **2003,** *107* (34), 8898-8904.

29. Meyre, M.-E.; Tréguer-Delapierre, M.; Faure, C., Radiation-Induced Synthesis of Gold Nanoparticles within Lamellar Phases. Formation of Aligned Colloidal Gold by Radiolysis. *Langmuir* **2008,** *24* (9), 4421-4425.

30. (a) Han, M. Y.; Quek, C. H., Photochemical Synthesis in Formamide and Room-Temperature Coulomb Staircase Behavior of Size-Controlled Gold Nanoparticles. *Langmuir* **1999,** *16* (2), 362-367; (b) Pietrobon, B.; Kitaev, V., Photochemical Synthesis of Monodisperse Size-Controlled Silver Decahedral Nanoparticles and Their Remarkable Optical Properties. *Chemistry of Materials* **2008,** *20* (16), 5186-5190; (c) Nemamcha, A.; Rehspringer, J.-L.; Khatmi, D., Synthesis of Palladium Nanoparticles by Sonochemical Reduction of Palladium(II) Nitrate in Aqueous Solution. *The Journal of Physical Chemistry B* **2005,** *110* (1), 383-387; (d) Anandan, S.; Grieser, F.; Ashokkumar, M., Sonochemical Synthesis of Au−Ag Core−Shell Bimetallic Nanoparticles. *The Journal of Physical Chemistry C* **2008,** *112* (39), 15102-15105; (e) Su, C.-H.; Wu, P.-L.; Yeh, C.-S., Sonochemical Synthesis of Well-Dispersed Gold Nanoparticles at the Ice Temperature. *The Journal of Physical Chemistry B* **2003,** *107* (51), 14240-14243; (f) Carrasco, N.; Schmitz-Afonso, I.; Bonnet, J. Y.; Quirico, E.; Thissen, R.; Dutuit, O.; Bagag, A.; Laprévote, O.; Buch, A.; Giulani, A.; Adandé, G.; Ouni, F.; Hadamcik, E.; Szopa, C.; Cernogora, G., Chemical Characterization of Titan's Tholins: Solubility, Morphology and Molecular Structure Revisited†. *The Journal of Physical Chemistry A* **2009,** *113* (42), 11195-11203; (g) Kundu, S.; Wang, K.; Liang, H., Size-Selective Synthesis and Catalytic Application of Polyelectrolyte Encapsulated Gold Nanoparticles Using Microwave Irradiation. *The Journal of Physical Chemistry C* **2009,** *113* (13), 5157-5163; (h) Harpeness, R.; Gedanken, A., Microwave Synthesis of Core−Shell Gold/Palladium Bimetallic Nanoparticles. *Langmuir* **2004,** *20* (8), 3431-3434.

31. Tanford, C., Micelle shape and size. *The Journal of Physical Chemistry* **1972,** *76* (21), 3020-3024.

32. (a) Khanal, A.; Inoue, Y.; Yada, M.; Nakashima, K., Synthesis of Silica Hollow Nanoparticles Templated by Polymeric Micelle with Core−Shell−Corona Structure. *Journal of the American Chemical Society* **2007,** *129* (6), 1534-1535; (b) Setua, P.; Chakraborty, A.; Seth, D.; Bhatta, M. U.; Satyam, P. V.; Sarkar, N., Synthesis, Optical Properties, and Surface Enhanced Raman Scattering of Silver Nanoparticles in Nonaqueous Methanol Reverse Micelles. *The Journal of Physical Chemistry C* **2007,** *111* (10), 3901-3907.

33. Khan, Z.; Al-Thabaiti, S. A.; El-Mossalamy, E.; Obaid, A., Studies on the kinetics of growth of silver nanoparticles in different surfactant solutions. *Colloids and Surfaces B: Biointerfaces* **2009,** *73* (2), 284-288.

34. Kalasad, M. N.; Rabinal, M. K.; Mulimani, B. G., Ambient Synthesis and Characterization of High-Quality CdSe Quantum Dots by an Aqueous Route. *Langmuir* **2009,** *25* (21), 12729-12735.

35. Wu, Z. G.; Munoz, M.; Montero, O., The synthesis of nickel nanoparticles by hydrazine reduction. *Advanced Powder Technology* **2010,** *21* (2), 165-168.

36. Khanna, P. K.; Gokhale, R.; Subbarao, V. V. V. S.; Vishwanath, A. K.; Das, B. K.; Satyanarayana, C. V. V., PVA stabilized gold nanoparticles by use of unexplored albeit conventional reducing agent. *Materials Chemistry and Physics* **2005,** *92* (1), 229-233.

37. Brust, M.; Walker, M.; Bethell, D.; Schiffrin, D. J.; Whyman, R., Synthesis of thiol-derivatised gold nanoparticles in a two-phase Liquid-Liquid system. *Journal of the Chemical Society, Chemical Communications* **1994,** (7), 801-802.

38. Giersig, M.; Mulvaney, P., Formation of ordered two-dimensional gold colloid lattices by electrophoretic deposition. *The Journal of Physical Chemistry* **1993,** *97* (24), 6334-6336.

39. Leff, D. V.; Brandt, L.; Heath, J. R., Synthesis and Characterization of Hydrophobic, Organically-Soluble Gold Nanocrystals Functionalized with Primary Amines. *Langmuir* **1996,** *12* (20), 4723-4730.

40. Premkumar, T.; Kim, D.; Lee, K.; Geckeler, K. E., Polysorbate 80 as a Tool: Synthesis of Gold Nanoparticles. *Macromolecular Rapid Communications* **2007,** *28* (7), 888-893.

41. Jagannathan, R.; Poddar, P.; Prabhune, A., Cephalexin-Mediated Synthesis of Quasi-Spherical and Anisotropic Gold Nanoparticles and Their in Situ Capping by the Antibiotic. *The Journal of Physical Chemistry C* **2007,** *111* (19), 6933-6938.

42. Chen, X.; Chen, C.-B.; Udalagama, Chammika N. B.; Ren, M.; Fong, Kah E.; Yung, Lin Y. L.; Giorgia, P.; Bettiol, Andrew A.; Watt, F., High-Resolution 3D Imaging and Quantification of Gold Nanoparticles in a Whole Cell Using Scanning Transmission Ion Microscopy. *Biophysical Journal* **2013,** *104* (7), 1419-1425.

43. Niu. J, Z. T. a. L. Z., One-step seed-mediated growth of 30–150 nm quasispherical gold nanoparticles with 2-mercaptosuccinic acid as a new reducing agent *Nanotechnology* **2007,** *18* (325607).

44. Aiken Iii, J. D.; Lin, Y.; Finke, R. G., A perspective on nanocluster catalysis: polyoxoanion and (n-C4H9)4N+ stabilized Ir(0)∼300 nanocluster 'soluble heterogeneous catalysts'. *Journal of Molecular Catalysis A: Chemical* **1996,** *114* (1–3), 29-51.

45. Freund, P. L.; Spiro, M., Colloidal catalysis: the effect of sol size and concentration. *The Journal of Physical Chemistry* **1985,** *89* (7), 1074-1077.

46. Chow, M.; Zukoski, C., Gold sol formation mechanisms: role of colloidal stability. *Journal of colloid and interface science* **1994,** *165* (1), 97-109.

47. (a) Hoyer, E., F. A. Cotton, G. Wilkinson, advanced inorganic chemistry. 3. Aufl. XXI, 1145 S. 295 Abb., 127 Tab., John Wiley & Sons Ltd., London-New York 1972. £ 6,50. *Journal für Praktische Chemie* **1973,** *315* (5), 991-992; (b) Cha, D. Y.; Parravano, G., Surface reactivity of supported gold: I. Oxygen transfer between CO and CO2. *Journal of Catalysis* **1970,** *18* (2), 200-211.

48. Bamwenda, G. R.; Tsubota, S.; Nakamura, T.; Haruta, M., *Catal. Lett.* **1997,** *44*, 83.

49. Schubert, M. M.; Hackenberg, S.; van Veen, A. C.; Muhler, M.; Plzak, V.; Behm, R. J., CO Oxidation over Supported Gold Catalysts—"Inert" and "Active" Support Materials and Their Role for the Oxygen Supply during Reaction. *Journal of Catalysis* **2001,** *197* (1), 113-122.

50. (a) Mallick, K.; Scurrell, M. S., *Appl. Catal. A: Gen.* **2003,** *253* (2), 527; (b) Okumura, M.; Nakamura, S.; Tsubota, S.; Nakamura, T.; Azuma, M.; Haruta, M., *Catal. Lett.* **1998,** *51*, 53.

51. Comotti, M.; Li, W.-C.; Spliethoff, B.; Schüth, F., Support Effect in High Activity Gold Catalysts for CO Oxidation. *Journal of the American Chemical Society* **2006,** *128* (3), 917-924.

52. Park, E. D.; Lee, J. S., *J. Catal.* **1999,** *186*, 1.

53. Akita, T.; Tanaka, K.; Tsubota, S.; Haruta, M., Analytical high–resolution TEM study of supported gold catalysts: orientation relationship between Au particles and Ti02 supports. *J. Electron Microsc.* **2000,** *49* (5), 657-662.

54. Lee, S. J.; Gavriilidis, A.; Pankhurst, Q. A.; Kyek, A.; Waner, F. E.; Won, P. C. L.; Yeun, L., *J. Catal.* **2001,** *200*, 298.

55. Boccuzzi, F.; Chiorino, A.; Tsibpta, S.; Haruta, M., *Catal. Lett* **1994,** *29* (null), 225.

56. Haruta, M.; Tsubota, S.; Kobayashi, T.; Kageyama, H.; Genet, M. J.; Delmon, B., *J. Catal.* **1993,** *144* (null), 175.

57. (a) Arrii, S.; Morfin, F.; Renouprez, A. J.; Rousset, J. L., Oxidation of CO on Gold Supported Catalysts Prepared by Laser Vaporization: Direct Evidence of Support Contribution. *Journal of the American Chemical Society* **2004,** *126* (4), 1199-1205; (b) Guczi, L.; Horváth, D.; Pászti, Z.; Tóth, L.; Horváth, Z. E.; Karacs, A.; Petõ, G., Modeling Gold Nanoparticles: Morphology, Electron Structure, and Catalytic Activity in CO Oxidation†. *The Journal of Physical Chemistry B* **2000,** *104* (14), 3183-3193; (c) Grisel, R. J. H.; Nieuwenhuys, B. E., A comparative study of the oxidation of CO and CH4 over Au/MOx/Al2O3 catalysts. *Catalysis Today* **2001,** *64* (1–2), 69-81; (d) Delannoy, L.; Weiher, N.; Tsapatsaris, N.; Beesley, A.; Nchari, L.; Schroeder, S. M.; Louis, C., Reducibility of supported gold (III) precursors: influence of the metal oxide support and consequences for CO oxidation activity. *Topics in Catalysis* **2007,** *44* (1-2), 263-273.

58. Haruta, M.; Date, M., *Appl. Catal. A. Gen.* **2001,** *222*, 427.

59. Haruta, M., Nanoparticulate gold catalysts for low-temperature CO oxidation. *Journal of New Materials for Electrochemical Systems* **2004,** *7* (3), 163-172.

60. Bond, G. C.; Thompson, D. T., Gold-catalysed oxidation of carbon monoxide. *Gold Bulletin* **2000,** *33* (2), 41-50.

61. (a) Mie, G., Beiträge zur Optik trüber Medien, speziell kolloidaler Metallösungen. *Annalen der Physik* **1908,** *330* (3), 377-445; (b) Creighton, J. A.; Eadon, D. G., Ultraviolet-visible absorption spectra of the colloidal metallic elements. *Journal of the Chemical Society, Faraday Transactions* **1991,** *87* (24), 3881-3891; (c) Mulvaney, P., Surface Plasmon Spectroscopy of Nanosized Metal Particles. *Langmuir* **1996,** *12* (3), 788-800.

62. Brennan, UV/VIS Spectroscopy. *University of Pretoria*. **2006**.

63. Xu, H.; Käll, M., Modeling the optical response of nanoparticle-based surface plasmon resonance sensors. *Sensors Actuators B: Chem.* **2002,** *87* (2), 244-249.

64. Cheary, R. W.; Coelho, A., A fundamental parameters approach to X-ray line-profile fitting. *J. Appl. Crystallogr.* **1992,** *25* (2), 109-121.

65. Pearce, R. B., GOLDSTEIN, J., NEWBURY, D., JOY, D., LYMAN, C., ECHLIN, P., LIFSHIN, E., SAWYER, L. & MICHAEL, J. 2003. Scanning Electron Microscopy and X-Ray Microanalysis, 3rd ed. xix + 689 pp. New York, Boston, Dordrecht, London, Moscow: Kluwer Academic/Plenum Publishers. Price Euros 76.00, US $75.00, £48.00 (hard covers). ISBN 0 306 47292 9. *Geol. Mag.* **2003,** *140* (06), 728-729.

66. McMullan, D., Scanning electron microscopy 1928–1965. *Scanning* **1995,** *17* (3), 175-185.

67. D. Briggs, M. P. S., *Practical Surface Analysis, Auger and X-ray Photoelectron Spectroscopy*. Wiley: 1990; Vol. 1 of Practical Surface Analysis, p 674 pages.

68. Levitt, M. H., *Spin dynamics: basics of nuclear magnetic resonance*. John Wiley & Sons: 2001.

69. (a) Mohamed, M. B.; Wang, Z. L.; El-Sayed, M. A., Temperature-dependent size-controlled nucleation and growth of gold nanoclusters. *The Journal of Physical Chemistry A* **1999,** *103* (49), 10255-10259; (b) Jana, N. R.; Gearheart, L.; Murphy, C. J., Seeding growth for size control of 5-40 nm diameter

gold nanoparticles. *Langmuir* **2001,** *17* (22), 6782-6786; (c) Chen, S.; Wang, Z. L.; Ballato, J.; Foulger, S. H.; Carroll, D. L., Monopod, Bipod, Tripod, and Tetrapod Gold Nanocrystals. *J. Am. Chem. Soc.* **2003,** *125* (52), 16186-16187; (d) Sau, T. K.; Murphy, C. J., Room Temperature, High-Yield Synthesis of Multiple Shapes of Gold Nanoparticles in Aqueous Solution. *J. Am. Chem. Soc.* **2004,** *126* (28), 8648-8649; (e) Fan, X.; Guo, Z. R.; Hong, J. M.; Zhang, Y.; Zhang, J. N.; Gu, N., Size-controlled growth of colloidal gold nanoplates and their high-purity acquisition. *Nanotechnology* **2010,** *21* (10), 105602.

70. (a) Simoncelli, S.; Roberti, M. J.; Araoz, B.; Bossi, M. L.; Aramendía, P. F., Mapping the Fluorescence Performance of a Photochromic–Fluorescent System Coupled with Gold Nanoparticles at the Single-Molecule–Single-Particle Level. *J. Am. Chem. Soc.* **2014,** *136* (19), 6878-6880; (b) Zhang, K.; Zhu, X.; Jia, F.; Auyeung, E.; Mirkin, C. A., Temperature-Activated Nucleic Acid Nanostructures. *J. Am. Chem. Soc.* **2013,** *135* (38), 14102-14105; (c) Degliangeli, F.; Kshirsagar, P.; Brunetti, V.; Pompa, P. P.; Fiammengo, R., Absolute and Direct MicroRNA Quantification Using DNA–Gold Nanoparticle Probes. *J. Am. Chem. Soc.* **2014,** *136* (6), 2264-2267; (d) Parry, A. L.; Clemson, N. A.; Ellis, J.; Bernhard, S. S. R.; Davis, B. G.; Cameron, N. R., 'Multicopy Multivalent' Glycopolymer-Stabilized Gold Nanoparticles as Potential Synthetic Cancer Vaccines. *J. Am. Chem. Soc.* **2013,** *135* (25), 9362-9365; (e) Bresee, J.; Bond, C. M.; Worthington, R. J.; Smith, C. A.; Gifford, J. C.; Simpson, C. A.; Carter, C. J.; Wang, G.; Hartman, J.; Osbaugh, N. A.; Shoemaker, R. K.; Melander, C.; Feldheim, D. L., Nanoscale Structure–Activity Relationships, Mode of Action, and Biocompatibility of Gold Nanoparticle Antibiotics. *J. Am. Chem. Soc.* **2014,** *136* (14), 5295-5300.

71. (a) Haruta, M., Chance and Necessity: My Encounter with Gold Catalysts. *Angew. Chem. Int. Ed.* **2014,** *53* (1), 52-56; (b) Liu, P.; Hensen, E. J. M., Highly Efficient and Robust Au/MgCuCr2O4 Catalyst for Gas-Phase Oxidation of Ethanol to Acetaldehyde. *J. Am. Chem. Soc.* **2013,** *135* (38), 14032-14035; (c) Kumar, M.; Jasinski, J.; Hammond, G. B.; Xu, B., Alkyne/Alkene/Allene-Induced Disproportionation of Cationic Gold(I) Catalyst. *Chem. Eur. J.* **2014,** *20* (11), 3113-3119; (d) Wang, W.; Kumar, M.; Hammond, G. B.; Xu, B., Enhanced Reactivity in Homogeneous Gold Catalysis through Hydrogen Bonding. *Org. Lett.* **2014,** *16* (2), 636-639; (e) Kumar, M.; Scobie, M.; Mashuta, M. S.; Hammond, G. B.; Xu, B., Gold-Catalyzed Addition of N-Hydroxy Heterocycles to Alkynes and Subsequent 3,3-Sigmatropic Rearrangement. *Org. Lett.* **2013,** *15* (4), 724-727; (f) Malhotra, D.; Liu, L.-P.; Mashuta, M. S.; Hammond, G. B., Gold-Catalyzed Annulations of 2-Alkynyl Benzaldehydes with Vinyl Ethers: Synthesis of Dihydronaphthalene, Isochromene, and Bicyclo[2.2.2]octane Derivatives. *Chem. Eur. J.* **2013,** *19* (12), 4043-4050; (g) Wang, W.; Hammond, G. B.; Xu, B., Ligand Effects and Ligand Design in Homogeneous Gold(I) Catalysis. *J. Am. Chem. Soc.* **2012,** *134* (12), 5697-5705; (h) Liu, L.-P.; Hammond, G. B., Gold-Catalyzed Cascade Annulations of 2-(Ynol)aryl Aldehydes: Facile Synthesis of Benzochromanes and Benzobicyclo[n.3.1]acetals. *Org. Lett.* **2010,** *12* (20), 4640-4643; (i) Boisselier, E.; Astruc, D., Gold nanoparticles in nanomedicine: preparations, imaging, diagnostics, therapies and toxicity. *Chem. Soc. Rev.* **2009,** *38* (6), 1759-1782; (j) Lal, S.; Clare, S. E.; Halas, N. J., Nanoshell-enabled photothermal cancer therapy: impending clinical impact. *Acc. Chem. Res.* **2008,** *41* (12), 1842-1851.

72. Turkevich, J.; Stevenson, P. C.; Hillier, J., *Discuss. Faraday Soc.* **1951,** *11*, 55.

73. (a) Millstone, J. E.; Park, S.; Shuford, K. L.; Qin, L.; Schatz, G. C.; Mirkin, C. A., Observation of a Quadrupole Plasmon Mode for a Colloidal Solution of Gold Nanoprisms. *J. Am. Chem. Soc.* **2005,** *127* (15), 5312-5313; (b) Grzelczak, M.; Perez-Juste, J.; Mulvaney, P.; Liz-Marzan, L. M., Shape control in gold nanoparticle synthesis. *Chem. Soc. Rev.* **2008,** *37* (9), 1783-1791; (c) Si, S.; Leduc, C.; Delville, M. H.; Lounis, B., Short gold nanorod growth revisited: the critical role of the bromide counterion. *Chemphyschem* **2012,** *13* (1), 193-202.

74. (a) Brown, K. R.; Walter, D. G.; Natan, M. J., Seeding of colloidal Au nanoparticle solutions. 2. Improved control of particle size and shape. *Chem. Mater.* **2000,** *12* (2), 306-313; (b) Male, K. B.; Li, J.; Bun, C. C.; Ng, S.-C.; Luong, J. H. T., Synthesis and Stability of Fluorescent Gold Nanoparticles by Sodium Borohydride in the Presence of Mono-6-deoxy-6-pyridinium-β-cyclodextrin Chloride. *J. Phys. Chem C* **2008,** *112* (2), 443-451.

75. (a) Meltzer, S.; Resch, R.; Koel, B. E.; Thompson, M. E.; Madhukar, A.; Requicha, A. A. G.; Will, P., Fabrication of Nanostructures by Hydroxylamine Seeding of Gold Nanoparticle Templates. *Langmuir* **2001,** *17* (5), 1713-1718; (b) Cao, L.; Zhu, T.; Liu, Z., Formation mechanism of nonspherical gold nanoparticles during seeding growth: Roles of anion adsorption and reduction rate. *J. Colloid Interface Sci.* **2006,** *293* (1), 69-76.

76. Jana, N. R.; Gearheart, L.; Murphy, C. J., *J. Phys. Chem. B* **2001,** *105*, 4065.

77. Badwaik, V. D.; Bartonojo, J. J.; Evans, J. W.; Sahi, S. V.; Willis, C. B.; Dakshinamurthy, R., Single-Step Biofriendly Synthesis of Surface Modifiable, Near-Spherical Gold Nanoparticles for Applications in Biological Detection and Catalysis. *Langmuir* **2011,** *27* (9), 5549-5554.

78. (a) Turkevich, J.; Stevenson, P. C.; Hillier, J., THE FORMATION OF COLLOIDAL GOLD. *J. Phys. Chem.* **1953,** *57* (7), 670-673; (b) Saha, K.; Agasti, S. S.; Kim, C.; Li, X.; Rotello, V. M., Gold Nanoparticles in Chemical and Biological Sensing. *Chem. Rev.* **2012,** *112* (5), 2739-2779; (c) Turkevich, J., *Gold Bull.* **1985,** *18* (null), 86.

79. (a) Dávila-Ibáñez, A. B.; Salgueiriño, V., Chemical and Kinetically Controllable Nucleation, Aggregation-Coalescence, and Ostwald Ripening Processes in the Synthesis of Magnetic Co–B Nanoparticles. *J. Phys. Chem C* **2013,** *117* (9), 4859-4865; (b) Mpourmpakis, G.; Vlachos, D. G., Growth Mechanisms of Metal Nanoparticles via First Principles. *Physical Review Letters* **2009,** *102* (15), 155505.

80. (a) Abdukayum, A.; Chen, J.-T.; Zhao, Q.; Yan, X.-P., Functional Near Infrared-Emitting Cr3+/Pr3+ Co-Doped Zinc Gallogermanate Persistent Luminescent Nanoparticles with Superlong Afterglow for in Vivo Targeted Bioimaging. *J. Am. Chem. Soc.* **2013,** *135* (38), 14125-14133; (b) Tian, Z. R. R.; Voigt, J. A.; Liu, J.; McKenzie, B.; McDermott, M. J.; Rodriguez, M. A.; Konishi, H.; Xu, H. F., Complex and oriented ZnO nanostructures. *Nature Materials* **2003,** *2* (12), 821-826.

81. Bohren, C. F.; Huffman, D. R., *Absorption and scattering of light by small particles*. John Wiley & Sons: 2008.

82. Green, M. L. H., A new approach to the formal classification of covalent compounds of the elements. *J. Organomet. Chem.* **1995,** *500* (1–2), 127-148.

83. Faraday, M., The Bakerian Lecture: Experimental Relations of Gold (and Other Metals) to Light. *Philosophical Transactions of the Royal Society of London* **1857,** *147*, 145-181.

84. (a) Daniel, M.-C.; Astruc, D., Gold nanoparticles: assembly, supramolecular chemistry, quantum-size-related properties, and applications toward biology, catalysis, and nanotechnology. *Chemical reviews* **2004,** *104* (1), 293-346; (b) Clark, J. N.; Beitra, L.; Xiong, G.; Higginbotham, A.; Fritz, D. M.; Lemke, H. T.; Zhu, D.; Chollet, M.; Williams, G. J.; Messerschmidt, M.; Abbey, B.; Harder, R. J.; Korsunsky, A. M.; Wark, J. S.; Robinson, I. K., Ultrafast Three-Dimensional Imaging of Lattice Dynamics in Individual Gold Nanocrystals. *Science* **2013,** *341* (6141), 56-59; (c) Langille, M. R.; Zhang, J.; Personick, M. L.; Li, S.; Mirkin, C. A., Stepwise Evolution of Spherical Seeds into 20-Fold Twinned Icosahedra. *Science* **2012,** *337* (6097), 954-957; (d) Pineider, F.; Campo, G.; Bonanni, V.; Fernandez, C. d. J.; Mattei, G.; Caneschi, A.; Gatteschi, D.; Sangregorio, C., Circular Magnetoplasmonic Modes in Gold Nanoparticles. *Nano Lett.* **2013,** *13* (10), 4785-4789; (e) Guan, Z.; Gao, N.; Jiang, X.-F.; Yuan, P.; Han, F.; Xu, Q.-H., Huge Enhancement in Two-Photon Photoluminescence of Au Nanoparticle Clusters Revealed by Single-Particle Spectroscopy. *J. Am. Chem. Soc.* **2013,** *135* (19), 7272-7277; (f) Woodham, A. P.; Meijer, G.; Fielicke, A., Charge Separation Promoted Activation of Molecular Oxygen by Neutral Gold Clusters. *J. Am. Chem. Soc.* **2013,** *135* (5), 1727-1730; (g) Liu, H.; Dong, C.; Ren, J., Tempo-Spatially Resolved Scattering Correlation Spectroscopy under Dark-Field Illumination and Its Application to Investigate Dynamic Behaviors of Gold Nanoparticles in Live Cells. *J. Am. Chem. Soc.* **2014,** *136* (7), 2775-2785; (h) Li, N.; Zhao, P.; Astruc, D.,

Anisotropic Gold Nanoparticles: Synthesis, Properties, Applications, and Toxicity. *Angew. Chem. Int. Ed.* **2014,** *53* (7), 1756-1789.

85. (a) Kim, Y.; Zhu, J.; Yeom, B.; Di Prima, M.; Su, X. L.; Kim, J. G.; Yoo, S. J.; Uher, C.; Kotov, N. A., Stretchable nanoparticle conductors with self-organized conductive pathways. *Nature* **2013,** *500* (7460), 59-U77; (b) Degliangeli, F.; Kshirsagar, P.; Brunetti, V.; Pompa, P. P.; Fiammengo, R., Absolute and Direct MicroRNA Quantification Using DNA-Gold Nanoparticle Probes. *J. Am. Chem. Soc.* **2014,** *136* (6), 2264-2267; (c) Zhu, W.; Michalsky, R.; Metin, O.; Lv, H.; Guo, S.; Wright, C. J.; Sun, X.; Peterson, A. A.; Sun, S., Monodisperse Au Nanoparticles for Selective Electrocatalytic Reduction of CO2 to CO. *J. Am. Chem. Soc.* **2013,** *135* (45), 16833-16836; (d) Cano, I.; Chapman, A. M.; Urakawa, A.; van Leeuwen, P. W. N. M., Air-Stable Gold Nanoparticles Ligated by Secondary Phosphine Oxides for the Chemoselective Hydrogenation of Aldehydes: Crucial Role of the Ligand. *J. Am. Chem. Soc.* **2014,** *136* (6), 2520-2528; (e) Li, G.; Zeng, C.; Jin, R., Thermally Robust Au99(SPh)42 Nanoclusters for Chemoselective Hydrogenation of Nitrobenzaldehyde Derivatives in Water. *J. Am. Chem. Soc.* **2014,** *136* (9), 3673-3679; (f) Wang, S.; Zhao, Q.; Wei, H.; Wang, J.-Q.; Cho, M.; Cho, H. S.; Terasaki, O.; Wan, Y., Aggregation-Free Gold Nanoparticles in Ordered Mesoporous Carbons: Toward Highly Active and Stable Heterogeneous Catalysts. *J. Am. Chem. Soc.* **2013,** *135* (32), 11849-11860.

86. Turkevich, J., *Gold Bull.* **1985,** *18*, 86.

87. Ji, X.; Song, X.; Li, J.; Bai, Y.; Yang, W.; Peng, X., Size control of gold nanocrystals in citrate reduction: The third role of citrate. *J. Am. Chem. Soc.* **2007,** *129* (45), 13939-13948.

88. (a) Ojea-Jimenez, I.; Campanera, J. M., Molecular Modeling of the Reduction Mechanism in the Citrate Mediated Synthesis of Gold Nanoparticles. *Journal of Physical Chemistry C* **2012,** *116* (44), 23682-23691; (b) Doyen, M.; Bartik, K.; Bruylants, G., UV-Vis and NMR study of the formation of gold nanoparticles by citrate reduction: Observation of gold-citrate aggregates. *J. Colloid Interface Sci.* **2013,** *399*, 1-5; (c) Shiba, F., Size control of monodisperse Au nanoparticles synthesized via a citrate reduction process associated with a pH-shifting procedure. *Crystengcomm* **2013,** *15* (42), 8412-8415.

89. (a) Polte, J.; Ahner, T. T.; Delissen, F.; Sokolov, S.; Emmerling, F.; Thuenemann, A. F.; Kraehnert, R., Mechanism of Gold Nanoparticle Formation in the Classical Citrate Synthesis Method Derived from Coupled In Situ XANES and SAXS Evaluation. *J. Am. Chem. Soc.* **2010,** *132* (4), 1296-1301; (b) Chow, M. K.; Zukoski, C. F., GOLD SOL FORMATION MECHANISMS - ROLE OF COLLOIDAL STABILITY. *J. Colloid Interface Sci.* **1994,** *165* (1), 97-109; (c) Rodriguez-Gonzalez, B.; Mulvaney, P.; Liz-Marzan, L. M., An electrochemical model for gold colloid formation via citrate reduction. *Zeitschrift Fur Physikalische Chemie-International Journal of Research in Physical Chemistry & Chemical Physics* **2007,** *221* (3), 415-426; (d) Kumar, S.; Gandhi, K. S.; Kumar, R., Modeling of formation of gold nanoparticles by citrate method. *Ind. Eng. Chem. Res.* **2007,** *46* (10), 3128-3136; (e) Ciganda, R.; Li, N.; Deraedt, C.; Gatard, S.; Zhao, P.; Salmon, L.; Hernández, R.; Ruiz, J.; Astruc, D., Gold nanoparticles as electron reservoir redox catalysts for 4-nitrophenol reduction: a strong stereoelectronic ligand influence. *Chem. Commun.* **2014,** *50* (70), 10126-10129.

90. (a) Biggs, S.; Mulvaney, P.; Zukoski, C. F.; Grieser, F., STUDY OF ANION ADSORPTION AT THE GOLD-AQUEOUS SOLUTION INTERFACE BY ATOMIC-FORCE MICROSCOPY. *J. Am. Chem. Soc.* **1994,** *116* (20), 9150-9157; (b) Lin, Y.; Pan, G. B.; Su, G. J.; Fang, X. H.; Wan, L. J.; Bai, C. L., Study of citrate adsorbed on the Au(111) surface by scanning probe microscopy. *Langmuir* **2003,** *19* (24), 10000-10003; (c) Park, J.-W.; Shumaker-Parry, J. S., Structural Study of Citrate Layers on Gold Nanoparticles: Role of Intermolecular Interactions in Stabilizing Nanoparticles. *J. Am. Chem. Soc.* **2014,** *136* (5), 1907-1921; (d) Wulandari, P.; Nagahiro, T.; Michioka, K.; Tamada, K.; Ishibashi, K.-i.; Kimura, Y.; Niwano, M., Coordination of carboxylate on metal nanoparticles characterized by Fourier transform infrared spectroscopy. *Chem. Lett.* **2008,** *37* (8), 888-889; (e) Arora, H.; Mukherjee, R., Coordination polymers using (2-pyridyl)alkylamine-appended carboxylates: magnetic properties. *New J. Chem.* **2010,** *34* (11), 2357-2365.

91. Kunze, J.; Burgess, I.; Nichols, R.; Buess-Herman, C.; Lipkowski, J., Electrochemical evaluation of citrate adsorption on Au(111) and the stability of citrate-reduced gold colloids. *J. Electroanal. Chem.* **2007,** *599* (2), 147-159.

92. (a) Floate, S.; Hosseini, M.; Arshadi, M. R.; Ritson, D.; Young, K. L.; Nichols, R. J., An in-situ infrared spectroscopic study of the adsorption of citrate on Au(111) electrodes. *J. Electroanal. Chem.* **2003,** *542*, 67-74; (b) McMahon, B. W.; Perez, J. P. L.; Yu, J.; Boatz, J. A.; Anderson, S. L., Synthesis of Nanoparticles from Malleable and Ductile Metals Using Powder-Free, Reactant-Assisted Mechanical Attrition. *ACS Applied Materials & Interfaces* **2014,** *6* (22), 19579-19591.

93. Berná, A.; Delgado, J. M.; Orts, J. M.; Rodes, A.; Feliu, J. M., Spectroelectrochemical study of the adsorption of acetate anions at gold single crystal and thin-film electrodes. *Electrochimica Acta* **2008,** *53* (5), 2309-2321.

94. Marbella, L. E.; Millstone, J. E., NMR Techniques for Noble Metal Nanoparticles. *Chem. Mater.* **2015**.

95. (a) Pulkkinen, P. M. S.; Wiktorowicz, S.; Aseyev, V.; Tenhu, H., Complexation of calix[4]arene protected gold nanoparticles with pyridinium and bipyridinium compounds. *RSC Advances* **2013,** *3* (3), 733-742; (b) Carr, J. A.; Wang, H.; Abraham, A.; Gullion, T.; Lewis, J. P., l-Cysteine Interaction with Au55 Nanoparticle. *J. Phys. Chem C* **2012,** *116* (49), 25816-25823; (c) Yu, C.; Zhu, L.; Zhang, R.; Wang, X.; Guo, C.; Sun, P.; Xue, G., Investigation on the Mechanism of the Synthesis of Gold(I) Thiolate Complexes by NMR. *J. Phys. Chem C* **2014,** *118* (19), 10434-10440; (d) Hu, H.; Reven, L.; Rey, A., First-Principles Density Functional Theory (DFT) Study of Gold Nanorod and Its Interaction with Alkanethiol Ligands. *J. Phys. Chem B* **2013,** *117* (41), 12625-12631; (e) Zelakiewicz, B. S.; de Dios, A. C.; Tong, 13C NMR Spectroscopy of 13C1-Labeled Octanethiol-Protected Au Nanoparticles: Shifts, Relaxations, and Particle-Size Effect. *J. Am. Chem. Soc.* **2002,** *125* (1), 18-19; (f) de Dios, A. C.; Abraham, A. E., 13C chemical shifts in octanethiols adsorbed on gold: a theoretical study. *J. Mol. Struct.* **2002,** *602–603* (0), 209-214; (g) Badia, A.; Demers, L.; Dickinson, L.; Morin, F.; Lennox, R.; Reven, L., Gold-sulfur interactions in alkylthiol self-assembled monolayers formed on gold nanoparticles studied by solid-state NMR. *J. Am. Chem. Soc.* **1997,** *119* (45), 11104-11105; (h) Badia, A.; Gao, W.; Singh, S.; Demers, L.; Cuccia, L.; Reven, L., Structure and chain dynamics of alkanethiol-capped gold colloids. *Langmuir* **1996,** *12* (5), 1262-1269; (i) Abraham, A.; Mihaliuk, E.; Kumar, B.; Legleiter, J.; Gullion, T., Solid-State NMR Study of Cysteine on Gold Nanoparticles. *J. Phys. Chem C* **2010,** *114* (42), 18109-18114; (j) Zhang, B.; Yan, B., Analytical strategies for characterizing the surface chemistry of nanoparticles. *Anal. Bioanal. Chem.* **2010,** *396* (3), 973-982; (k) Zhou, H.; Du, F.; Li, X.; Zhang, B.; Li, W.; Yan, B., Characterization of Organic Molecules Attached to Gold Nanoparticle Surface Using High Resolution Magic Angle Spinning 1H NMR. *J. Phys. Chem C* **2008,** *112* (49), 19360-19366; (l) Schmitt, H.; Badia, A.; Dickinson, L.; Reven, L.; Lennox, R. B., The Effect of Terminal Hydrogen Bonding on the Structure and Dynamics of Nanoparticle Self-Assembled Monolayers (SAMs): An NMR Dynamics Study. *Adv. Mater.* **1998,** *10* (6), 475-480; (m) Pérez, Y.; Mann, E.; Herradón, B., Preparation and characterization of gold nanoparticles capped by peptide–biphenyl hybrids. *J. Colloid Interface Sci.* **2011,** *359* (2), 443-453; (n) Milette, J.; Toader, V.; Soulé, E. R.; Lennox, R. B.; Rey, A. D.; Reven, L., A Molecular and Thermodynamic View of the Assembly of Gold Nanoparticles in Nematic Liquid Crystal. *Langmuir* **2013,** *29* (4), 1258-1263.

96. (a) Sharma, R.; Taylor, R. E.; Bouchard, L.-S., Intramolecular Ligand Dynamics in d15-(PPh3)-Capped Gold Nanoparticles Investigated by 2H NMR. *J. Phys. Chem C* **2011,** *115* (8), 3297-3303; (b) Sharma, R.; Holland, G. P.; Solomon, V. C.; Zimmermann, H.; Schiffenhaus, S.; Amin, S. A.; Buttry, D. A.; Yarger, J. L., NMR Characterization of Ligand Binding and Exchange Dynamics in Triphenylphosphine-Capped Gold Nanoparticles. *J. Phys. Chem C* **2009,** *113* (37), 16387-16393; (c) Fiurasek, P.; Reven, L., Phosphonic and Sulfonic Acid-Functionalized Gold Nanoparticles: A Solid-State NMR Study. *Langmuir* **2007,** *23* (5), 2857-2866; (d) Gutmann, T.; Grünberg, A.; Rothermel, N.; Werner, M.; Srour, M.; Abdulhussain, S.; Tan, S.; Xu, Y.; Breitzke, H.; Buntkowsky, G., Solid-state NMR concepts for the investigation of supported transition metal catalysts and nanoparticles. *Solid State Nucl. Magn.*

Reson. **2013,** *55–56* (0), 1-11; (e) Pawsey, S.; McCormick, M.; De Paul, S.; Graf, R.; Lee, Y. S.; Reven, L.; Spiess, H. W., 1H Fast MAS NMR Studies of Hydrogen-Bonding Interactions in Self-Assembled Monolayers. *J. Am. Chem. Soc.* **2003,** *125* (14), 4174-4184.

97. Rodriguez-Castillo, M.; Laurencin, D.; Tielens, F.; van der Lee, A.; Clement, S.; Guari, Y.; Richeter, S., Reactivity of gold nanoparticles towards N-heterocyclic carbenes. *Dalton Transactions* **2014,** *43* (16), 5978-5982.

98. (a) Gutmann, T.; Bonnefille, E.; Breitzke, H.; Debouttiere, P.-J.; Philippot, K.; Poteau, R.; Buntkowsky, G.; Chaudret, B., Investigation of the surface chemistry of phosphine-stabilized ruthenium nanoparticles - an advanced solid-state NMR study. *PCCP* **2013,** *15* (40), 17383-17394; (b) Crudden, C. M.; Horton, J. H.; Ebralidze, I. I.; Zenkina, O. V.; McLean, A. B.; Drevniok, B.; She, Z.; Kraatz, H.-B.; Mosey, N. J.; Seki, T.; Keske, E. C.; Leake, J. D.; Rousina-Webb, A.; Wu, G., Ultra stable self-assembled monolayers of N-heterocyclic carbenes on gold. *Nat. Chem.* **2014,** *6* (5), 409-414; (c) Green, M. L. H.; Parkin, G., Application of the Covalent Bond Classification Method for the Teaching of Inorganic Chemistry. *J. Chem. Educ.* **2014,** *91* (6), 807-816.

99. (a) Dozol, H.; Mériguet, G.; Ancian, B.; Cabuil, V.; Xu, H.; Wang, D.; Abou-Hassan, A., On the Synthesis of Au Nanoparticles Using EDTA as a Reducing Agent. *J. Phys. Chem C* **2013,** *117* (40), 20958-20966; (b) Dorris, A.; Rucareanu, S.; Reven, L.; Barrett, C. J.; Lennox, R. B., Preparation and Characterization of Polyelectrolyte-Coated Gold Nanoparticles. *Langmuir* **2008,** *24* (6), 2532-2538.

100. (a) Sachleben, J. R.; Colvin, V.; Emsley, L.; Wooten, E. W.; Alivisatos, A. P., Solution-State NMR Studies of the Surface Structure and Dynamics of Semiconductor Nanocrystals. *J. Phys. Chem B* **1998,** *102* (50), 10117-10128; (b) Li, Q.; Kirkpatrick, R. J., Organic anions in layered double hydroxides: An experimental investigation of citrate hydrotalcite. *American Mineralogist* **2007,** *92* (2-3), 397-402; (c) Polito, L.; Colombo, M.; Monti, D.; Melato, S.; Caneva, E.; Prosperi, D., Resolving the Structure of Ligands Bound to the Surface of Superparamagnetic Iron Oxide Nanoparticles by High-Resolution Magic-Angle Spinning NMR Spectroscopy. *Journal of the American Chemical Society* **2008,** *130* (38), 12712-12724.

101. Doyen, M.; Bartik, K.; Bruylants, G., UV–Vis and NMR study of the formation of gold nanoparticles by citrate reduction: Observation of gold–citrate aggregates. *J. Colloid Interface Sci.* **2013,** *399* (0), 1-5.

102. Delgado, J. M.; Berná, A.; Orts, J. M.; Rodes, A.; Feliu, J. M., In Situ Infrared Study of the Adsorption and Surface Acid−Base Properties of the Anions of Dicarboxylic Acids at Gold Single Crystal and Thin-Film Electrodes. *The Journal of Physical Chemistry C* **2007,** *111* (27), 9943-9952.

103. Provorse, M. R.; Aikens, C. M., Binding of carboxylates to gold nanoparticles: A theoretical study of the adsorption of formate on Au20. *Computational and Theoretical Chemistry* **2012,** *987*, 16-21.

104. Yoon, B.; Häkkinen, H.; Landman, U., Interaction of O2 with Gold Clusters: Molecular and Dissociative Adsorption. *The Journal of Physical Chemistry A* **2003,** *107* (20), 4066-4071.

105. Campbell, C. T., The Energetics of Supported Metal Nanoparticles: Relationships to Sintering Rates and Catalytic Activity. *Accounts of Chemical Research* **2013,** *46* (8), 1712-1719.

106. Schantz, S.; Hoppu, P.; Juppo, A. M., A solid-state NMR study of phase structure, molecular interactions, and mobility in blends of citric acid and paracetamol. *Journal of Pharmaceutical Sciences* **2009,** *98* (5), 1862-1870.

107. Pines, A.; Gibby, M. G.; Waugh, J. S., Proton-Enhanced Nuclear Induction Spectroscopy. A Method for High Resolution NMR of Dilute Spins in Solids. *The Journal of Chemical Physics* **1972,** *56* (4), 1776-1777.

108. Feng, J.; Lee, Y. J.; Kubicki, J. D.; Reeder, R. J.; Phillips, B. L., NMR spectroscopy of citrate in solids: cross-polarization kinetics in weakly coupled systems. *Magn. Reson. Chem.* **2008,** *46* (5), 408-417.

109. Kim, Y.-H.; Kim, S.-K.; Park, J.-G.; Paik, U., Increase in the adsorption density of anionic molecules on ceria for defect-free STI CMP. *J. Electrochem. Soc.* **2010,** *157* (1), H72-H77.

110. Preisenberger, M.; Schier, A.; Schmidbaur, H., (Phosphine)gold(I) trifluoromethanesulfonates, trifluoroacetates and trichlorothioacetates [dagger]. *J. Chem. Soc., Dalton Trans.* **1999,** (10), 1645-1650.

111. van Lenthe, E.; Snijders, J. G.; Baerends, E. J., The zero-order regular approximation for relativistic effects: The effect of spin–orbit coupling in closed shell molecules. *The Journal of Chemical Physics* **1996,** *105* (15), 6505-6516.

112. (a) Pickard, C. J.; Mauri, F., All-electron magnetic response with pseudopotentials: NMR chemical shifts. *Physical Review B* **2001,** *63* (24), 245101; (b) Clark Stewart, J.; Segall Matthew, D.; Pickard Chris, J.; Hasnip Phil, J.; Probert Matt, I. J.; Refson, K.; Payne Mike, C., First principles methods using CASTEP. In *Zeitschrift für Kristallographie*, 2005; Vol. 220, p 567; (c) Yates, J. R.; Pickard, C. J.; Mauri, F., Calculation of NMR chemical shifts for extended systems using ultrasoft pseudopotentials. *Physical Review B* **2007,** *76* (2), 024401; (d) Profeta, M.; Mauri, F.; Pickard, C. J., Accurate First Principles Prediction of 17O NMR Parameters in SiO2: Assignment of the Zeolite Ferrierite Spectrum. *J. Am. Chem. Soc.* **2003,** *125* (2), 541-548.

113. (a) Vanderbilt, D. H., *Phys. Rev. B* **1990,** *41*, 7892; (b) Tkatchenko, A.; Scheffler, M., Accurate Molecular Van Der Waals Interactions from Ground-State Electron Density and Free-Atom Reference Data. *Phys. Rev. Lett.* **2009,** *102* (7), 073005.

114. Wei, K.-T.; Ward, D. L., Sodium acetate trihydrate: a redetermination. *Acta Crystallographica Section B* **1977,** *33* (2), 522-526.

115. Fischer, A. P., G., Acta Cryst. E, **2003,** *E 59*, m1080-m1082.

116. Jones, P., Acetato(triphenylphosphine)gold(I), [Au(C2H3O2)(C18H15P)]. *Acta Crystallographica Section C* **1984,** *40* (8), 1320-1322.

117. Fischer, A.; Palladino, G., Trisodium citrate dihydrate. *Acta Crystallographica Section E* **2003,** *59* (11), m1080-m1082.

118. Harris, R. K., NMR crystallography: the use of chemical shifts. *Solid state sciences* **2004,** *6* (10), 1025-1037.

119. Biella, S.; Castiglioni, G. L.; Fumagalli, C.; Prati, L.; Rossi, M., Application of gold catalysts to selective liquid phase oxidation. *Catal. Today* **2002,** *72* (1–2), 43-49.

120. Hashmi, A. S., Homogeneous gold catalysts and alkynes: A successful liaison. *Gold Bull* **2003,** *36* (1), 3-9.

121. Haruta, M.; Kobayashi, T.; Sano, H.; Yamada, N., *Chem. Lett.* **1987**, 405.

122. Gajan, D.; Guillois, K.; Delichère, P.; Basset, J.-M.; Candy, J.-P.; Caps, V.; Coperet, C.; Lesage, A.; Emsley, L., Gold Nanoparticles Supported on Passivated Silica: Access to an Efficient Aerobic

Epoxidation Catalyst and the Intrinsic Oxidation Activity of Gold. *Journal of the American Chemical Society* **2009,** *131* (41), 14667-14669.

123. Haruta, M.; Ueda, A.; Tsubota, S.; Torres Sanchez, R. M., *Catal. Today* **1996,** *29*, 443.

124. (a) Ueda, A.; Haruta, M., Nitric Oxide Reduction with Hydrogen, Carbon Monoxide, and Hydrocarbons over Gold Catalysts. *Gold Bull* **1999,** *32* (1), 3-11; (b) Seker, E.; Cavataio, J.; Gulari, E.; Lorpongpaiboon, P.; Osuwan, S., Nitric oxide reduction by propene over silver/alumina and silver–gold/alumina catalysts: effect of preparation methods. *Applied Catalysis A: General* **1999,** *183* (1), 121-134; (c) Grisel, R. J. H.; Kooyman, P. J.; Nieuwenhuys, B. E., Influence of the Preparation of Au/Al2O3 on CH4 Oxidation Activity. *J. Catal.* **2000,** *191* (2), 430-437.

125. Centeno, M. A.; Paulis, M.; Montes, M.; Odriozola, J. A., Catalytic combustion of volatile organic compounds on Au/CeO2/Al2O3 and Au/Al2O3 catalysts. *Applied Catalysis A: General* **2002,** *234* (1–2), 65-78.

126. (a) Thompson, D. T., Perspective on industrial and scientific aspects of gold catalysis. *Applied Catalysis A: General* **2003,** *243* (2), 201-205; (b) Thompson, D., New advances in gold catalysis part I. *Gold Bull* **1998,** *31* (4), 111-118.

127. (a) Sanchez, A.; Abbet, S.; Heiz, U.; Schneider, W. D.; Häkkinen, H.; Barnett, R. N.; Landman, U., When Gold Is Not Noble: Nanoscale Gold Catalysts. *The Journal of Physical Chemistry A* **1999,** *103* (48), 9573-9578; (b) Yoon, B.; Häkkinen, H.; Landman, U.; Wörz, A. S.; Antonietti, J.-M.; Abbet, S.; Judai, K.; Heiz, U., Charging effects on bonding and catalyzed oxidation of CO on Au8 clusters on MgO. *Science* **2005,** *307* (5708), 403-407.

128. Lee, S.-J.; Gavriilidis, A., Supported Au Catalysts for Low-Temperature CO Oxidation Prepared by Impregnation. *Journal of Catalysis* **2002,** *206* (2), 305-313.

129. Kozlova, A. P.; Sugiyama, S.; Kozlov, A. I.; Asakura, K.; Iwasawa, Y., Iron-oxide supported gold catalysts derived from gold-phosphine complex Au (PPh 3)(NO 3): state and structure of the support. *J. Catal.* **1998,** *176* (2), 426-438.

130. Okumura, M.; Nakamura, S.; Tsubota, T.; Nakamura, T.; Azuma, M.; Haruta, M., *Catal. Lett.* **1998,** *51*, 53.

131. Mavrikakis, M.; Stoltze, P.; Norskov, J. K., *Catal. Lett.* **2000,** *64*, 101.

132. Grunwaldt, J. D.; Baiker, A., *J. Phys. Chem.* **1999,** *103*, 1002.

133. (a) Lin, S. D.; Bollinger, M.; Vannice, M. A., *Catal. Lett.* **1993,** *17*, 245; (b) Kang, T. M.; Wan, B. Z., *Appl. Catal. A: Gen* **1995,** *128* (null), 53.

134. Foger, K., Dispersed Metal Catalysts. In *Catalysis*, Anderson, J.; Boudart, M., Eds. Springer Berlin Heidelberg: 1984; Vol. 6, pp 227-305.

135. Bond, G., Metal-support and Metal-additive Effects in Catalysis. *Platinum Met. Rev.* **1983,** *27* (1), 16-18.

136. Haruta, M., Catalysis of Gold Nanoparticles Deposited on Metal Oxides. *CATTECH* **2002,** *6* (3), 102-115.

137. Radnik, J.; Mohr, C.; Claus, P., On the origin of binding energy shifts of core levels of supported gold nanoparticles and dependence of pretreatment and material synthesis. *PCCP* **2003,** *5* (1), 172-177.

138. Grunwaldt, J.-D.; Maciejewski, M.; Becker, O. S.; Fabrizioli, P.; Baiker, A., Comparative study of Au/TiO 2 and Au/ZrO 2 catalysts for low-temperature CO oxidation. *J. Catal.* **1999,** *186* (2), 458-469.

139. Lopez, N.; Nørskov, J. K.; Janssens, T. V. W.; Carlsson, A.; Puig-Molina, A.; Clausen, B. S.; Grunwaldt, J. D., The adhesion and shape of nanosized Au particles in a Au/TiO2 catalyst. *J. Catal.* **2004,** *225* (1), 86-94.

140. Haruta, M., Size-and support-dependency in the catalysis of gold. *Catalysis Today* **1997,** *36* (1), 153-166.

141. Haruta, M.; Tsubota, S.; Kobayashi, T.; Kageyama, H.; Genet, M. J.; Delmon, B., *J. Catal.* **1993,** *144*, 175.

142. Valden, M.; Pak, S.; Lai, X.; Goodman, D. W., *Catal. Lett.* **1998,** *56*, 7.

143. (a) Okumura, M.; Tanaka, K.; Ueda, A.; Haruta, M., *Solid State Ionics* **1997,** *95* (null), 143; (b) Valden, M.; Lai, X.; Goodman, D. W., Onset of Catalytic Activity of Gold Clusters on Titania with the Appearance of Nonmetallic Properties. *Science* **1998,** *281* (5383), 1647-1650.

144. Haruta, M., *Catal. Today* **1997,** *36*, 153.

145. Tsubota, S.; Haruta, M.; Kobayashi, T.; Ueda, A.; Nakahara, Y., Preparation of Highly Dispersed Gold on Titanium and Magnesium Oxide. In *Stud. Surf. Sci. Catal.*, G. Poncelet, P. A. J. P. G.; Delmon, B., Eds. Elsevier: 1991; Vol. Volume 63, pp 695-704.

146. Horvath, A.; Beck, A.; Koppany, Z.; Sarkany, A.; Guczi, L., *J. Mol. Catal. A: Chem.* **2002**, 182.

147. Gupta, N.; Tripathi, A., The role of nanosized gold particles in adsorption and oxidation of carbon monoxide over Au/Fe2O3 Catalyst. *Gold Bull* **2001,** *34* (4), 120-128.

148. Boccuzzi, F.; Chiorino, A.; Manzoli, M.; Lu, P.; Akita, T.; Ichikawa, S.; Haruta, M., *J. Catal.* **2001,** *202*, 256.

149. Chang, C.-K.; Chen, Y.-J.; Yeh, C.-t., Characterizations of alumina-supported gold with temperature-programmed reduction. *Applied Catalysis A: General* **1998,** *174* (1–2), 13-23.

150. Ba-Abbad, M. M.; Kadhum, A. A. H.; Mohamad, A. B.; Takriff, M. S.; Sopian, K., Synthesis and catalytic activity of TiO2 nanoparticles for photochemical oxidation of concentrated chlorophenols under direct solar radiation. *Int. J. Electrochem. Sci* **2012,** *7*, 4871-4888.

151. Thamaphat, K.; Limsuwan, P.; Ngotawornchai, B., Phase characterization of TiO2 powder by XRD and TEM. *Kasetsart J.(Nat. Sci.)* **2008,** *42* (5), 357-361.

152. Primo, A.; Corma, A.; García, H., Titania supported gold nanoparticles as photocatalyst. *PCCP* **2011,** *13* (3), 886-910.

153. Lin, C.-H.; Lin, S.; Lee, J.-F., Chlorine Residue in the Au/γ-Al2O3 Prepared by AuCl3 Impregnation—an EXAFS Analysis. *Catal. Lett.* **2003,** *89* (3-4), 235-242.

154. Kosmulski, M., The pH-Dependent Surface Charging and the Points of Zero Charge. *J. Colloid Interface Sci.* **2002,** *253* (1), 77-87.

155. Moreau, F.; Bond, G. C.; Taylor, A. O., Gold on titania catalysts for the oxidation of carbon monoxide: control of pH during preparation with various gold contents. *J. Catal.* **2005,** *231* (1), 105-114.

156. Benfield, R. E., Mean coordination numbers and the non-metal-metal transition in clusters. *J. Chem. Soc., Faraday Trans.* **1992,** *88* (8), 1107-1110.

157. Bergeret, G.; Gallezot, P., Particle Size and Dispersion Measurements. In *Handbook of Heterogeneous Catalysis*, Wiley-VCH Verlag GmbH & Co. KGaA: 2008.

158. Van Hardeveld, R.; Hartog, F., The statistics of surface atoms and surface sites on metal crystals. *Surf. Sci.* **1969,** *15* (2), 189-230.

159. Gavrilina, L. Y.; Vyakhirev, D. A., GAS CHROMATOGRAPHY IN CATALYTIC STUDIES. *Russian Chemical Reviews* **1967,** *36* (2), 135.

160. (a) Sylvestre, J.-P.; Poulin, S.; Kabashin, A. V.; Sacher, E.; Meunier, M.; Luong, J. H. T., Surface Chemistry of Gold Nanoparticles Produced by Laser Ablation in Aqueous Media. *The Journal of Physical Chemistry B* **2004,** *108* (43), 16864-16869; (b) Sault, A. G.; Madix, R. J.; Campbell, C. T., Adsorption of oxygen and hydrogen on Au(110)-(1 × 2). *Surf. Sci.* **1986,** *169* (2–3), 347-356.

161. Park, E. D.; Lee, J. S., Effects of pretreatment conditions on CO oxidation over supported Au catalysts.

162. (a) Qu, Z.; Huang, W.; Cheng, M.; Bao, X., Restructuring and Redispersion of Silver on SiO2 under Oxidizing/Reducing Atmospheres and Its Activity toward CO Oxidation. *J. Phys. Chem B* **2005,** *109* (33), 15842-15848; (b) Ma, Z.; Dai, S., Development of novel supported gold catalysts: A materials perspective. *Nano Research* **2011,** *4* (1), 3-32.

163. (a) Schwank, J., *Gold Bull.* **1983,** *16* (null), 103; (b) Haruta, M.; Yamada, N.; Kobayashi, T.; Iijima, S., *J. Catal.* **1989,** *115*, 301; (c) Haruta, M.; Tsubota, S.; Kageyama, H.; Genet, M. J.; Delmon, B., *J. Catal.* **1993,** *144*, 175.

164. Oh, H.-S.; Yang, J.; Costello, C.; Wang, Y.; Bare, S.; Kung, H.; Kung, M., Selective catalytic oxidation of CO: effect of chloride on supported Au catalysts. *Journal of Catalysis* **2002,** *210* (2), 375-386.

165. Hayashi, T.; Tanaka, K.; Haruta, M., *J. Catal.* **1998,** *178*, 566.

166. Kozlova, P.; Kozlov, I.; Sugiyama, S.; Matsui, Y.; Asakura, K.; Iwasawa, Y., *J. Catal.* **1999,** *181*, 37.

167. (a) Soares, J. C.; Hall, M.; Cristofolini, M.; Bowker, M., The Role of Impurities on the Low Temperature CO Oxidation on Au/TiO2. *Catalysis Letters* **2006,** *109* (1-2), 103-108; (b) Finch, R. M.; Hodge, N. A.; Hutchings, G. J.; Meagher, A.; Pankhurst, Q. A.; Siddiqui, M. R. H.; Wagner, F. E.; Whyman, R., *PhysChemChemPhys* **1999,** *1*, 485.

168. Ilieva, L. I.; Andreeva, D. H.; Andreev, A. A., TPR and TPD investigation of Auα-Fe2O3. *Thermochimica Acta* **1997,** *292* (1–2), 169-174.

169. Bond, G.; Thompson, D., Gold-catalysed oxidation of carbon monoxide. *Gold Bull* **2000,** *33* (2), 41-50.

170. Costello, C. K.; Yang, J. H.; Law, H. Y.; Wang, Y.; Lin, J. N.; Marks, L. D.; Kung, M. C.; Kung, H. H., On the potential role of hydroxyl groups in CO oxidation over Au/Al2O3. *Applied Catalysis A: General* **2003,** *243* (1), 15-24.

171. Wolf, A.; Schüth, F., A systematic study of the synthesis conditions for the preparation of highly active gold catalysts. *Applied Catalysis A: General* **2002,** *226* (1–2), 1-13.

172. Eichele, K.; Wasylishen, R. E. *WSolids1*, 1.19.11; Universität Tübingen, Tübingen, Germany.

173. Engelhardt, G.; Kentgens, A. P. M.; Koller, H.; Samoson, A., Strategies for extracting NMR parameters from ^{23}Na MAS, DOR and MQMAS spectra. A case study for $Na_4P_2O_7$. *Solid State Nucl. Magn. Reson.* **1999,** *15*, 171-180.

174. (a) Fonseca Guerra, C.; Snijders, J. G.; te Velde, G.; Baerends, E. J., Towards an order-*N* DFT method. *Theor. Chem. Acc.* **1998,** *99*, 391-403; (b) te Velde, G.; Bickelhaupt, F. M.; Baerends, E. J.; Fonseca Guerra, C.; van Gisbergen, S. J. A.; Snijders, J. G.; Ziegler, T., Chemistry with ADF. *J. Comp. Chem.* **2001,** *22* (9), 931-967.

175. Suh, I.-K.; Ohta, H.; Waseda, Y., High-temperature thermal expansion of six metallic elements measured by dilatation method and X-ray diffraction. *J. Mat. Sci.* **1988,** *23*, 757-760.

176. Park, J.-W.; Shumaker-Parry, J. S., Structural Study of Citrate Layers on Gold Nanoparticles: Role of Intermolecular Interactions in Stabilizing Nanoparticles. *J. Am. Chem. Soc.* **2014,** *136*, 1907-1921.

177. Singh-Miller, N. E.; Marzari, N., Surface energies, work functions, and surface relaxations of low-index metallic surfaces from first principles. *Phys. Rev. B* **2009,** *80*, 235407.

178. (a) Perdew, J. P.; Burke, K.; Ernzerhof, M., *Phys. Rev. B.* **1996,** *77*, 3865; (b) Perdew, J. P.; Burke, K.; Ernzerhof, M., Generalized Gradient Approximation Made Simple. *Phys. Rev. Lett.* **1997,** *78* (7), 1396.

179. Grimme, S.; Antony, J.; Ehrlich, S.; Krieg, H., A consistent and accurate *ab initio* parametrization of density functional dispersion correction (DFT-D) for the 94 elements H-Pu. *J. Chem. Phys.* **2010,** *132*, 154104.

180. Mura, M.; Gulans, A.; Thonhauser, T.; Kantorovich, L., Role of van der Waals interaction in forming molecule-metal junctions: flat organic molecules on the Au(111) surface. *Phys. Chem. Chem. Phys.* **2010,** *12*, 4759-4767.

181. (a) van Lenthe, E.; Baerends, E. J.; Snijders, J. G., Relativistic regular two-component Hamiltonians. *J. Chem. Phys.* **1993,** *99* (6), 4597-4610; (b) van Lenthe, E.; Baerends, E. J.; Snijders, J. G., Relativistic total energy using regular approximations. *J. Chem. Phys.* **1994,** *101*, 9783-9792; (c) van Lenthe, E.; Ehlers, A.; Baerends, E.-J., Geometry optimizations in the zero order regular approximation for relativistic effects. *J. Chem. Phys.* **1999,** *110*, 8943-8953.

182. (a) Kresse, G.; Hafner, J., *Ab initio* molecular dynamics for liquid metals. *Phys. Rev. B* **1993,** *47* (1), 558-561; (b) Kresse, G.; Hafner, J., *Ab initio* molecular-dynamics simulation of the liquid-metal-amorphous-semiconductor transition in germanium. *Phys. Rev. B* **1994,** *49* (20), 14251-14269; (c) Kresse, G.; Furthmüller, J., Efficiency of ab-initio energy calculations for metals and semiconductors using a plane-wave basis set. *Comput. Mat. Sci.* **1996,** *6*, 15-50; (d) Kresse, G.; Furthmüller, J., Efficient iterative schemes for *ab initio* total-energy calculations using a plane-wave basis set. *Phys. Rev. B* **1996,** *54* (16), 11169-11186.

183. (a) Blöchl, P. E., Projector augmented-wave method. *Phys. Rev. B* **1994,** *50* (24), 17953-17979; (b) Kresse, G.; Joubert, D., From ultrasoft pseudopotentials to the projector augmented-wave method. *Phys. Rev. B* **1999,** *59* (3), 1758-1775.

184. (a) Klamt, A.; Schüürmann, G., COSMO: A New Approach to Dielectric Screening in Solvents with Explicit Expressions for the Screening Energy and its Gradient. *J. Chem. Soc. Perkin Trans. 2* **1993**, 799-805; (b) Klamt, A., Conductor-like Screening Model for Real Solvents: A New Approach to the Quantitative Calculation of Solvation Phenomena. *J. Phys. Chem.* **1995,** *99*, 2224-2235.

185. Provorse, M. R.; Aikens, C. M., Binding of carboxylates to gold nanoparticles: A theoretical study of the adsorption of formate on Au_{20}. *Comput. Theor. Chem.* **2012,** *987*, 16-21.

186. van Lenthe, E.; Snijders, J. G.; Baerends, E. J., The zero-order regular approximation for relativistic effects: The effect of spin-orbit coupling in closed shell molecules. *J. Chem. Phys.* **1996,** *105* (15), 6505-6516.

187. (a) Pickard, C. J.; Mauri, F., All-electron magnetic response with pseudopotentials: NMR chemical shifts. *Phys. Rev. B* **2001,** *63*, 245101; (b) Clark, S. J.; Segall, M. D.; Pickard, C. J.; Hasnip, P. J.; Probert, M. I. J.; Refson, K.; Payne, M. C., First principles methods using CASTEP. *Z. Kristallogr.* **2005,** *220*, 567-570; (c) Yates, J. R.; Pickard, C. J.; Mauri, F., Calculation of NMR chemical shifts for extended systems using ultrasoft pseudopotentials. *Phys. Rev. B* **2007,** *76*, 024401; (d) Profeta, M.; Mauri, F.; Pickard, C. J., Accurate First Principles Prediction of ^{17}O NMR Parameters in SiO_2: Assignment of the Zeolite Ferrierite Spectrum. *J. Am. Chem. Soc.* **2003,** *125*, 541-548.

188. Tkatchenko, A.; Scheffler, M., Accurate Molecular Van Der Waals Interactions from Ground-State Electron Density and Free-Atom Reference Data. *Phys. Rev. Lett.* **2009,** *102*, 073005.

189. (a) Palatinus, L.; Chapuis, G., SUPERFLIP - a computer program for the solution of crystal structures by charge flipping in arbitrary dimensions. *Journal of Applied Crystallography* **2007,** *40* (4), 786-790; (b) Palatinus, L.; van der Lee, A., Symmetry determination following structure solution in P1. *Journal of Applied Crystallography* **2008,** *41* (6), 975-984; (c) Palatinus, L.; Prathapa, S. J.; van Smaalen, S., EDMA: a computer program for topological analysis of discrete electron densities. *Journal of Applied Crystallography* **2012,** *45* (3), 575-580.

190. (a) Betteridge, P. W.; Carruthers, J. R.; Cooper, R. I.; Prout, K.; Watkin, D. J., CRYSTALS version 12: software for guided crystal structure analysis. *Journal of Applied Crystallography* **2003,** *36* (6), 1487-1487; (b) Cooper, R. I.; Thompson, A. L.; Watkin, D. J., CRYSTALS enhancements: dealing with hydrogen atoms in refinement. *Journal of Applied Crystallography* **2010,** *43* (5 Part 1), 1100-1107.